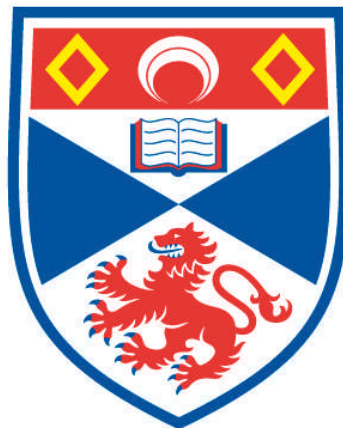


EQUILIBRIUM AND ERUPTION OF SOLAR CORONAL MAGNETIC STRUCTURES

C. D. C. STEELE

**A Thesis Submitted for the Degree of PhD
at the
University of St Andrews**



1990

**Full metadata for this item is available in
Research@StAndrews:FullText
at:**

<http://research-repository.st-andrews.ac.uk/>

Please use this identifier to cite or link to this item:

<http://hdl.handle.net/10023/4654>

This item is protected by original copyright

**This item is licensed under a
Creative Commons License**

**EQUILIBRIUM AND ERUPTION
OF SOLAR CORONAL
MAGNETIC STRUCTURES**

C. D. C. STEELE

Thesis submitted for the degree of Doctor of Philosophy of
the University of St. Andrews



Abstract

In this thesis magnetostatic and thermal equilibria of several coronal magnetic structures are considered.

A model is set up for the eruption of a prominence (modelled as a twisted flux tube) magnetically coupled to a coronal mass ejection (an overlying void and magnetic bubble). Two different prominence models are considered. In one a globally stable equilibrium becomes unstable and, in the other, equilibrium ceases to exist. In both cases, the components accelerate upwards before reaching constant velocities in a manner consistent with observations.

A cylindrically symmetric magnetic arcade in equilibrium with its axis on the photosphere is subjected to a base pressure perturbation. The perturbation is examined with the aim of seeking equilibrium configurations close to the original equilibrium. It is found that equilibria can only be found when the integral of the excess base pressure is zero. For an initial arcade whose field increases linearly with radial distance from the axis, neighbouring equilibria have been found.

Equations of thermal equilibrium along coronal loops with footpoint temperatures of 2×10^4 K are solved. Three fundamentally different categories of solution are found, namely hot loops, (corresponding to the hot corona), cool loops (relevant to fibrils, cool cores, and active-region prominences) and hot-cool loops with cool summits but much

hotter parts between the summit and the footpoints. Quiescent prominences may be modelled as hot-cool loops inclined to the prominence axis. Furthermore, warm loops at intermediate summit temperatures (8×10^4 K to 4×10^5 K) can exist, but the observed differential emission measure suggests these are uncommon. Thermal catastrophe may occur when the loop length or pressure is too small.

Many loops can be superimposed to form a coronal arcade. Two types of arcade are considered - one has its axis on the photosphere; the other is isobaric and has its axis below the photosphere. In both cases, cool material can exist high in the corona as is observed for prominences.

DECLARATIONS

I, Colin Duncan Constable Steele, hereby certify that this thesis has been composed by myself, that it is the record of my own work, and that it has not been accepted in partial or complete fulfilment of any other degree or professional qualification

Signed [REDACTED]

Date 20TH DEC 1989

I was admitted to the Faculty of Science of the University of St. Andrews under Ordinance General No. 12 in October 1986 and as a candidate for the degree of Ph.D. in October 1987.

Signed [REDACTED]

Date 20TH DEC 1989

I hereby certify that the candidate has fulfilled the conditions of the Resolution and Regulations appropriate to the degree of Ph.D.

Signature of Supervisor Date

In submitting this thesis to the University of St. Andrews I understand that I am giving permission for it to be made available for use in accordance with the regulations of the University Library for the time being in force, subject to any copyright vested in this work not being affected thereby. I also understand that the title and abstract will be published and that a copy of the work may be made and supplied to any bona fide library or research worker.

ACKNOWLEDGEMENTS

It would be incorrect for me to claim that this thesis could be produced without interactions with others.

First and foremost, I would like to thank my supervisor, Professor Eric Priest, whose advice, encouragement and inspiration were central to the work behind this thesis. Working as a member of a large group has allowed interactions and discussions with many other (both visitors and longer-term members of the group). In this capacity, I would particularly like to thank Dr. Alan Hood and Dr. Tahar Amari.

I would like to thank the University Computing Laboratory for use of their machines. I am grateful to all members of the Department of Mathematical Sciences for creating a pleasant atmosphere in which to work. In particular I would mention those inhabitants of the front corridor who contributed to the humour and friendship I associate with the place.

I acknowledge gratefully the financial support from the Science and Engineering Research Council.

To work effectively requires being in the correct frame of mind and there are many people (formerly or currently) in St. Andrews who have helped create the good times and see me through the bad times. To mention all by name would be impractical but I would particularly like to

mention those people I met through the Observatory, the
Astronomical Society, St. Leonards Church and Herkless
House.

CONTENTS

Chapter 1: Introduction	1
1.1 The Solar Corona	1
1.2 Solar Prominences	4
1.3 Solar Coronal Mass Ejections	8
1.4 Solar Coronal Loops	12
1.5 Equations	15
1.6 Outline of Thesis	23
Chapter 2: The Eruption of a Prominence and Coronal Mass Ejection which Drive Reconnection	26
2.1 Introduction	26
2.2 A Model for the Eruption	28
2.3 Results	42
2.4 Conclusions	51
Chapter 3: Non-Equilibrium of Cylindrical Magnetic Arcade	54
3.1 Introduction	54
3.2 The Analytical Model	55
3.3 Results	65
3.4 Conclusions	67

Chapter 4: Thermal Equilibrium of Coronal Magnetic Loops	69
4.1 Introduction	69
4.2 Equations of Thermal Equilibrium	69
4.3 Results	79
4.4 Conclusions	87
Chapter 5: Thermal Equilibrium of Coronal Magnetic Arcades with Axes on Photosphere	90
5.1 Introduction	90
5.2 Thermal Structure of Cylindrically Symmetric Arcades	90
5.3 Results	96
5.4 Variation of Parameters	106
5.5 Conclusions	109
Chapter 6: Thermal Equilibrium of Isobaric Coronal Magnetic Arcades with Axes Below Photosphere	113
6.1 Introduction	113
6.2 Results for Uniform Heating	114
6.3 Results for Magnetic Heating	119
6.4 Effects of Shearing the Arcade	127
6.5 Conclusions	146
Chapter 7: Conclusions and Suggestions for Further Work	150

CHAPTER ONE - INTRODUCTION

1.1 The Solar Corona

In addition to its obvious role in providing energy, the Sun plays a vital part in our understanding of the universe.

Although the Sun is a fairly typical middle-aged, main sequence star, it is the only star that can be observed in great detail. In order to understand the processes occurring in more distant stars, where observation yields only a limited amount of information, it is necessary to understand the equivalent processes on the Sun where detailed observations can be made.

Furthermore the Sun has been thought of as an astrophysical laboratory (albeit a laboratory where the conditions and experiments cannot be controlled). Here it is possible to observe the occurrence of physical processes which cannot be reproduced in the laboratory for reasons of temperature, and scale. The processes occurring in the Sun also give clues to similar processes occurring on larger scales in other parts of the universe.

Of particular interest to this study is the solar corona, one of three layers of atmosphere of the Sun. The lowest layer is the photosphere, a thin layer about 1 Mm in height, at temperatures between about 6600 K at its lower edge and 4300 K at its upper edge (Priest, 1982). The photosphere is at temperatures emitting in the visible part of the spectrum and so it forms the apparent surface of

the Sun.

Stretching above the photosphere for about 2 Mm is the chromosphere. Moving outwards in the chromosphere the temperature increases gradually from the temperature minimum at the top of the photosphere to a maximum of about 40 000 K at the top of the chromosphere. Certain visible spectral lines originate in the chromosphere, hence its name.

The corona starts at the top of the chromosphere and extends out to join onto the interstellar medium becoming more rarefied as one moves out. The corona is at much higher temperatures than the chromosphere. The boundary between the chromosphere and the corona (about 0.5 Mm thick) is known as the transition region and the temperature gradients here are the highest found on the Sun. At the top of the transition region the corona is at a temperature of about 2×10^6 K. This temperature reduces gradually as one moves outwards. The corona, in common with the other constituent parts of the Sun, exists in the plasma state where the atoms have been stripped of some or all of their electrons. The great majority of the corona is composed of hydrogen, of which each atom has lost its solitary electron; other rarer elements such as Iron, Nickel, Calcium and Argon have lost ten to fifteen electrons.

Historically the corona was visible only at total solar eclipses. Recently, however, coronagraphs have been developed and using these the corona has been studied in considerable detail for much longer periods of time.

Because the plasma pressure is small in the corona, the effects of the magnetic field are considerable. Rather than having a simple dipole field, the Sun has a magnetic field of considerable complexity which changes with time.

The effects of the magnetic field are two-fold. The magnetic field shepherds the plasma and is thought to be responsible for enhancements or deficiencies of the density in the corona. The second role is to provide energy for motion of the plasma. The magnetic field may change to a configuration with lower energy. The energy is released and this may cause motions in the corona.

Although motions take place in the corona, there are certain structures which remain static for considerable lengths of time. For this to be the case, the associated magnetic fields must be in stable equilibrium. A structure which is in a stable equilibrium will remain in such a condition when perturbed, as forces will restore the structure to its original condition. If, however, a structure in an unstable equilibrium is perturbed, the instability will tend to increase the magnitude of the perturbation and the structure will rapidly evolve away from the equilibrium.

Of particular interest is a stable equilibrium which becomes unstable as a parameter crosses a threshold value. This explains how a structure can remain stationary for a considerable length of time (stable equilibrium) but can then change rapidly (evolution from unstable equilibrium). Also of interest is the case where a stable equilibrium exists for a

range of values of a parameter up to a critical value beyond which no equilibria can be found at all. This is another way of a structure remaining stationary for a considerable time and then evolving rapidly.

The equilibria of certain coronal magnetic structures will be studied in succeeding chapters. The next few sections describe the relevant structures.

1.2 Solar Prominences

Prominences are regions of the solar corona which are cooler and denser than their surroundings by factors of 100 or more. The length of a prominence is much greater (up to around 1000 Mm) than its width or its vertical height and so prominences appear as long thin filaments. When seen against the bright disk, prominences appear dark, but when they appear on the limb they are seen as bright objects. For a full description of prominences see Tandberg Hanssen (1974), Ballester and Priest (1988b), Priest (1988b).

Prominences are known to be associated with magnetic fields and are observed to lie along the line of reversal of the line of sight polarity of the field.

Although prominences can be divided into many different types, two main divisions exist, namely quiescent prominences and active-region prominences. Quiescent prominences are the longer lived of the two, (up to about six months). They are located higher in the corona (about 50 Mm) and are associated with weaker magnetic fields (5 to

10 G). Active-region prominences are located in areas of stronger magnetic field.

Many models have been put forward for the magnetic structure of a prominence, some of the more notable models being mentioned below. These utilise the fact that the magnetic field is in equilibrium. The first models (Menzel, 1951, Dungey, 1953), were isothermal and magnetostatic. A model by Kippenhahn and Schluter (1957), Fig 1.1 assumes that the prominence exists in a dip at the top of a coronal arcade. This involves no X-type neutral line beneath the prominence and no field reversal.

A variation on the Kippenhahn-Schluter model is that proposed by Poland and Anzer (1971) where the prominence is considered in two parts, an isothermal central region and a region outside where the temperature varies.

A second model (Kuperus and Raadu, 1974) (Figure 1.2) places an X-type neutral line beneath the prominence and an arcade over the prominence thus shielding it from the hot corona. This model was extended by Anzer and Priest (1985) who included a potential field in the corona.

Ballester and Priest (1988a) modelled a prominence as a sheet in two dimensions. They extended the

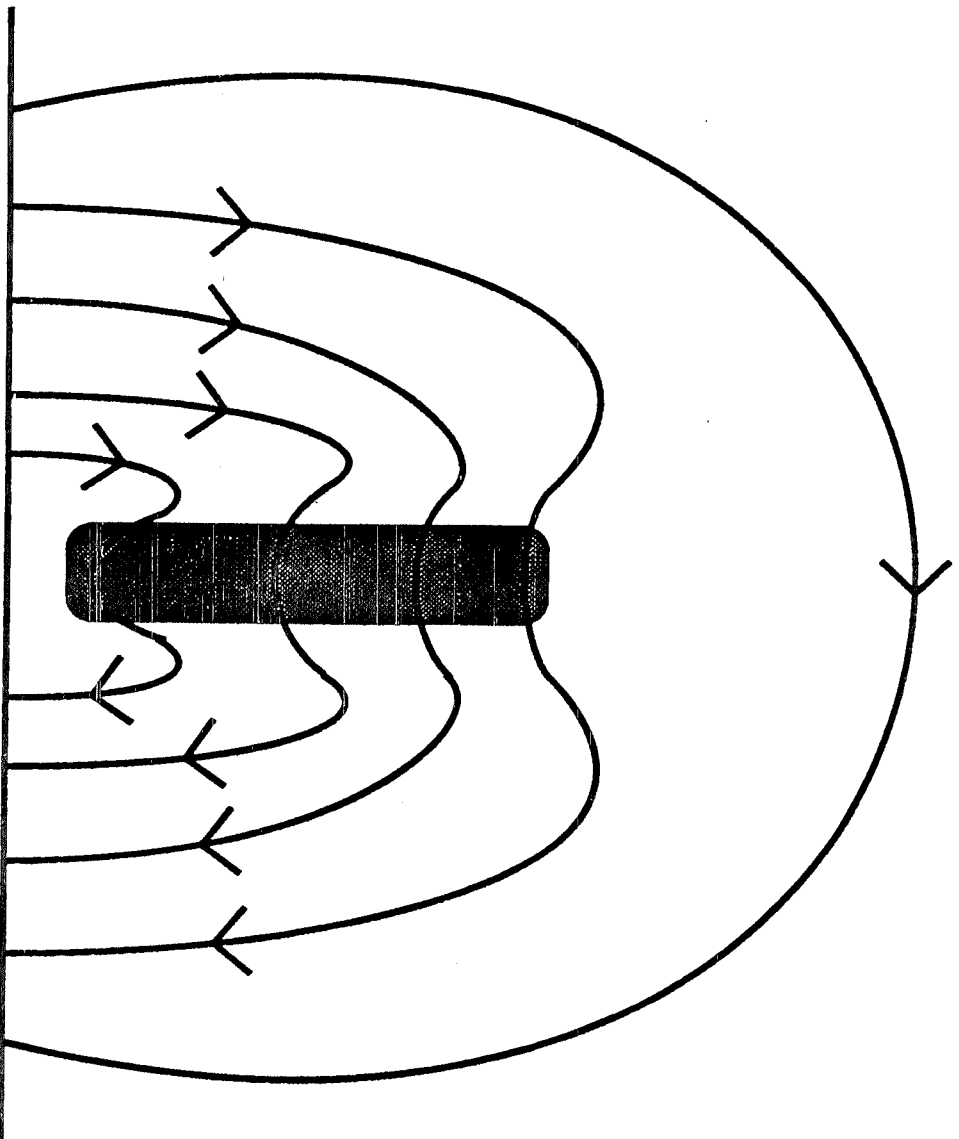


Figure 1.1 The form of the Kippenhahn-Schluter prominence model. The prominence is represented by the shaded region.

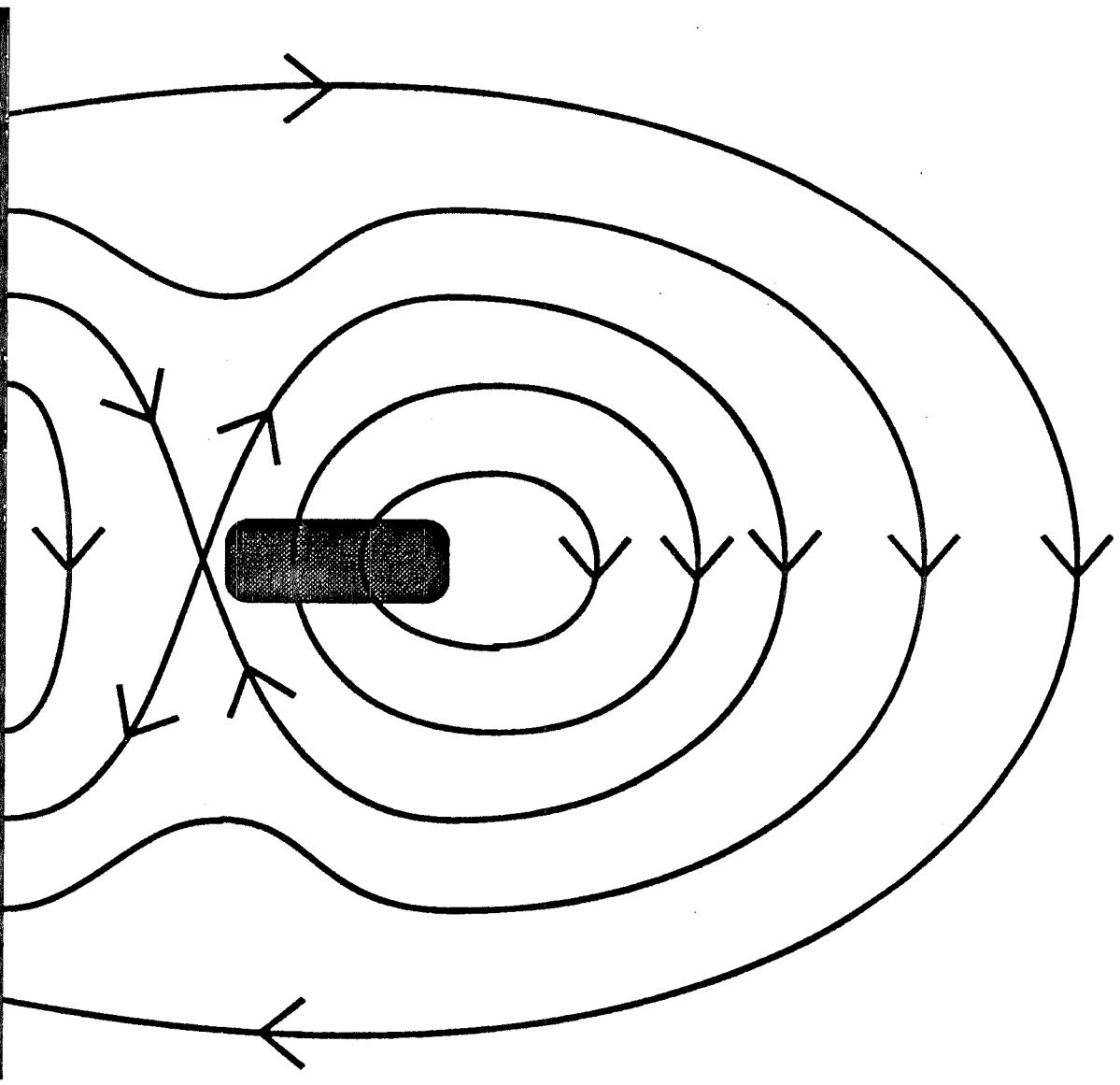


Figure 1.2 The form of the Kuperus-Raadu prominence model. The prominence is represented by the shaded region.

Kippenhahn-Schluter model to allow vertical variations. As only the area close to the prominence itself was modelled, the analysis applies to the Kuperus-Raadu model as well.

Observations (Leroy et. al., 1984) of a sample of several hundred prominences would indicate that those closer to the solar surface are mainly of Normal Polarity (i.e. the magnetic field in the prominence is in the same direction as the overlying field) while those further from the solar surface tend to be of the Inverse Polarity type.

The models proposed above are two-dimensional whereas the magnetic field of a prominence exists in three dimensions. The models above assume that no fields exist along the prominences while observations (Tandberg Hanssen and Anzer, 1970, Leroy, 1988) indicate that the longitudinal component is the dominant one.

Priest, Hood and Anzer (1989) (Figure 1.3) proposed a model where the prominence is represented as a curved and twisted flux tube. If the twist is great enough, the prominence is supported against gravity by the field lines which are concave upwards.

So far prominences have been considered in equilibrium but they are known to erupt i.e. to move upwards rapidly and gradually disperse into space, sometimes reforming at the same point.

For a study of the eruption of prominences the role of the equilibrium is crucial. Obviously a prominence in stable

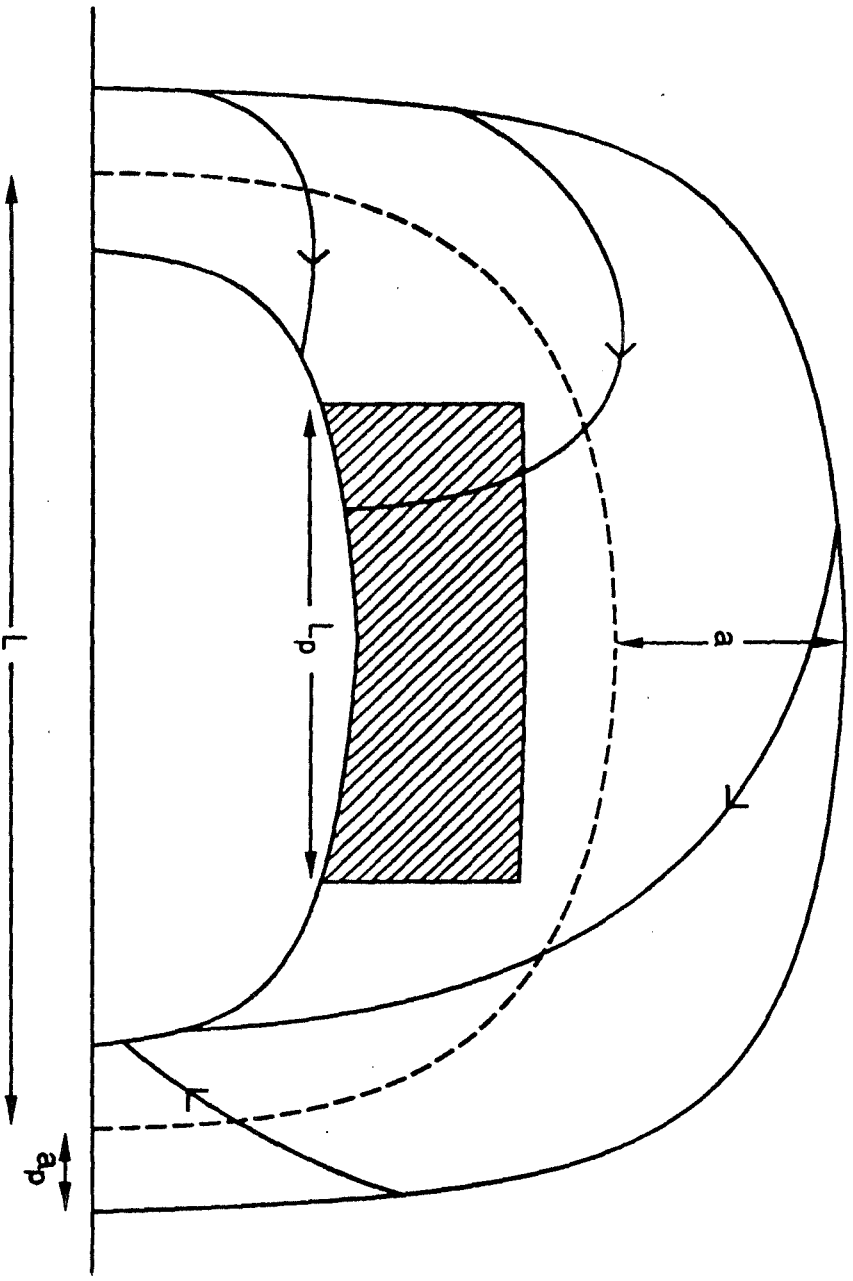


Figure 1.3 The Priest-Hood-Anzer prominence model. The prominence is the hatched area in the centre.
[Courtesy E. R. Priest.]

equilibrium will not erupt. For an eruption to take place either the equilibrium must become unstable or it must be lost.

In general magnetic structures of the arcade-type configuration would be unstable (Anzer, 1968) were it not for line tying at the dense photosphere suppressing the kink instability (Raadu, 1972).

Equilibrium can be lost if the prominence height (Hood and Priest, 1980), the twist of the magnetic field (De Moulin and Priest, 1988) or the inter-footpoint distance (Browning and Priest, 1986) become too great.

If a prominence is modelled as a line current (Van Tend and Kuperus, 1978) an equilibrium can be found. Stability analysis (Kuperus and Van Tend, 1981) showed that stable equilibrium is lost if the current is too great.

Priest and Forbes (1989) considered a prominence as a twisted flux tube being repelled from the solar surface by magnetic pressure. Originally this repulsion is balanced by a background field, but if the background field becomes too small, equilibrium is lost and an eruption begins.

Once the prominence eruption has begun, reconnection of the magnetic field lines can aid the further rise of the prominence. This has the additional effect of creating a solar flare, a region of radically enhanced brightness, due to the release of energy. However flares are observed to begin after rather than before eruption (Harrison, 1986) so it is

the eruption that drives the flare rather than vice-versa.

Several models exist where a prominence erupts at the same time as a coronal mass ejection. Some of these models will be mentioned in section 1.3.

1.3 Solar Coronal Mass Ejections (CME's)

Coronal transients or mass ejections occur when large amounts of plasma are ejected from the Sun at velocities ranging from 100 km/s to more than 1000 km/s (MacQueen, 1980, Gosling et. al., 1976). They are in more than 60% of cases associated with prominences (Webb and Hundhausen, 1987) and sometimes also with solar flares. Observations (Gosling et al, 1976) indicate that those events associated with flares have higher eruption velocities than those associated with prominences alone. Their appearance is generally loop-like but Solar Maximum Mission and P-78 coronagraph observations (Hundhausen et al, 1984b; Fisher, 1984; Wagner, 1984; Hildner et al, 1986; Low, 1986) and polarisation measurements (Crifo, Picat and Cailloux, 1983) suggest the loop is merely a section across a three-dimensional bubble or arcade. This represents magnetic flux and plasma ahead of a cavity which is thought to contain a stronger magnetic field and moves ahead of an erupting prominence (Hundhausen, MacQueen and Sime, 1984). This three-fold picture of bubble, cavity and prominence is quite different from the earlier ideas and models which were stimulated by Skylab observations.

Most coronal mass ejections (including all events

observed on the Skylab mission) are preceded by a forerunner, a tenuous broad envelope leading the main component (Jackson and Hildner, 1978, Jackson, 1981). During eruption the thickness of the bubble or arcade increases with its height (MacQueen and Cole, 1985). The mass and density of the plasma in the legs of the coronal mass ejection varies with time indicating that mass flows are taking place (Anzer and Poland, 1979).

Rates of coronal mass ejections are greater at sunspot maximum (Hundhausen, et. al. 1984a, Howard et. al. 1985) than at sunspot minimum (Hildner et. al., 1976). At sunspot minimum only 10% of Coronal Mass Ejections are observed at latitudes greater than 30 degrees (Munro et. al., 1979) while at sunspot maximum, Coronal Mass Ejections are observed at higher latitudes, (Sheeley et. al., 1980, Howard et. al., 1985, Hundhausen et. al., 1984a, Wagner, 1984).

An inverse correlation has been found between the CME rate and the 'correlation lifetime', a measure of the time it takes the corona in general to change i.e. the greater the amount of change in the corona, the greater the rate of coronal mass ejections (Sime, 1989).

Pneuman (1980) modelled a coronal mass ejection as a simple, curved flux tube without an associated prominence. This is subject to the forces caused by a longitudinal field within the flux tube, a field beneath the flux tube supporting it, and gravity. The flux tube is originally in neutrally stable equilibrium but, when the underlying field is increased, the resulting upward force causes the flux

tube to rise like a coronal mass ejection. Pneuman's model does not, however, include a prominence underneath and, since the equilibrium is neutrally stable, the model does not explain how the structure remains stationary before the eruption since any small perturbation would set the flux loop in motion.

Anzer and Pneuman (1982) considered a magnetically coupled coronal mass ejection and prominence. The coronal mass ejection takes the form of either an arcade or a loop in their model. There is a longitudinal field in the prominence and a field along the loop (or arcade). Reconnection takes place under the prominence and this helps to drive the system upwards. The system starts from equilibrium but not a stable equilibrium so that any small perturbation sets the system in motion.

Mouschovias and Poland (1978) modelled the coronal mass ejection as a loop with a longitudinal magnetic field and an azimuthal magnetic field. However, it is assumed that this twisted loop rises at a constant velocity so that it is always in equilibrium.

Yeh and Dryer (1981) showed that forces other than a self-induced magnetic force (such as pressure gradients or the magnetic buoyancy force) are necessary to propel a loop outwards.

The above authors have modelled a coronal mass ejection as a loop or an arcade, but observational evidence now indicates that the proper form is a bubble. Since the

cross-section through a bubble is the same as the lateral cross-section through an arcade, similar equations hold.

Initially the configuration of prominence and overlying arcade or bubble is in equilibrium but later the eruption takes place. Either the equilibrium has become unstable or equilibrium has been lost. One limiting possibility is that the magnetic field around the prominence evolves into an unstable or non-equilibrium configuration and then drives the overlying magnetic arcade.

An alternative to the prominence initiating the eruption is that the overlying arcade evolves until it is no longer in stable equilibrium and then its eruption stimulates the prominence to erupt by removing stabilising field lines (Low, 1981; Wolfson, 1982; Priest, 1988a).

Priest (1988a) considered a cylindrically symmetrical arcade with its axis below or on the photosphere and free to move, and introduced an excess pressure at the centre of the base. When the axis of this arcade is below the photosphere (and the field is contained in a segment smaller than a semi-circle) this excess pressure causes the axis to rise and the field to cover a larger segment. When the axis lies on the photosphere, and the arcade is semi-circular, a further increase in the axial pressure does not give an equilibrium of the form sought. Priest speculated that an eruption may take place when this occurs. However the arcade was constrained to be cylindrically symmetric so that no radial field component was permitted and it is important to decide whether more general equilibria may

indeed be possible.

1.4 Solar Coronal Loops

Instead of being homogeneous and uniform as was previously thought, it is now known that the solar corona contains a large number of loops which probably outline the coronal magnetic field. An individual loop normally lasts from about a day upwards with a loop system having a much greater lifetime. Loops can be divided into 5 broad categories (Priest, 1982) namely interconnecting loops which link two active regions, active region-loops within active-regions, quiet region loops outside active-regions and simple-flare and post-flare loops which are observed during and after solar flares.

There has been considerable work on the equilibrium profiles of the temperature along these loops (Priest 1978,1981), the following list of authors being representative rather than exhaustive. One facet of this problem which is of particular interest is the existence of cool loops (with temperatures less than about 10^5 K) since these may form elementary structures of a solar prominence and they may explain the existence of excess plasma in differential emission curves at low temperature, which has long represented a major puzzle in solar physics (Athay, 1966). Observations of Dollfus (1971) and Fisher (1972) give evidence of cooler material in the corona.

Rosner, Tucker and Vaiana (1978), using an order of magnitude analysis, derived a relation between the loop

length, the plasma pressure, and the maximum temperature along the loop. Hood and Priest (1979) solved the equations of thermal equilibrium along a coronal loop in the absence of gravity. They discovered the existence of cool solutions with summit temperatures below 10^5 K and suggested that they may explain the existence of active region prominences. Craig, McClymont and Underwood (1978) also considered loops at constant pressure. Priest and Smith (1979) applied these techniques to an arcade consisting of a succession of loops and gravitational effects were considered by Wragg and Priest (1981) who used a footpoint temperature of 2×10^4 K. Landini and Monsignori Fossi (1975) also considered the effect of gravity and considered the case for stars other than the Sun. She, Malherbe and Raadu (1986) and Landini and Monsignori Fossi (1981) found hot solutions again with a more realistic footpoint temperature of 2×10^4 K. A great deal of work has been done too on the stability of these loops (e.g. Antiochos (1979), Habbal and Rosner (1979), Craig, Robb and Rollo (1982)).

Observations show that the differential emission measure (representing the amount of coronal material at a particular temperature) has a strong minimum at temperatures around 10^5 K, but is greater at higher and lower temperatures (Athay 1966, Dupree and Goldberg 1967). Several explanations have been put forward to explain the cooler material. Athay (1984) suggested spicules. Rabin and Moore (1984) put forward the idea that the high emission at low temperatures was due to electric currents. The general form of the observed differential emission curve is uniform, not only for different portions of the Sun but also

for different stars so the emissions at high and low temperatures must be caused by coupled mechanisms, or more likely, by the same mechanism. For this reason, Antiochos and Noci (1986) proposed that the high emission measure at low temperatures is caused by the cool loop solutions discovered by Hood and Priest (1979) with temperatures between 2×10^4 K and 10^5 K.

Loops at coronal temperatures have often been observed. For example Sheeley et al (1975) report emission from Fe XV, Mg IX and Ne VII which occur at temperatures in excess of 2×10^6 K, 10^6 K and 5×10^5 K respectively.

Cool loops have been observed in the solar corona. Foukal (1975) studied some of the brightest loops from the Skylab data and found temperatures as low as 10^4 K. These cool loops formed the cores of brighter, hotter loops. Foukal (1976) subsequently found similar temperatures in active-region loops. Temperatures in such loops were subsequently found to be as low as 6×10^3 K (Foukal 1981).

Levine and Withbroe (1977) observed cores to loops visible at Lyman α and Lyman continuum temperatures - as low as 10^4 K. Cool loops were also observed by Bonnet and Tsiropoula (1981).

An extreme example of a cool loop is a solar prominence. The temperature is of the order of 10^4 K, much less than the surrounding corona. In or near an active region the magnetic field is aligned along the prominence and it may be modelled by a loop that is cool along its length. A

quiescent prominence consists of many threads inclined to the prominence axis. Each thread may be modelled by a magnetic loop with a cool summit and with hot legs either side of the prominence.

Craig, McClymont and Underwood (1978) showed that the observed differential emission measure cannot be produced by a single loop and that an assembly of loops of some form must be present. Loops are known to form arcades in the corona (Vaiana et. al. 1973, Serio et. al. 1978).

Hood and Anzer (1988) reconsidered qualitatively the equations of thermal equilibrium with footpoint temperatures of 2×10^4 K (i.e. much lower than those of Hood and Priest (1979)). They used a phase plane analysis to identify the different types of solution that are possible.

1.5 Equations

The equations used as a starting point are Maxwell's Equations

$$\nabla \times \underline{B} = \mu \underline{j} + \frac{1}{c^2} \frac{\partial \underline{E}}{\partial t} \quad (1.1)$$

$$\nabla \cdot \underline{B} = 0 \quad (1.2)$$

$$\nabla \times \underline{E} = - \frac{\partial \underline{B}}{\partial t} \quad (1.3)$$

$$\nabla \cdot \underline{E} = \frac{\rho^*}{\epsilon} \quad (1.4)$$

where \underline{E} and \underline{B} represent the electric and magnetic field strengths respectively, \underline{j} is the current density, μ and ϵ are the magnetic permeability and the permeativity of free space respectively, ρ^* is the charge density and c is the speed of

light in a vacuum.

1.5.1 Magnetohydrodynamics

In magnetohydrodynamics, the study of the interactions between a plasma and a magnetic field, certain assumptions are made (Priest, 1982) which normally include the following.

The plasma is treated as a single continuous fluid and is assumed to be in thermodynamic equilibrium.

The coefficients ϵ and μ (equations (1.1) and (1.4)) are assumed to be uniform and the plasma properties are assumed to be isotropic except for the coefficient of thermal conductivity which is much greater along the field than across the field.

It is assumed that all velocities are much less than that of light and that relativistic effects can be ignored. It is assumed that the Sun provides an interial frame of reference despite its rotation and that the magnetic field is independent of the choice of frame.

It is assumed that the electric field is determined by

$$\mathbf{E} = -\nabla \times \mathbf{B} + \mathbf{j} / \sigma \quad (1.5)$$

where σ is the electrical conductivity. This is the simple form of Ohm's Law.

Equations (1.1) and (1.2) are of particular interest as they state how the magnetic field varies. Equation (1.2)

states that the divergence of the magnetic field is zero, i.e. there are no sources or sinks of magnetic field lines. From the vector identity

$$\nabla \cdot (\nabla \times \mathbf{E}) = 0$$

for all vectors \mathbf{E} , \mathbf{B} can be expressed as

$$\mathbf{B} = \nabla \times \mathbf{A} \quad (1.6)$$

where \mathbf{A} is referred to as the magnetic potential.

1.5.2 Ampere's Law

The first Maxwell equation (1.1) provides a useful expression for the current density \mathbf{j} . The equation, however, can be simplified. Firstly, the orders of magnitude of the two terms on the right-hand side of (1.1) are compared.

If l_0 and t_0 are typical length and time scales and E_0 and B_0 are typical values of the electric and magnetic fields, then in order of magnitude, (1.3) can be expressed as

$$\frac{E_0}{l_0} \approx \frac{B_0}{t_0} \quad (1.7)$$

The ratio of the second term on the right-hand side of (1.1) to the left-hand side is, in order of magnitude

$$\begin{aligned} \frac{\frac{1}{c^2} \frac{E_0}{t_0}}{\frac{B_0}{l_0}} &\approx \frac{1}{c^2} \frac{l_0^2}{t_0^2} \quad \text{by (1.7)} \\ &= \frac{v_0^2}{c^2} \end{aligned} \quad (1.8)$$

where $v_0 = l_0 / t_0$ is a typical velocity.

It is an inherent assumption of magnetohydrodynamics that all velocities are negligible compared to c . The conclusion is that the first term on the right-hand side of (1.1) is dominant i.e.

$$\mathbf{j} = \frac{1}{\mu} \nabla \times \mathbf{B} \quad (1.9)$$

1.5.3 The Lorentz Force

The equation of motion of a particle is

$$\rho \frac{D\mathbf{v}}{Dt} = -\nabla p + \mathbf{j} \times \mathbf{B} + \mathbf{E} \quad (1.10)$$

(Priest, 1982) where D/Dt is the time derivative following the motion of the particle. The term ∇p represents a plasma pressure gradient, the term $\mathbf{j} \times \mathbf{B}$ represents the Lorentz force and \mathbf{E} represents any further forces (e.g. gravity, which is considered in chapter 2 and viscosity which is not considered here).

The Lorentz term can be investigated in more depth. Considering equation (1.9) gives

$$\mathbf{j} \times \mathbf{B} = \frac{1}{\mu} (\nabla \times \mathbf{B}) \times \mathbf{B} \quad (1.11)$$

which by a vector identity becomes

$$\mathbf{j} \times \mathbf{B} = (\mathbf{B} \cdot \nabla) \mathbf{B} / \mu - \nabla \left(\frac{B^2}{2\mu} \right) \quad (1.12)$$

Equation (1.12) has two terms on the right-hand side. The first of these represents the change in \mathbf{B} along the field lines and the term can be written

$$\frac{B}{\mu} \frac{d}{ds} (B \hat{\mathbf{s}}) = \frac{d}{ds} \left(\frac{B^2}{2\mu} \right) \hat{\mathbf{s}} + \frac{B^2}{\mu} \frac{\hat{\mathbf{n}}}{R_c} \quad (1.13)$$

where $\hat{\mathbf{u}}$ is the unit vector parallel to the field \mathbf{B} and $\hat{\mathbf{n}}$ is the unit vector perpendicular to the field in the plane of curvature and R_c is the radius of curvature. The second term in (1.13) represents a magnetic tension term which acts to pull particles towards the centre of curvature should the field lines be curved. If the field line is straight, this term is zero. Its magnitude increases as the radius of curvature of the field decreases. The magnitude of this tension term is proportional to the square of the magnetic field strength.

The second term on the right-hand side of (1.12) represents a magnetic pressure gradient where the magnetic pressure is given by $B^2/2\mu$. The component parallel to the field cancels with the first term on the right-hand side of (1.13) leaving only forces perpendicular to the magnetic field. This magnetic pressure acts to force field lines from areas of high magnetic pressure to areas of low magnetic pressure.

Sometimes it is useful to consider the Lorentz force as $\mathbf{j} \times \mathbf{B}$ while on other occasions it is more convenient to treat the magnetic pressure and magnetic tension terms separately. Both approaches will be used in subsequent chapters.

1.5.4 Flux Tubes

A flux tube is the volume enclosed by the set of field lines which intersect a closed curve (Priest, 1982). A coronal loop is an example of a flux tube.

Equation (1.2) may be integrated over the three

dimensions of a flux tube

$$\iiint_V \nabla \cdot \underline{B} \, dv' = 0 \quad (1.14)$$

so by Gauss's Law, where V is the volume of the flux tube, and if S represents the surface of the tube, the left hand side of (1.14) equals

$$\iint_S \underline{B} \cdot d\underline{S} = 0 = \iint_{S_1} \underline{B} \cdot d\underline{s} + \iint_{S_2} \underline{B} \cdot d\underline{s} \quad (1.15)$$

where S_1 and S_2 represent the surfaces at the ends of the flux tube. There is no contribution from the curved sides of the flux tube as the field there is perpendicular to the normal to the surface. Since the normals to S_1 and S_2 point in opposite directions, (1.15) reveals that the quantity

$$\iint_S \underline{B} \cdot d\underline{S}$$

is constant as one travels along the flux tube. This quantity is known as the magnetic flux.

In the case where the field is constant over the flux surface, the flux can be written as BA where B is the field strength and A is the area of the surface. Thus as one travels along a flux tube where the field does not vary laterally,

$$BA = \text{constant} \quad (1.16)$$

1.5.5 Thermal Equilibrium

The equation of thermal conduction may be written

$$L = \underline{\nabla} \cdot \underline{q} + L_r - j^2 / \sigma - h \quad (1.17)$$

where L is the net rate of energy loss, which will be zero in the case of thermal equilibrium. Of the terms on the right-hand side of (1.17), \underline{q} is the heat flux due to particle conduction, L_r is the net radiation, j^2/σ is the ohmic dissipation and h represents all other heating sources (the source considered here being coronal heating).

The heat flux may be written as

$$\underline{q} = -\kappa \underline{\nabla} T \quad (1.18)$$

where κ is the thermal conduction tensor. The term $\underline{\nabla} \cdot \underline{q}$ may now be written

$$\underline{\nabla} \cdot \underline{q} = -\underline{\nabla}_{\parallel} (\kappa_{\parallel} \underline{\nabla}_{\parallel} T) - \underline{\nabla}_{\perp} (\kappa_{\perp} \underline{\nabla}_{\perp} T) \quad (1.19)$$

At the temperatures and fields found in the solar corona, the terms perpendicular to the field can be neglected (Spitzer, 1962).

If the field strength varies (and hence the area enclosed by a flux tube varies) the field is orientated in slightly different directions at different points and to talk about a rectilinear coordinate along the field is incorrect. Coordinates used must be one along the field, and two perpendicular to the field. Equation (1.19) becomes

$$\underline{\nabla} \cdot \underline{q} = -\frac{1}{h_2 h_3} \frac{d}{ds} \left(\frac{\kappa_{\parallel} h_2 h_3}{h_1} \frac{dT}{ds} \right) \quad (1.20)$$

where h_1 , h_2 and h_3 , are the scale factors for the three directions used. The factor h_1 is equal to unity and $h_2 h_3$ is

proportional to the area enclosed by the flux tube. Thus (1.19) becomes

$$\begin{aligned} \nabla \cdot \mathbf{q} &= - \frac{1}{A} \frac{d}{ds} \left(A \kappa \frac{dT}{ds} \right) \\ &= - B \frac{d}{ds} \left(\frac{\kappa}{B} \frac{dT}{ds} \right) \end{aligned} \quad (1.21)$$

Equation (1.17) thus becomes (in the case of thermal equilibrium and neglecting ohmic dissipation)

$$0 = - B \frac{d}{ds} \left[\frac{\kappa}{B} \frac{dT}{ds} \right] + L_r - h \quad (1.22)$$

The coefficient $\kappa_{||}$ behaves as $\kappa_0 T^{5/2}$ where κ_0 is given the value $10^{-11} T^{5/2} \text{ W m}^{-1} \text{ K}^{-1}$ (Spitzer, 1962). Thus

$$B \frac{d}{ds} \left[\frac{\kappa_0}{B} T^{5/2} \frac{dT}{ds} \right] = L_r - h \quad (1.23)$$

As the mechanisms responsible for coronal heating are not, as yet, fully understood, the exact form of the term h is not clear. It is, however, a reasonable assumption that the heating is proportional to the plasma density.

The radiative loss function L_r (the amount of radiation emitted by the plasma) has been calculated by a number of different authors (e.g. Cox and Tucker, 1969, Tucker and Koren, 1971, McWhirter et al., 1975, Raymond and Smith, 1977). There is a peak at around 10^5 K but the loss function is less at higher and lower temperatures.

Hildner (1974) assumed that the radiative function could be approximated by the function $\rho^2 X T^\alpha$, where X and α constant for particular ranges of the temperature (see Table 1.1).

Table 1.1

Temperature Range	X (kg ⁻¹ m ⁵ s ⁻³ K ^{-α})	α
T ≤ 1.5 x 10 ⁴ K	4.92 x 10 ⁻⁶⁷	7.4
1.5 x 10 ⁴ K ≤ T ≤ 8 x 10 ⁴ K	1.2 x 10 ⁻⁴³	1.8
8 x 10 ⁴ K ≤ T ≤ 3 x 10 ⁵ K	8.0 x 10 ⁻³⁵	0.0
3 x 10 ⁵ K ≤ T ≤ 8 x 10 ⁵ K	3.94 x 10 ⁻²¹	-2.5
8 x 10 ⁵ K ≤ T	5.51 x 10 ⁻³⁰	-1.0

This division of the temperature into five ranges was an extension of an earlier scheme with three temperature ranges (Hildner, 1971)

Thus, the equation of thermal equilibrium in a coronal loop becomes

$$B \frac{d}{ds} \left[\frac{\kappa_0}{B} T^{5/2} \frac{dT}{ds} \right] = \frac{p^2}{4 R^2} X T^{\alpha-2} - h \quad (1.24)$$

1.6 Outline of Thesis

In subsequent chapters equilibria and evolution from equilibrium of several coronal magnetic structures will be considered.

Chapter 2 (see also Steele and Priest 1988, 1989a) deals with a prominence, modelled as a twisted flux tube, originally in magnetostatic equilibrium when the forces of magnetic pressure, magnetic tension and gravity are considered. Equations describing this equilibrium will be

derived and the stability tested by means of a linear perturbation analysis. Of particular interest is the transition from stable to unstable equilibria or a loss of equilibrium when a parameter is changed. In those cases it is possible to perturb a stable equilibrium in such a way that an eruption occurs. In this way it is hoped to model the eruption of a prominence. If necessary reconnection beneath the prominence can be modelled to aid the eruption once it has started.

Subsequently an overlying bubble is fitted over the prominence with a gap or cavity lying between the two components. Again equations of equilibrium are derived and perturbation of a stable equilibrium can result in an eruption of a prominence and coronal mass ejection

Chapter 3 (see also Steele et. al. 1989) deals with the equilibrium of a cylindrical arcade with its axis on the photosphere. This arcade originally contains magnetic field and plasma within a certain radius of the axis and only plasma further from the axis. The pressure exerted at the photosphere is perturbed to see whether neighbouring equilibria can be found. If no neighbouring equilibria can be found, the arcade will either erupt or collapse depending on the sign of the base perturbation. Should an eruption take place it may model the eruption of a coronal mass ejection.

Thermal equilibria of coronal loops is considered in Chapter 4 (see also Steele and Priest (1989b)). Hood and Anzer (1988) considered in detail equations describing such a situation but did not find numerical solutions. It is hoped to

find numerical solutions for the thermal structure of coronal loops with footpoint temperatures of 20 000 K and zero temperature gradients at the summits and to find out how such solutions change as two parameters are varied. The case is considered where the effects of gravity are neglected and the cross-sectional area of the loop (and hence the magnetic field strength) is constant along the loop.

In Chapters 5 and 6, the same equations as in Chapter 4 are solved, but rather than considering an isolated field line, an assembly of such field lines is considered to form a cylindrical arcade and the thermal structure of this arcade is to be found. Of the many possible forms for a cylindrical arcade two are chosen. The first (Chapter 5, see also Steele and Priest, 1989c) incorporates pressure variations within the arcade and places the axis on the solar photosphere. The second is an isobaric arcade with its axis beneath the photosphere. The latter arcade (Chapter 6) is subsequently sheared and the resultant thermal structure is found.

Finally, in chapter 7, the conclusions and suggestions for further work are presented.

CHAPTER TWO - THE ERUPTION OF A PROMINENCE AND CORONAL MASS EJECTION WHICH DRIVE RECONNECTION

2.1 Introduction

Some of the properties of prominences and coronal mass ejections have been presented in sections 1.2 and 1.3 together with descriptions of some of the relevant models. The Coronal Mass Ejection eruption models due to Pneuman (1980), Anzer and Pneuman (1982) and Mouschovias and Poland (1978) are particularly relevant although each model contains weak features on which it is proposed to improve.

Pneuman and Mouschovias and Poland modelled their Coronal Mass Ejections as loop structures. It is now well known that a three dimensional structure is more appropriate. Anzer and Pneuman's model applies to both loop and arcade structures. A bubble structure may, however, be more appropriate.

The treatment of equilibrium and stability thereof is another area where care must be taken. The model of Mouschovias and Poland assumes that the loop rises at a constant velocity so that the forces always balance. The models due to Pneuman and due to Anzer and Pneuman both have the system erupting from a neutrally stable equilibrium. None of the above cases explains how the system can start from a stable equilibrium.

Anzer and Pneuman assumed that magnetic reconnection takes place beneath the prominence. The amount of reconnected flux is imposed and the eruption is allowed to proceed accordingly. Thus the reconnection leads the eruption in their model, but flare observations (Harrison, 1986) show that reconnection follows eruption by several tens of minutes.

Yeh and Dryer (1981) showed that forces other than a self-induced magnetic force (such as pressure gradients or the magnetic buoyancy force included here) are necessary to propel a loop outwards.

The object of this study is to produce a qualitative model for a coronal mass ejection which takes account of the current understanding of bubble, cavity and prominence. It combines some of the properties of each of the models due to Pneuman, Anzer and Pneuman, and Mouschovias and Poland in a more realistic manner. The loop transient is modelled here as a bubble. The prominence underneath is modelled as a twisted flux tube with both longitudinal and azimuthal field components. The field in the "loop" of the coronal mass ejection is assumed to be in the same direction as the azimuthal field. In the cavity between the prominence and bubble the magnetic field is orientated in the same direction. Finally the field in the region beneath the prominence is allowed to reconnect as the prominence rises.

Reconnection in this model is driven by the rising prominence rather than being itself the driver. Clearly this

qualitative model complements fully numerical solutions of the MHD equations which have their own limitations too.

2.2 A Model for the Eruption

The coronal mass ejection is regarded here as a hemispherical bubble reaching down to the solar surface at its edges (Figure 2.1). At its uppermost point its upper edge is a distance S_1 from the solar centre and its lower edge is a distance S_2 from the solar centre. The midpoint between the upper and lower edges is a distance S from the solar centre and the thickness of the bubble is D . The bubble subtends an angle 2θ at the solar centre. Inside this bubble of curvature R_a there is a field of strength B , and a plasma of mass density ρ .

The prominence is modelled as a flux loop with radius of curvature R_c lying below the bubble. At its highest the centre of the loop is a height R above the solar centre and its thickness is h . The loop possesses a magnetic field of strength B_l orientated in the same direction as the loop, and an azimuthal field of strength B_{az} . The prominence contains plasma of density ρ_f and subtends an angle 2ϕ at the solar centre.

Between the prominence and the bubble there is a magnetic field of strength B_2 orientated in the same direction as the fields B and B_{az} . This field curves round underneath the prominence. Part of it goes down to the solar

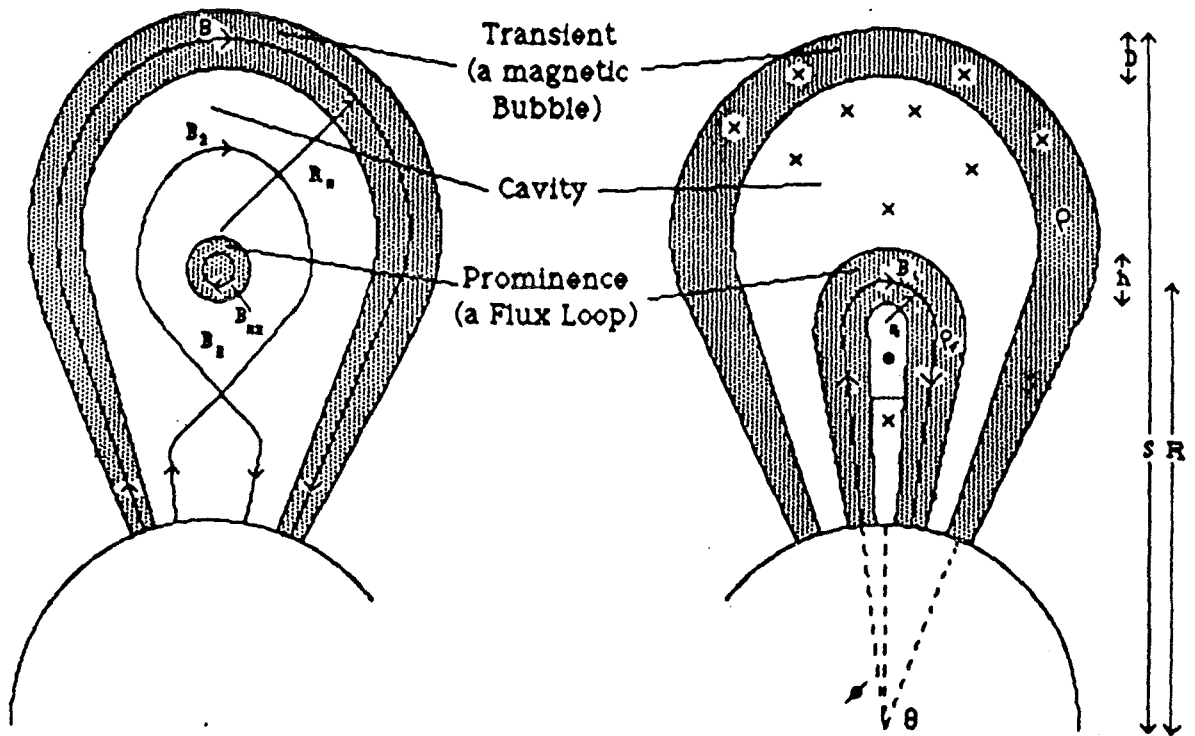


Figure 2.1 Two orthogonal sections through the prominence and coronal mass ejection, the second being in the plane of the prominence.

surface but part of it closes upon itself below the prominence. This field can be supplemented by reconnection beneath the prominence.

Two views of the configuration are shown in Figure 2.1.

An element at the top of the bubble is subject to the following forces (Priest, 1982): an upward force of magnitude $B^2/\mu D$ due to a magnetic pressure gradient between a point midway between the inner and outer edges of the bubble and the outside; a downward magnetic tension force of magnitude $B^2/\mu R_a$; a downward gravitational attraction of the Sun of magnitude GM_\odot/S_1^2 . It is assumed that all quantities vary smoothly across the prominence and bubble and approach the external quantities at the boundaries (Pneuman, 1980). Thus the MHD equation of motion may be written

$$\rho \frac{d^2 S_1}{dt^2} = \frac{B^2}{\mu D} - \frac{B^2}{\mu R_a} - \rho \frac{GM_\odot}{S_1^2} \quad (2.1)$$

An element at the highest point of the underside of the bubble is subject to the following forces: an upward force of magnitude $(B_2^2 - B^2)/\mu D$ due to the magnetic pressure gradient; a downward magnetic tension force of magnitude $B^2/\mu R_a$ due to the field B ; a gravitational force acting downwards with magnitude GM_\odot/S_2^2 . Thus the MHD equation of motion here is

$$\rho \frac{d^2 S_2}{dt^2} = \frac{B_2^2}{\mu D} - \frac{B^2}{\mu D} - \frac{B^2}{\mu R_a} - \frac{GM_\odot}{S_2^2} \rho \quad (2.2)$$

Linear combinations of (2.1) and (2.2) can be taken to find differential equations for the behaviour of S and D, namely

$$\frac{d^2S}{dt^2} = \frac{B_2^2}{2\mu\rho D} - \frac{B^2}{\mu\rho R_a} - \frac{GM_\odot}{S^2} \quad (2.3)$$

$$\frac{d^2D}{dt^2} = \frac{2B^2}{\mu\rho D} - \frac{B_2^2}{\mu\rho D} \quad (2.4)$$

The top of the prominence is subject to the following forces: a downward gravitational force of magnitude $GM_\odot\rho_l/R^2$; a downwards magnetic tension force due to B_1 of magnitude $B_1^2/\mu R_c$; an upward force $(B_3^2 - B_2^2)/\mu h$ due to the difference in magnetic pressure caused by B_3 and B_2 ; an upward magnetic pressure force $B_{az}^2/\mu R_c$ caused by B_{az} . This last pressure force comes from the fact that in the lower half of the prominence the curvature compresses the flux and increases the field by an average factor of $R_c/(R_c - h/4)$ and correspondingly the field in the upper half of the prominence is decreased by an average factor of $R_c/(R_c + h/4)$. Thus the pressure force is (considering points midway between the prominence centre and edge)

$$\begin{aligned} F_{\text{pres}} &= \frac{B_{az}^2 \left(1 + \frac{h}{4R_c}\right)^2 - B_{az}^2 \left(1 - \frac{h}{4R_c}\right)^2}{2\mu \frac{h}{2}} \\ &= \frac{B_{az}^2}{\mu R_c} \end{aligned} \quad (2.5)$$

The resulting MHD equation of motion is

$$\frac{d^2R}{dt^2} = \frac{B_3^2 - B_2^2}{\mu\rho_f h} + \frac{B_{az}^2}{\mu\rho_f R_c} - \frac{B_1^2}{\mu\rho_f R_c} - \frac{GM_\odot}{R^2} \quad (2.6)$$

Equations (2.3),(2.4) and (2.6) are supplemented by conservation relations. It is assumed that mass and magnetic flux are conserved in the upper hemispherical portion of the bubble. The conservation of mass and flux give $DS^2\rho = \text{const}$ and $DSB = \text{const}$. The same equations would apply to an arcade but not to a loop. They imply

$$\rho = \rho_0 \frac{R_\odot}{D} \left[\frac{R_\odot}{S} \right]^2 \quad (2.7)$$

$$B = B_0 \frac{R_\odot}{D} \frac{R_\odot}{S} \quad (2.8)$$

where B_0 and ρ_0 are the values that the magnetic field and density would take if $D=S=R_\odot$.

The radius of curvature R_a is given by

$$R_a = \frac{S}{1 + \cot\theta} \quad (2.9)$$

Also the magnetic flux between the prominence top and the underside of the bubble is assumed to be conserved, so that

$$B_2 = \frac{B_1}{\left[\frac{S}{R_0} - \frac{D}{2R_0} \right]^2 - \left[\frac{R}{R_0} + \frac{h}{2R_0} \right]^2} \quad (2.10)$$

Further conservation relations can be found depending on the geometry of the prominence. Two possibilities referred to as the "simple prominence" and the "line-tied prominence" are described below. Note that the three-dimensional nature of the bubble is taken account of in equations (2.7), (2.9) and (2.10).

2.2.1 Simple Prominence

For this model it is assumed that the length of the prominence and the radius of curvature are both proportional to R so that

$$R_c = R_{co} \frac{R}{R_0} \quad (2.11)$$

$$l = l_0 \frac{R}{R_0} \quad (2.12)$$

The conservation of longitudinal and azimuthal flux give

$$B_l h^2 = \text{const} = B_{l_0} h_0^2$$

$$B_{az} h l = \text{const} = B_{az_0} h_0 l_0$$

$$\rho_f h^2 l = \text{const} = \rho_{f_0} h_0^2 l_0$$

It is also assumed for simplicity that

$$\frac{B_l}{B_{az}} = \text{const} = \frac{B_{l_0}}{B_{azo}}$$

These may be solved to give

$$h = h_0 \frac{R}{R_\odot} \quad (2.13)$$

$$B_{az} = B_{azo} \left[\frac{R_\odot}{R} \right]^2 \quad (2.14)$$

$$B_l = B_{l_0} \left[\frac{R_\odot}{R} \right]^2 \quad (2.15)$$

$$\rho_f = \rho_{f_0} \left[\frac{R_\odot}{R} \right]^3 \quad (2.16)$$

The field B_3 is affected by reconnection and is given in terms of the flux (F) between the prominence and neutral line by

$$B_3 = \frac{2F}{\phi \left[\left[R - \frac{h}{2} \right]^2 - R_N^2 \right]} \quad (2.17)$$

The height R_N of the neutral line is assumed to satisfy

$$\frac{R_N}{R_\odot} = 1 + \alpha \left[\frac{R}{R_\odot} - \frac{h}{2R_\odot} - 1 \right] \quad (2.18)$$

where α is a constant between 0 and 1, so that the reconnection point varies in such a way that its distance from the surface remains at the same fraction of the height

of the underside of the prominence from the solar limb. In this model the form (2.18) is assumed for simplicity; only a full MHD numerical model would determine it more precisely.

F is assumed to satisfy

$$\frac{F}{F_0} = F^* = \begin{cases} (2 - 20N) + (20N - 1) R^*, & R^* < R_{\max} \\ (2 - 20N) + (20N - 1) R_{\max}, & R^* > R_{\max} \end{cases} \quad (2.19)$$

for relevant values of N and R_{\max} , as shown in Figure 2.2a. The form (2.19) is also assumed for simplicity; again a full MHD numerical model would be needed for a more precise form. Thus

$$B_3 = \frac{2 F_0 F^*}{\phi R_{\odot}^2 \left[\left[\frac{R}{R_{\odot}} - \frac{h}{2R_{\odot}} \right]^2 - \frac{R_N^2}{R_{\odot}^2} \right]} \quad (2.20)$$

The following dimensionless variables are defined

$$R^* = \frac{R}{R_{\odot}}, \quad S^* = \frac{S}{R_{\odot}}, \quad D^* = \frac{D}{R_{\odot}}, \quad t^* = t \frac{B_{10} R_{\odot}^{-1}}{\sqrt{\mu \rho_{f0}}}$$

Equations (2.3),(2.4),(2.6) then become

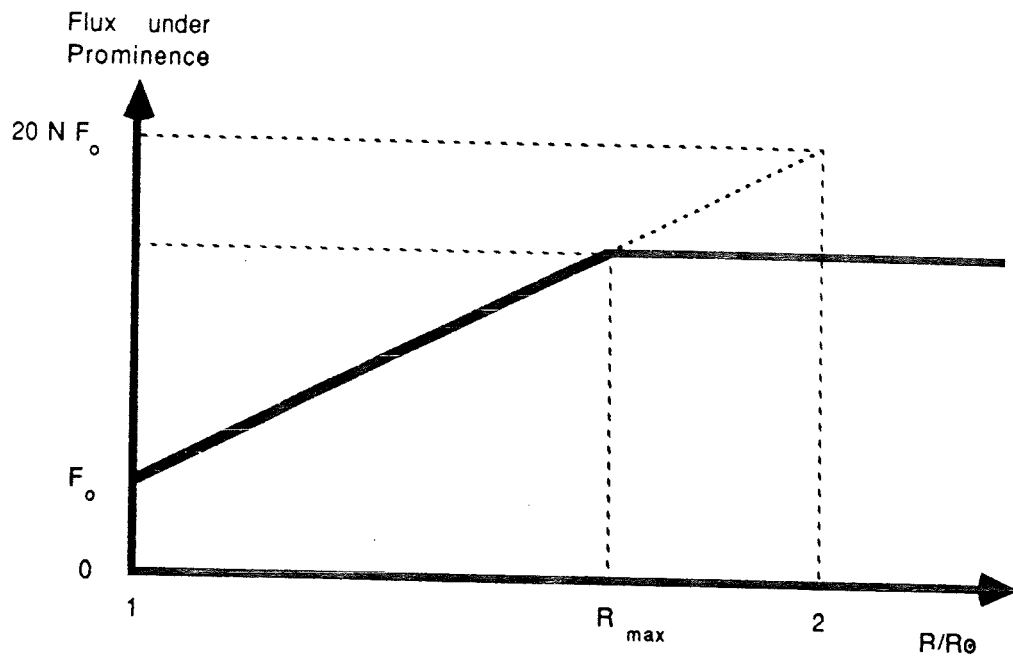


Figure 2.2a Dependence of the magnetic flux under the prominence on prominence height for the simple prominence

$$\frac{d^2 S^*}{dt^{*2}} = \frac{B_i^2 \rho_{fo} S^{*2}}{2 B_{lo}^2 \rho_o \left[\left[S^* - \frac{D^*}{2} \right]^2 - R^{*2} \left[1 + \frac{h_o}{2 R_\odot} \right]^2 \right]^2} - \frac{B_o^2 \rho_{fo} (1 + \cot \theta)}{B_{lo}^2 \rho_o S^* D^*} - \frac{G M_\odot \mu \rho_{fo}}{R_\odot B_{lo}^2 S^{*2}} \quad (2.21)$$

$$\frac{d^2 D^*}{dt^{*2}} = \frac{2 B_o^2 \rho_{fo}}{B_{lo}^2 \rho_o D^{*2}} - \frac{B_i^2 \rho_{fo} S^{*2}}{B_{lo}^2 \rho_o \left[\left[S^* - \frac{D^*}{2} \right]^2 - R^{*2} \left[1 + \frac{h_o}{2 R_\odot} \right]^2 \right]^2} \quad (2.22)$$

$$\frac{d^2 R^*}{dt^{*2}} = \left[\left[\frac{B_{azo}^2}{B_{lo}^2} - 1 \right] \frac{R_\odot}{R_\infty} - \frac{G M_\odot \mu \rho_{fo}}{R_\odot B_{lo}^2} \right] R^{*-2} + \frac{4 F_o^2 F^{*2} R^{*2}}{\phi^2 R_\odot^3 \left[R^{*2} \left[1 - \frac{h_o}{2 R_\odot} \right]^2 - \frac{R_N^2}{R_\odot^2} \right]^2} h_o B_{lo}^2 - \frac{B_i^2 R_\odot R^{*2}}{B_{lo}^2 h_o \left[\left[S^* - \frac{D^{*2}}{2} \right]^2 - R^{*2} \left[1 + \frac{h_o}{2 R_\odot} \right]^2 \right]^2} \quad (2.23)$$

where

$$\frac{R_N}{R_\odot} = 1 + \alpha \left[R^* - \frac{h_o R^*}{2R_\odot} - 1 \right]$$

$$\frac{F}{F_o} = F^* = \begin{cases} (2 - 20 N) + (20 N - 1) R^*, & R^* < R_{\max} \\ (2 - 20 N) + (20 N - 1) R_{\max}, & R^* > R_{\max} \end{cases} \quad (2.19)$$

The parameters B_{azo} , B_{lo} , B_o , B_j , ρ_o , ρ_{fo} , R_\odot , R_{\max} , h_o , θ , G , M_\odot , μ , F_o , ϕ , N and α all remain constant so that equations (2.21), (2.22) and (2.23) represent a set of three coupled second-order differential equations for S^* , D^* , R^* .

2.2.2 Line-Tied Prominence

The line-tied prominence consists of a twisted loop of mass density ρ_f anchored at two footpoints a distance $2L$ apart where $L = R_\odot \sin \phi$. The distance between the solar centre and the highest point of the middle of the prominence is given by R . For $R/R_\odot \leq (1 + \sin \phi)/\cos \phi$ the prominence forms an arc of a circle as shown in Figure 2.3a. $B'GB$ represents the solar surface and A the solar centre. $B'EB$ represents the prominence. The distances DB and AE are given by L and R and the angle DAB is given by ϕ .

As R is increased, the prominence forms a longer arc of a circle until the limiting case when $R/R_\odot = (1 + \sin \phi)/\cos \phi$ and the prominence becomes vertical to the solar surface at B' and B (see Figure 2.3b). The centre of curvature of the prominence is at C and the prominence now

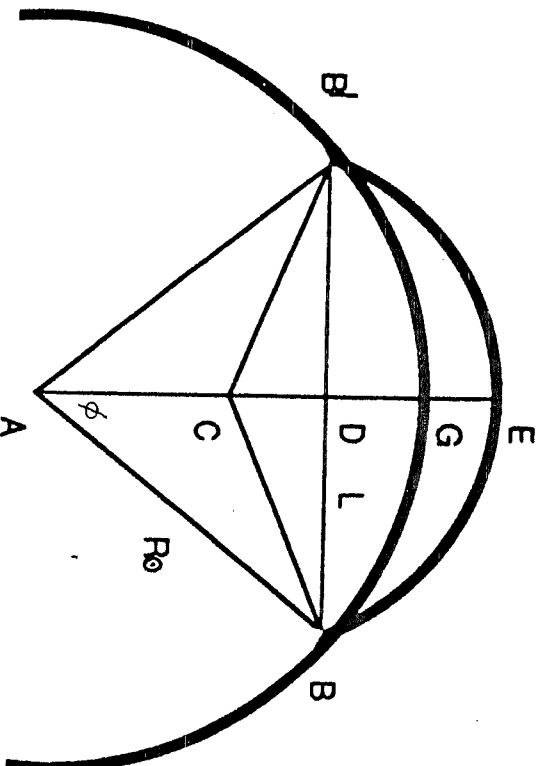


Figure 2.3a The shape of the line-tied prominence for $R/R_0 \leq (1 + \sin \phi)/\cos \phi$

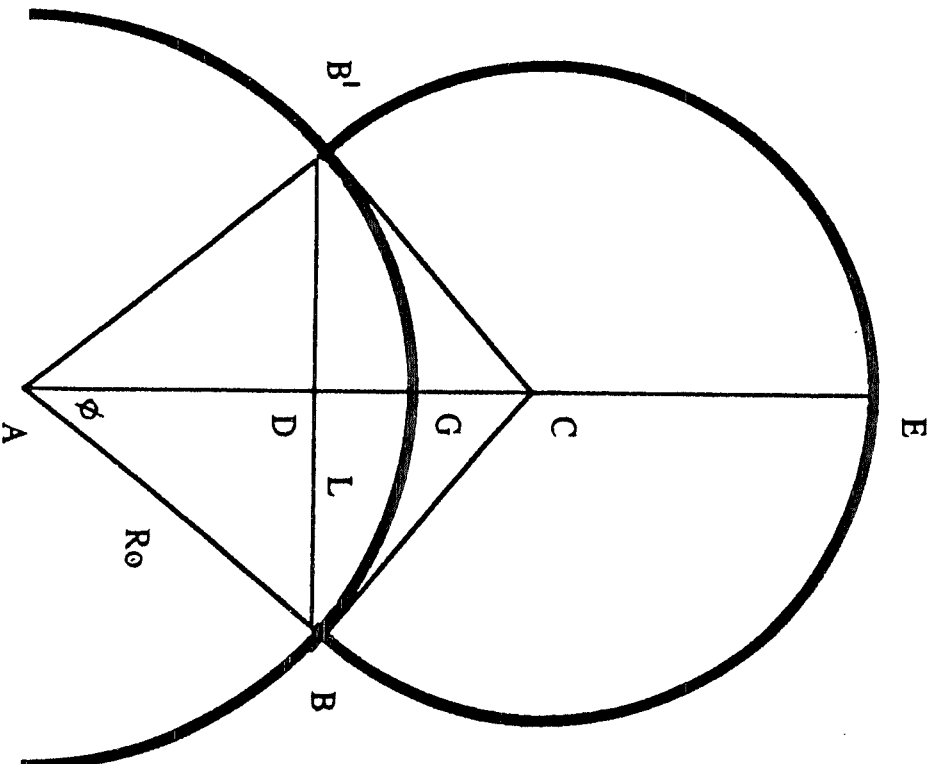


Figure 2.3b The shape of the line-tied prominence for $R/R_0 = (1 + \sin \phi)/\cos \phi$

forms an arc of a circle just greater than a semi-circle. When R is increased further the prominence is represented by $F'B'EBF$ in Figure 2.3c. $B'EB$ forms an arc of a circle just greater than a semi-circle while BF and $B'F'$ are the straight legs going down to the surface.

The prominence length l can now be found as follows. In the case when $R/R_0 \leq (1 + \sin \phi)/\cos \phi$, the theorem of Pythagoras can be applied to triangle BCD (Figure 2.3a) so that the radius of curvature is

$$R_c = \frac{L^2 + (R - R_0 \cos \phi)^2}{2(R - R_0 \cos \phi)} \quad (2.24)$$

Also

$$l = 2R_c \sin^{-1} L/R_c \quad (2.25)$$

When $R/R_0 \geq \sin \phi + \cos \phi$, the point C rises to a location above the point D and the angle BCE becomes greater than $\phi/2$. In the case when $R/R_0 \geq (1 + \sin \phi)/\cos \phi$, AC is equal to $R - R_c$. From triangle ACF , $R_c = R/(1 + \operatorname{cosec} \phi)$ and $AF = R_c/\tan \phi = R/(\sec \phi + \tan \phi)$ so that the length of each leg is given by $R \cot \phi/(1 + \operatorname{cosec} \phi) - R_0$. The length of the arc $F'EF$ is $(\pi + 2\phi)R_c$ which is equal to $(\pi + 2\phi)R/(1 + \operatorname{cosec} \phi)$ and so the length of the prominence is

$$l = R \frac{2 \cot \phi + \pi + 2\phi}{1 + \operatorname{cosec} \phi} - 2R_0 \quad (2.26)$$

Conservation relations can be established for the line-tied prominence as follows. Conservation of azimuthal

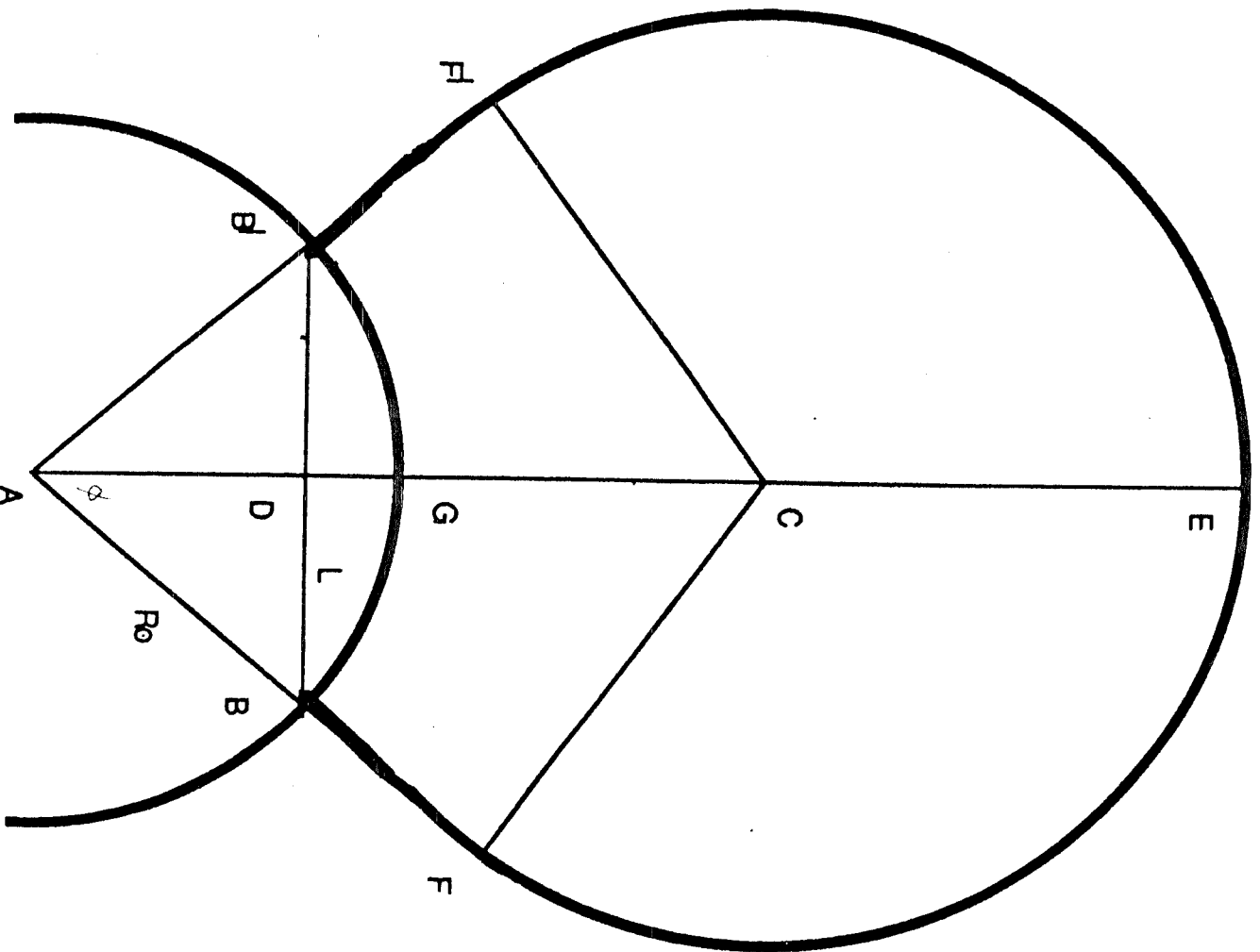


Figure 2.3c The shape of the line-tied prominence for $R/R_0 \geq (1 + \sin \phi)/\cos \phi$

flux, longitudinal flux and mass give $B_{az}hl = \text{constant}$, $B_l h^2 = \text{constant}$ and $\rho_f h^2 l = \text{constant}$ and it is assumed that the ratio B_{az}/B_l of azimuthal to longitudinal flux remains constant.

Thus

$$h = h_0 l/l_0 \quad (2.27)$$

$$B_l = B_{l_0} (l/l_0)^{-2} \quad (2.28)$$

$$B_{az} = B_{az_0} (l/l_0)^{-2} \quad (2.29)$$

$$\rho_f = \rho_{f_0} (l/l_0)^{-3} \quad (2.30)$$

where $l_0, h_0, B_{l_0}, B_{az_0}, \rho_{f_0}$ are the values taken by $l, h, B_l, B_{az}, \rho_f$ in the (hypothetical) case when $R = R_\odot$. The ratio l/l_0 is given by

$$\frac{l}{l_0} = \frac{\sin^2 \phi + \left[\frac{R}{R_\odot} - \cos \phi \right]^2}{2 \phi \left[\frac{R}{R_\odot} - \cos \phi \right]} \sin^{-1} \left[\frac{2 \sin \phi \left[\frac{R}{R_\odot} - \cos \phi \right]}{\sin^2 \phi + \left[\frac{R}{R_\odot} - \cos \phi \right]^2} \right]$$

$$\frac{R}{R_\odot} \leq \frac{1 + \sin \phi}{\cos \phi}$$

$$\left[\frac{R}{R_\odot} \frac{2 \cot \phi + \pi + 2 \phi - 2}{1 + \operatorname{cosec} \phi} - 2 \right] / 2 \phi, \quad \frac{R}{R_\odot} \geq \frac{1 + \sin \phi}{\cos \phi} \quad (2.31)$$

In the presence of reconnection, B_3 is inversely proportional to the area between the lower edge of the prominence and the neutral line and directly proportional to the total flux in that area. Thus

$$B_3 = \frac{2F}{\phi \left[\left[R_\odot - \frac{h}{2} \right]^2 - R_N^2 \right]} \quad (2.32)$$

where R_N is assumed to satisfy

$$\frac{R_N}{R_\odot} = 1 + \alpha \left[\frac{R}{R_\odot} - \frac{h}{2R_\odot} - 1 \right]$$

In other words the neutral line remains the same fraction of the distance between the solar limb and the lower edge of the prominence.

The flux F is assumed to satisfy

$$\frac{F}{F_0} = \begin{cases} 1 & R/R_\odot \leq 1.5 \\ 2R/R_\odot - 2 & 1.5 \leq R/R_\odot \leq R_{\max} \\ 2R_{\max} - 2 & R/R_\odot \geq R_{\max} \end{cases} \quad (2.33)$$

as shown in Figure 2.2b. If R_{\max} is set equal to 2 then, $F/F_0 = 2$ for $R/R_\odot \geq 2$. It is assumed that reconnection will occur once the prominence reaches a certain height (in this case $1.5 R_\odot$). There is a limit to the amount of flux that reconnects so the reconnection is assumed to stop and the flux to remain constant when R/R_\odot becomes equal to R_{\max} (see Figure 2.2b). In this model the form (2.33) is assumed for simplicity with R_{\max} being an adjustable parameter; a full numerical solution of the MHD equations is required to determine it more precisely. Again the variables are non-dimensionalised by putting $R^*=R/R_\odot$, $S^*=S/R_\odot$, $D^*=D/R_\odot$, $t^*=tB_{10}/R_\odot\sqrt{\mu\rho_{f0}}$, $F^*=F/F_0$, $l^*=l/l_0$.

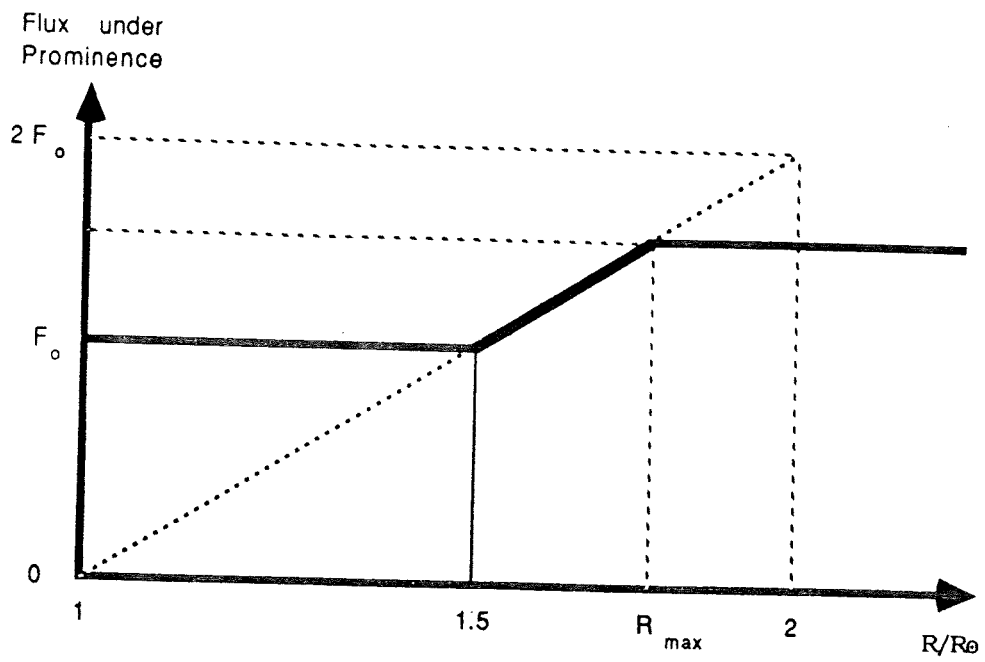


Figure 2.2b Dependence of the magnetic flux under the prominence on prominence height for the line-tied prominence

The second order equations (2.3),(2.4) and (2.6) then become

$$\begin{aligned} \frac{d^2 R^*}{dt^{*2}} &= \left[\frac{B_{azo}^2}{B_{lo}^2} - 1 \right] \frac{T}{l^*} \\ &+ \frac{4 l^{*2} F_o^2 F^{*2}}{\phi^2 B_{lo}^2 h_o R_o^3 \left[\left[R^* - \frac{h_o l^*}{2 R_o} \right]^2 - \frac{R_N^2}{R_o^2} \right]^2} - \frac{G M_o \mu \rho_{fo}}{R_o B_{lo}^2 R^{*2}} \\ &- \frac{B_o^2 R_o l^{*2}}{B_{lo}^2 h_o \left[\left[S^* - \frac{D^*}{2} \right]^2 - \left[R^* + \frac{h_o l^*}{2 R_o} \right]^2 \right]^2} \end{aligned} \quad (2.34)$$

$$\begin{aligned} \frac{d^2 S^*}{dt^{*2}} &= \frac{B_o^2 \rho_{fo} S^{*2}}{2 B_{lo}^2 \rho_o \left[\left[S^* - \frac{D^*}{2} \right]^2 - \left[R^* + \frac{h_o l^*}{2 R_o} \right]^2 \right]^2} \\ &- \frac{B_o^2 \rho_{fo} (1 + \cot \theta)}{B_{lo}^2 \rho_o S^* D^*} - \frac{G M_o \mu \rho_{fo}}{R_o B_{lo}^2 S^{*2}} \end{aligned} \quad (2.35)$$

$$\begin{aligned} \frac{d^2 D^*}{dt^{*2}} &= \frac{2 B_o^2 \rho_{fo}}{B_{lo}^2 \rho_o D^{*2}} \\ &- \frac{B_o^2 \rho_{fo} S^{*2}}{B_{lo}^2 \rho_o \left[\left[S^* - \frac{D^*}{2} \right]^2 - \left[R^* + \frac{h_o l^*}{2 R_o} \right]^2 \right]^2} \end{aligned} \quad (2.36)$$

where $l^* = l/l_0$ is given by

$$\frac{l}{l_0} = \frac{\sin^2 \phi + \left[\frac{R}{R_0} - \cos \phi \right]^2}{2 \phi \left[\frac{R}{R_0} - \cos \phi \right]} \sin^{-1} \left[\frac{2 \sin \phi \left[\frac{R}{R_0} - \cos \phi \right]}{\sin^2 \phi + \left[\frac{R}{R_0} - \cos \phi \right]^2} \right]$$

$$\frac{R}{R_0} \leq \frac{1 + \sin \phi}{\cos \phi}$$

$$\left[\frac{\frac{R}{R_0} \frac{2 \cot \phi + \pi + 2 \phi}{1 + \operatorname{cosec} \phi} - 2}{2 \phi} \right], \quad \frac{R}{R_0} \geq \frac{1 + \sin \phi}{\cos \phi} \quad (2.31)$$

$$T = \frac{2 (R^* - \cos \phi)}{\sin^2 \phi + (R^* - \cos \phi)^2}$$

$$R^* \leq \frac{1 + \sin \phi}{\cos \phi}$$

$$= \frac{1 + \operatorname{cosec} \phi}{R^*}$$

$$R^* \geq \frac{1 + \sin \phi}{\cos \phi}$$

$$\frac{R_N}{R_0} = 1 + \alpha \left[R^* - \frac{h_0 l^*}{2 R_0} - 1 \right]$$

$$\frac{F}{F_0} = \begin{cases} 1 & R/R_0 \leq 1.5 \\ 2 R/R_0 - 2 & 1.5 \leq R/R_0 \leq R_{\max} \\ 2 R_{\max} - 2 & R/R_0 \geq R_{\max} \end{cases} \quad (2.33)$$

2.3 Results

2.3.1 Prominence Alone

Before looking at the situation where the prominence and mass ejection evolve together, a situation is considered where the prominence evolves on its own. The first case to be considered will be that of the simple prominence using Equation (2.23) without the term in B_j . Thus the evolution is given by

$$\begin{aligned} \frac{d^2 R^*}{dt^{*2}} = & \left[\left[\frac{B_{azo}^2}{B_{lo}^2} - 1 \right] \frac{R_{\odot}}{R_{\infty}} - \frac{GM_{\odot} \mu \rho_{fo}}{R_{\odot} B_{lo}^2} \right] R^{*-2} \\ & + \frac{4 F_o^2 F^{*2} R^{*2}}{\phi^2 R_{\odot}^3 \left[R^{*2} \left[1 - \frac{h_o}{2R_{\odot}} \right]^2 - \frac{R_N^2}{R_{\odot}^2} \right]^2 h_o B_{lo}^2} \end{aligned} \quad (2.37)$$

and the equilibrium height by

$$\begin{aligned} & \left[\left[\frac{B_{azo}^2}{B_{lo}^2} - 1 \right] \frac{R_{\odot}}{R_{\infty}} - \frac{GM_{\odot} \mu \rho_{fo}}{R_{\odot} B_{lo}^2} \right] R^{*-2} \\ & + \frac{4 F_o^2 F^{*2} R^{*2}}{\phi^2 R_{\odot}^3 \left[R^{*2} \left[1 - \frac{h_o}{2R_{\odot}} \right]^2 - \frac{R_N^2}{R_{\odot}^2} \right]^2 h_o B_{lo}^2} = 0 \end{aligned} \quad (2.38)$$

If one parameter, such as F_0 say, is allowed to vary, then equation (2.38) determines the equilibrium height R^* as a function of the free parameter F_0 . For any value of R^* , one positive value of F^* can be found and the flux $F = F_0 F^*$ can be found.

The following values for the constants were adopted. $B_{azo} = 1G$, $B_{lo} = 30G$, $R_{co} = 200Mm$, $\rho_{fo} = 10^{-10}kgm^{-3}$, $h_o = 20Mm$, $\phi = 0.07$ (giving a footpoint separation of about 100Mm). A plot of R^* against F in Figure 2.4a shows that, the greater the flux under the prominence, the higher the position of equilibrium. This equilibrium is stable for values of R^* less than 1.18 (126Mm above the solar surface). For example, one equilibrium has $R^* = 1.16$, $F_0 = 6.16 \times 10^{11} Wb$, $F = 4.46 \times 10^{12} Wb$, and if F_0 is increased to $6.17 \times 10^{12} Wb$ an oscillatory solution results with period 17000 seconds. The equilibrium with $F_0 = 6.18 \times 10^{12} Wb$ on the other hand is locally unstable and Figure 2.4b shows the resulting non-linear evolution for four different values for R_{max} .

In cases C and D the prominence leaves equilibrium, accelerates and tends towards a constant velocity. In cases A and B the prominence leaves the equilibrium position and accelerates at first, but, after the reconnection stops, the prominence does not have a high enough velocity to escape and it eventually returns to the equilibrium.

Next consider the line-tied prominence on its own, whose motion is determined by equation (2.34) with the term in B_j absent. It is therefore assumed that the large scale

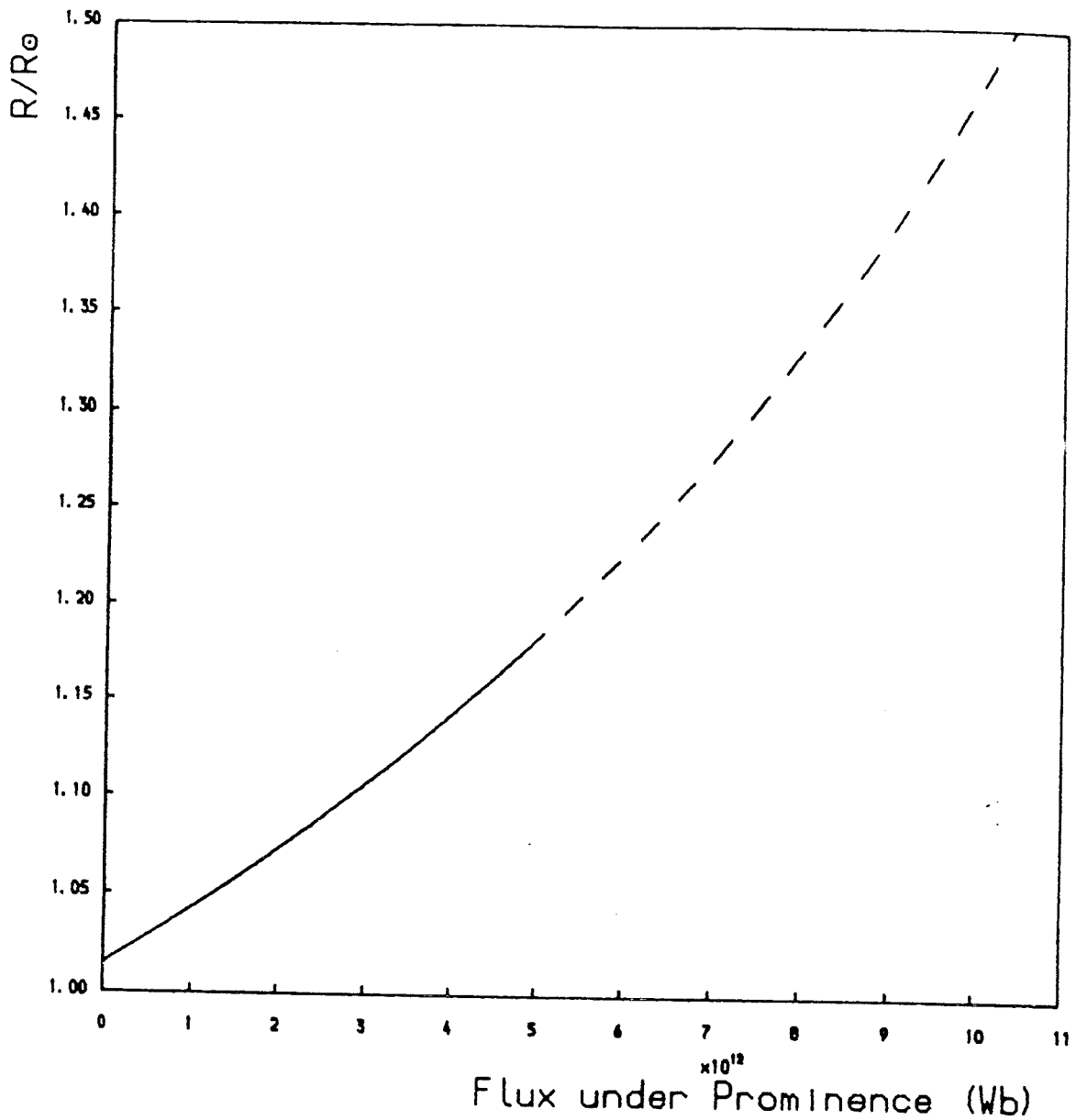


Figure 2.4 The evolution of the simple prominence by itself

(a) The equilibrium distance of the prominence from the solar centre as a function of the magnetic flux under the prominence. The continuous curve represents stable equilibria while the dashed curve represents unstable equilibria.

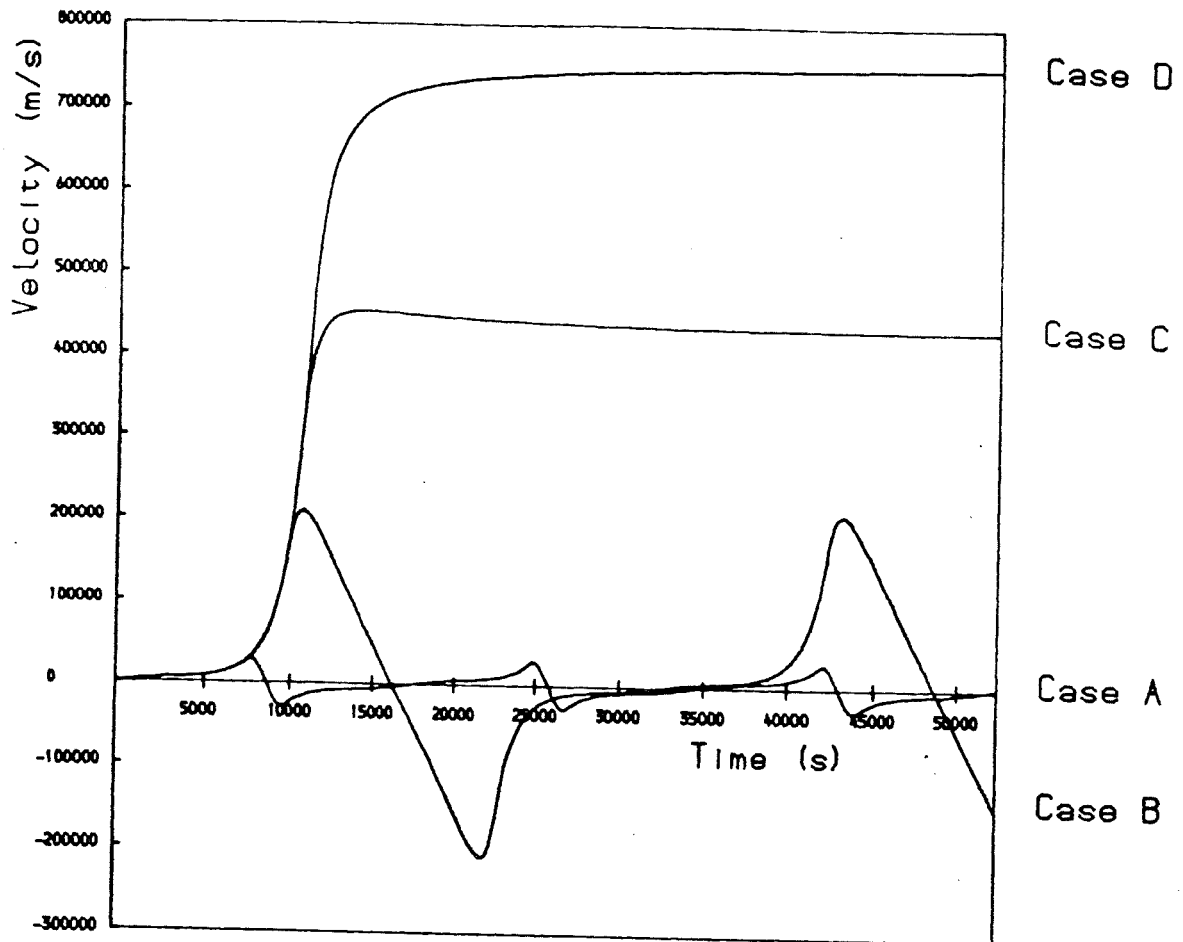


Figure 2.4 The evolution of the simple prominence by itself

(b) The time evolution of the speed of rise of the prominence away from an unstable equilibrium for

$R_{\max} = 1.25$ (Case A), $R_{\max} = 1.50$ (Case B),

$R_{\max} = 1.75$ (Case C), $R_{\max} = 2.00$ (Case D).

field closing over the prominence is too weak to affect its evolution. The prominence evolution and equilibrium are therefore given by

$$\begin{aligned} \frac{d^2 R^*}{dt^{*2}} = & \left[\frac{B_{azo}^2}{B_{lo}^2} - 1 \right] \frac{T}{l^*} \\ & + \frac{4 l^{*2} F_o^2 F^{*2}}{\phi^2 B_{lo}^2 h_o R_o^3 \left[\left[R^* - \frac{h_o l^*}{2 R_o} \right]^2 - \frac{R_N^2}{R_o^2} \right]^2} \\ & - \frac{GM_o \mu \rho_{fo}}{R_o B_{lo}^2 R^{*2}} \end{aligned} \quad (2.39)$$

and

$$\begin{aligned} & \left[\frac{B_{azo}^2}{B_{lo}^2} - 1 \right] \frac{T}{l^*} + \frac{4 l^{*2} F_o^2 F^{*2}}{\phi^2 B_{lo}^2 h_o R_o^3 \left[\left[R^* - \frac{h_o l^*}{2 R_o} \right]^2 - \frac{R_N^2}{R_o^2} \right]^2} \\ & - \frac{GM_o \mu \rho_{fo}}{R_o B_{lo}^2 R^{*2}} = 0 \end{aligned} \quad (2.40)$$

When the dependence of T , l^* , F^* , R_N on R is known, equation (2.40) determines the prominence height as a function of F_o .

For every R^* one positive value of F^* can be found. Using the following parameters $B_{azo} = 1G$, $B_{lo} = 30G$, $\rho_{fo} = 10^{-10} \text{kgm}^{-3}$, $\rho = 0.07$, $h_o = 20\text{Mm}$, the functional variation

of R^* with F_0 is given in Figure 2.5a. For values of F_0 less than $1.7 \times 10^{12} \text{Wb}$, there are two values of R^* . A stability analysis shows that the lower branch is stable and the upper branch is unstable.

One particular equilibrium, for example, is at $R^* = 1.10$, $F_0 = 1.68 \times 10^{12} \text{Wb}$. This is on the lower stable branch and, if F_0 is increased to $1.69 \times 10^{12} \text{Wb}$, then an oscillatory solution results with period 6000 seconds.

If F_0 is increased to $1.70 \times 10^{12} \text{Wb}$, then no equilibrium height exists. The effect of the perturbation is to cause the prominence to rise and reach a constant velocity.

Figure 2.5b shows this evolution for three different values of R_{max} . In case A $R_{\text{max}} = 1.50$ and no reconnection is taking place.

2.3.2 Prominence Plus Bubble

The coupled system of the prominence and overlying bubble is now considered first of all using equations (2.21), (2.22) and (2.23) to model the simple prominence plus bubble. The equilibrium equations are derived by setting the right hand sides of equations (2.21), (2.22) and (2.23) to zero, namely.

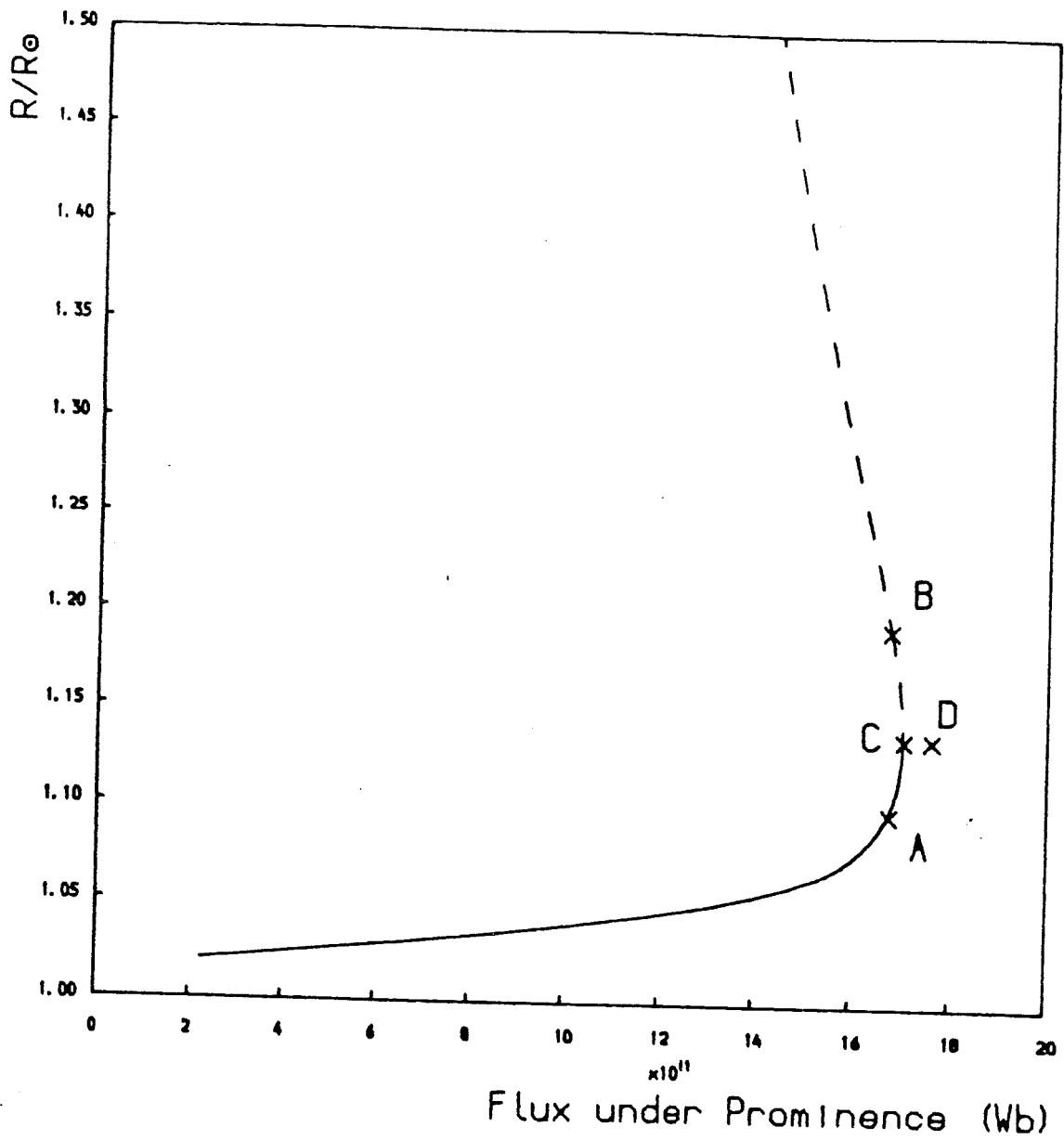


Figure 2.5 The evolution of the line-tied prominence by itself
 (a) The equilibrium height of the prominence as a function of the magnetic flux below it.

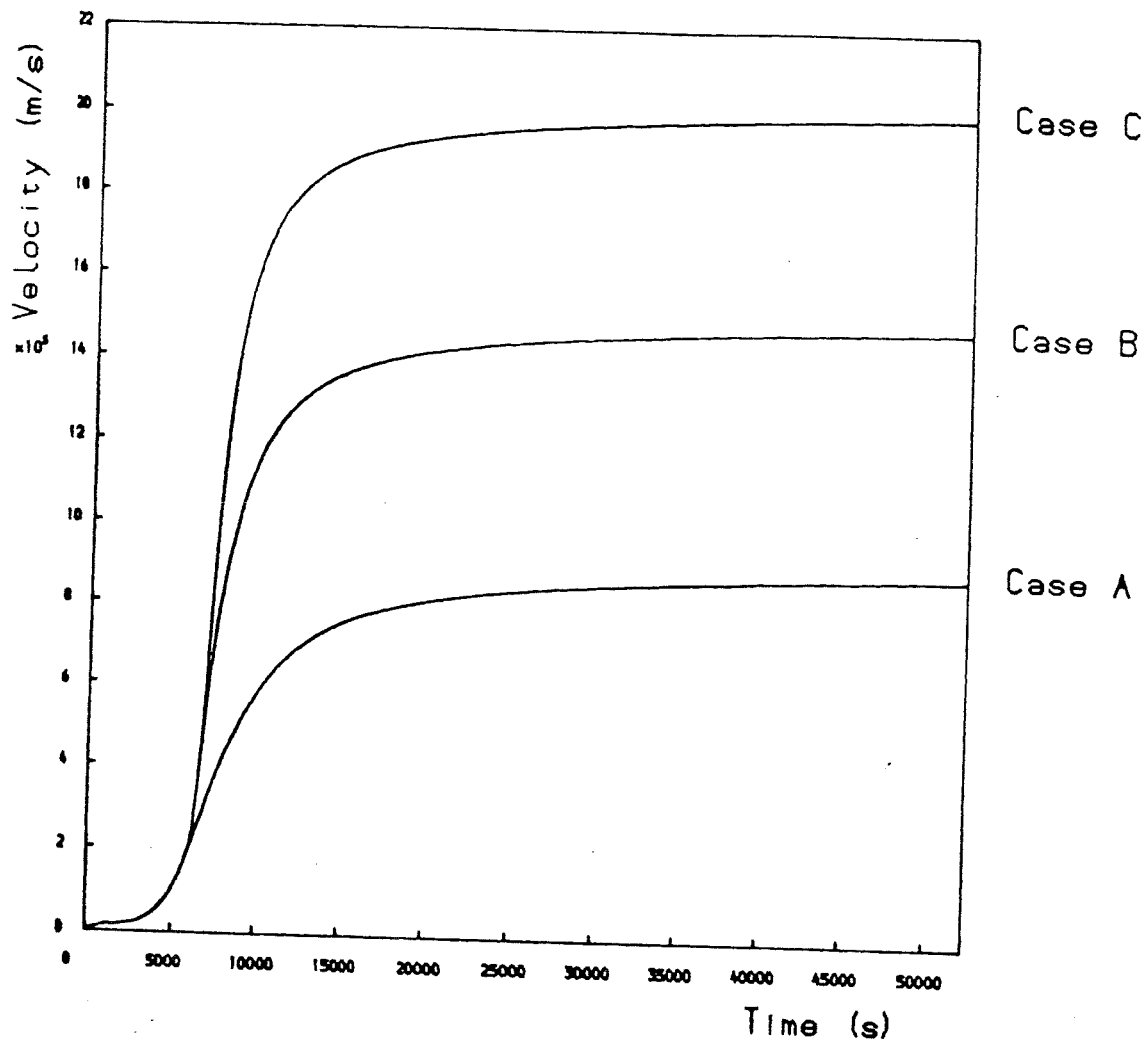


Figure 2.5 The evolution of the line-tied prominence by itself
 (b) The time evolution of the speed of rise of the prominence away from non-equilibrium near point C for $R_{\max} = 1.50$ (Case A), $R_{\max} = 1.75$ (Case B), $R_{\max} = 2.00$ (Case C).

$$\begin{aligned}
& \frac{B_i^2 \rho_{fo} S^{*2}}{2 B_{lo}^2 \rho_o \left[\left[S^* - \frac{D^*}{2} \right]^2 - R^{*2} \left[1 + \frac{h_o}{2 R_\odot} \right]^2 \right]^2} \\
& - \frac{B_o^2 \rho_{fo} (1 + \cot \theta)}{B_{lo}^2 \rho_o S^* D^*} - \frac{GM_\odot \mu \rho_{fo}}{R_\odot B_{lo}^2 S^{*2}} = 0 \quad (2.41)
\end{aligned}$$

$$\begin{aligned}
& \frac{2 B_o^2 \rho_{fo}}{B_{lo}^2 \rho_o D^{*2}} \\
& - \frac{B_i^2 \rho_{fo} S^{*2}}{B_{lo}^2 \rho_o \left[\left[S^* - \frac{D^*}{2} \right]^2 - R^{*2} \left[1 + \frac{h_o}{2 R_\odot} \right]^2 \right]^2} = 0 \quad (2.42)
\end{aligned}$$

$$\begin{aligned}
& \left[\left[\frac{B_{azo}^2}{B_{lo}^2} - 1 \right] \frac{R_\odot}{R_\infty} - \frac{GM_\odot \mu \rho_{fo}}{R_\odot B_{lo}^2} \right] R^{*-2} \\
& + \frac{4 F_o^2 F^{*2} R^{*2}}{\phi^2 R_\odot^3 \left[R^{*2} \left[1 - \frac{h_o}{2 R_\odot} \right]^2 - \frac{R_N^2}{R_\odot^2} \right]^2 h_o B_{lo}^2} \\
& - \frac{B_i^2 R_\odot R^{*2}}{B_{lo}^2 h_o \left[\left[S^* - \frac{D^*}{2} \right]^2 - R^{*2} \left[1 + \frac{h_o}{2 R_\odot} \right]^2 \right]^2} = 0 \quad (2.43)
\end{aligned}$$

If all parameters except F_o are assumed given, then equations (2.41), (2.42) and (2.43) determine R^* , S^* , D^* as functions of F_o . The method of solution is to assume a value

for R^* and to eliminate the term in $(S^* - D^*/2)^2 - R^{*2}(1 + h_0/2R_0)^2$ between equations (2.41) and (2.42). This gives a quadratic equation in S^*/D^* with one positive root (and one negative root which is neglected). This root is substituted into equation (2.42) and after finding S^* and D^* , equation (2.43) is easily solved for F_0 , and the flux $F_0 F^*$ calculated.

The parameters are fixed as follows: $B_{az0} = 1G$, $B_{l0} = 30G$, $B_0 = 0.4G$, $B_j = 0.6G$, $\rho_f = 10^{-10} \text{kgm}^{-3}$, $\theta = 0.7$, $\phi = 0.07$, $\alpha = 0.1$, $h_0 = 20\text{Mm}$, $N=2$.

Figure 2.6a shows the relevant equilibrium curves. The lower, continuous part represents a series of stable equilibria while the upper dashed part represents unstable equilibria. One equilibrium, for example, is at $F = 3.27 \times 10^{12} \text{Wb}$, $F_0 = 4.78 \times 10^{11} \text{Wb}$, $R^* = 1.15$, $S^* = 2.03$, $D^* = 0.69$. This is on the stable part of the curve but close to the transition to instability. If a perturbation is applied to F_0 to increase it to $4.80 \times 10^{11} \text{Wb}$, the evolution of the system is as shown in Figures 2.6b, 2.6c and 2.6d giving a stable oscillatory solution with a superposition of normal modes.

If, however, F_0 is increased to $4.81 \times 10^{11} \text{Wb}$, this has the effect of moving the equilibrium point from the stable to the unstable part of the curve.

The evolution proceeds as shown in Figure 2.7. Four different cases are considered corresponding to four different

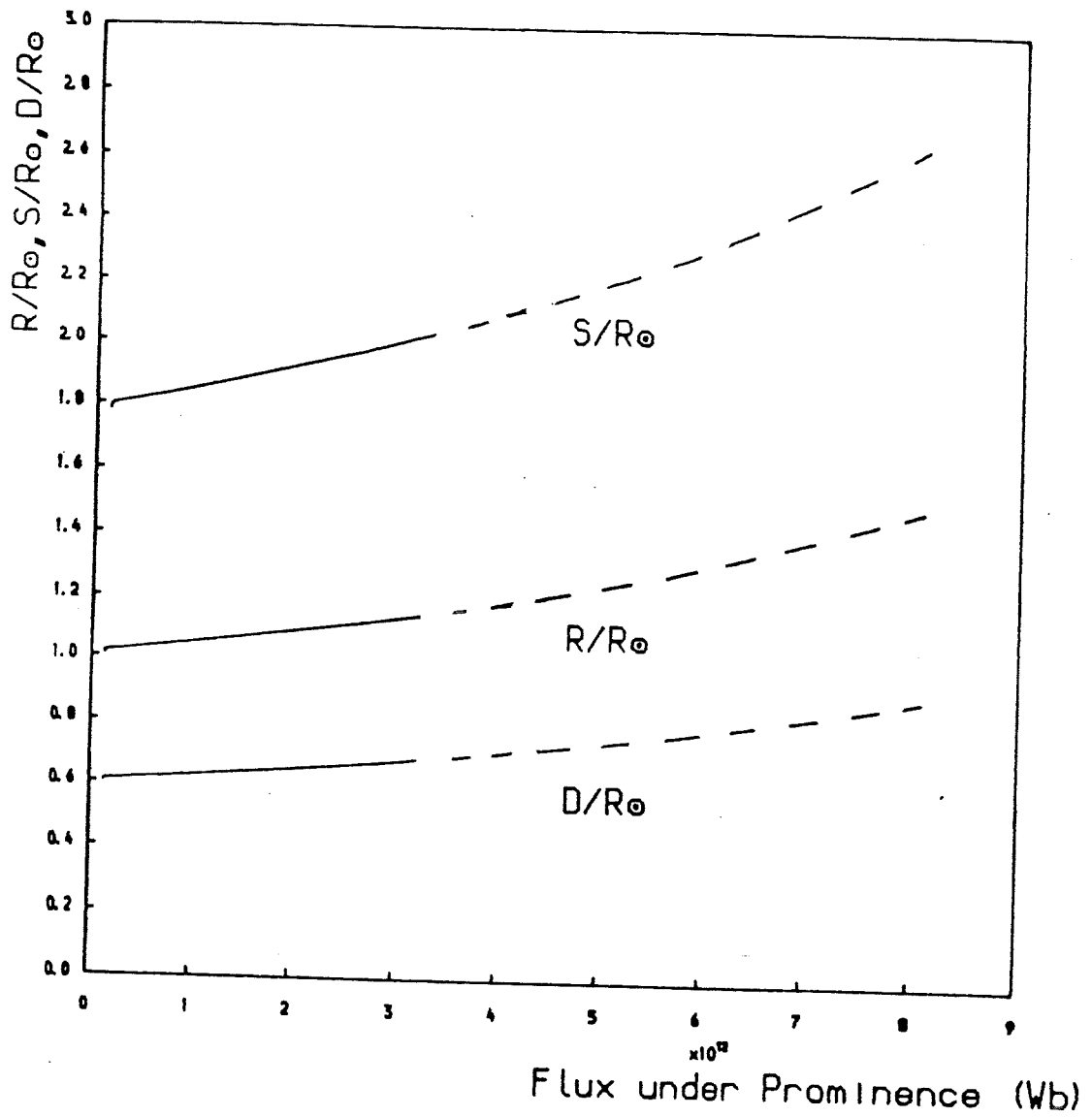


Figure 2.6 Evolution of simple prominence and overlying bubble from a stable equilibrium.

(a) Variation of equilibrium heights of prominence (R), and bubble (S), and width (D) of bubble as the magnetic flux underneath the prominence is varied.

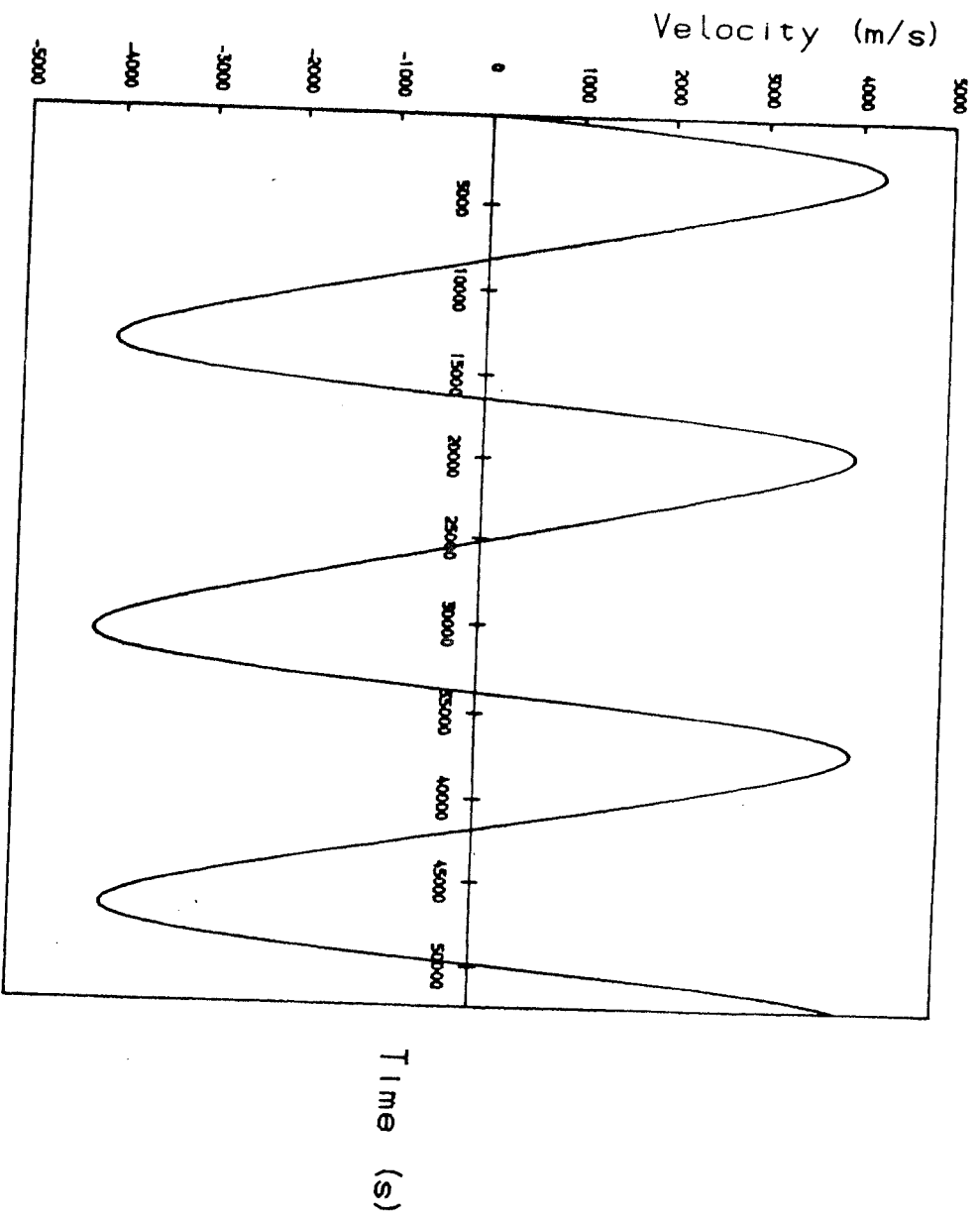


Figure 2.6 Evolution of simple prominence and overlying bubble from a stable equilibrium.
(b) the speed of rise of the prominence

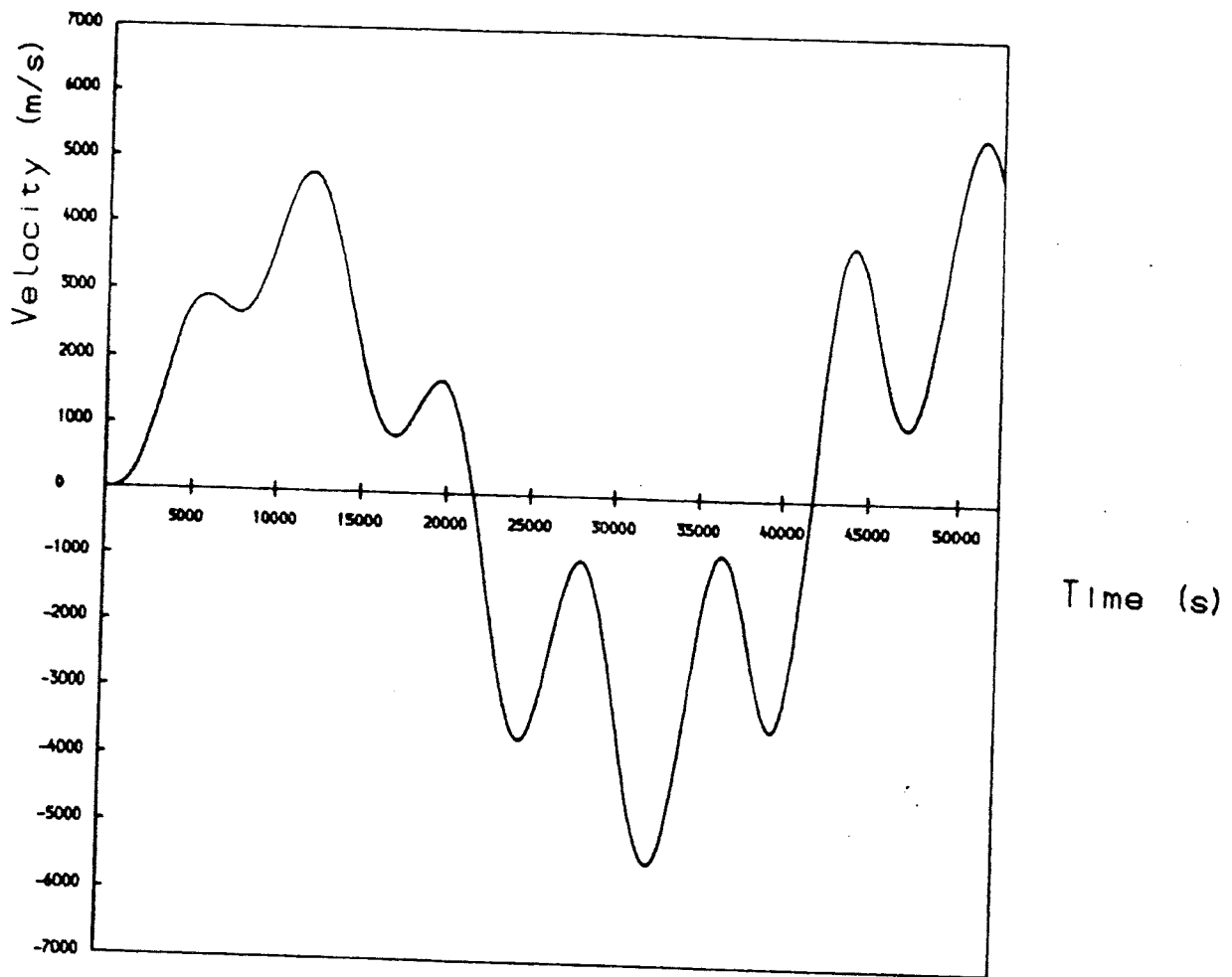


Figure 2.6 Evolution of simple prominence and overlying bubble from a stable equilibrium.
(c) the speed of rise of the bubble

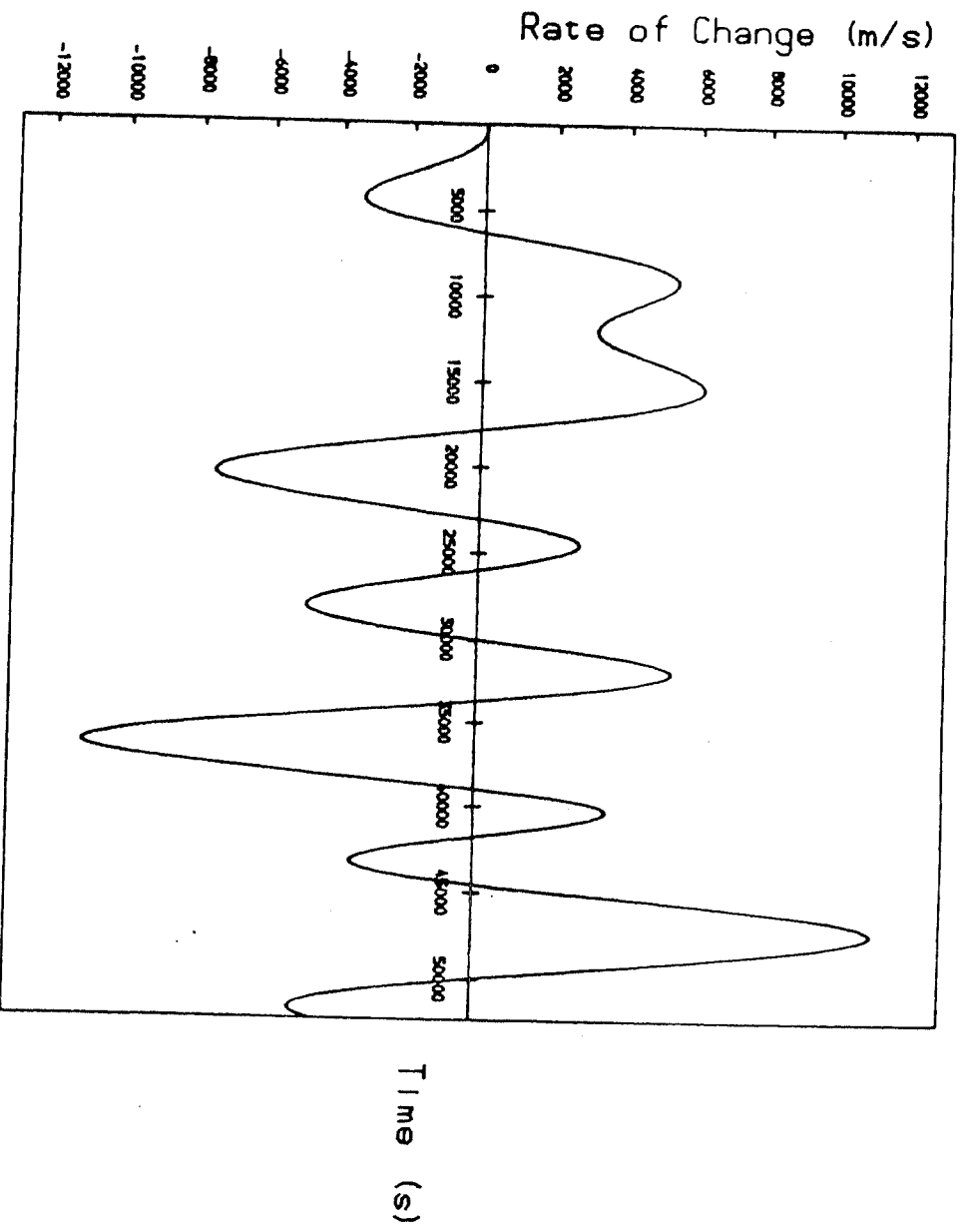


Figure 2.6 Evolution of simple prominence and overlying bubble from a stable equilibrium.
(d) the rate of change of bubble width.

values of R_{\max} . In cases C and D the prominence and bubble both accelerate upwards before reaching constant velocities. In case A there is an oscillation: first of all one sees upward acceleration until the reconnection ceases, after which the prominence and bubble slow down and eventually undergo downward motion. Case B is, however, different. The bubble accelerates upwards to reach a constant velocity but the prominence does not reach escape velocity before reconnection stops, and so it returns to the original equilibrium. This behaviour is found to hold for values of R_{\max} between 1.3 and 1.6.

The effect of varying the value of N is shown in Figure 2.8 with R_{\max} set equal to 1.75. Each value of N gives a similarly shaped equilibrium curve (Figure 2.8a) but the point of transition from stability to instability varies. Figures 2.8b, 2.8c and 2.8d show the evolution of the system once a perturbation has been applied to F_0 to move it from the stable to unstable region. It is seen that the greater the amount of reconnection, the higher the eventual speed of the coronal mass ejection.

The remaining case to be considered is that of the line-tied prominence with the overlying coronal mass ejection. Equations (2.34), (2.35) and (2.36) describe the evolution and the equilibrium is given by

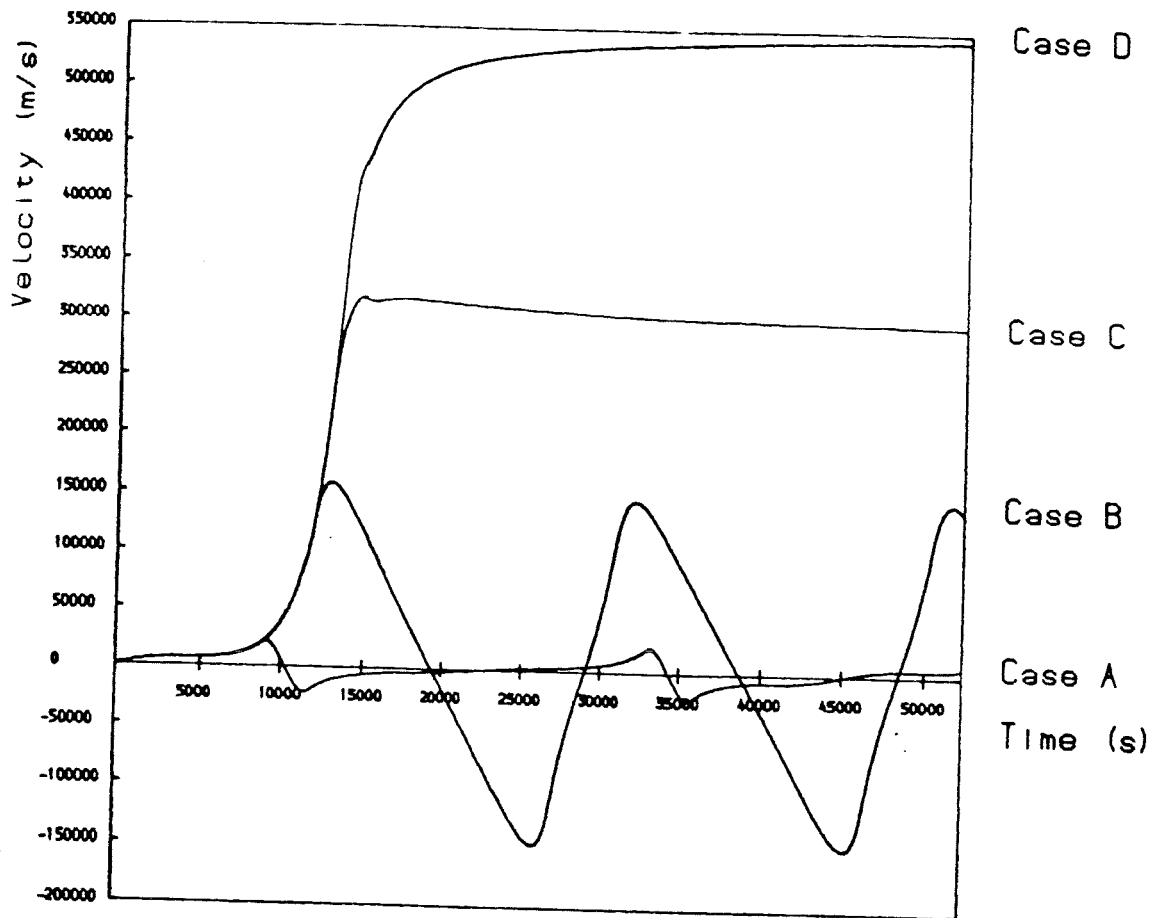


Figure 2.7 Evolution of the simple prominence and overlying bubble from a locally unstable equilibrium for $R_{\max}=1.25, 1.50, 1.75$ and 2.00 (cases A-D respectively). The time evolution of (a) the speed of rise of the prominence

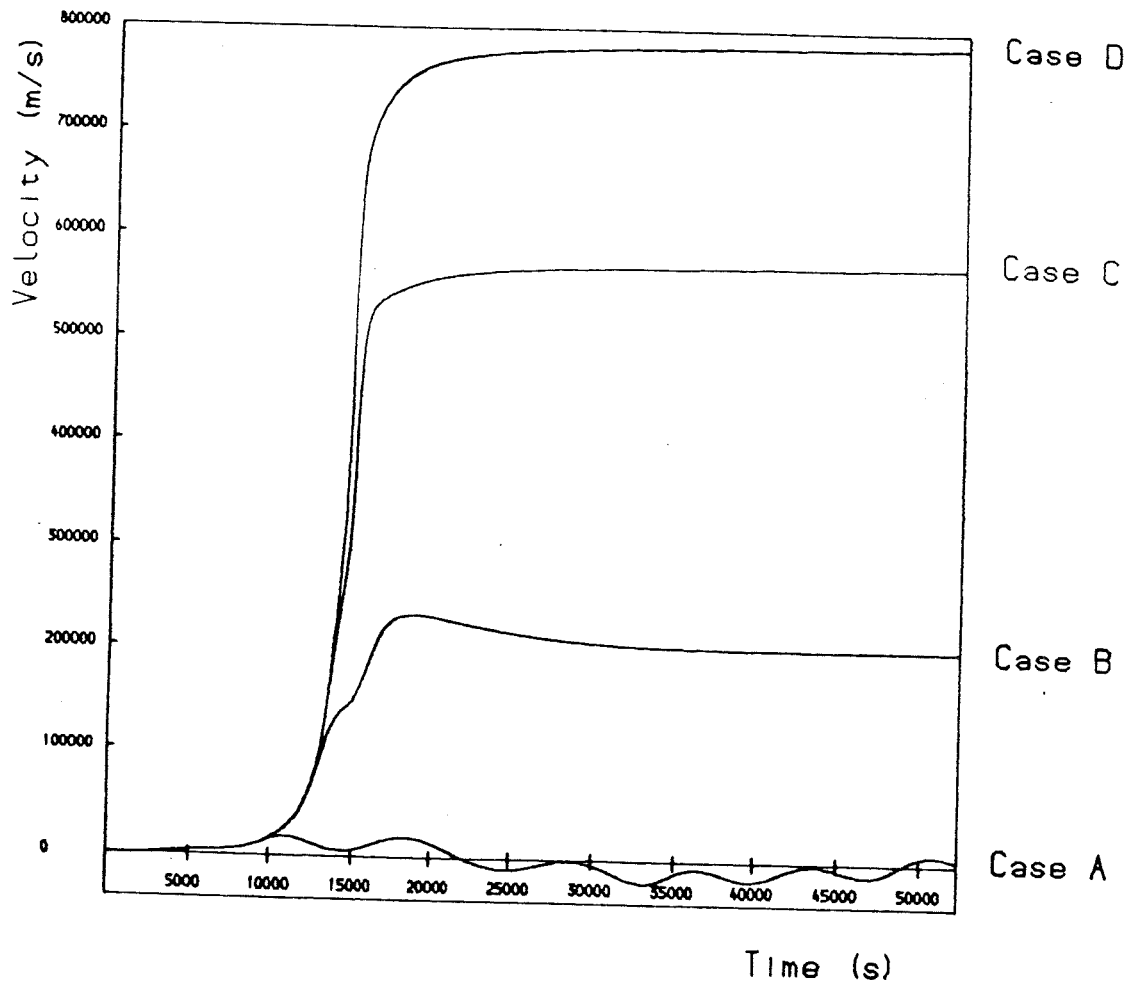


Figure 2.7 Evolution of the simple prominence and overlying bubble from a locally unstable equilibrium for $R_{\max}=1.25, 1.50, 1.75$ and 2.00 (cases A-D respectively). The time evolution of (b) the speed of rise of the bubble

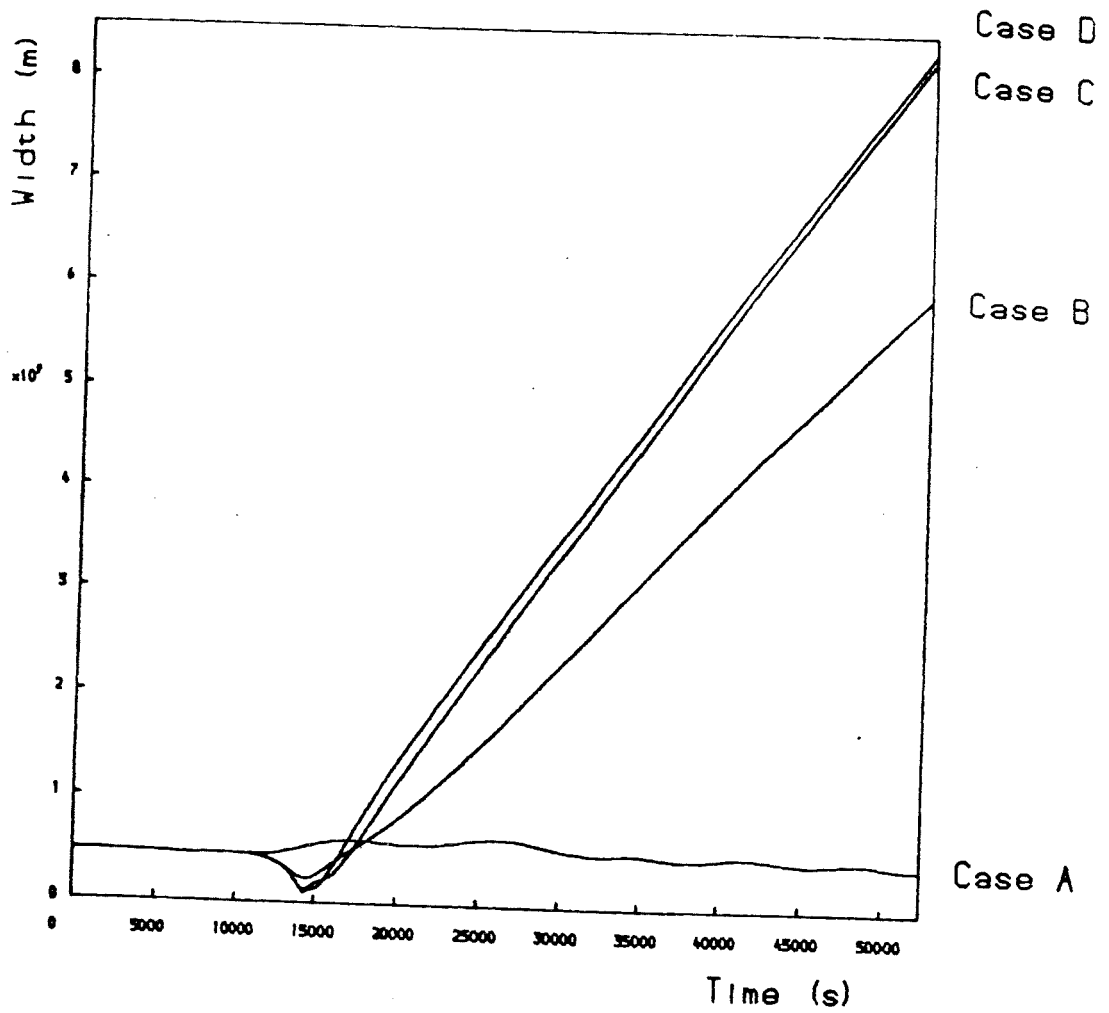


Figure 2.7 Evolution of the simple prominence and overlying bubble from a locally unstable equilibrium for $R_{\max}=1.25, 1.50, 1.75$ and 2.00 (cases A-D respectively). The time evolution of (c) the width of the bubble

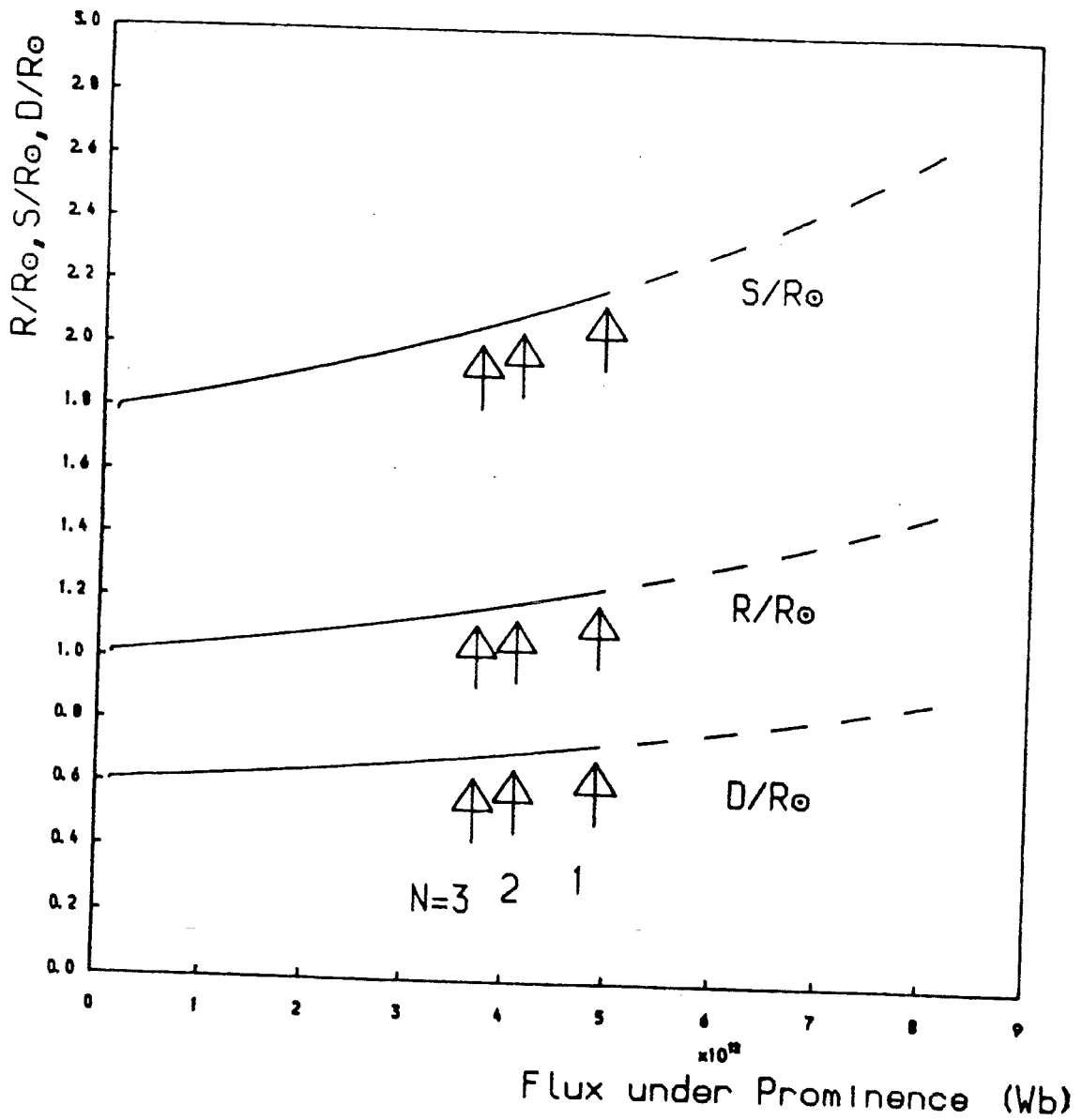


Figure 2.8 Evolution of the simple prominence and overlying bubble from an unstable equilibrium for different values of N , the rate of increase of the flux under the prominence. (a) Variation of the equilibrium parameters with the flux under the prominence, the arrows showing the transition from stable to unstable equilibrium.

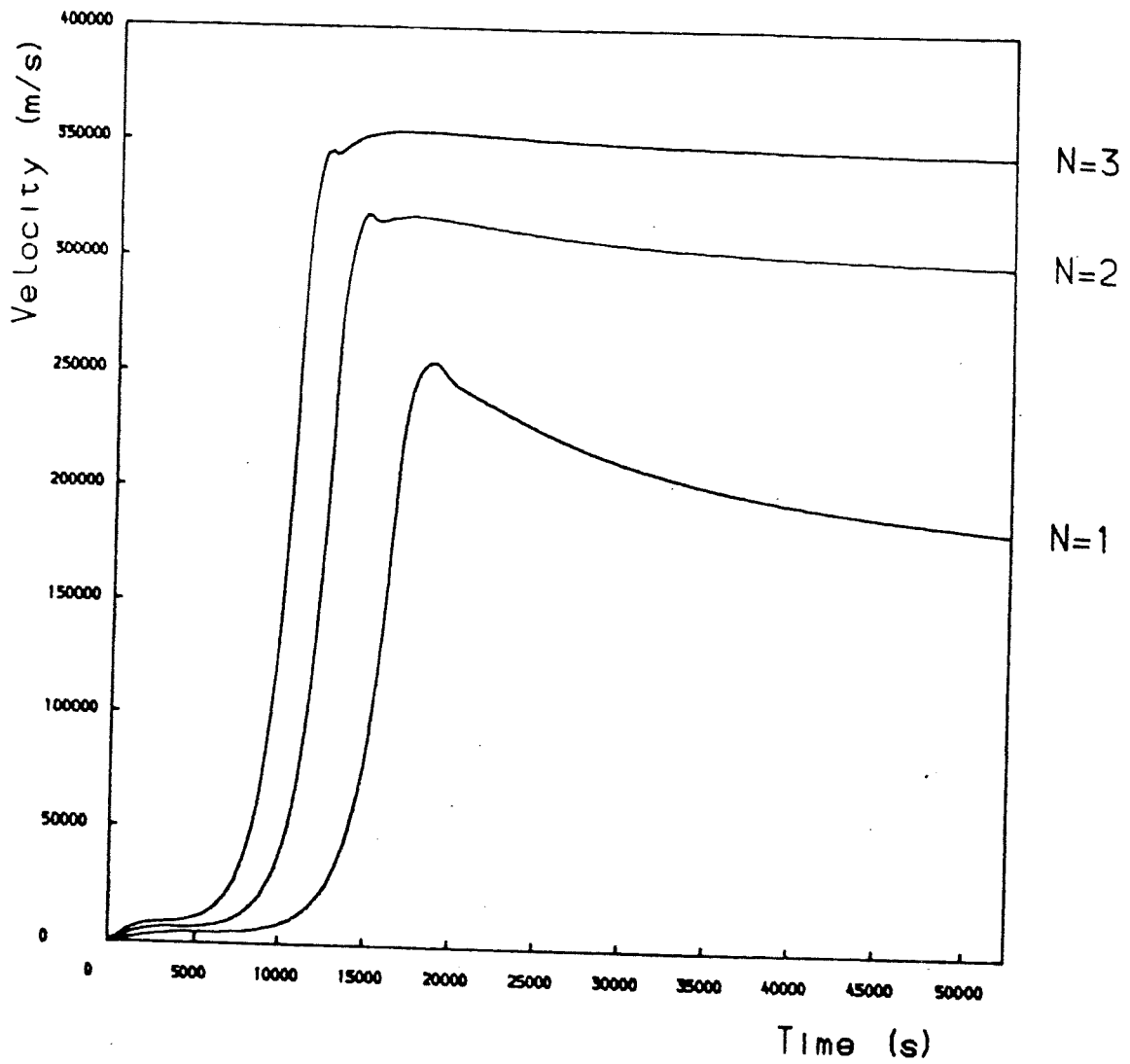


Figure 2.8 Evolution of the simple prominence and overlying bubble from an unstable equilibrium for different values of N , the rate of increase of the flux under the prominence. The time evolution of
 (b) the speed of rise of the prominence

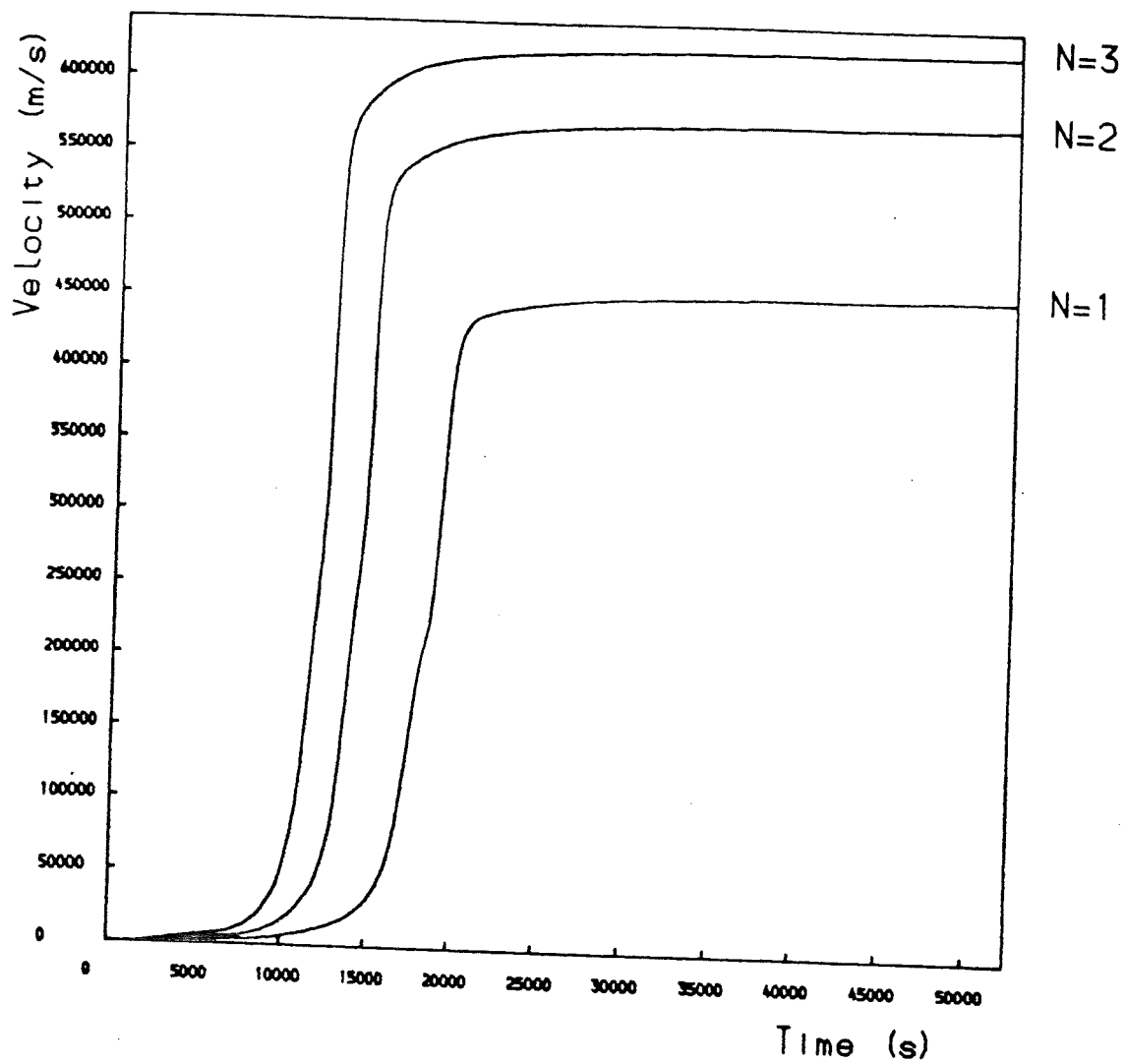


Figure 2.8 Evolution of the simple prominence and overlying bubble from an unstable equilibrium for different values of N , the rate of increase of the flux under the prominence. The time evolution of
(c) the speed of rise of the bubble

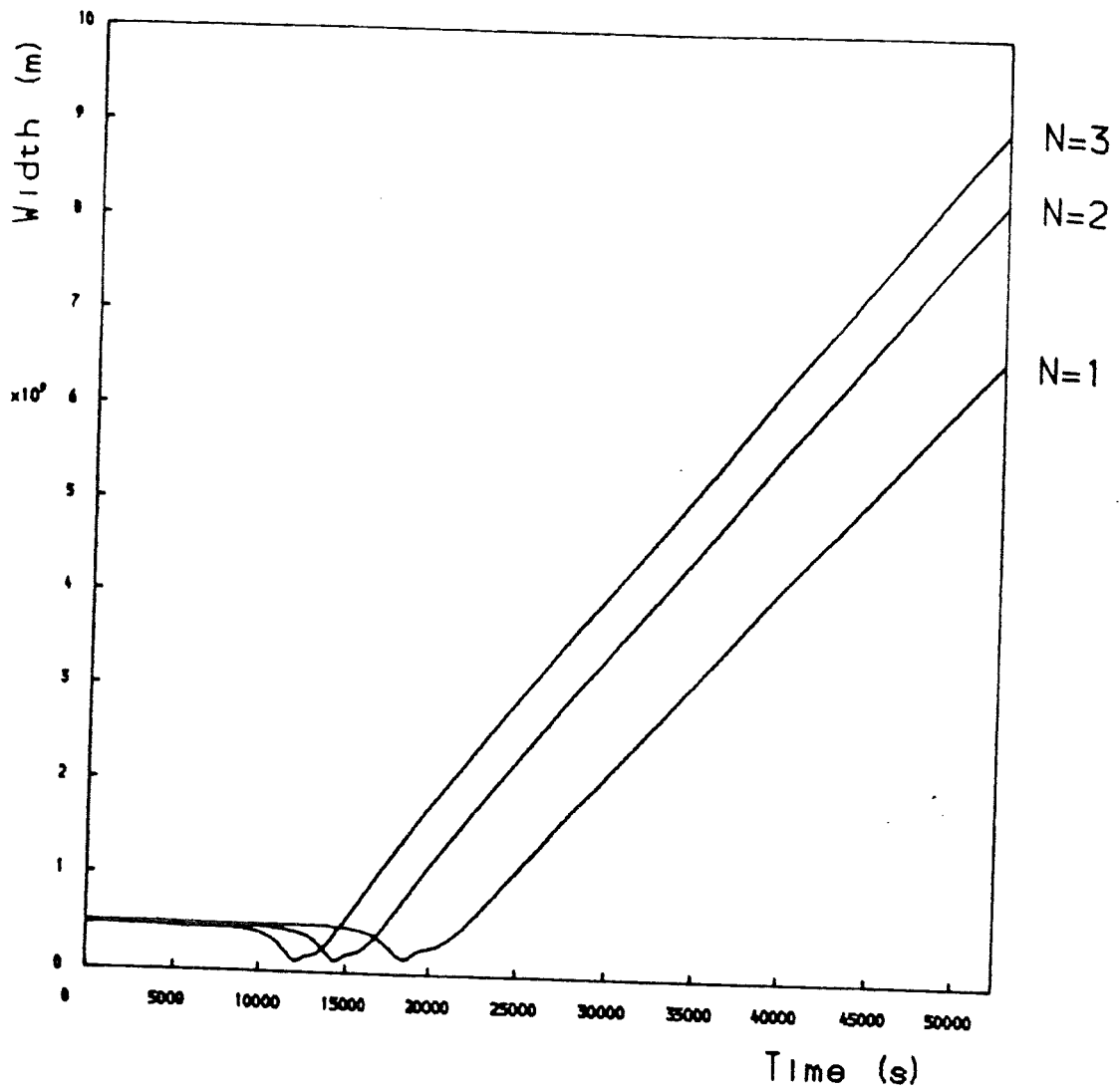


Figure 2.8 Evolution of the simple prominence and overlying bubble from an unstable equilibrium for different values of N , the rate of increase of the flux under the prominence. The time evolution of
(d) the width of the bubble

$$\begin{aligned}
& \frac{B_i^2 \rho_{fo} S^{*2}}{2 B_{lo}^2 \rho_o \left[\left[S^* - \frac{D^*}{2} \right]^2 - \left[R^* + \frac{h_o l^*}{2R_\odot} \right]^2 \right]^2} \\
& - \frac{B_o^2 \rho_{fo} (1 + \cot \theta)}{B_{lo}^2 \rho_o S^* D^*} - \frac{GM_\odot \mu \rho_{fo}}{R_\odot B_{lo}^2 S^{*2}} = 0 \quad (2.44)
\end{aligned}$$

$$\begin{aligned}
& \frac{2B_o^2 \rho_{fo}}{B_{lo}^2 \rho_o D^{*2}} \\
& - \frac{B_i^2 \rho_{fo} S^{*2}}{B_{lo}^2 \rho_o \left[\left[S^* - \frac{D^*}{2} \right]^2 - \left[R^* + \frac{h_o l^*}{2R_\odot} \right]^2 \right]^2} = 0 \quad (2.45)
\end{aligned}$$

$$\begin{aligned}
& \left[\frac{B_{az0}^2}{B_o^2} - 1 \right] \frac{T}{l^*} + \frac{4 l^{*2} F_o^2 F^{*2}}{\phi^2 B_{lo}^2 h_o R_\odot^3 \left[\left[R^* - \frac{h_o l^*}{2R_\odot} \right]^2 - \frac{R_N^2}{R_\odot^2} \right]^2} \\
& - \frac{GM_\odot \mu \rho_{fo}}{R_\odot B_{lo}^2 R^{*2}} \\
& - \frac{B_i^2 R_\odot l^{*2}}{B_{lo}^2 h_o \left[\left[S^* - \frac{D^*}{2} \right]^2 - \left[R^* - \frac{h_o l^*}{2R_\odot} \right]^2 \right]^2} = 0 \quad (2.46)
\end{aligned}$$

Figure 2.9a shows how the equilibrium values of R^* , S^* , and D^* vary with F_o , the flux under the prominence and with all other parameters held fixed at $B_{az0} = 1G$, $B_{lo} = 30G$,

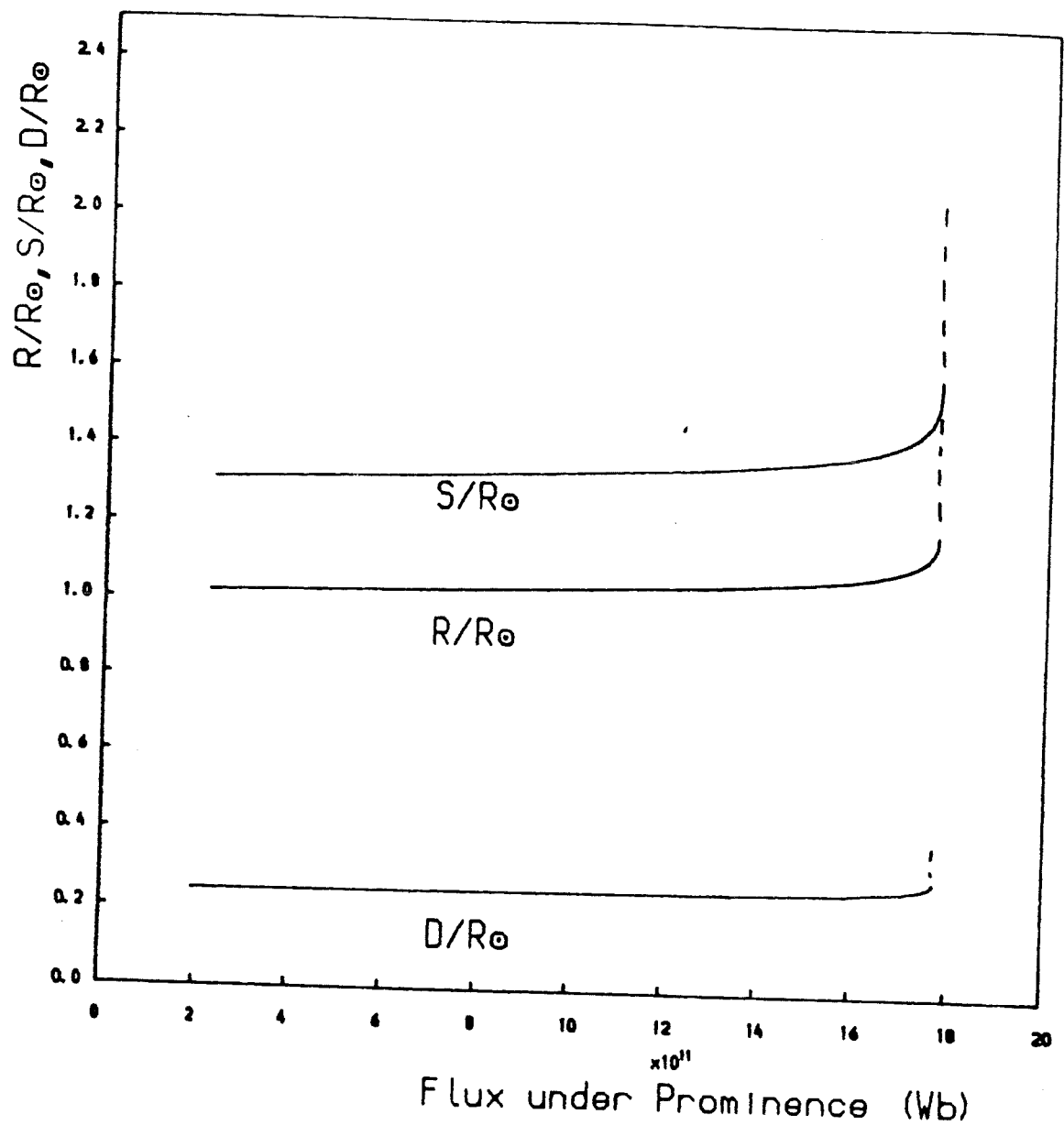


Figure 2.9 The equilibrium and oscillation around a stable equilibrium of a configuration consisting of a line-tied prominence plus an overlying bubble. (a) The variation of the equilibrium parameters with the flux under the prominence.

$B_o = 0.4G$, $B_j = 0.6G$, $\rho_{fo} = 10^{-10}kgm^{-3}$, $\rho_o = 10^{-13}kgm^{-3}$, $\theta = 0.7$,
 $\phi = 0.07$, $\alpha = 0.1$, $h_o = 20Mm$. For values of F_o less than or
 equal to $1.77 \times 10^{12}Wb$ equilibrium solutions exist. On each
 curve the lower branch is stable and the upper branch is
 unstable. One possible equilibrium is at $F_o = 1.76 \times 10^{12}Wb$,
 $R^* = 1.14$, $S^* = 1.49$, $D^* = 0.28$. This is on the stable branch
 but close to the point where the curves turn back upon
 themselves. If a perturbation is applied to the stable system
 by increasing F_o to $1.77 \times 10^{12}Wb$ a stable oscillatory
 solution results as shown in Figures 2.9b, 2.9c and 2.9d. If,
 however, F_o is increased to $1.78 \times 10^{12}Wb$, beyond the
 non-equilibrium point the configuration has no choice but to
 continue to rise as shown in Figure 2.10. The different cases
 are characterised by different values of R_{max} . In case A
 ($R_{max} = 1.50$) no reconnection takes place and in all cases the
 prominence and bubble accelerate outwards before tending to
 constant velocities.

The effect of changing some of the parameters is shown
 in Figure 2.11. Evolution from three different equilibrium
 curves was investigated, namely :

Case I	$B_{jo} = 30G$	$\phi = 0.07$	[Corresponding to footpoints 100Mm apart]
Case II	$B_{jo} = 27.5G$	$\phi = 0.07$	
Case III	$B_{jo} = 30G$	$\phi = 0.105$	[Corresponding to footpoints 150Mm apart]

Figures 2.11a, 2.11b and 2.11c show how the equilibrium
 values of R^* , S^* and D^* respectively vary with F_o . The

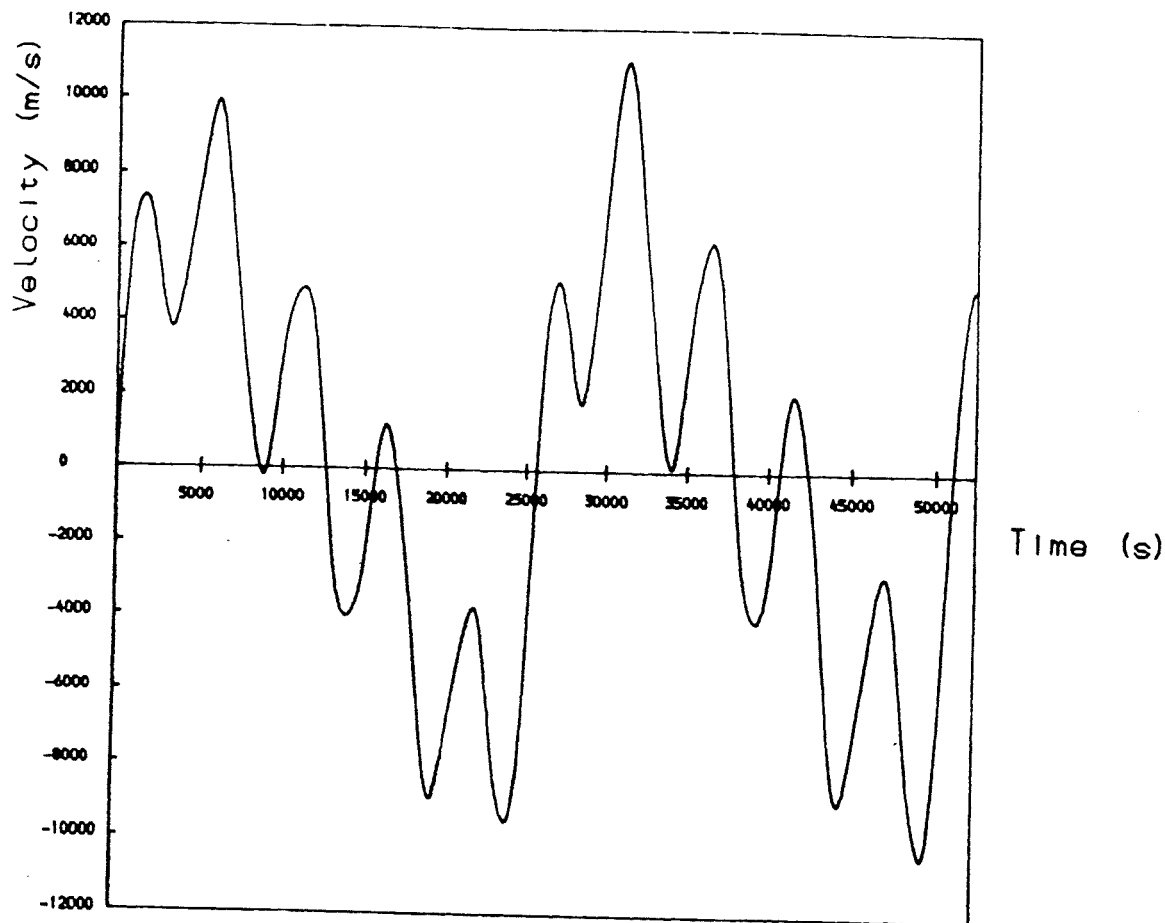


Figure 2.9 The equilibrium and oscillation around a stable equilibrium of a configuration consisting of a line-tied prominence plus an overlying bubble. (b) The time evolution of the speed of rise of the prominence

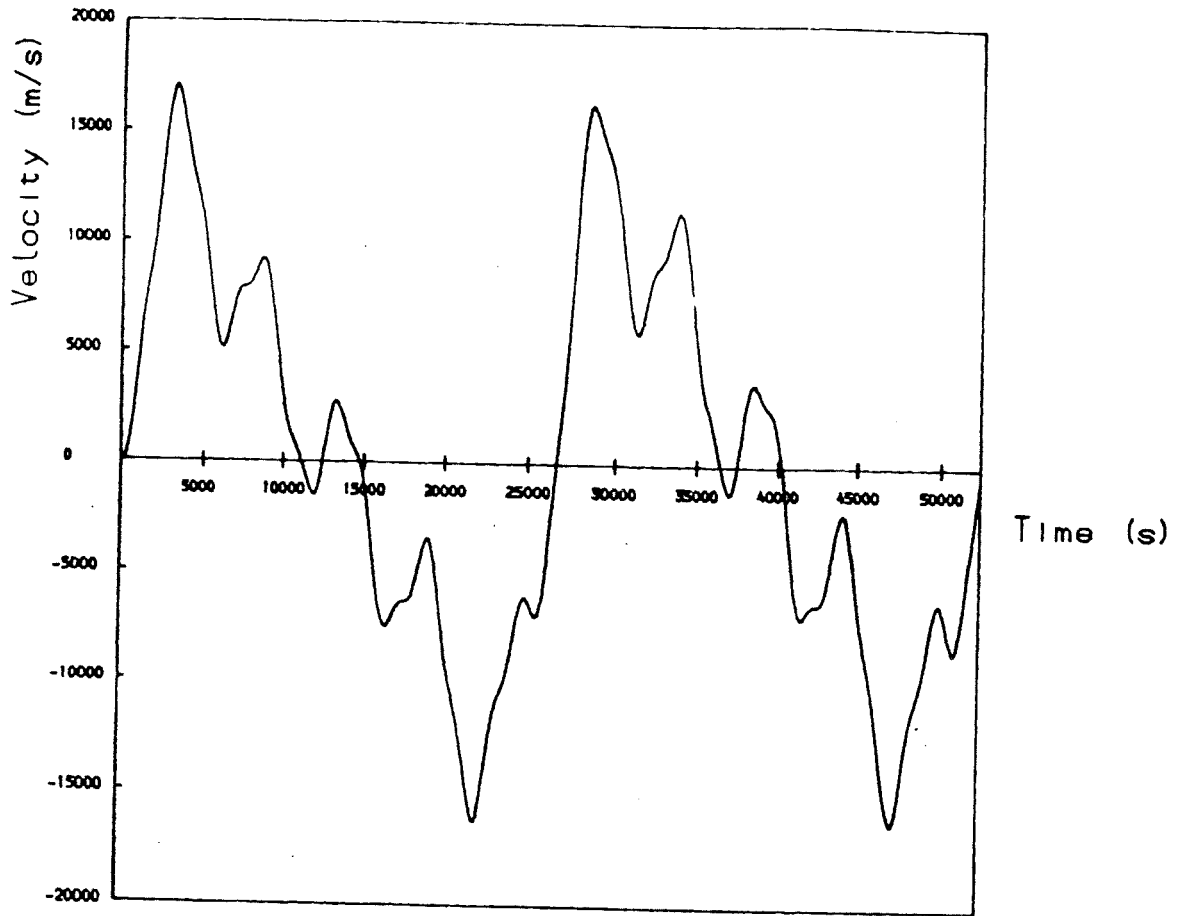


Figure 2.9 The equilibrium and oscillation around a stable equilibrium of a configuration consisting of a line-tied prominence plus an overlying bubble. (c) The time evolution of the speed of rise of the bubble.

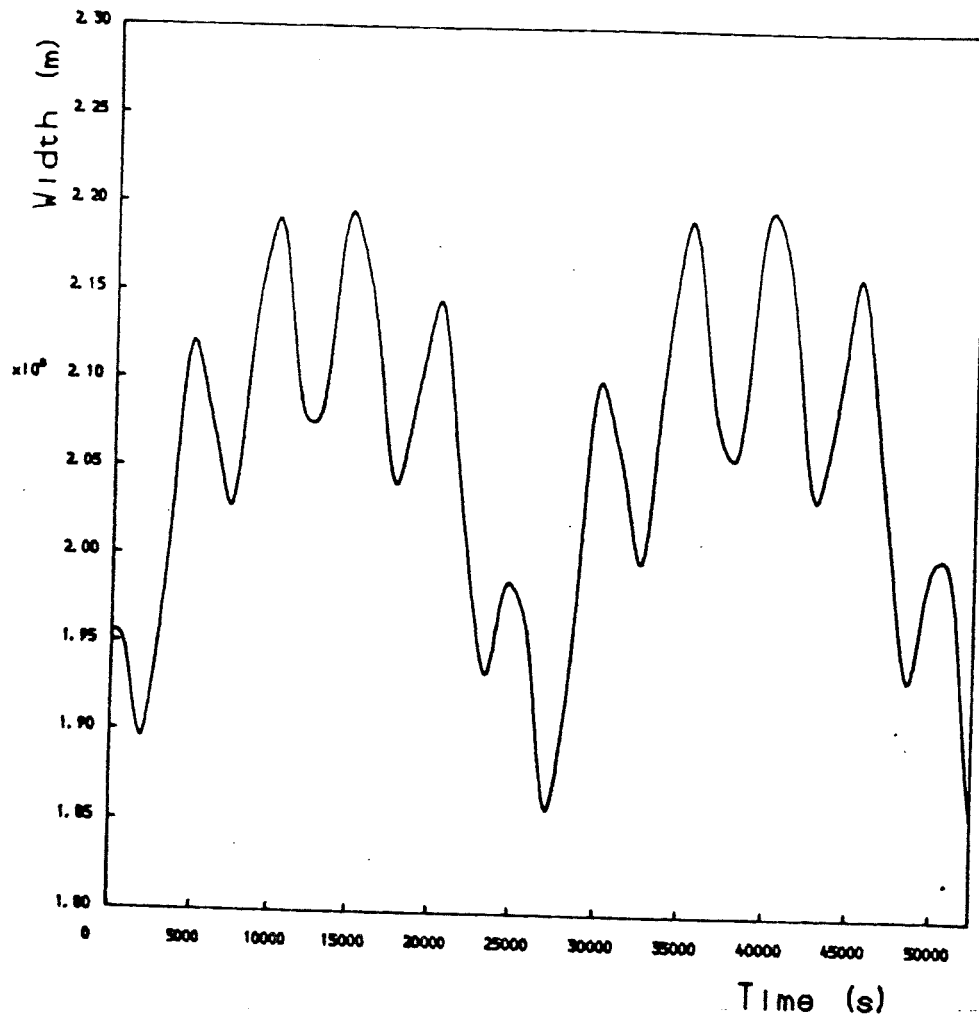


Figure 2.9 The equilibrium and oscillation around a stable equilibrium of a configuration consisting of a line-tied prominence plus an overlying bubble. (d) The time evolution of the width of the bubble.

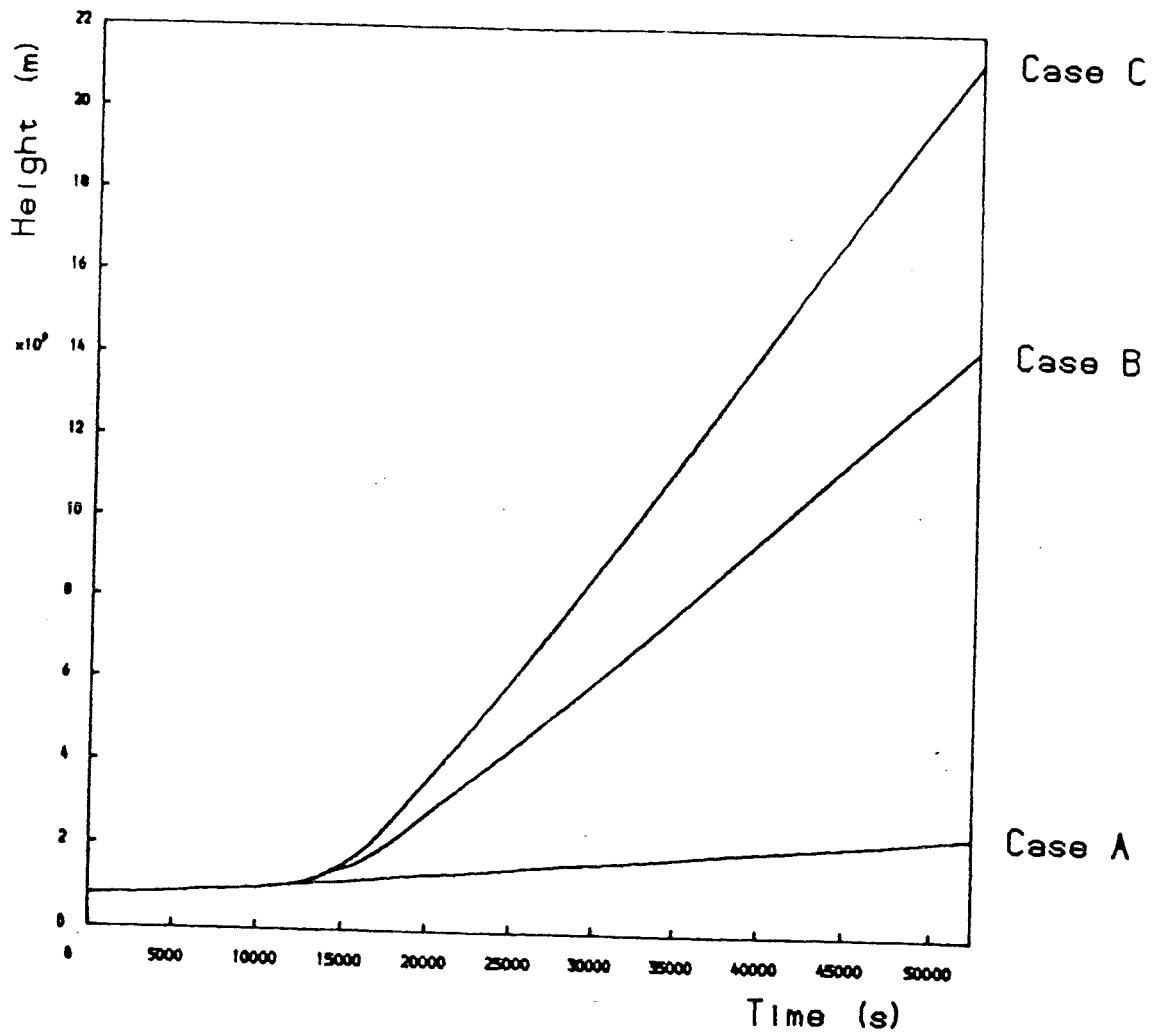


Figure 2.10 The evolution from non-equilibrium of a configuration consisting of a line-tied prominence plus a bubble for $R_{\max} = 1.5, 1.75, 2.0$ (Cases A-C respectively). The time evolution of (a) the height of the prominence

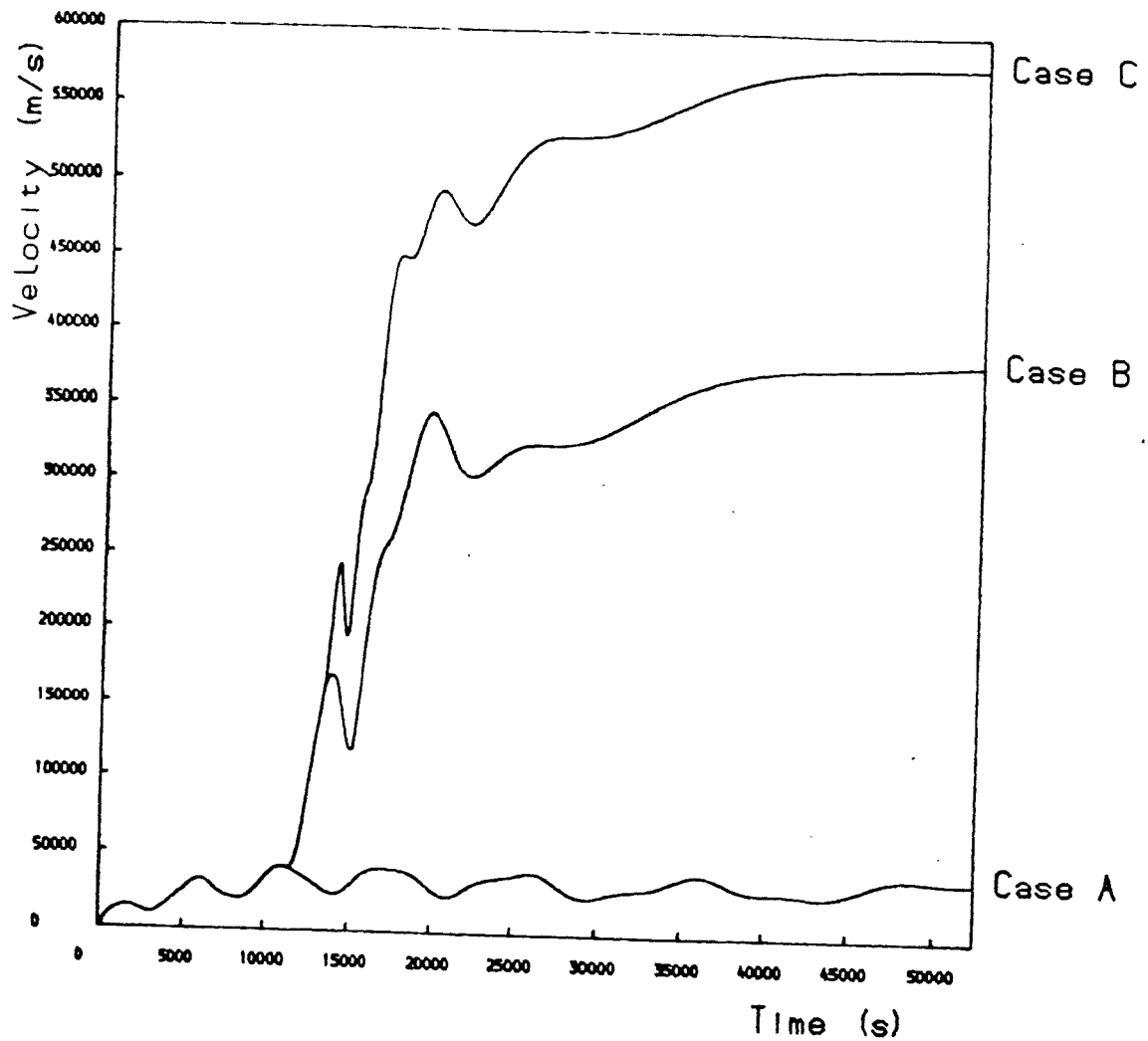


Figure 2.10 The evolution from non-equilibrium of a configuration consisting of a line-tied prominence plus a bubble for $R_{\max} = 1.5, 1.75, 2.0$ (Cases A-C respectively). The time evolution of (b) the speed of rise of the prominence

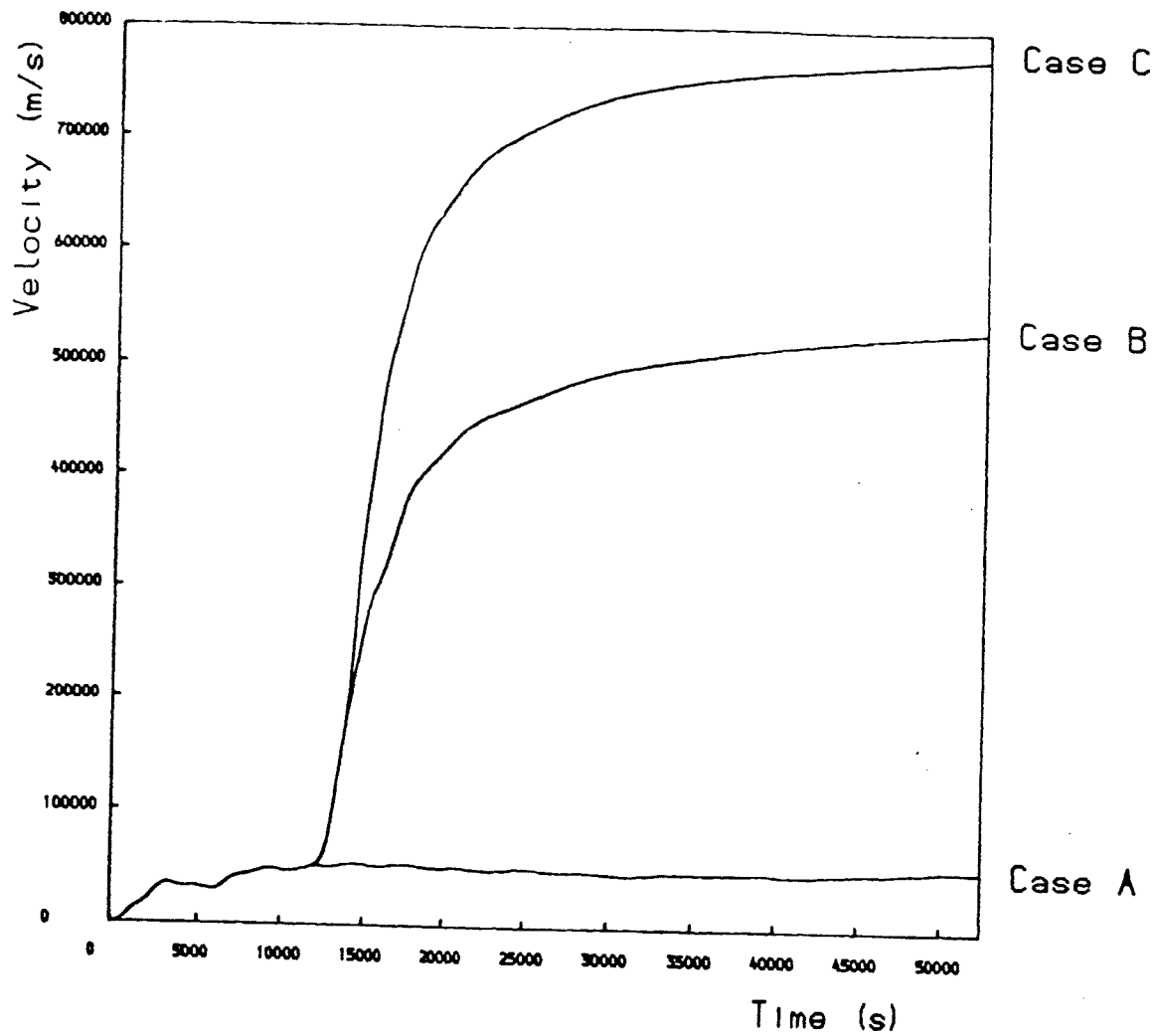


Figure 2.10 The evolution from non-equilibrium of a configuration consisting of a line-tied prominence plus a bubble for $R_{\max} = 1.5, 1.75, 2.0$ (Cases A-C respectively). The time evolution of (c) the speed of rise of the bubble.

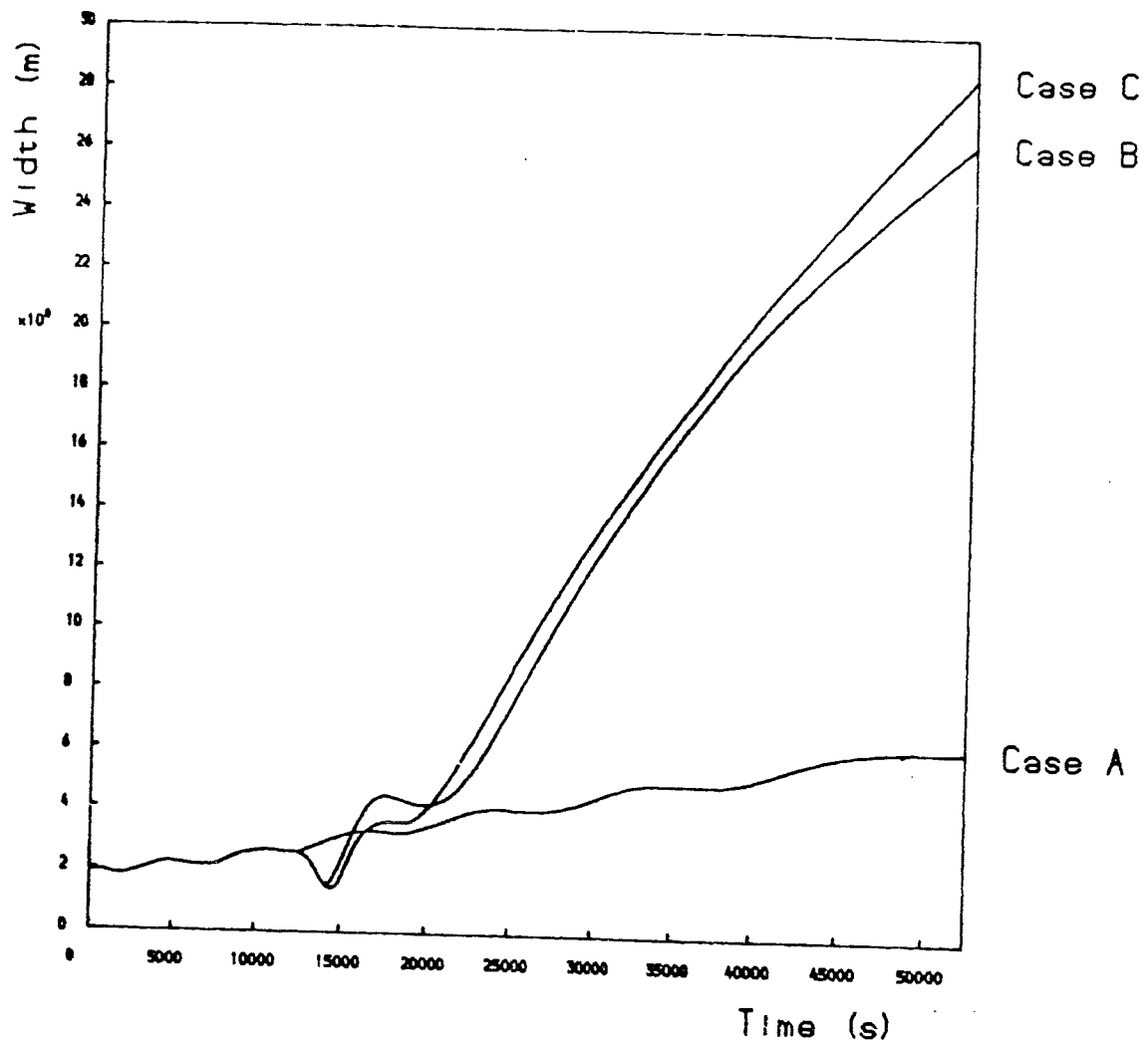


Figure 2.10 The evolution from non-equilibrium of a configuration consisting of a line-tied prominence plus a bubble for $R_{\max} = 1.5, 1.75, 2.0$ (Cases A-C respectively). The time evolution of (d) the width of the bubble.

transition from continuous to dashed curves represents a change from stability to instability. For each case the evolution of the prominence and bubble are shown as they erupt (Figures 2.11d, 2.11e and 2.11f).

2.4 Conclusions

It has been possible here to produce a simple model of a magnetic arcade overlying a prominence which evolve through a series of stable equilibria and then, beyond a critical point they erupt outwards. Two different models for the prominence have been used although the line-tied prominence represents a more realistic model than the simple prominence.

In both cases, when eruption takes place the prominence and bubble accelerate and tend towards constant velocities. This behaviour was also found by Pneuman (1980) and Anzer and Pneuman (1982). However, these authors only modelled the eruption of the coronal mass ejection and not the preceding stable equilibrium. These models were based on the perturbation of a neutrally stable equilibrium which would not remain stable for long periods of time in the presence of ambient disturbances. Mouschovias and Poland (1978) assume a constant velocity for the CME but again do not model the previous evolution.

Pneuman (1980) and Mouschovias and Poland (1978) modelled the coronal mass ejection on its own without an associated prominence, but 70% of coronal mass ejections

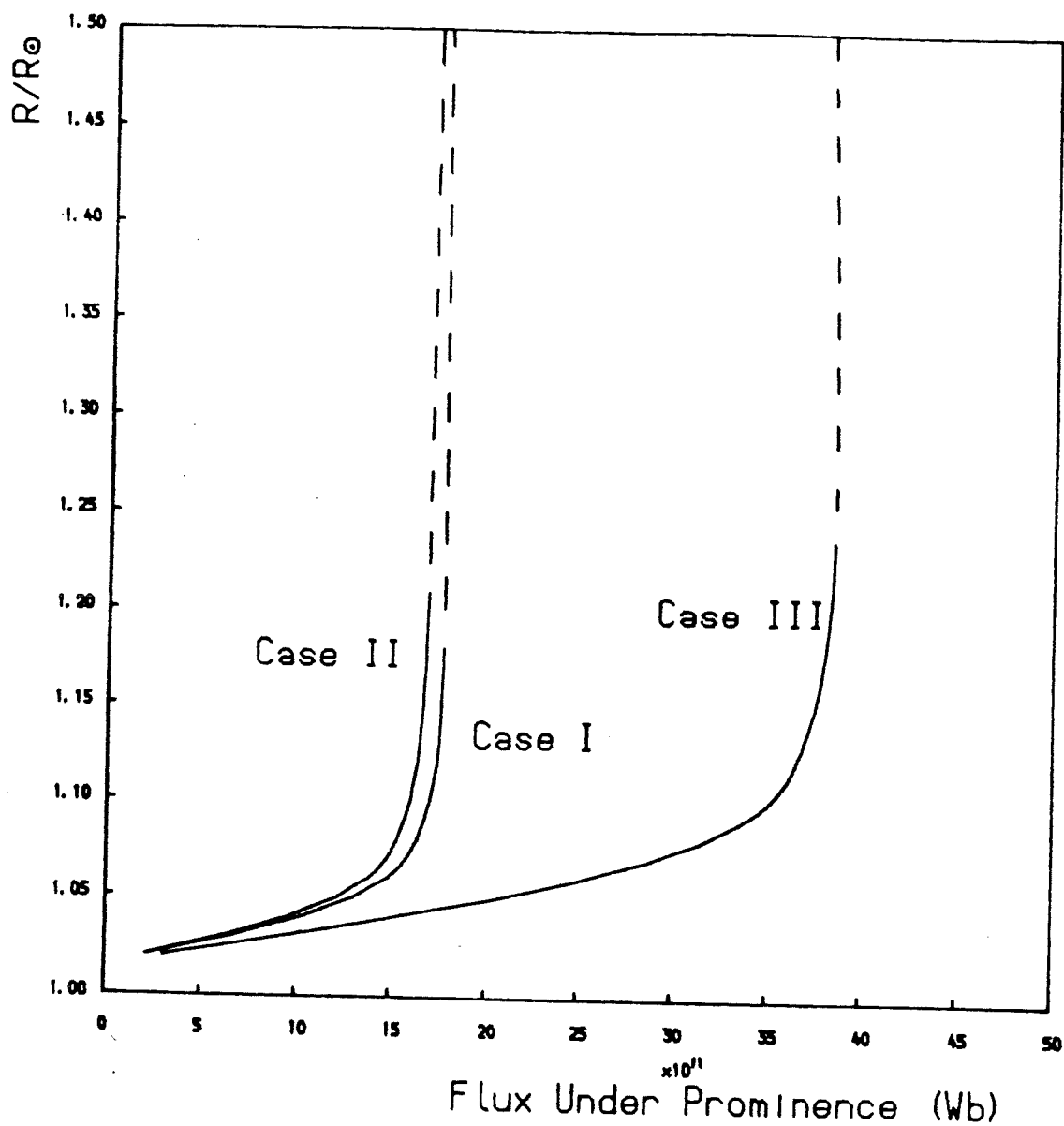


Figure 2.11 The equilibrium of a line-tied prominence and a bubble for: $B_{10} = 30G$, $\phi = 0.07$ (Case I); $B_{10} = 27.5G$, $\phi = 0.07$ (Case II); $B_{10} = 30G$, $\phi = 0.105$ (Case III).
 (a) Variation of equilibrium height of the prominence with the flux under the prominence.

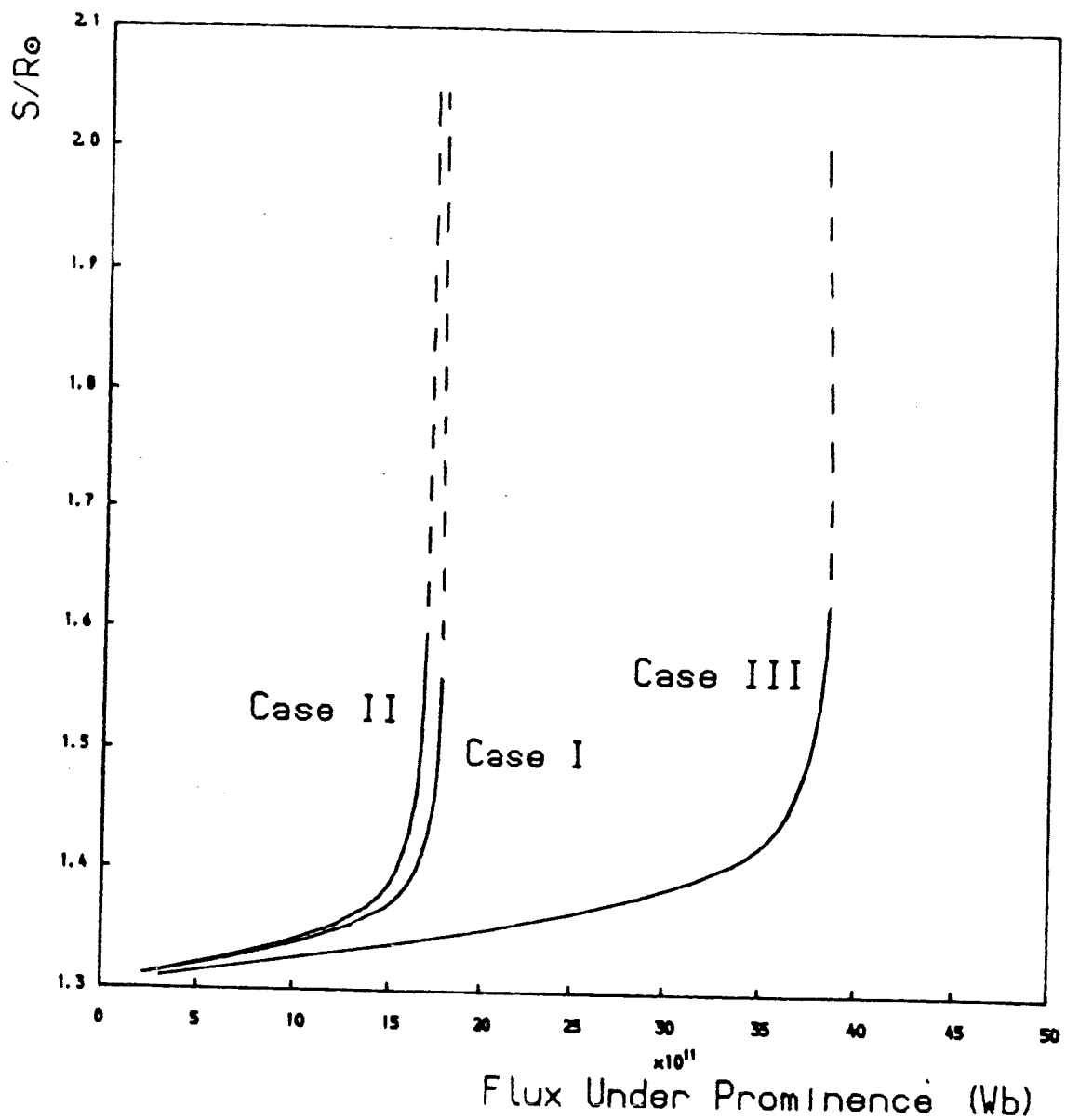


Figure 2.11 The equilibrium of a line-tied prominence and a bubble for: $B_{10} = 30\text{G}$, $\phi = 0.07$ (Case I);
 $B_{10} = 27.5\text{G}$, $\phi = 0.07$ (Case II);
 $B_{10} = 30\text{G}$, $\phi = 0.105$ (Case III).
 (b) Variation of equilibrium height of the overlying bubble with the flux under the prominence.

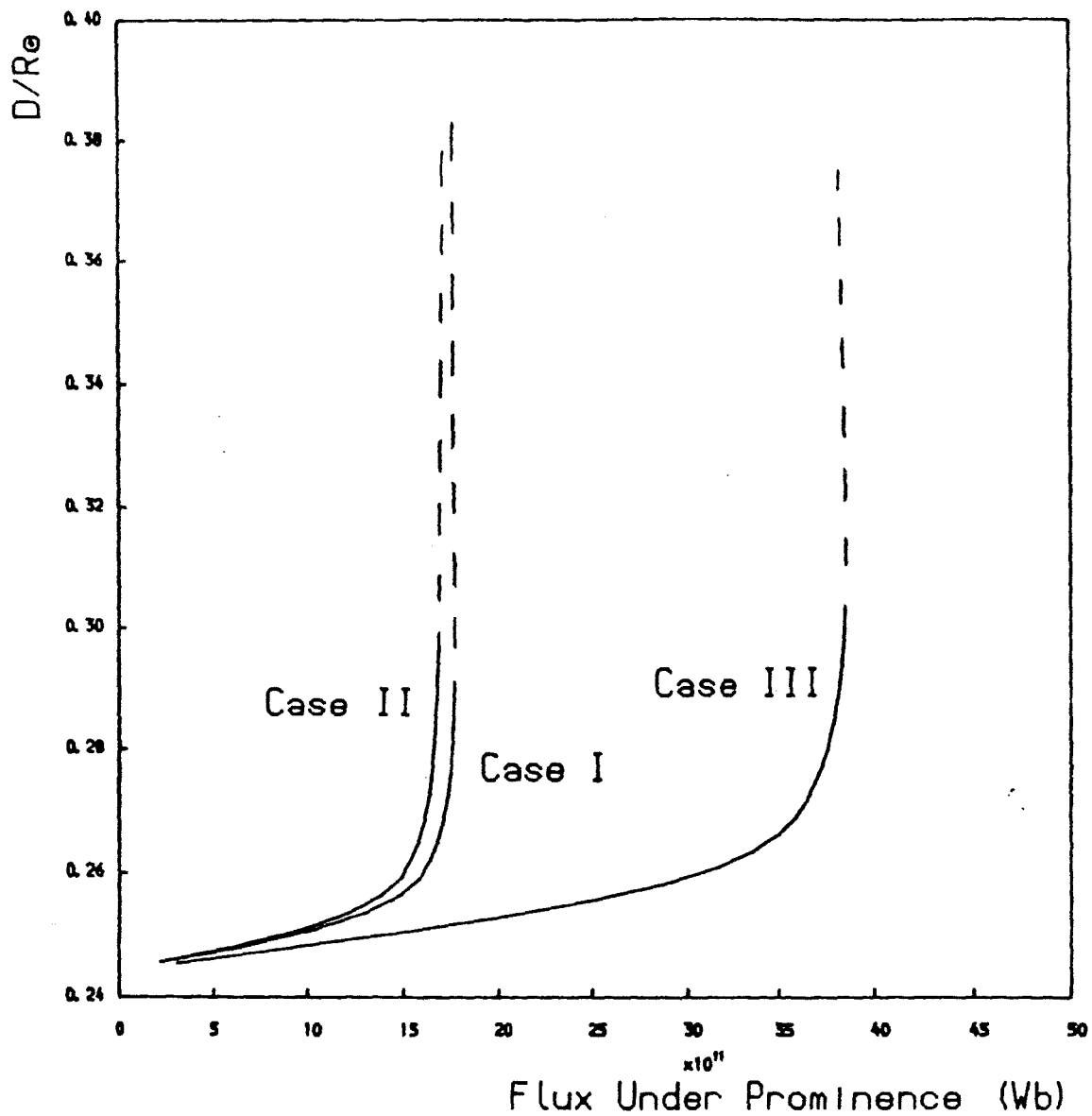


Figure 2.11 The equilibrium of a line-tied prominence and a bubble for: $B_{10} = 30\text{G}$, $\phi = 0.07$ (Case I);
 $B_{10} = 27.5\text{G}$, $\phi = 0.07$ (Case II);
 $B_{10} = 30\text{G}$, $\phi = 0.105$ (Case III).
(c) Variation of equilibrium width of the overlying bubble with the flux under the prominence.

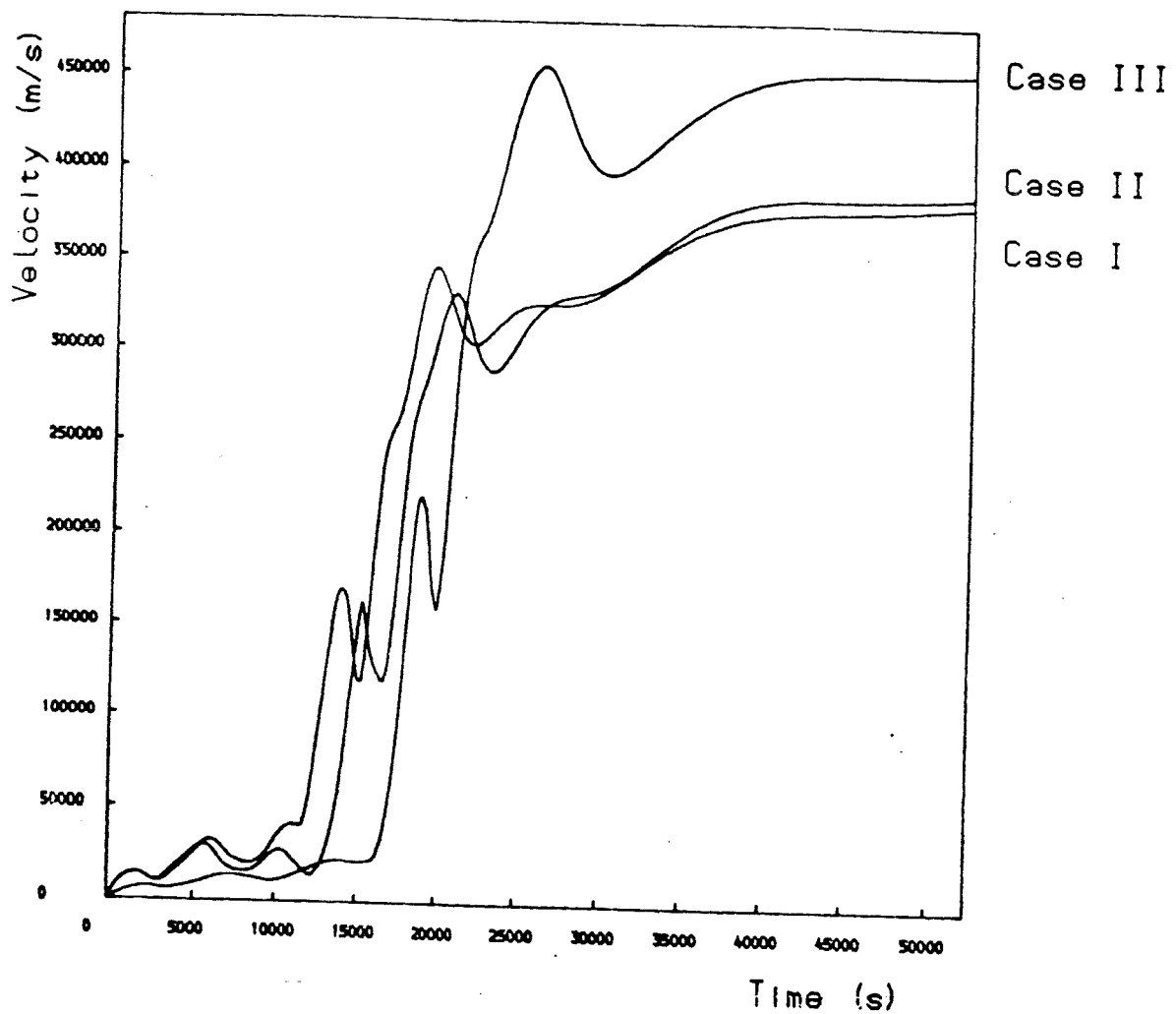


Figure 2.11 The time evolution of a line-tied prominence and a bubble for: $B_{10} = 30\text{G}$, $\phi = 0.07$ (Case I); $B_{10} = 27.5\text{G}$, $\phi = 0.07$ (Case II); $B_{10} = 30\text{G}$, $\phi = 0.105$ (Case III).
 The time evolution of
 (d) the speed of rise of the prominence

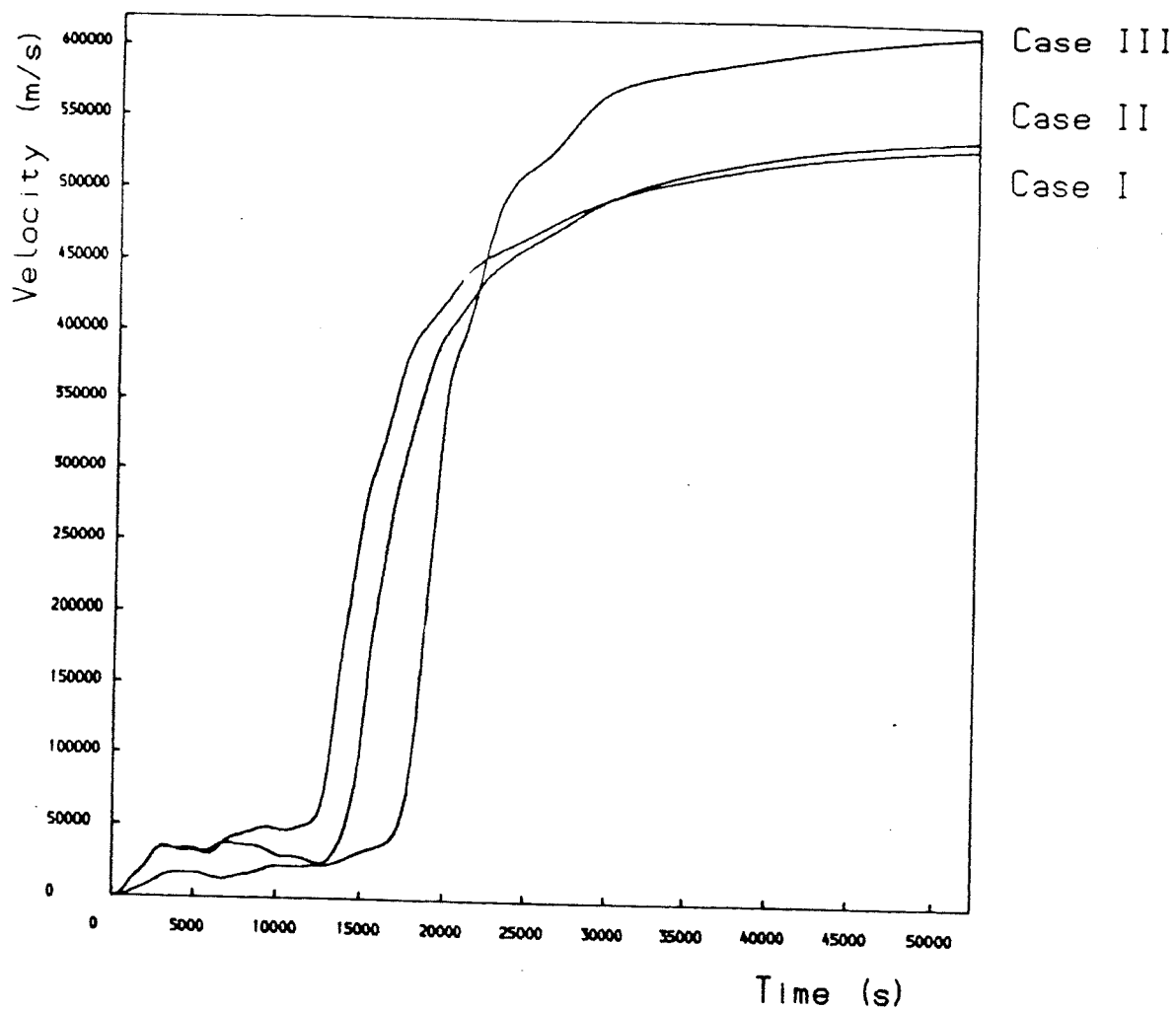


Figure 2.11 The time evolution of a line-tied prominence and a bubble for: $B_{10} = 30G$, $\phi = 0.07$ (Case I); $B_{10} = 27.5G$, $\phi = 0.07$ (Case II); $B_{10} = 30G$, $\phi = 0.105$ (Case III).
The time evolution of
(e) the speed of rise of the bubble.

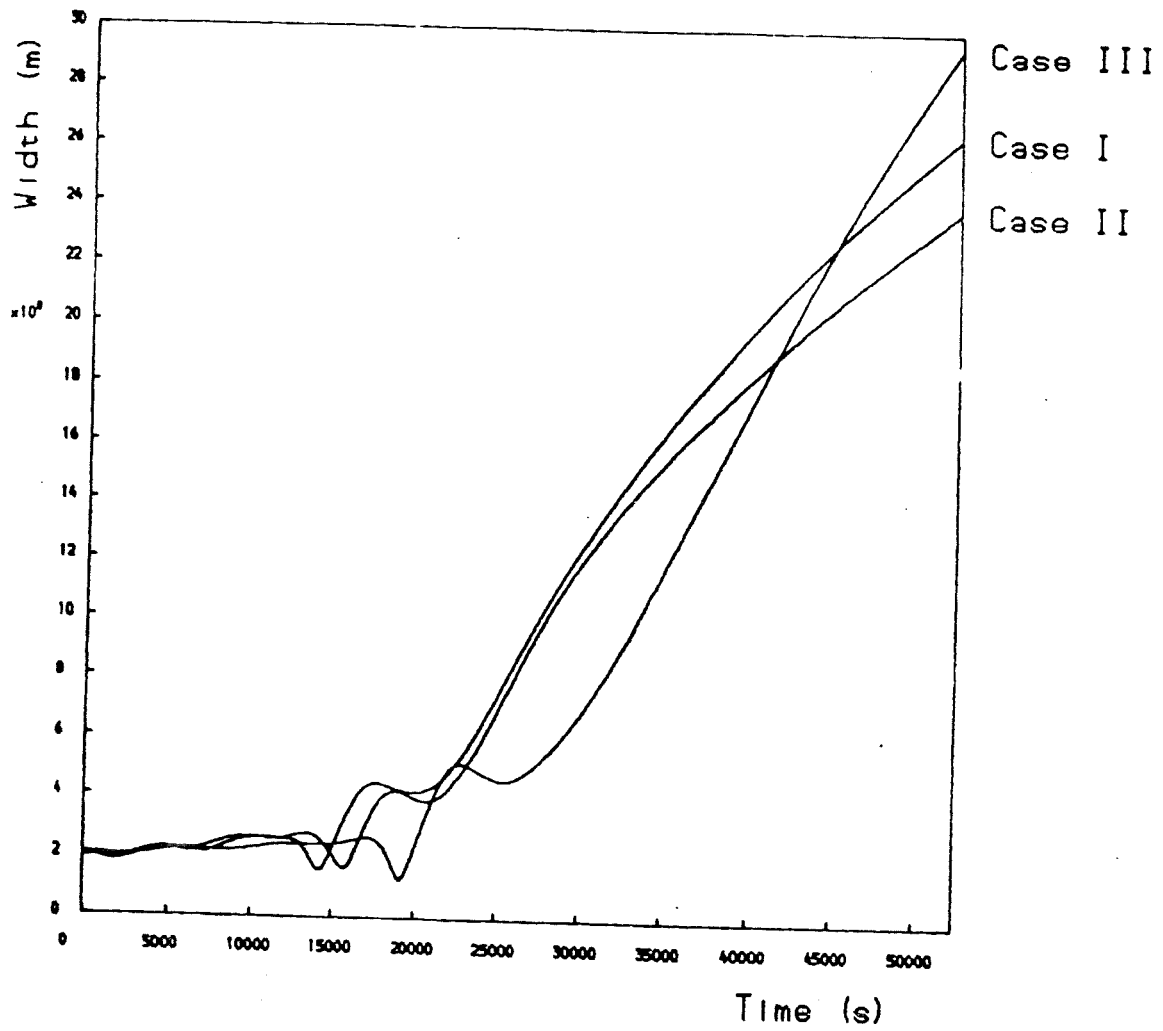


Figure 2.11 The time evolution of a line-tied prominence and a bubble for: $B_{l_0} = 30\text{G}$, $\phi = 0.07$ (Case I); $B_{l_0} = 27.5\text{G}$, $\phi = 0.07$ (Case II); $B_{l_0} = 30\text{G}$, $\phi = 0.105$ (Case III).
 The time evolution of
 (f) the rate of change of the width of the bubble

are seen to have associated erupting prominences. Also coronal mass ejections are often associated with large flares in which reconnection is probably occurring beneath an erupting active-region prominence.

It is useful to consider energy curves in order to understand the transition from stability to instability. Figure 2.12 shows the integral of equation (2.39) for a line-tied prominence with $F_0 = 1.68 \times 10^{12} \text{Wb}$, $1.69 \times 10^{12} \text{Wb}$ and $1.70 \times 10^{12} \text{Wb}$ respectively. Figure 2.12a shows an energy curve with a stable equilibrium corresponding to point A on Figure 2.5a; and an unstable equilibrium point corresponding to point B. Figure 2.12b shows the energy curve with an equilibrium point C where the stable and unstable equilibria merge and Figure 2.12c shows the energy curve where point D is not an equilibrium. A slight increase in flux can thus transform the energy curve from one with a stable equilibrium and an unstable equilibrium to one with no equilibria at all.

Whenever the prominence erupts it accelerates upwards and reaches a constant velocity compatible with those found from observation (MacQueen, 1980). The constant velocity occurs since all forces decrease with increasing R , and so when the prominence becomes high enough the acceleration becomes negligible.

When the stable equilibrium is perturbed, an oscillatory motion is found. For the cases where the prominence exists on its own this is simply the normal mode of oscillation of

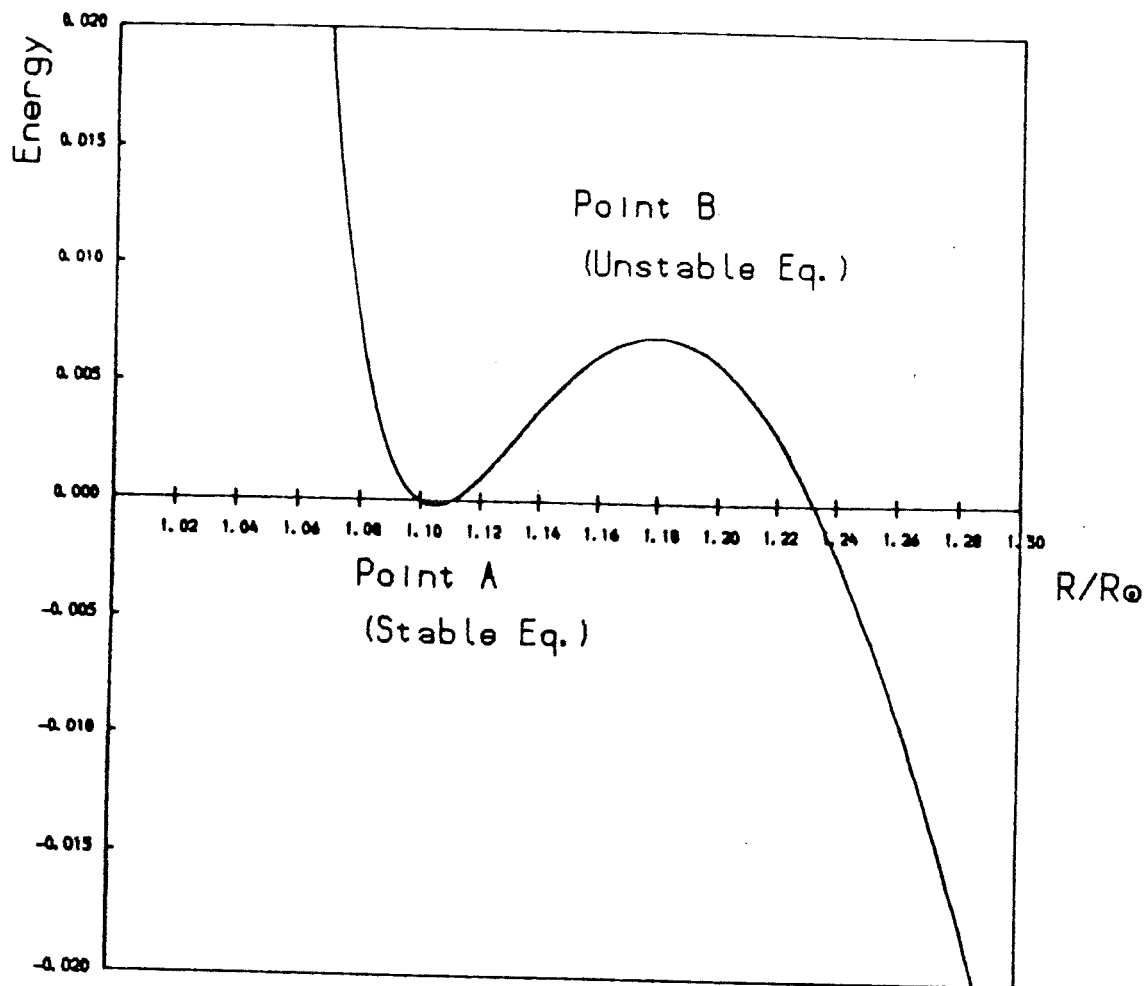


Figure 2.12 The variation of the potential energy of a line-tied prominence alone. The points A, B, C, D, refer to the locations on figure 2.5a. Energy curve for
 (a) the equilibrium case

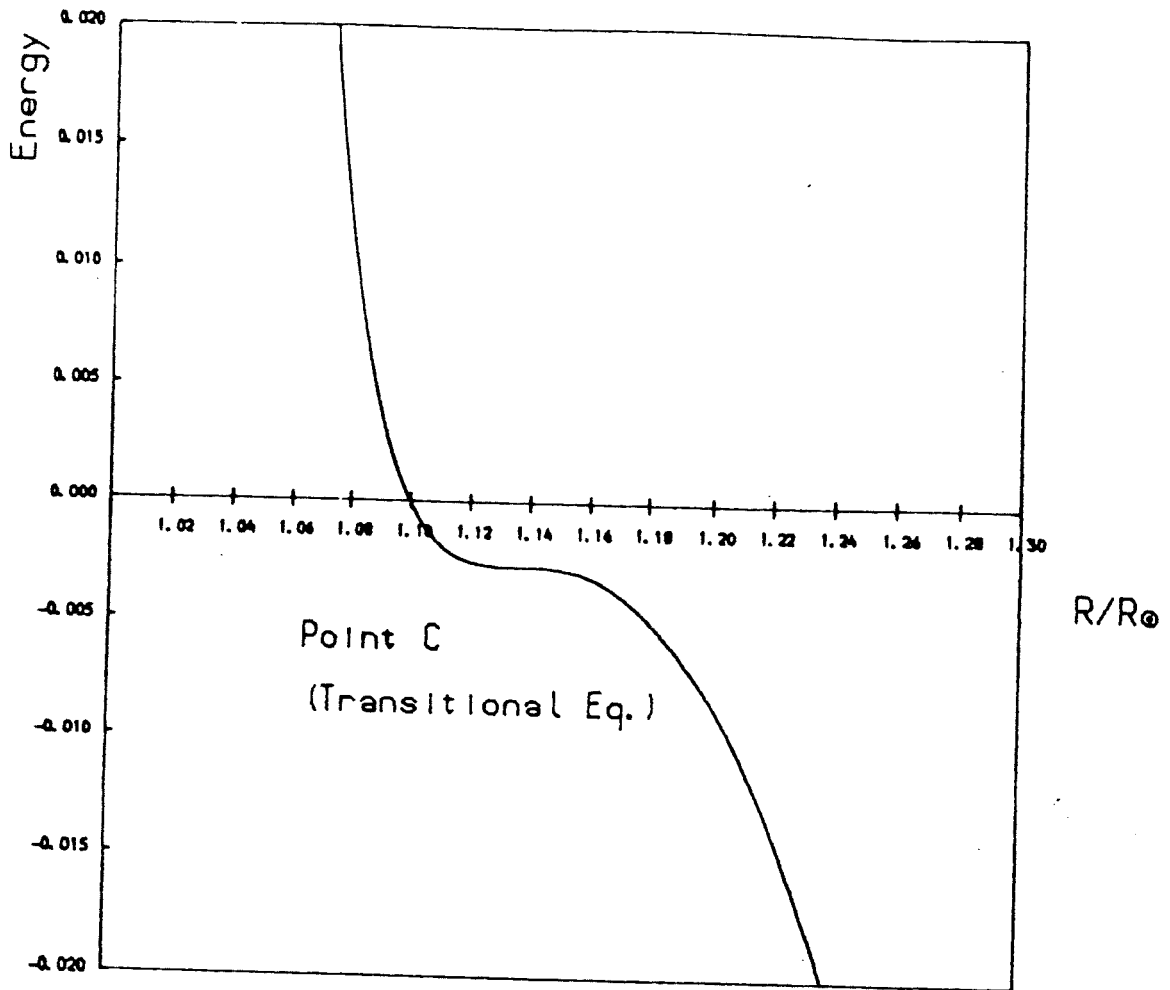


Figure 2.12 The variation of the potential energy of a line-tied prominence alone. The points A, B, C, D, refer to the locations on figure 2.5a. Energy curve for
 (b) the limiting equilibrium case

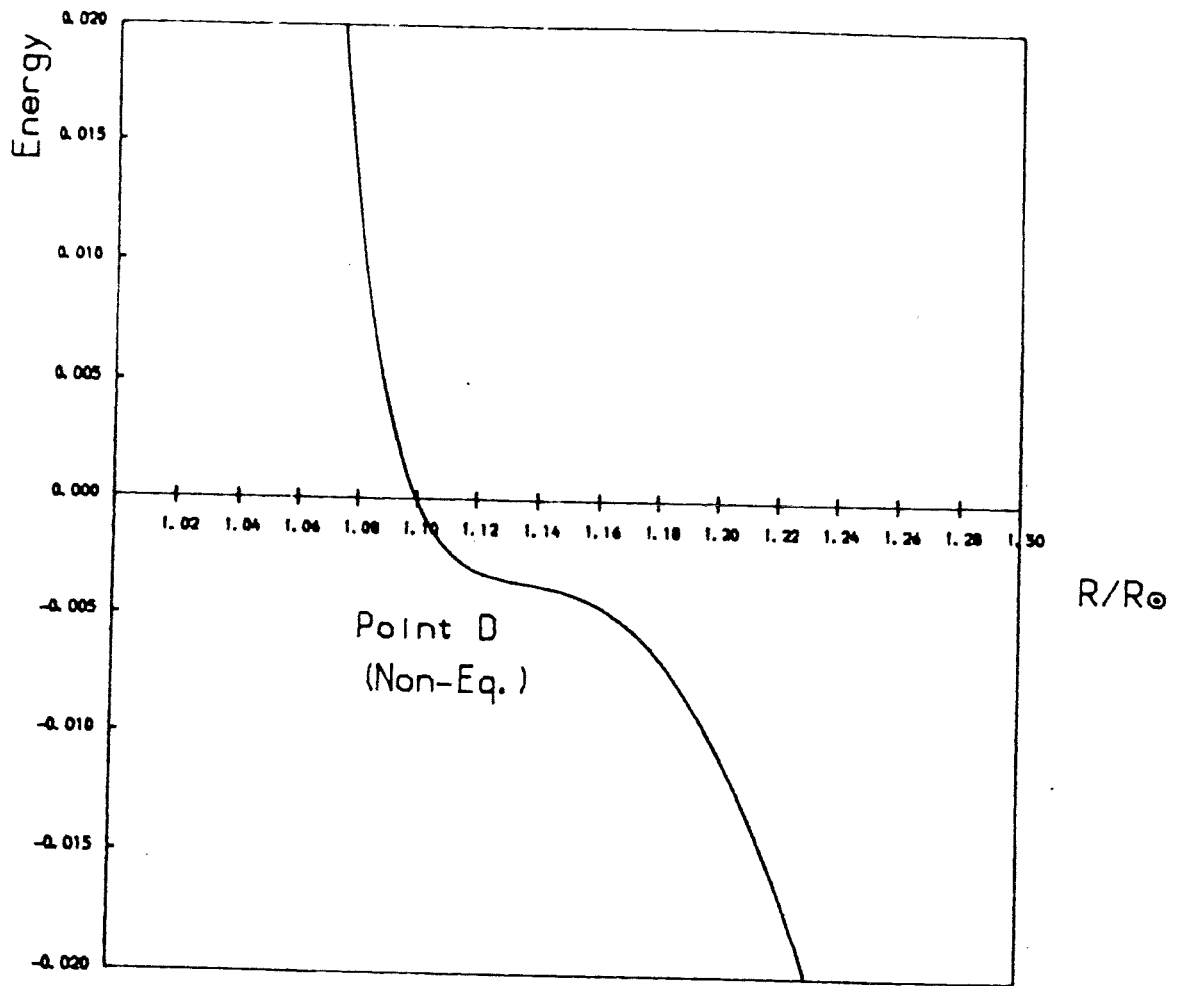


Figure 2.12 The variation of the potential energy of a line-tied prominence alone. The points A, B, C, D, refer to the locations on figure 2.5a. Energy curve for
(c) the non-equilibrium case

the first-order system. In the case where the CME exists above the prominence the oscillations are more complicated since they represent the superposition of the three normal modes of the third-order system. In the present work both the stable and eruptive stages of the coronal mass ejection are modelled in a simple global but non-linear manner. It complements alternative approaches such as the full linear stability analysis of a magnetic arcade (Hood 1983, 1985) and it suggests ingredients which may help future more sophisticated analytical and numerical models.

CHAPTER THREE - NON-EQUILIBRIUM OF A CYLINDRICAL MAGNETIC ARCADE

3.1 Introduction

As mentioned in section 1.3, one limiting possibility for the eruption of a coronal mass ejection is that the overlying bubble or arcade loses equilibrium, removing stabilising field lines above the prominence (Figure 3.1) (Low, 1981, Wolfson, 1982, Priest, 1988a). In the model due to Priest (see section 1.3), the field lines in the arcade are constrained to remain cylindrically symmetric when the arcade is perturbed. Priest found that such equilibria ceased to exist when the arcade was perturbed from the limiting case with the axis lying on the photosphere. It is an obvious generalisation to see if equilibria are possible when the constraint of cylindrical symmetry is removed.

The object of the present work is to investigate in more detail a field arcade which is originally cylindrically symmetric and is in the threshold equilibrium considered by Priest. The pressure along the base of the arcade is altered and the field is allowed to vary freely in both the radial and azimuthal directions but with the footpoints held fixed. Neighbouring equilibria are sought with the aim of clarifying the nature of the onset of arcade eruptions by non-equilibrium.

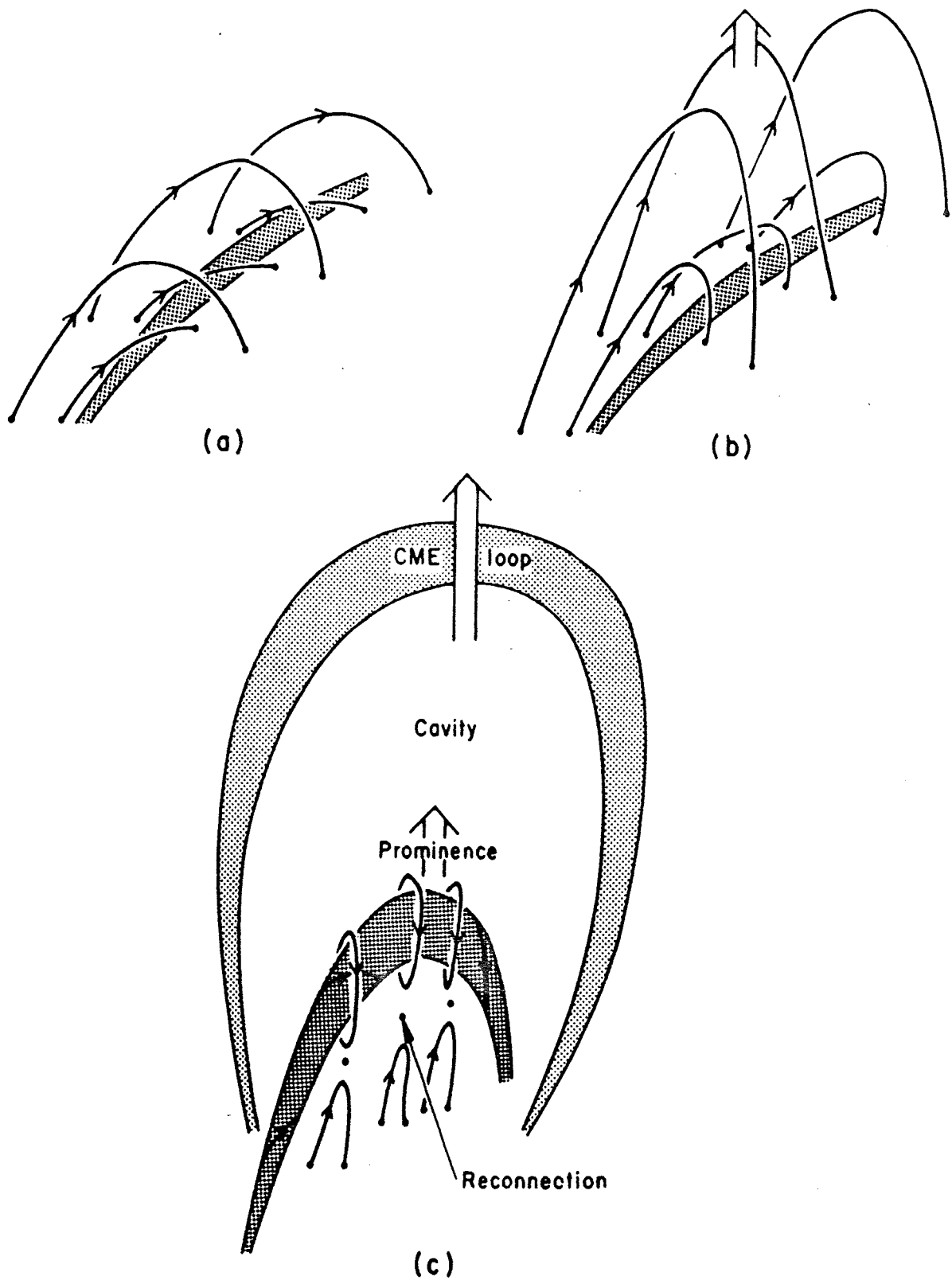


Figure 3.1 a) A prominence in equilibrium beneath a coronal arcade
 b) The arcade loses equilibrium or stability and erupts
 c) The prominence moves up slowly and then erupts rapidly when reconnection begins below it. [Courtesy E. R. Priest]

3.2 The Analytical Model

3.2.1 The Original Equilibrium

The configuration representing the original equilibrium in this model problem is described as follows and is shown in Figure 3.2. A semi-circular region OABC contains plasma and magnetic field and is surrounded by a field-free region. The semi-circular region represents a section through a three-dimensional arcade, with radius a_0 . Inside this area, the field has no radial or shear component and the azimuthal component at a distance r from the axis O is given by $B_0(r)$. The equilibrium plasma pressure can be found by integrating the equation of motion (1.10) with the right-hand side equal to zero and considering only pressure and magnetic forces.

$$\frac{dp}{dr} + \frac{d}{dr} \left(\frac{B_o^2}{2\mu} \right) + \frac{B_o^2}{\mu r} = 0 \quad (3.1)$$

where gravity is neglected. Integrating,

$$p(a_0) - p(r) + \frac{1}{2\mu} \left[B_o^2(a_0) - B_o^2(r) \right] + \frac{1}{\mu} \int_r^{a_0} \frac{B_o^2}{r} dr = 0 \quad (3.2)$$

and thus $p_o = p(r)$ is given by

$$p_o = p_e + \frac{1}{\mu} \int_r^{a_0} \frac{B_o^2}{r} dr - \frac{B_o^2}{2\mu} \quad (3.3)$$

where

$$p_e = \frac{B_{\infty}^2}{2\mu} - p(a_0) \quad (3.4)$$

and B_{∞} is the value B_0 takes when $r = a_0$.

Above and to either side of this region, the plasma is

at a pressure p_e , giving pressure balance on the semi-circular boundary ABC. Below the straight boundary COA, there exists a pressure of

$$p = p_e + \frac{1}{\mu} \int_x^{a_0} \frac{B_o^2}{x} dx - \frac{B_o^2}{2\mu} \quad (3.5)$$

balancing the internal plasma pressure.

3.2.2 The Perturbation

One possible class of perturbation is to alter the pressure along the base COA by an amount that varies continuously and symmetrically between C and A and is zero at, and outside, the boundary at C and A.

If an equilibrium field configuration can be found to match this base pressure it will satisfy the equation

$$\nabla p = \mathbf{j} \times \mathbf{B} \quad (3.6)$$

where

$$\mathbf{j} = \frac{1}{\mu} \nabla \times \mathbf{B} \quad (3.7)$$

and

$$\mathbf{B} = \nabla \times \mathbf{A} \quad (3.8)$$

Linearising (3.6) by setting $\mathbf{B} = \mathbf{B}_o + \mathbf{B}_1$ where $\mathbf{B}_1 \ll \mathbf{B}_o$, etc. gives

$$\mathbf{j}_1 \times \mathbf{B}_o + \mathbf{j}_o \times \mathbf{B}_1 = \nabla p_1 \quad (3.9)$$

$$\mathbf{j}_1 = \frac{1}{\mu} \nabla \times \mathbf{B}_1 \quad (3.10)$$

$$\mathbf{B}_1 = \nabla \times \mathbf{A}_1 \quad (3.11)$$

The potential \mathbf{A}_1 is assumed to be of the form $A_1 \hat{\mathbf{z}}$. The field lines will be assumed to be line-tied on the

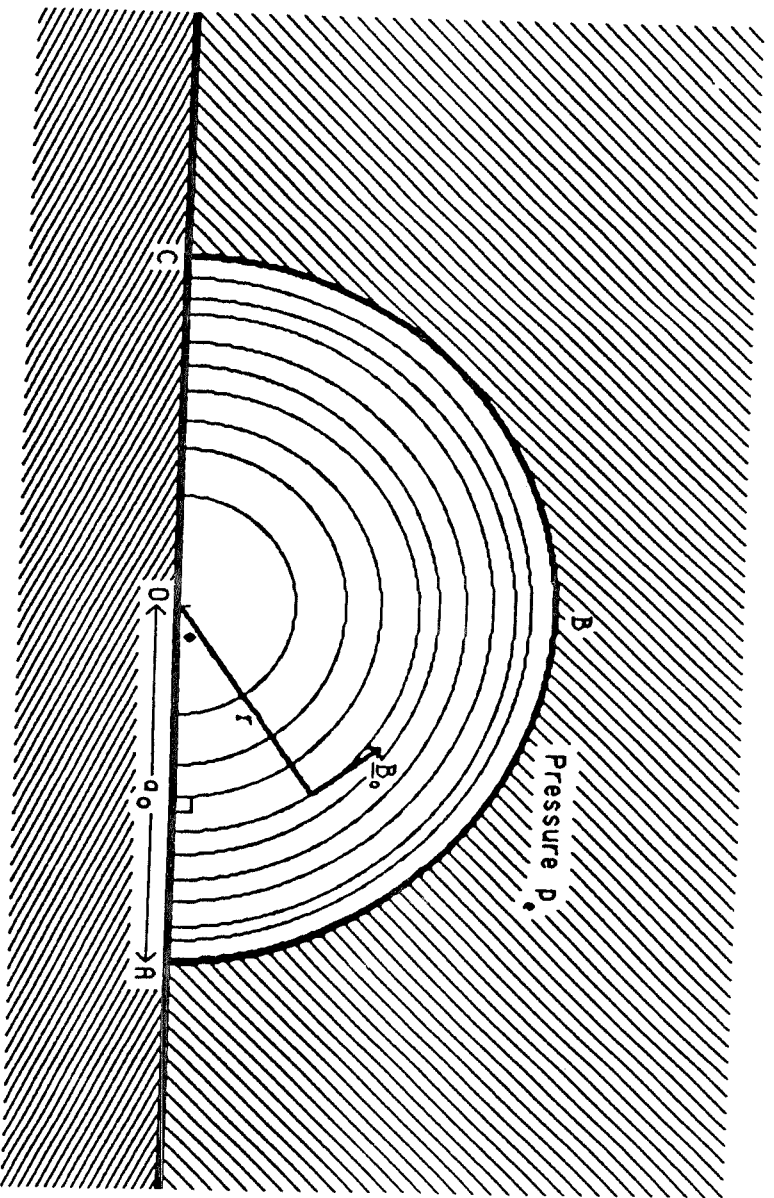


Figure 3.2 The equilibrium notation for the magnetic arcade

base COA so that $dA_1/dr = 0$ (i.e. A_1 is a constant) on $\phi = 0$ and π . Due to the potential nature of A_1 this constant can be set equal to zero. Thus a first boundary condition is

$$A_1 = 0 \quad \text{on } \phi = 0, \pi. \quad (3.12)$$

Also on the base, the perturbed pressure is imposed in the form

$$p_1 = \epsilon (B_{o0}^2 / 2\mu) f(r) \quad \text{on } \phi = 0, \pi \quad (3.13)$$

which will be expressed below (equation (3.39)) as a polynomial in r^2 .

A third boundary condition, describes the pressure balance on the outer boundary $r = a_0$. This boundary is perturbed from $r = a_0$ to $r = a_0 + \xi$, where the potential is given by

$$\begin{aligned} A(a + \xi) &\equiv A_0(a_0 + \xi) + A_1(a_0 + \xi) \\ &= A_0(a_0) + \xi A_0'(a_0) + A_1(a_0) = A_0(a_0) \end{aligned} \quad (3.14)$$

since the boundary field-line preserves its potential. This implies that

$$\xi = - \frac{A_1(a_0)}{\frac{dA_0}{dr}(r = a_0)} = \frac{A_1(a_0)}{B_0'(a_0)} \quad (3.15)$$

At $r = a_0 + \xi(a_0, \phi)$ it is required that the total perturbed pressure vanishes. Since the plasma pressure is

$$p(a_0 + \xi) = p_0(a_0) + \xi p_0'(a_0) + p_1(a_0)$$

and the magnetic pressure is

$$\frac{B \cdot B}{2\mu} = \frac{B_o^2(a_o)}{2\mu} + \frac{B_o(a_o) B_o'(a_o) \xi}{\mu} + \frac{B_o(a_o) B_{1\phi}(a_o)}{\mu}$$

this condition becomes

$$\xi p_o'(a_o) + p_1(a_o) + \frac{\xi B_o(a_o) B_o'(a_o)}{\mu} - \frac{B_o(a_o)}{\mu} \frac{dA_1}{dr} \Big|_{r=a_o} = 0 \quad (3.16)$$

Combining (3.15) and (3.16),

$$\begin{aligned} \frac{A_1(a_o)}{B_o(a_o)} p_o'(a_o) + p_1(a_o) + \frac{A_1(a_o) B_o'(a_o)}{\mu} \\ - \frac{B_o(a_o)}{\mu} \frac{dA_1}{dr} \Big|_{r=a_o} = 0 \end{aligned} \quad (3.17)$$

Differentiating (3.3)

$$p_o'(a_o) = - \frac{1}{\mu} \frac{B_o^2}{r} \Big|_{r=a_o} - \frac{1}{\mu} B_o(a_o) \frac{dB_o}{dr} \Big|_{r=a_o} \quad (3.18)$$

Also, integrating (3.23)

$$p_1 = \frac{1}{\mu r} \frac{d}{dr} (r B_o) A_1 + g(r) \quad (3.19)$$

where $g(r) = \epsilon B_{o0} / 2\mu f(r)$ by (3.13). So

$$p_1(a_o) = \frac{A_1(a_o)}{\mu a_o} (B_{\infty} + a_o B_o'(a_o)) \quad (3.20)$$

Thus equation (3.17) becomes

$$A_1(a_o) \frac{dB_o}{dr} \Big|_{r=a_o} = B_o(a_o) \frac{dA_1}{dr} \Big|_{r=a_o} \quad (3.21)$$

When Δ_1 is set equal to $A_1 \hat{z}$ and equations (3.10) and (3.11) are substituted into equation (3.9), the \hat{r} - and $\hat{\phi}$ -components become

$$\frac{\partial p_1}{\partial r} = \frac{1}{\mu} \left[\frac{1}{r} \frac{d}{dr} (r B_o) \frac{\partial A_1}{\partial r} + \frac{B_o}{r} \frac{\partial}{\partial r} \left(r \frac{\partial A_1}{\partial r} \right) + \frac{B_o}{r^2} \frac{\partial^2 A_1}{\partial \phi^2} \right] \quad (3.22)$$

$$\frac{\partial p_1}{\partial \phi} = \frac{1}{\mu r} \frac{d}{dr} (r B_o) \frac{\partial A_1}{\partial \phi} \quad (3.23)$$

After integrating (3.23), utilising the boundary condition

(3.13), and substituting into (3.22) the basic equation describing the perturbed equilibrium becomes

$$\begin{aligned} & \frac{d}{dr} \left(r \frac{dA_1}{dr} \right) + \frac{1}{r} \frac{d^2 A_1}{d\phi^2} - \frac{r A_1}{B_0} \frac{d}{dr} \left[\frac{1}{r} \frac{d}{dr} (r B_0) \right] \\ & = \frac{\epsilon B_0^2}{2 B_0} r f'(r) \end{aligned} \quad (3.24)$$

3.2.3 A Constraint on the Perturbation

Perturbations from the cylindrical equilibrium are described by equation (3.24) subject to the boundary conditions (3.12), (3.13) and (3.21). Before proceeding with the solution it is useful to establish a constraint on the form of the pressure function $f(r)$ as follows. Equation (3.24) may be multiplied by $B_0 \sin \phi$ and integrated over the semi-circle $0 \leq r \leq a_0$, $0 \leq \phi \leq \pi$ to give

$$\begin{aligned} & \int_0^\pi \int_0^{a_0} B_0 \frac{d}{dr} \left(r \frac{dA_1}{dr} \right) dr \sin \phi \, d\phi + \int_0^\pi \int_0^{a_0} \frac{B_0}{r} \frac{d^2 A_1}{d\phi^2} dr \sin \phi \, d\phi \\ & - \int_0^\pi \int_0^{a_0} \frac{d}{dr} \left[\frac{1}{r} \frac{d}{dr} (r B_0) \right] r A_1 dr \sin \phi \, d\phi \\ & = \frac{\epsilon B_0^2}{2} \int_0^\pi \int_0^{a_0} r \sin \phi f'(r) dr \, d\phi \end{aligned} \quad (3.25)$$

Consider each of the four terms in (3.25) in turn. The last term is separable and integrates by parts to

$$- \epsilon B_0^2 \int_0^{a_0} f(r) dr$$

The third term is

$$\begin{aligned}
& - \int_0^\pi \int_0^{a_0} \frac{d}{dr} \left[\frac{1}{r} \frac{d}{dr} (r B_0) \right] r A_1 dr \sin \phi d\phi \\
& = - \int_0^\pi \left[A_1 B_0 + r A_1 \frac{dB_0}{dr} \right]_0^{a_0} \sin \phi d\phi \\
& + \int_0^\pi \int_0^{a_0} \left(\frac{B_0}{r} + \frac{dB_0}{dr} \right) \left(r \frac{dA_1}{dr} + A_1 \right) dr \sin \phi d\phi \\
& = - \int_0^\pi a_0 B_0(a_0) \frac{dA_1}{dr} \Big|_{r=a_0} \sin \phi d\phi + \int_0^\pi \int_0^{a_0} B_0 \frac{A_1}{r} dr \sin \phi d\phi \\
& + \int_0^\pi \int_0^{a_0} r \frac{dB_0}{dr} \frac{dA_1}{dr} dr \sin \phi d\phi \tag{3.26}
\end{aligned}$$

on integration by parts and application of the boundary conditions. The second term in (3.25) is

$$\begin{aligned}
& \int_0^{a_0} \left[\left[\sin \phi \frac{dA_1}{d\phi} \right]_0^\pi - \int_0^\pi \cos \phi \frac{dA_1}{d\phi} d\phi \right] \frac{B_0}{r} dr \\
& = - \int_0^{a_0} \left[\left[A_1 \cos \phi \right]_0^\pi - \int_0^\pi (-\sin \phi A_1) d\phi \right] \frac{B_0}{r} dr \\
& = - \int_0^{a_0} \int_0^\pi \sin \phi A_1 d\phi \frac{B_0}{r} dr \tag{3.27}
\end{aligned}$$

since $A_1 = 0$ on $\phi = 0, \pi$.

Integrating by parts the r -dependent part of the first term in (3.25), one obtains

$$a_0 B_0(a_0) \frac{dA_1}{dr} \Big|_{r=a_0} - \int_0^{a_0} \frac{dB_0}{dr} r \frac{dA_0}{dr} dr$$

Thus the first term becomes

$$\begin{aligned} &= \int_0^\pi a_0 B_0(a_0) \frac{dA_1}{dr} \Big|_{r=a_0} \sin \phi \, d\phi \\ &- \int_0^\pi \int_0^{a_0} r \frac{dA_1}{dr} \frac{dB_0}{dr} dr \sin \phi \, d\phi \end{aligned} \quad (3.28)$$

Since the first and second terms exactly cancel with the third term, (3.25) reduces to

$$\int_0^{a_0} f(r) \, dr = 0 \quad (3.29)$$

and so a solution to (3.24) can only be found when the excess pressure integrated along the base is zero.

3.2.4 Method of Solution

As a particular case suppose that the form of the initial equilibrium field is $B_0(r) = B_{00} r / a_0$. In this case equation (3.24) becomes

$$\frac{d}{dr} \left(r \frac{dA_1}{dr} \right) + \frac{1}{r} \frac{d^2 A_1}{d\phi^2} = \frac{\epsilon B_{00} a_0}{2} f'(r) \quad (3.30)$$

and condition (3.21) reduces to

$$\frac{A_1(a_0)}{a_0} = \frac{dA_1}{dr} \Big|_{r=a_0} \quad (3.31)$$

A method of solving (3.30) subject to the boundary

conditions (3.12),(3.13) and (3.21) is to write A_1 as the sum of a particular integral

$$A_{1 \text{ PI}} = - \frac{\epsilon B_{\infty} a_0}{2} \int_r^{a_0} \frac{1}{r} f(r) dr \quad (3.32)$$

and a complementary function satisfying

$$\frac{d}{dr} \left(r \frac{dA_1}{dr} \right) + \frac{1}{r} \frac{d^2 A_1}{d\phi^2} = 0 \quad (3.33)$$

A separable solution of (3.33) in the form $A_1 = R(r) \Phi(\phi)$ is sought, giving

$$r^2 \frac{R''}{R} + r \frac{R'}{R} = - \frac{\Phi''}{\Phi} = K \quad (3.34)$$

Considering zero and positive values of K [negative values would give a solution exponential in ϕ], (3.30) gives

$$\begin{aligned} A(r, \phi) = & \left[\alpha_1 \log_e \frac{r}{a_0} + \alpha_2 \right] [a\phi + b] \\ & + \sum_{n=1}^{\infty} \left[a_n \sin \sqrt{K_n} \phi + b_n \cos \sqrt{K_n} \phi \right] \left[\frac{r}{a_0} \right]^{\sqrt{K_n}} \\ & - \frac{\epsilon B_{\infty} a_0}{2} \int_r^{a_0} \frac{1}{r} f(r) dr \end{aligned} \quad (3.35)$$

where $\alpha_1, \alpha_2, a, b, K_n, a_n, b_n$ remain to be determined. Only positive values of $K_n^{1/2}$ are considered in order to avoid a singularity on the axis $r = 0$. Considering the case of (3.35) where $\phi = 0, r = a_0$ (and using condition (3.12)) one has

$$\alpha_2 b + \sum_{n=1}^{\infty} b_n = 0 \quad (3.36)$$

The case where $\phi = \pi, r = a_0$ gives

$$a \alpha_2 \pi + \alpha_2 b + \sum_{n=1}^{\infty} b_n \cos \sqrt{K_n} \pi = 0 \quad (3.37)$$

Equations (3.36) and (3.37) are consistent if $a = 0$, $K_n^{1/2} = n$ (with $b_{2n+1} = 0$). Furthermore, b can be set equal to unity. Thus (3.35) becomes

$$\begin{aligned}
 A_1(r, \phi) &= \alpha_1 \log_e \frac{r}{a_0} - \sum_{n=1}^{\infty} b_n \\
 &+ \sum_{n=1}^{\infty} (a_n \sin n\phi + b_n \cos n\phi) \left(\frac{r}{a_0}\right)^n \\
 &- \frac{\epsilon B_{\infty} a_0}{2} \int_r^{a_0} \frac{1}{r} f(r) dr
 \end{aligned} \tag{3.38}$$

The prescribed function $f(r)$ for $0 \leq r \leq a_0$ is assumed to take the form (where the odd c_i are equal to zero)

$$f(r) = \sum_{i=0}^m c_i \left[\frac{r}{a_0}\right]^i \tag{3.39}$$

Substituting (3.39) into (3.38) where $\phi = 0$,

$$\begin{aligned}
 0 &= \alpha_1 \log_e \frac{r}{a_0} + \sum_{n=1}^{\infty} b_{2n} \left[1 - \left(\frac{r}{a_0}\right)^{2n}\right] \\
 &- \frac{\epsilon B_{\infty} a_0}{2} \int_r^{a_0} \sum_{i=0}^m c_{2i} \frac{r^{2i-1}}{a_0^{2i}} dr \\
 &= \alpha_1 \log_e \frac{r}{a_0} + \sum_{n=1}^{\infty} b_{2n} \left[1 - \left(\frac{r}{a_0}\right)^{2n}\right] \\
 &- \frac{\epsilon B_{\infty} a_0}{2} \left[-c_0 \log_e \frac{r}{a_0} + \sum_{i=1}^m \frac{c_{2i}}{2i} \left[1 - \left(\frac{r}{a_0}\right)^{2i}\right] \right]
 \end{aligned} \tag{3.40}$$

Thus, comparing like terms $\alpha_1 = -\epsilon B_{\infty} a_0 c_0/2$,

$b_{2i} = -\epsilon B_{\infty} a_0 c_{2i}/4i$ and so

$$A_1(r, \phi) = \sum_{n=1}^{\infty} \left[a_n \sin n\phi + \frac{\epsilon B_{\infty} a_0 c_n}{2n} (1 - \cos n\phi) \right] \left[\frac{r}{a_0}\right]^n \tag{3.41}$$

Substituting (3.41) in the boundary condition (3.31) gives

$$\begin{aligned} & \sum_{m=1}^{\infty} (m-1) a_m \sin m\phi \\ &= \frac{\epsilon B_{\infty} a_0}{2} \sum_{n=1}^{\infty} \frac{2n-1}{2n} c_{2n} (\cos 2n\phi - 1) \end{aligned} \quad (3.42)$$

Fourier series analysis determines the coefficients a_m for $m > 1$ as

$$(m-1)a_m = \frac{2}{\pi} \int_0^{\pi} \frac{\epsilon B_{\infty} a_0}{2} \sum_{n=1}^{\infty} \frac{2n-1}{2n} c_{2n} (\cos 2n\phi - 1) \sin m\phi \, d\phi \quad (3.43)$$

i.e.

$$\begin{aligned} a_m &= 2 \frac{\epsilon B_{\infty} a_0}{(m-1)\pi} \sum_{n=1}^{\infty} (2n-1) c_{2n} \frac{2n}{m(m^2 - 4n^2)} \quad m \text{ odd} \\ &= 0 \quad m \text{ even} \end{aligned} \quad (3.44)$$

The value of a_1 is not determined by (3.44) and indeed multiplying by $\sin \phi$ and integrating yields the constraint (3.29) although the proof in Section 3.2.3 is more powerful since it does not depend on the assumption (3.35) of the form of the series and works for more general functions $B_0(r)$. It is found that as more terms in the series for A_1 are taken convergence occurs everywhere in the region $r \leq a_0$.

3.3 Results

Once $A_1(r, \phi)$ has been found in the semi-circle $0 \leq r \leq a_0$, $0 \leq \phi \leq \pi$, the new potential $A(r, \phi) \approx A_0(r) + \xi A_0'(r) + A_1(r)$ can be found at any point. Each field line is perturbed from $r = r_0$ to $r = r_0 + \xi$ where ξ is a function of both r_0 and ϕ . However, for a particular field line ξ is a function of ϕ only. The value of ξ can therefore be found from

$$\xi = - \frac{A_1(r_0, \phi)}{A_0'(r_0)} = \frac{a_0}{B_\infty} \frac{A_1(r_0, \phi)}{r_0} \quad (3.45)$$

The value A_0 of the potential that initially existed at r_0 is now present at $r_0 + \xi$. Thus the potential and hence the field can be found at any point.

Figure 3.3a shows the effect of a perturbation $f_1(r) = 1 - 6r^2 + 5r^4$ with $\epsilon = 0.2$ and $a_0=1$ and the dashed curve showing the initial position of the curved boundary. The function $f_1(r)$ is the only quadratic in r^2 which satisfies both the constraint (3.29) and the condition that it is zero when $r = a_0$. The field lines are moved inwards. The maximum effect is found at an angle of $\phi = \pi / 2$, and the field lines are symmetrical about this line. If the amplitude of the perturbation is increased, its effect increases accordingly.

Figure 3.3b shows the variation with r of the azimuthal component of the magnetic field at $\phi = \pi / 2$. The azimuthal component is given by

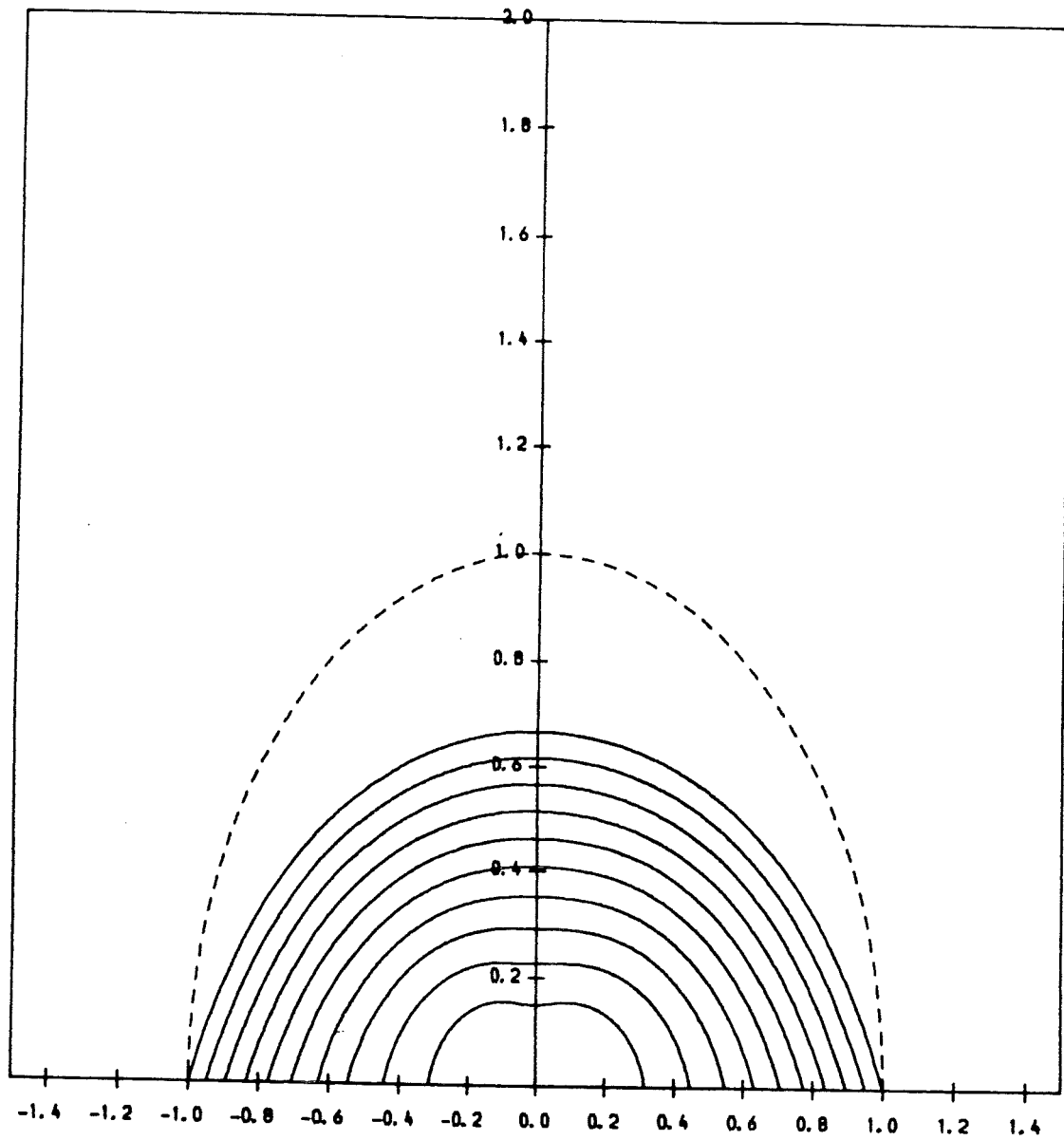


Figure 3.3 The effect of a perturbation of $f_1(r) = 1 - 6r^2 + 5r^4$.

a) The perturbed field lines with $\epsilon = 0.2$. The original outer boundary is shown with a broken line.

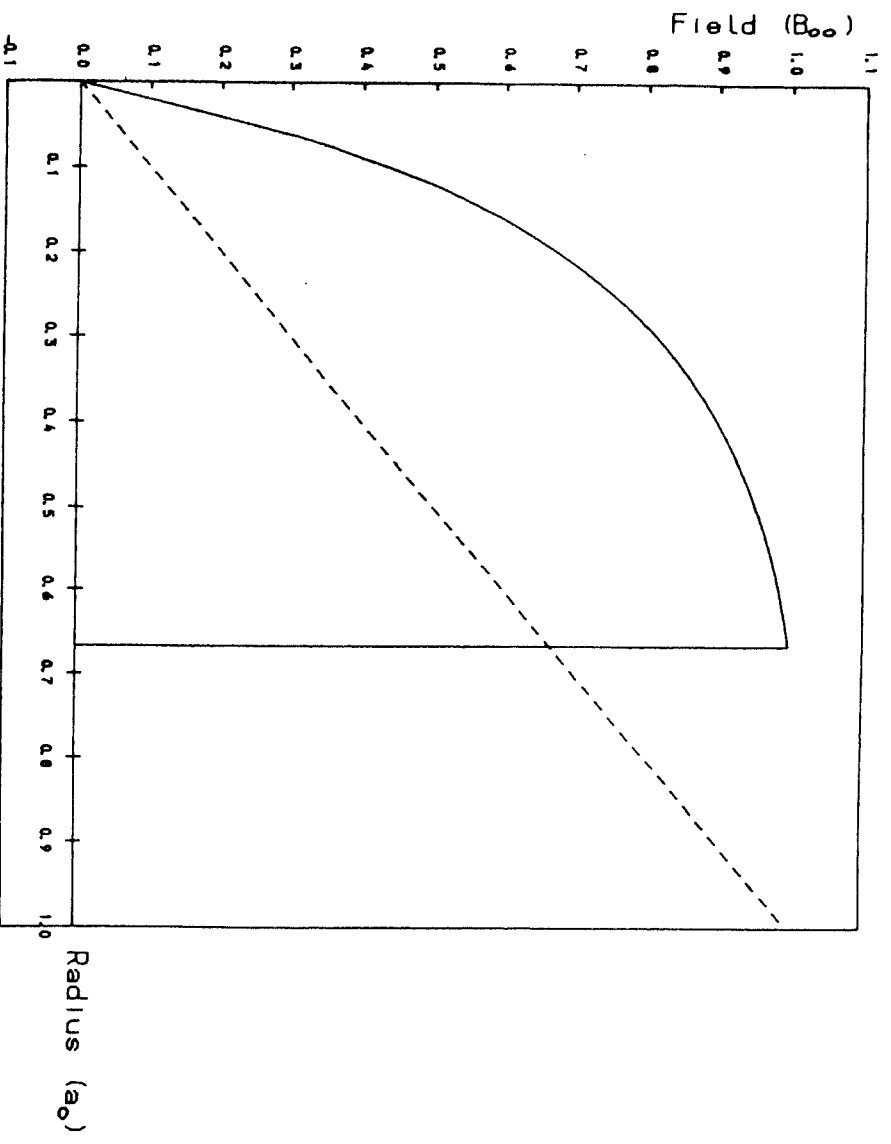


Figure 3.3 The effect of a perturbation of

$$f_1(r) = 1 - 6r^2 + 5r^4.$$

b) The magnetic field strength on $\phi = \pi/2$. The original field profile is shown in broken.

$$B_{\phi}(r + \xi) = - \frac{dA_0}{d(r + \xi)} \quad (3.46)$$

Its strength increases with r . The broken line shows the initial field profile. The resultant field is greater than the original field because the magnetic flux has been compressed.

Figure 3.3c shows the corresponding plot for plasma pressure excess. This is higher than the initial pressure (shown by the broken curve) at small r and lower at large r . It reflects the form of the pressure perturbation at the base.

Figures 3.3d and 3.3e show the variation with r and ϕ of the displacement ξ . Figure 3.3d shows the variation with r for three different values of ϕ . Figure 3.3e is a contour plot of how ξ varies with both variables. It can clearly be seen that the field lines are perturbed inwards for all values of r and ϕ . This inward displacement is zero at the origin and increases monotonically with r . The displacement is at a maximum when $\phi = \pi/2$ and vanishes when $\phi = 0$ or π . The displacement is never constant as ϕ is varied (over more than an infinitesimal range) so it is never possible to consider a solution dependent on r only.

If a value of ϵ less than zero e.g. -0.2, is used the opposite effect occurs and the field lines are moved outwards (Fig 3.3f) .

Two more profiles for $f(r)$, namely $f_2(r) = 1 - 3r^2 - 5r^4 + 7r^6$ and $f_3(r) = 1 - 4r^2 + 3r^8$ were considered (figure 3.4) and the perturbed field lines were similar to those for $f_1(r)$

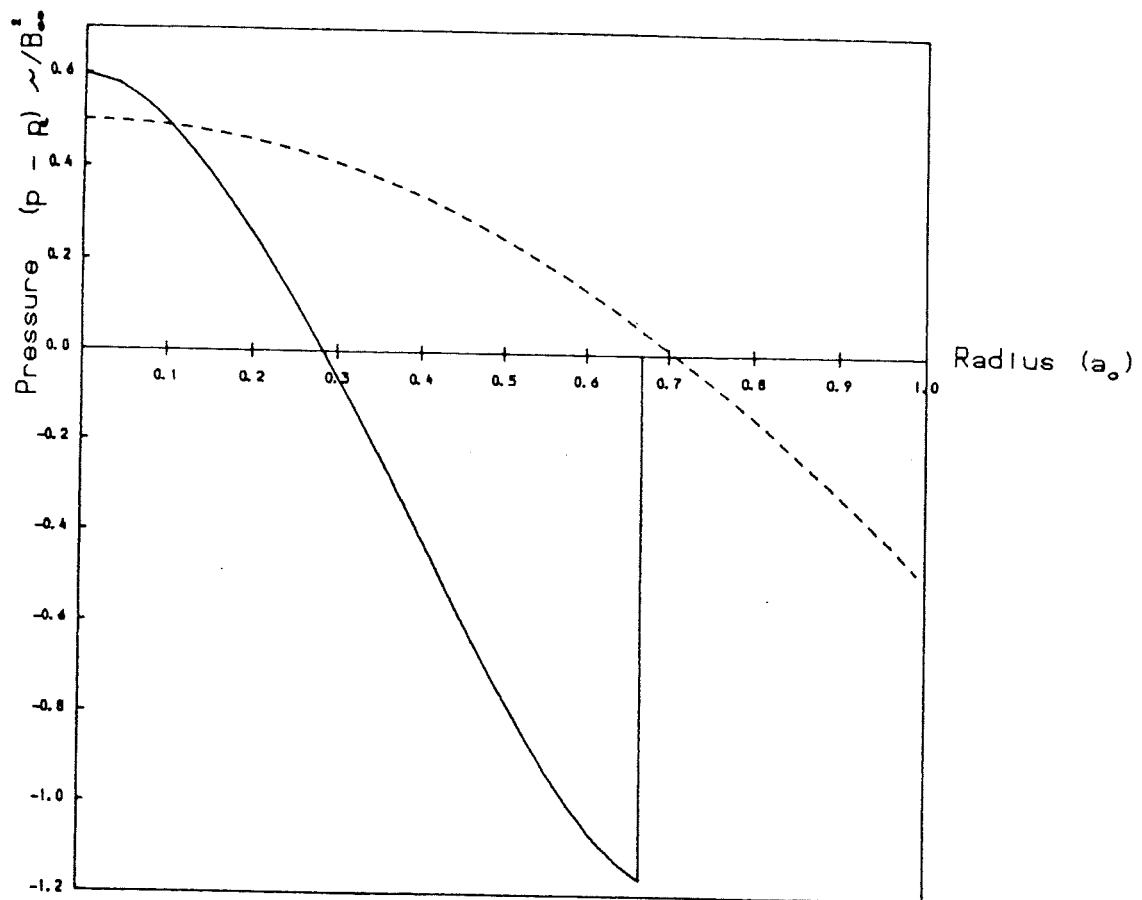


Figure 3.3 The effect of a perturbation of $f_1(r) = 1 - 6r^2 + 5r^4$.
 c) The plasma pressure excess $(p - p_0)$ on $\phi = \pi/2$.
 The original pressure profile is shown in broken.

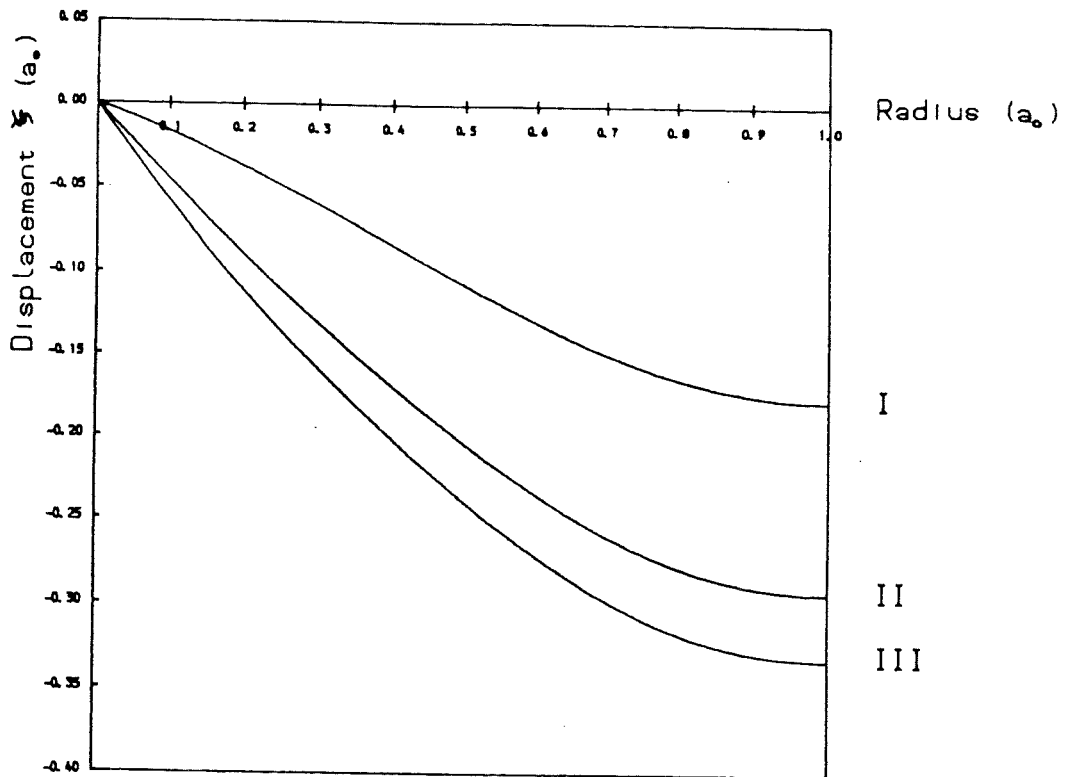


Figure 3.3 The effect of a perturbation of $f_1(r) = 1 - 6r^2 + 5r^4$.
 d) The variation of the displacement ξ with radius r for, (I) $\phi = \pi/6$, (II) $\phi = \pi/3$, (III) $\phi = \pi/2$

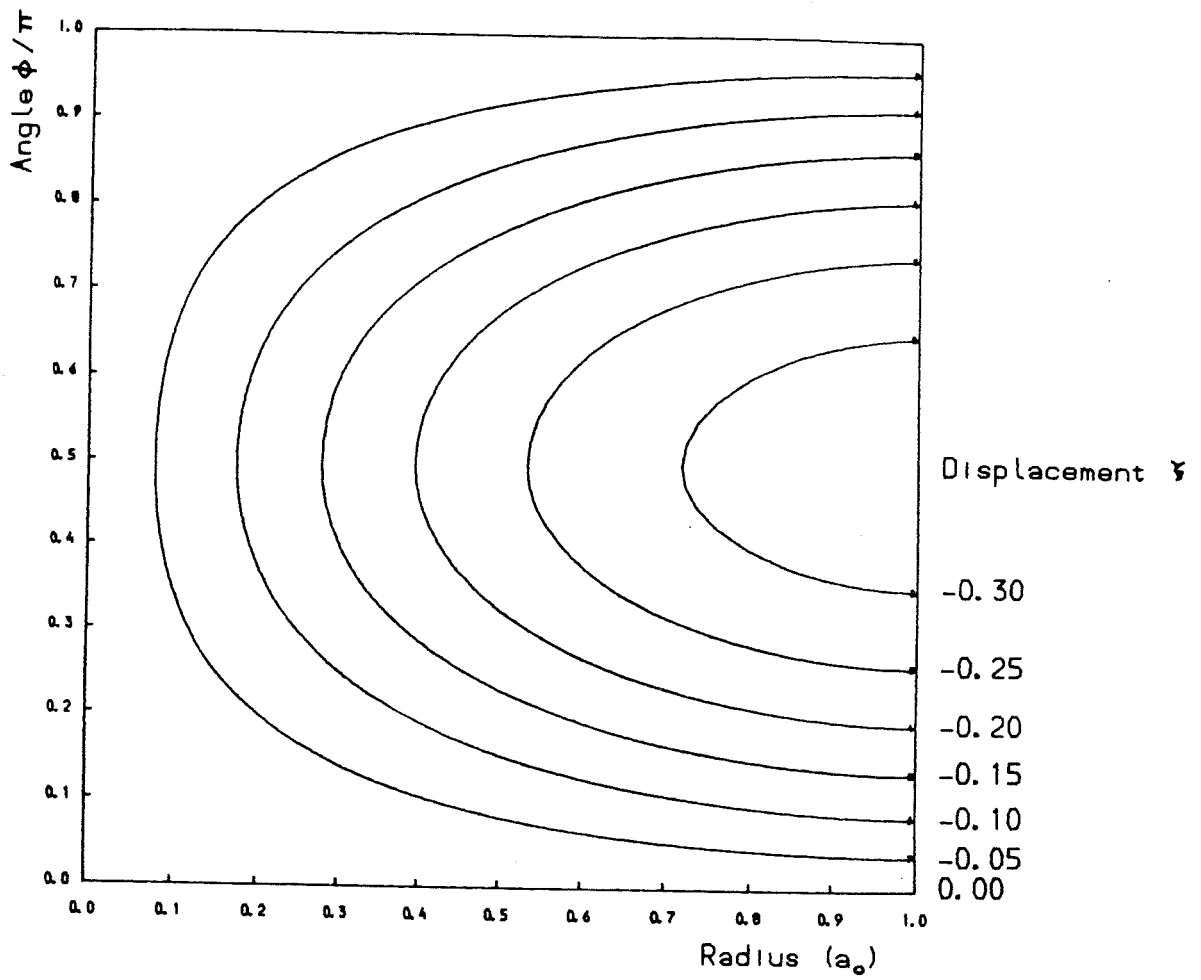


Figure 3.3 The effect of a perturbation of $f_1(r) = 1 - 6r^2 + 5r^4$.
 e) A contour plot showing the variation of the displacement ξ with radius r and angle ϕ

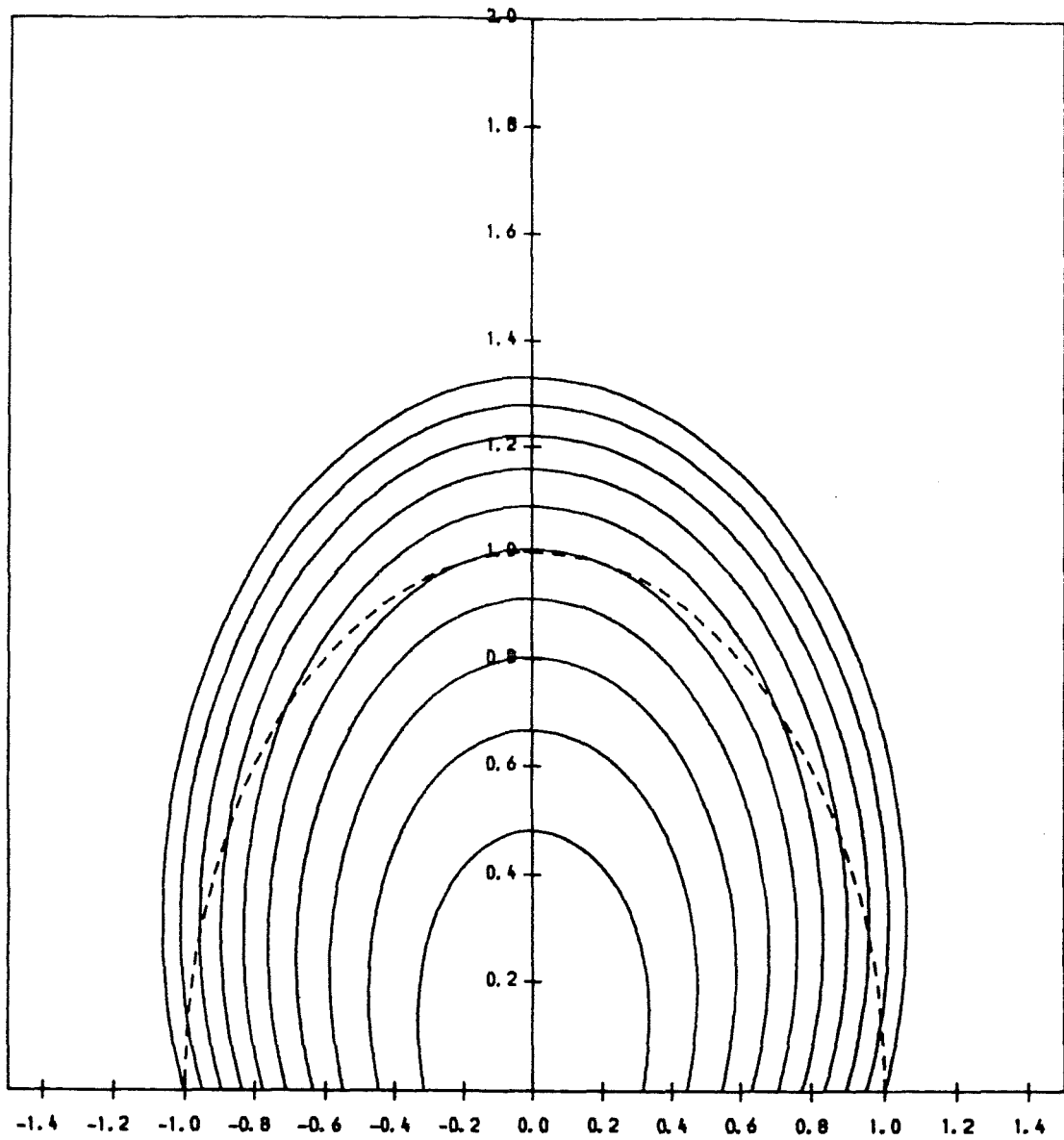


Figure 3.3 The effect of a perturbation of $f_1(r) = 1 - 6r^2 + 5r^4$.
 f) The perturbed field lines with $\varepsilon = -0.2$. The original outer boundary is shown with a broken line.

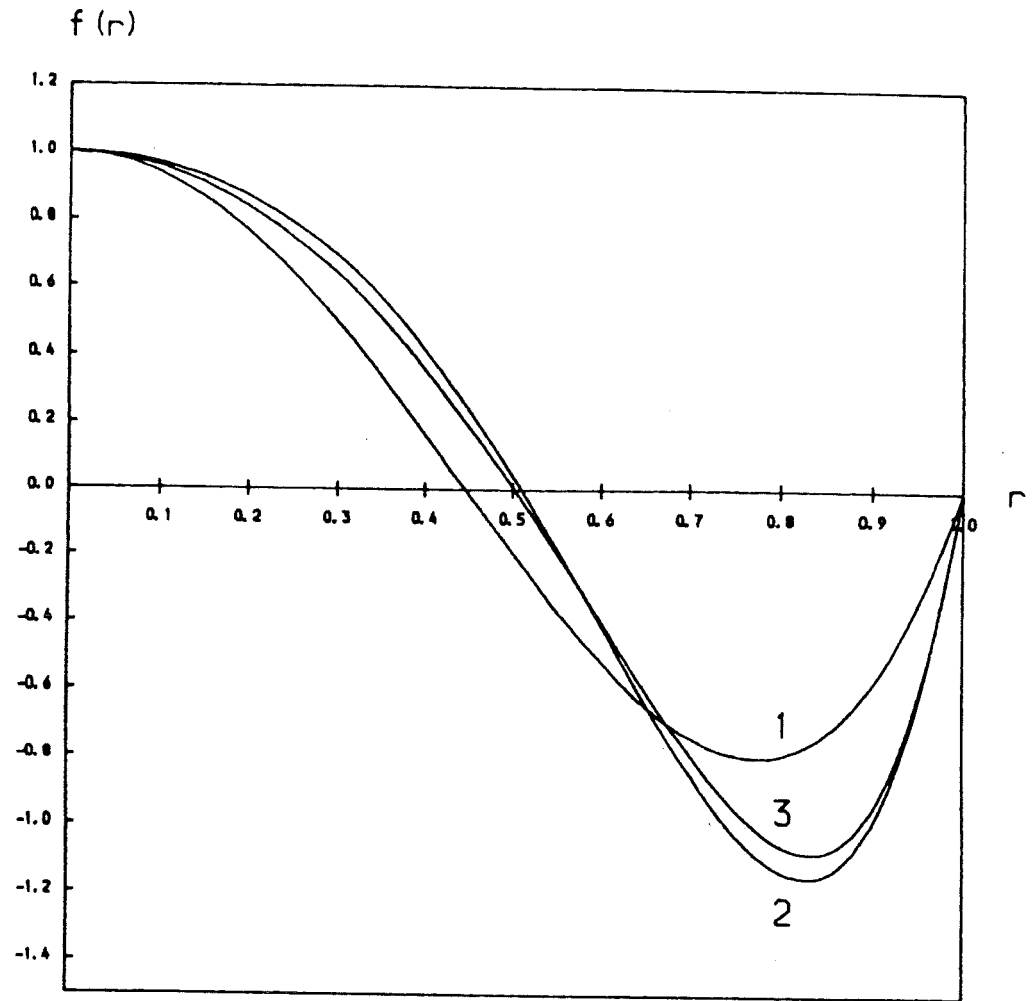


Figure 3.4 The profiles of the functions
 $f_1(r) = 1 - 6r^2 + 5r^4$, $f_2(r) = 1 - 3r^2 - 5r^4 + 7r^6$,
 $f_3(r) = 1 - 4r^2 + 3r^8$

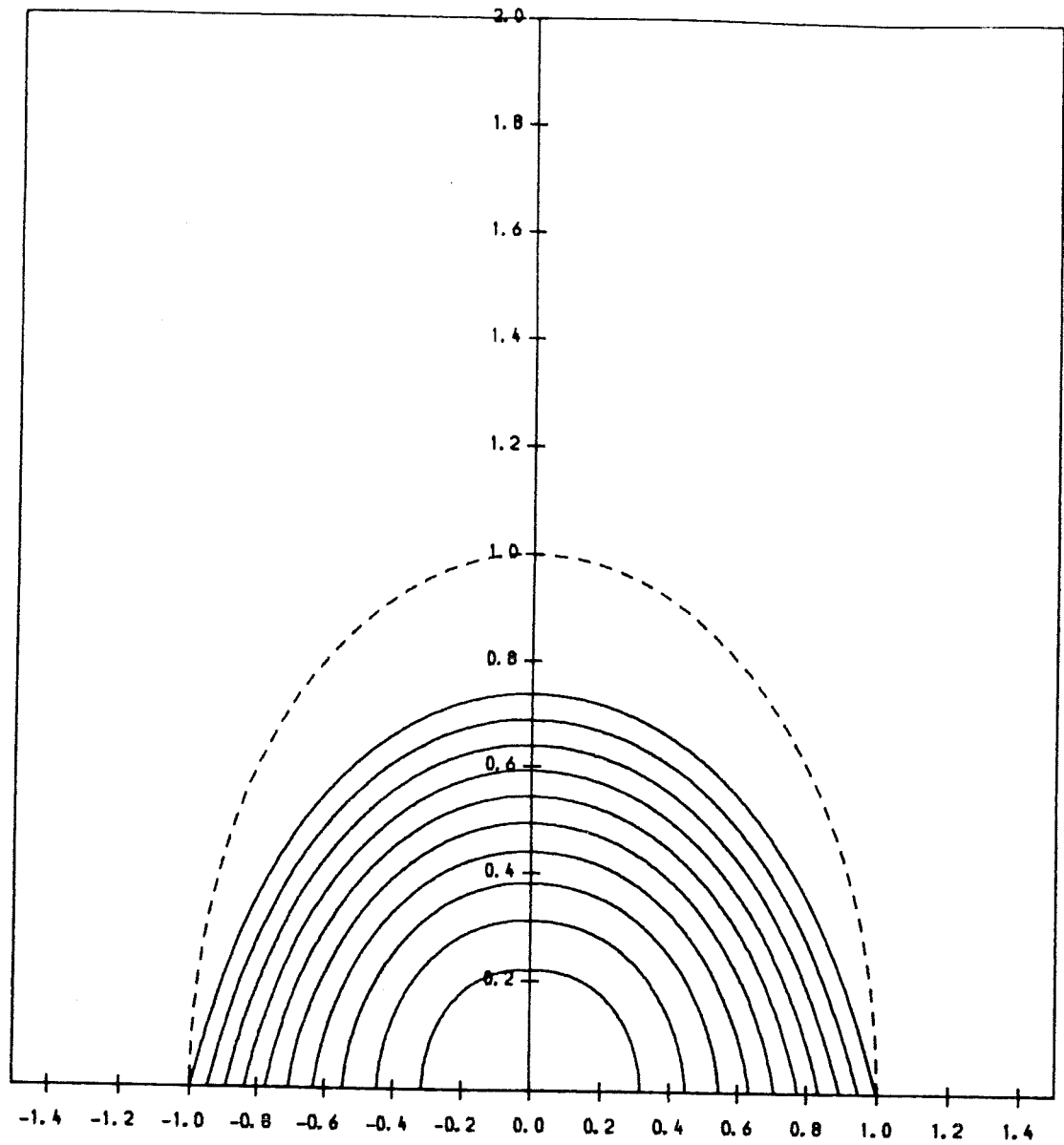


Figure 3.5 The effect of a perturbation of
 $f_2(r) = 1 - 3r^2 - 5r^4 + 7r^6$
 a) The perturbed field lines with $\epsilon = 0.2$. The original outer boundary is shown with a broken line.

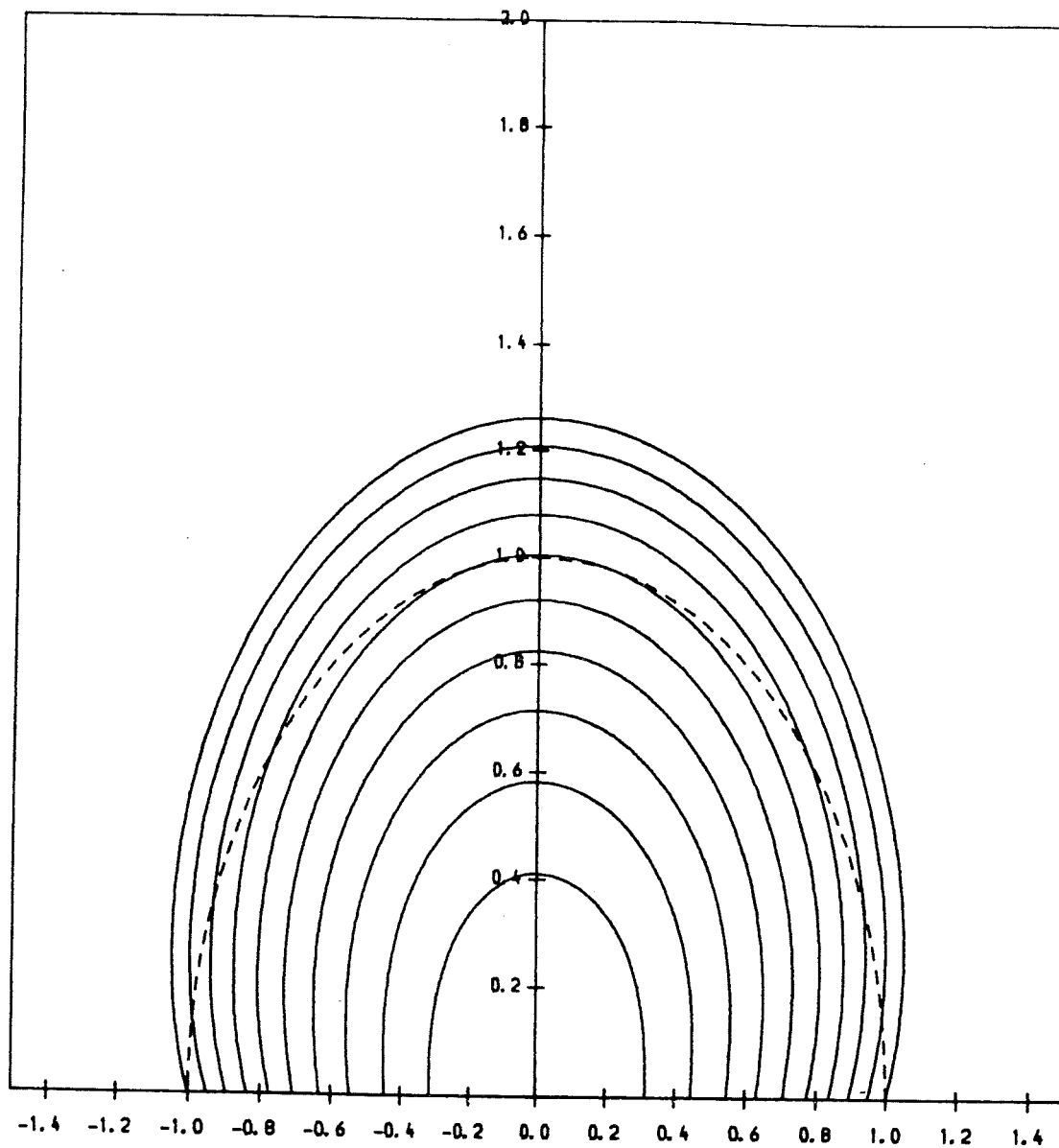


Figure 3.5 The effect of a perturbation of
 $f_2(r) = 1 - 3r^2 - 5r^4 + 7r^6$
 b) The perturbed field lines with $\epsilon = -0.2$. The original outer boundary is shown with a broken line.

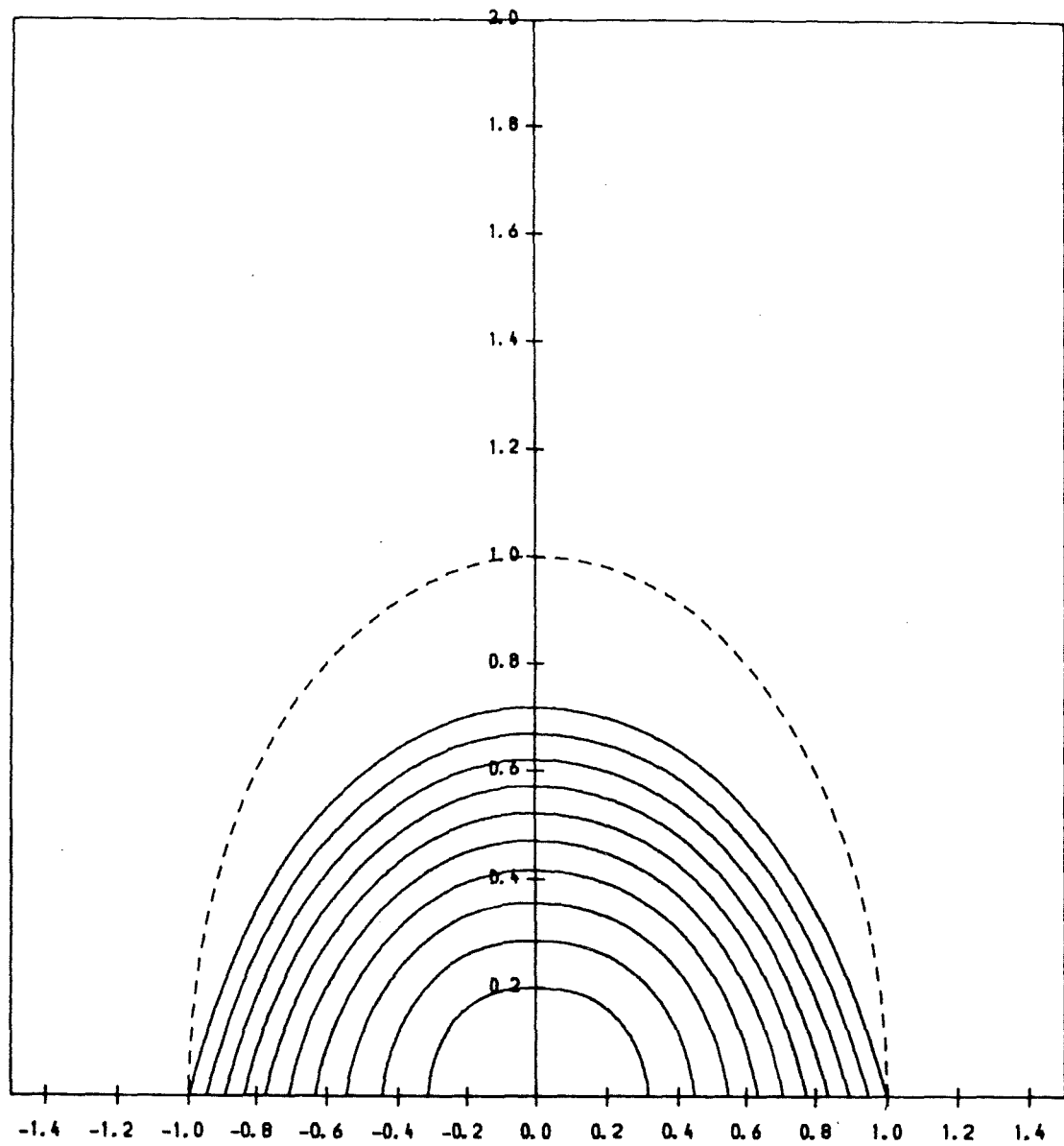


Figure 3.6 The effect of a perturbation of
 $f_3(r) = 1 - 4r^2 + 3r^8$
 a) The perturbed field lines with $\epsilon = 0.2$. The original outer boundary is shown with a broken line.

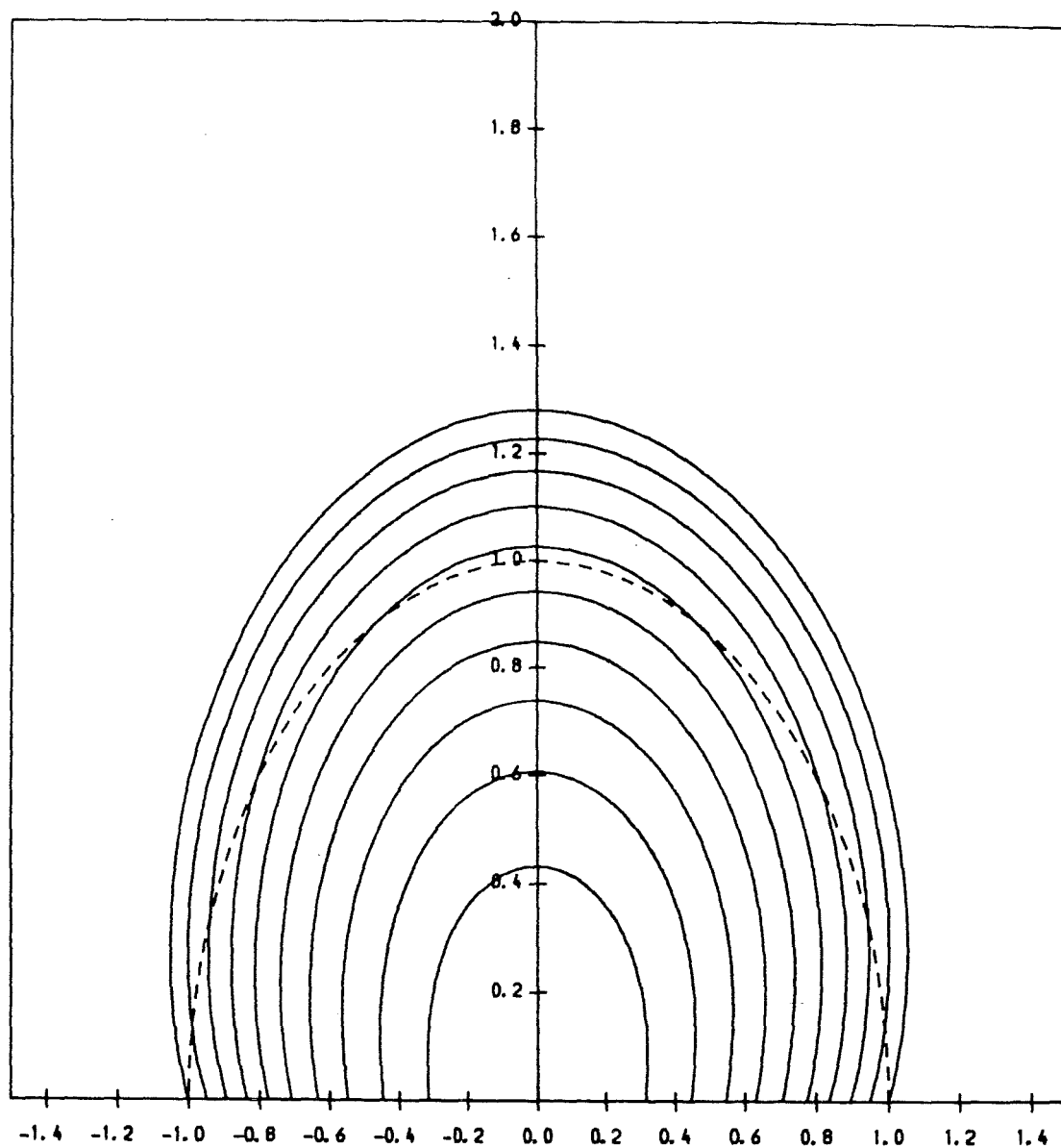


Figure 3.6 The effect of a perturbation of
 $f_3(r) = 1 - 4r^2 + 3r^8$
 b) The perturbed field lines with $\varepsilon = -0.2$. The original outer boundary is shown with a broken line.

(figures 3.5 and 3.6). Again, a positive value of ϵ i.e. a positive excess pressure on the axis, gave field-lines which are moved inwards, while those for negative ϵ had field lines perturbed outwards.

3.4 Conclusions

Solutions have been found for certain forms of equilibrium close to a cylindrically symmetric state (with the axis of the cylinder on the photosphere) but not for others. In particular, equilibrium solutions are only found when the constraint that the excess pressure, integrated along the base is zero is satisfied. This represents a redistribution of pressure rather than a net increase or decrease. The constraint reflects the fact that physically when the initial equilibrium with the axis on the photosphere is perturbed, there is no change in the net pressure on the curved upper surface and so if global vertical equilibrium is maintained, there can be no change in the net pressure on the straight lower boundary of the semi-circle. When this constraint is not satisfied the arcade is likely either to erupt or to collapse downwards, depending on the sign of the change in the total pressure. The eruption or collapse may perhaps continue until non-linear effects counteract it.

The constraint showed up initially by chance when equation (3.30) was solved with a wide range of base pressures and no numerical solutions were found when the constraint was not satisfied. The proof of section 3.2.3

demonstrates that it depends on the differential equation (3.24) and the imposed boundary conditions. Clearly, taking different boundary conditions may give a different conclusion.

However, the main conclusion is that the suggestion by Priest (1988a) that eruptions by non-equilibrium are likely when the base pressure is too great has been confirmed by the present more general treatment. Priest found neighbouring equilibria only when the axis is below the photosphere. When the axis lies on the photosphere (the case considered in more detail in this chapter), he found no equilibria of a particular form are possible, but the possibility of neighbouring equilibria of a different form was still open. Here it has been demonstrated that, when the total integrated pressure is increased, such neighbouring equilibria are in general not possible and so the arcade will erupt since the net force balance is upward. Indeed it has been proved for more general equilibria than Priest considered. The result that when the base pressure is too large there is no coronal equilibrium is a natural one, which has been found in other studies such as those Birn and Schindler (1981), Heyvaerts et al (1982), Zwingman (1985) and Amari and Aly (1988).

CHAPTER FOUR - THERMAL EQUILIBRIA OF CORONAL MAGNETIC LOOPS

4.1 Introduction

As mentioned in section 1.4, Hood and Anzer (1988) studied in detail equations describing thermal equilibrium along a coronal loop. They identified qualitatively several forms of solution using a phase plane analysis but did not follow the work up quantitatively. The aim of this work is therefore to find numerical solutions to the equations presented by Hood and Anzer.

4.2 Equations of Thermal Equilibrium

For a coronal loop, the temperature (T) and the gas pressure (p) obey the following equations (Hood and Anzer, 1988), (see also Section 1.5.5).

$$\frac{dp}{ds} = \frac{g(s) p}{2 R T} \quad (4.1)$$

$$B \frac{d}{ds} \left(\frac{K_0 T^{5/2}}{B} \frac{dT}{ds} \right) = \frac{p^2}{4 R^2} X T^{\alpha-2} - h \quad (4.2)$$

where s represents the distance along the loop, $g(s)$ is the component of gravity along the loop, B is the magnetic field strength, and $K_0 = 10^{-11} \text{ W m}^{-1} \text{ K}^{-7/2}$ (Spitzer, 1962). The first term on the right-hand side of (4.2) is the radiative loss term where $X T^{\alpha-2}$ forms a piecewise continuous function (Hildner 1974), (see also Table 1.1). The second term on the right-hand side of (4.2) is the unknown heating function which may depend on p , T , B , or s . It will, however, be assumed here that h is simply proportional to the plasma

density i.e.

$$h = h_0 \frac{p}{p_0} \frac{T_0}{T} \quad (4.3)$$

where h_0 is the value h takes when p and T are equal to reference values p_0 and T_0 .

Equations (4.1) and (4.2) are non-dimensionalised by setting

$$s = s^* L_0, \quad B = B^* B_0, \quad p = p^* p_0, \quad T = T^* T_0$$

in which T_0 will be taken as 10^5 K, p_0 is equal to 0.013 Pascals and L_0 is the half-length of the loop so that $s^* = 0$ at the footpoints and $s^* = 1$ at the loop summit. For a symmetrical loop only half of it need be considered. Equations (4.1) and (4.2) become

$$\frac{dp^*}{ds^*} = g^*(s^*) \frac{p^*}{T^*} \quad (4.4)$$

$$B^* \frac{d}{ds^*} \left(\frac{T^{*5/2}}{B^*} \frac{dT^*}{ds^*} \right) = (L^* p^*)^2 \left[X^* T^{*\alpha-2} - \frac{h^*}{p^* T^*} \right] \quad (4.5)$$

where

$$g^*(s^*) = \frac{g(s) L_0}{2 R T_0}$$

$$L^{*2} = \frac{L_0^2 p_0^2 X_0 T_0^{\alpha_0 - 11/2}}{4 R^2 K_0} = \frac{L_0^2}{L_\infty^2}$$

$$h^* = \frac{4 R^2 h_0}{p_0^2 X_0 T_0^{\alpha_0 - 2}}$$

When non-dimensionalisation is carried out, the radiative loss coefficients become, $X_0 = 8.0 \times 10^{-35} \text{ kg}^{-1} \text{ m}^5 \text{ s}^{-3}$, $\alpha_0 = 0.0$ and the other coefficients as shown in Table 4.1

Table 4.1

Range of T^*	X	α
$T^* \leq 0.15$	61400	7.4
$0.15 \leq T^* \leq 0.8$	1.49	1.8
$0.8 \leq T^* \leq 3.0$	1.00	0.0
$3.0 \leq T^* \leq 8.0$	15.6	-2.5
$8.0 \leq T^*$	0.689	-1.0

The simplest case to consider is that where the effect of gravity is neglected and where the cross-sectional area of the loop (and hence the field strength) is constant along the loop. Equation (4.4) then simply implies that the pressure is constant along the loop and equation (4.5) reduces to

$$\frac{d}{ds^*} \left(T^{*5/2} \frac{dT^*}{ds^*} \right) = (L^* p^*)^2 \left[X^* T^{*\alpha - 2} - \frac{h^*}{p^* T^*} \right] \quad (4.6)$$

This equation possesses the two dimensionless parameters ($L^* p^*$ and h^*/p^*) and requires two boundary conditions to be imposed. The question of boundary conditions has been debated at length (e.g. Habbal and Rosner (1979), Antiochos et al (1985), Craig and McClymont (1987)). This work follows Hood and Anzer (1988) in assuming a footpoint temperature of $2 \times 10^4 \text{ K}$ (i.e. $T^* = 0.2$) and a zero temperature gradient at the loop summit by symmetry:

i.e.

$$\begin{aligned} T^* &= 0.2 & \text{at } s^* &= 0 \\ \frac{dT^*}{ds^*} &= 0 & \text{at } s^* &= 1 \end{aligned}$$

For the particular case of a thermally isolated loop (as suggested by Basri et al (1979), Vernazza, Avrett and Loeser (1981)) with $dT^*/ds^* = 0$ at $s^* = 0$ there is a constraint on the values of L^*p^* and h^*/p^* (Figure 4.5).

More information about the nature of the solutions can be found by considering the phase plane (Figure 4.1). Setting

$$V = T^{*5/2} \frac{dT^*}{ds^*} \quad (4.7)$$

(4.6) becomes

$$\frac{dT^*}{ds^*} = V T^{*-5/2} \quad (4.8)$$

$$\frac{dV}{ds^*} = (L^*p^*)^2 \left[X^* T^{*\alpha-2} - \frac{h^*}{p^* T^*} \right] \quad (4.9)$$

with critical points where

$$V = 0 \quad T^* = \left[\frac{h^*}{p^* X^*} \right]^{\frac{1}{\alpha-1}} = T_{\text{crit}}$$

It must be remembered that X^* and α are different for different ranges of T^* . Figure 4.2 shows the variation with temperature of $X^*T^{*\alpha-2}$ (full lines), and h^*/p^*T^* (broken lines) for two values of h^*/p^* . Where the full and broken lines cross (i.e. the two terms are equal) a critical point exists. From Figure 4.2 it can be seen that when $h^*/p^* < 1.25$ two different values of T_{crit} can be found - one greater than 0.8 and one less than this value.

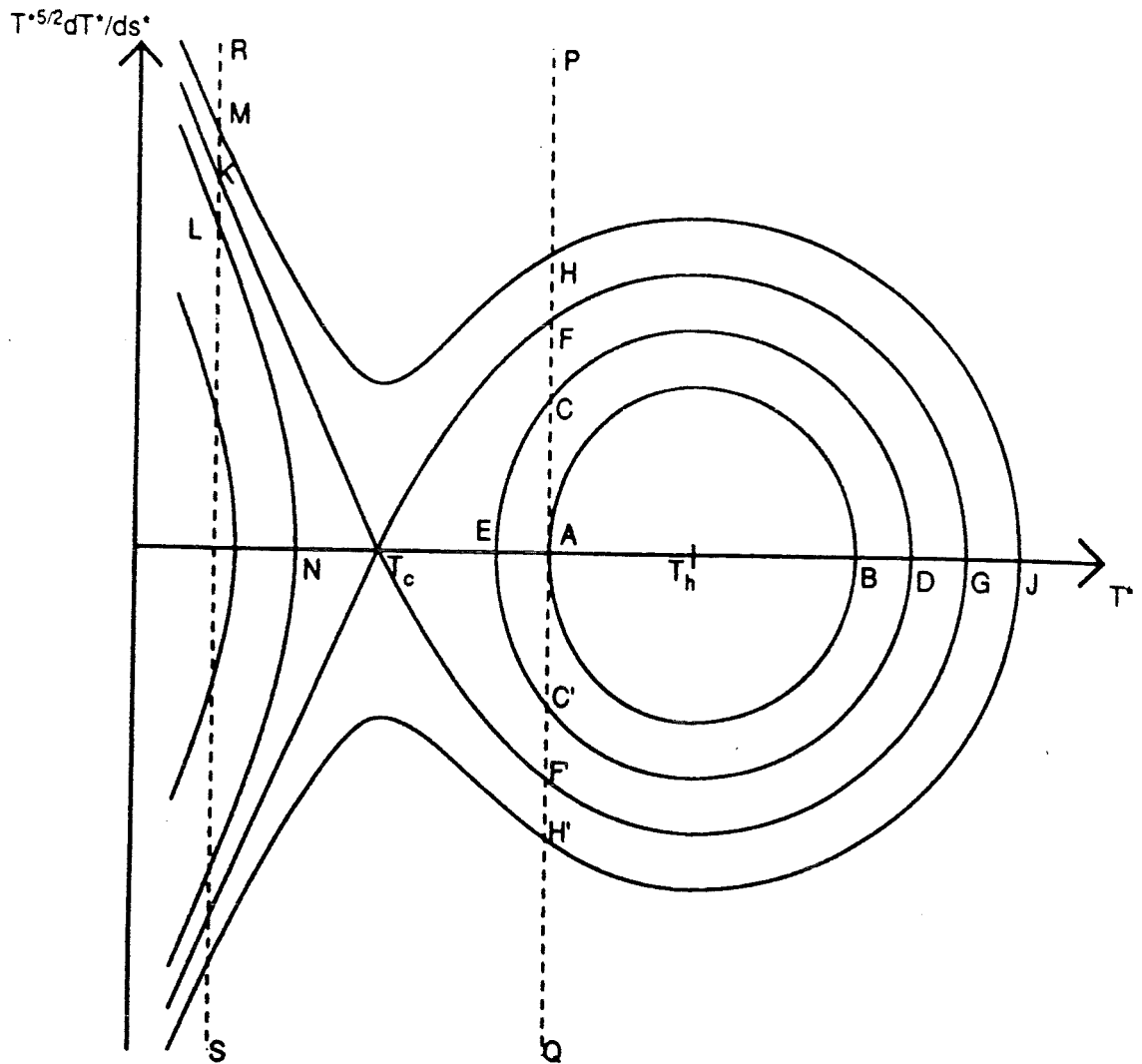


Figure 4.1a The form of the phase plane for the solution of equation (4.6) in $T^* - T^{*5/2}dT^*/ds^*$ space when $h^*/p^* < 1.25$. The footpoints (for which $T^* = 0.2$) lie along the line PQ or the line RS and the loop summits lie along the T^* -axis.

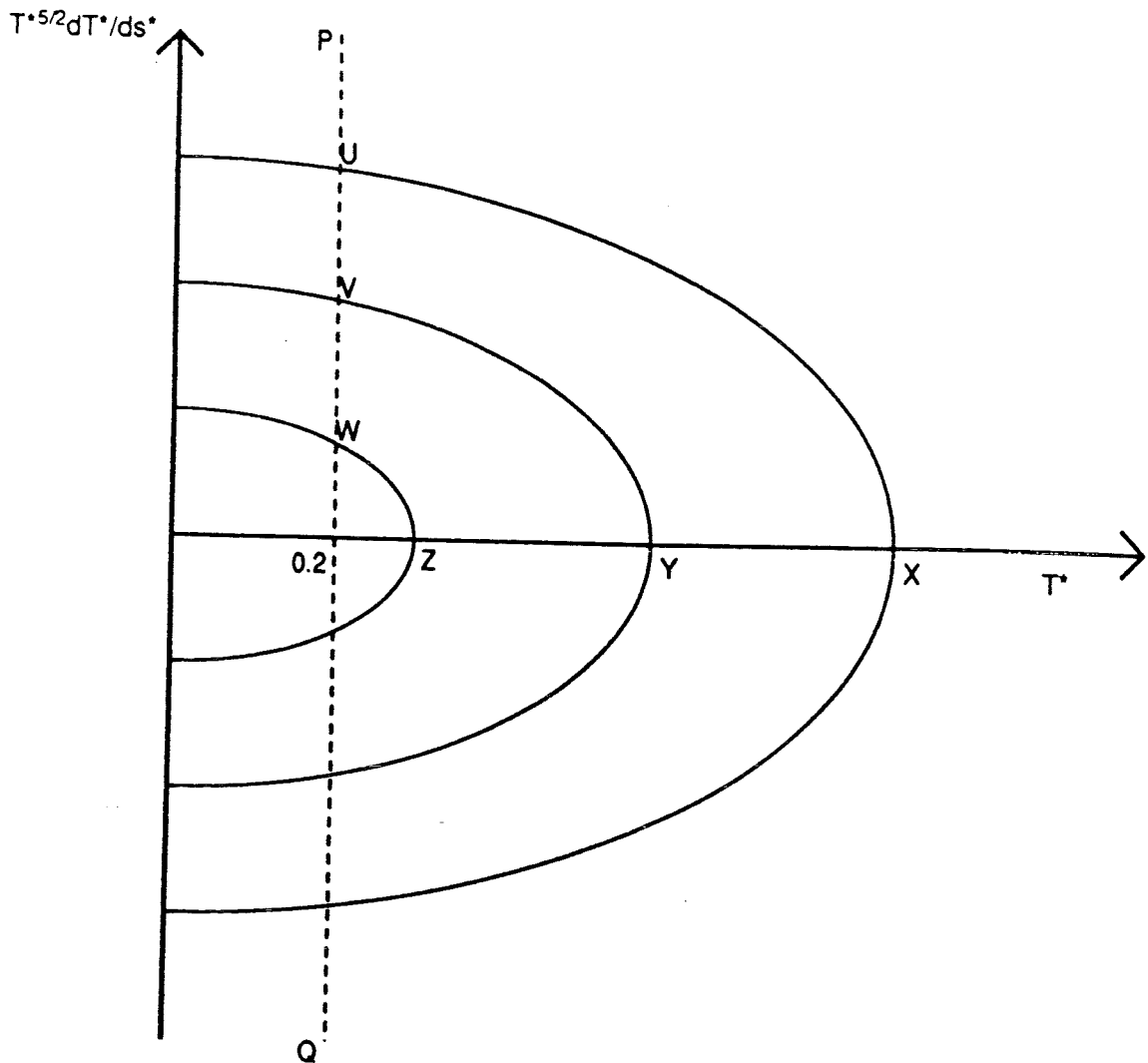


Figure 4.1b The form of the phase plane for the solution of equation (4.6) in $T^* - T^{5/2}dT^*/ds^*$ space when $h^*/p^* > 1.25$. The footpoints lie along the line PQ where $T^* = 0.2$ and the loop summits lie on the T^* -axis.

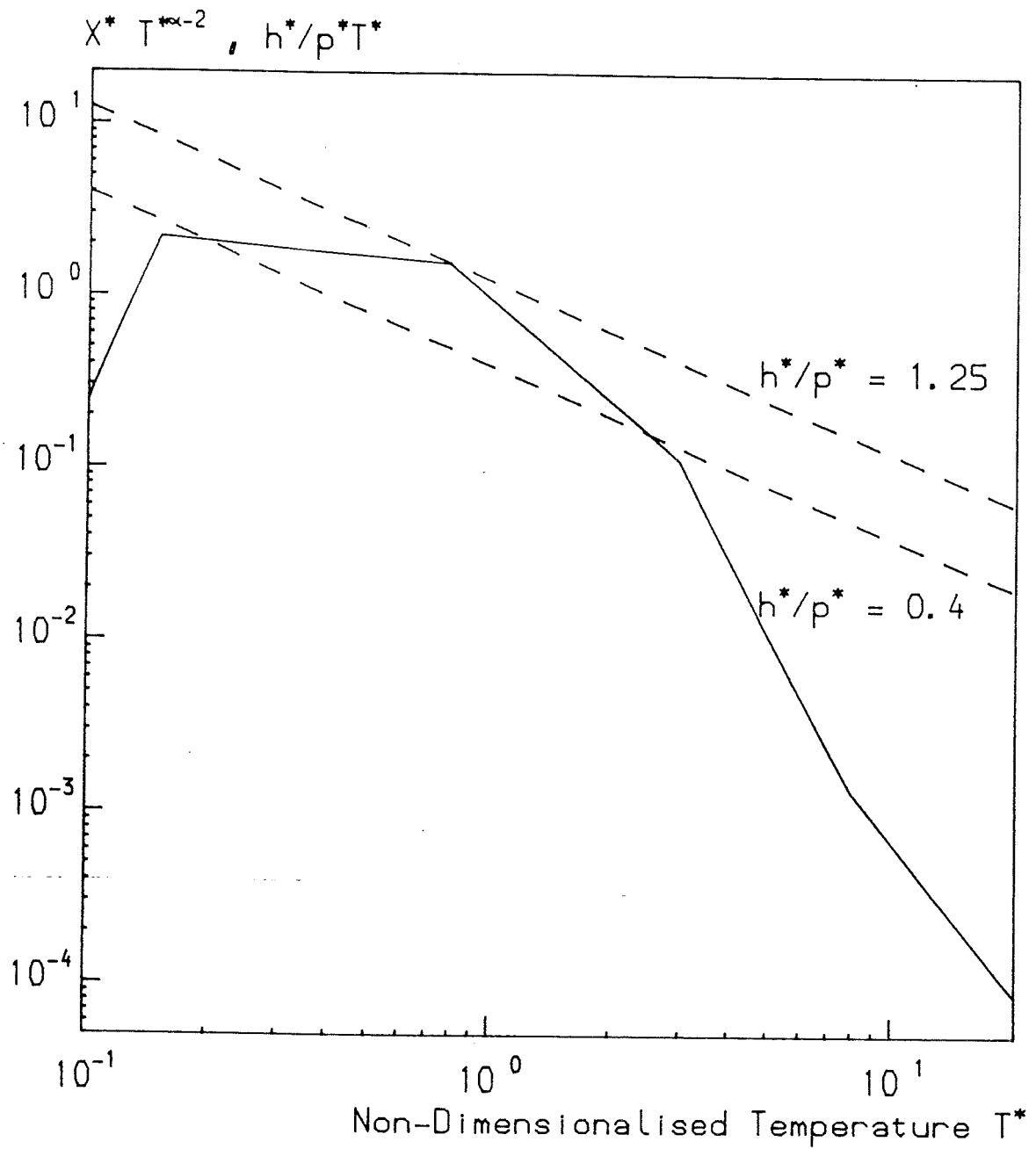


Figure 4.2 The relative strengths of the radiative loss term ($X^* T^{\alpha-2}$, in full) and the heating term ($h^*/p^* T^*$, in broken) in equation (4.6). Two values of h^*/p^* are shown. When $h^*/p^* > 1.25$ the two terms are never equal; when $h^*/p^* < 1.25$ there are two temperatures at which the two terms are equal.

By setting $\tau = T^* - T_{crit}$, (4.8) and (4.9) become, neglecting squares and products of t and V ,

$$\frac{d\tau}{ds^*} = V T_{crit}^{-5/2} \quad (4.10)$$

$$\frac{dV}{ds^*} = (L^* p^*)^2 \left[X^* T_{crit}^{\alpha-3} (\alpha - 1) \right] \tau = R \tau \quad (4.11)$$

If V and τ are of the form $e^{\lambda s}$ then

$$\lambda^2 = R T_{crit}^{-5/2} = (L^* p^*)^2 X^* \left[\frac{h^*}{p^* X^*} \right]^{\frac{\alpha - 11/2}{\alpha - 1}} (\alpha - 1) \quad (4.12)$$

If $\alpha < 1$, then $T_{crit} > 0.8$, and the critical point is a centre point, but if $\alpha > 1$, then $T_{crit} < 0.8$ and a saddle point exists. So for $h^*/p^* < 1.25$ two critical points can be found, a saddle point at $T_c < 0.8$ and a centre point at $T_h > 0.8$ (Figure 4.1a).

When $h^*/p^* > 1.25$ no critical points exist and Figure 4.1b gives the shape of the phase plane.

If $h^*/p^* < 0.41$, the saddle point T_c lies at a value of T^* less than 0.2. The footpoint therefore lies along the line PQ and, as the temperature gradient is assumed to be positive, it lies between point A and point H. The point corresponding to the loop summit (where $dT^*/ds^* = 0$) will lie on the T^* axis.

Starting from point A (or a point very close to it) will give a hot summit at point B (this will henceforth be known as a **hot solution**) and a cool summit when the contour is

extended onwards around the centre point and back to A. As such a loop has a cool summit but is hot along at least part of its length, it will henceforth be referred to as a **hot-cool solution**. Another possible solution with several oscillations along its length can be found by extending the contour further to point B again, but solutions of this form will not be considered.

Beginning at point C gives a hot solution with a summit at point D and a hot-cool solution with the summit at point E. This existence of both a hot solution and a hot-cool solution will occur for all footpoints between A and F where the hot-cool solution at point T_c has the coolest possible summit temperature for the particular value of h^*/p^* . When the summit is at T_c , the loop will be of infinite length due to the saddle point. Starting from a higher temperature gradient such as at point H, one finds a hot solution with summit at point J but no hot-cool solution.

When h^*/p^* lies between 0.41 and 1.25, the saddle point T_c is at a value of T^* greater than 0.2 and the point corresponding to the footpoint lies on the line RS. Starting with the footpoint at point L gives a cool solution with summit at point N. As this loop is cool along its entire length, it will be referred to simply as a **cool solution**. Normally such a loop will be very short but as point L approaches point K, point N approaches the saddle point T_c and the value of L^*p^* tends towards infinity. The cool solution studied by Antiochos and Noci (1986) is a special case of this solution.

Beginning with the footpoint at point M gives a hot solution with summit at point J but no cool solution. If point M is close to point K, the contour passes very close to the saddle point and so the loop will be very long. Also point J is close to point G and so the summit temperature lies in the range 8×10^4 K to 4×10^5 K. A large fraction of the loop will be at a temperature close to that of the saddle point i.e. between 20 000 K and 80 000 K. Thus these **warm** loops have the same phase-plane topology as hot loops but have cooler summits.

When h^*/p^* is greater than 1.25 the two critical points T_c and T_h do not exist and the form of the phase plane is as shown in Figure 4.1b. Starting from footpoints at W,V,U will give contours going as far as the summits at Z,Y,X respectively. In this case there is no division into hot and cool solutions.

When h^*/p^* is large (in practice, larger than about 100), the summit temperature can be found analytically as a function of the parameters L^*p^* and h^*/p^* . The heating term on the right hand side of (4.6) dominates and so the radiative term can be ignored. Equation (4.6) becomes

$$\frac{d}{ds^*} \left(T^{*5/2} \frac{dT^*}{ds^*} \right) = - \frac{L^{*2} h^* p^*}{T^*} \quad (4.13)$$

where $T^* = T_0$ ($= 0.2$) when $s^* = 0$ and $T^* = T_1$ and $dT^*/ds^* = 0$ when $s^* = 1$

Equation (4.13) can be multiplied by $T^{*5/2} dT^*/ds^*$ and integrated with respect to s^* .

$$\frac{1}{2} \left[T^{*5/2} \frac{dT^*}{ds^*} \right]^2 = - \frac{2 L^{*2} h^* p^*}{5} T^{*5/2} + c \quad (4.14)$$

The value of c is given by considering $s^* = 1$, so

$$T^{*5} \left[\frac{dT^*}{ds^*} \right]^2 = \frac{4 L^{*2} h^* p^*}{5} \left[T_1^{5/2} - T^{*5/2} \right] \quad (4.15)$$

Separating and integrating between $s^* = 0$ and $s^* = 1$ gives

$$\begin{aligned} 1 &= \frac{1}{\sqrt{\frac{4}{5} L^{*2} h^* p^*}} \int_{T_0}^{T_1} \frac{T^{*5/2} dT^*}{\sqrt{T_1^{5/2} - T^{*5/2}}} \\ &= \sqrt{\frac{4/5}{L^{*2} h^* p^*}} T_1^{9/4} I \end{aligned}$$

where

$$I = \int_{\theta_1}^{\frac{\pi}{2}} \sin^{9/5} \theta d\theta \quad (4.16)$$

and

$$\sin \theta_1 = \left[\frac{T_0}{T_1} \right]^{5/4}$$

using the substitution

$$\left[\frac{T^*}{T_1} \right]^{5/2} = \sin^2 \theta$$

In the case where $T_0 \ll T_1$,

$$I = \frac{2^{4/5} \left[\Gamma\left(\frac{7}{5}\right) \right]^2}{\Gamma\left(\frac{14}{5}\right)} = 0.8176$$

as

$$\int_0^{\frac{\pi}{2}} \sin^{p-1} x \, dx = \frac{2^{p-2} (\Gamma(p/2))^2}{\Gamma(p)} \quad (4.17)$$

(De Haan, 1939), and so

$$L^* p^* = \frac{0.7313 T_1^{9/4}}{\sqrt{\frac{h^*}{p^*}}} = \frac{0.5348 T_1^{9/2}}{L^* h^*} \quad (4.18)$$

When T_0 is not much less than T_1 (in practice $T_1 < 3$) it is necessary to evaluate the integral I, and

$$\begin{aligned} L^* p^* &= \frac{0.8945}{\sqrt{h^*/p^*}} T_1^{9/4} \int_{\theta_1}^{\frac{\pi}{2}} \sin^{9/5} \theta \, d\theta \\ &= \frac{0.8 T_1^{9/2}}{L^* h^*} \int_{\theta_1}^{\frac{\pi}{2}} \sin^{9/5} \theta \, d\theta \end{aligned} \quad (4.19)$$

Thus for every value of T_1 (the summit temperature) the corresponding value of the parameter $L^* p^*$ can be found. For h^*/p^* constant $L^* p^*$ varies as $T_1^{9/4}$; for $L^* h^*$ constant, $L^* p^*$ varies as $T_1^{9/2}$.

For lower values of h^*/p^* it is necessary to seek a numerical solution. As (4.8),(4.9) constitute a boundary-value problem, with unknowns at both limits, it may appear at first sight that iteration is necessary. This, however, is not the case as in (4.8), (4.9) the right-hand sides are functions of T^* and V only and not s^* .

If the equation

$$\frac{d}{dS} \left(T^{5/2} \frac{dT^*}{dS} \right) = (L' p')^2 \left[X^* T^{\alpha-2} - \frac{h^*}{p^* T^*} \right] \quad (4.20)$$

is integrated, from $S = 0$, $T^* = 0.2$, $dT^*/dS = T'$, and the integration is continued until $dT^*/dS = 0$, say at $S = S_1$, then one may set $s^* = S / S_1$, to make (4.20) become

$$\frac{d}{ds^*} \left(T^{5/2} \frac{dT^*}{ds^*} \right) = (L^* p^*)^2 \left[X^* T^{\alpha-2} - \frac{h^*}{p^* T^*} \right] \quad (4.6)$$

with $L^* p^* = L' p' S_1$ and all the boundary conditions imposed on (4.8) and (4.9) satisfied. By scanning through T' all possible solutions for the particular value of h^*/p^* can be found together with the corresponding values of $L^* p^*$. When considering hot-cool solutions it is necessary to integrate as far as the second zero of dT^*/ds^* rather than the first.

For the hot-cool solution of very large length a numerical solution is difficult to find since a very limited value of T' is required and so it is useful to consider the following analytical solution near the critical point.

From (4.10) and (4.11) and considering equation (4.12),

$$V = V_1 e^{\lambda S} + V_2 e^{-\lambda S} \quad (4.21a)$$

$$\tau = \tau_1 e^{\lambda S} + \tau_2 e^{-\lambda S} = \frac{T_c^{-5/2} V_1}{\lambda} e^{\lambda S} - \frac{T_c^{-5/2} V_2}{\lambda} e^{-\lambda S} \quad (4.21b)$$

At the loop summit, $V = 0$, $\tau = \tau_0$, and a shift will be applied to S transforming it to S'' which is zero there i.e.

$$V = \lambda \tau_0 T_c^{5/2} \sinh(\lambda S'') \quad (4.22a)$$

$$\tau = \tau_0 \cosh(\lambda S'') \quad (4.22b)$$

When V takes the value V_a ,

$$S'' = \frac{1}{\lambda} \sinh^{-1} \frac{V_a T_c^{-5/2}}{\lambda (T - T_c)} \quad (4.23)$$

and if V_a is suitably chosen then this is the value of S that is added to the contour by the presence of the saddle point. The numerical solution closest to the saddle point gives a summit temperature of T_1 and a contour length of S_1 , so

$$V_a = \lambda (T_1 - T_c) T_c^{5/2} \sinh (\lambda S_1) \quad (4.24)$$

Values of S (the total contour length) and the relevant L^*p^* for temperatures closer to T_c can be found from

$$L^*p^* = L' p' S = L' p' \left[S_1 + \frac{1}{\lambda} \log_e \frac{T_1 - T_c}{T - T_c} \right] \quad (4.25)$$

Since λ is large (between 50 and 10^6) the value of L^*p^* differs significantly from a constant only extremely close to the saddle point.

4.3 Results

The parameter h^*/p^* was assumed to lie in the range 0.001 to 100. The correct range for the parameter L^*p^* was identified by considering the physical properties of different kinds of loops, shown in Table 4.II (see Priest, 1982). The pressure is found from the temperature and density and this together with the loop length, gives the value of the parameter L^*p^*

Table 4.II, Parameters for Interconnecting (I), Quiet Region (Q), Active Region (A), Post Flare (P), and Simple Flare (S) loops.

	I	Q	A	P	S
Half-Length (Mm)	5-175	5-175	2-25	2-25	1-10
Temperature (10^6 K)	2-3	1.8	0.01-2.5	0.01-4	≤ 40
Particle Density (10^{14} m^{-3})	7	2-10	5-50	100	≤ 1000
Pressure (Pa)					
Lower Limit	0.02	0.005	7×10^{-5}	0.01	
Upper Limit	0.03	0.025	0.17	5	500
Parameter L^*p^*					
Lower Limit	200	50	0.3	50	
Upper Limit	10^4	10^4	10^4	5×10^5	5×10^7

Since this study is most relevant to Interconnecting, Quiet Region and Active Region loops, the parameter L^*p^* will be restricted to the range 10^{-1} to 10^4 .

Figure 4.3 shows the calculated summit temperature $T(1)$ as a function of the parameter L^*p^* for various values of h^*/p^* . Smaller values of h^*/p^* than 0.001 would give values of L^*p^* greater than the upper limit of the realistic range. Several different categories of solution can be identified, as follows.

Hot solutions exist with $T^*(1)$ greater than 4 i.e. the summit temperature is in excess of 400 000 K can be found for L^*p^* greater than about 10 and for any value of h^*/p^* .

For $h^*/p^* \leq 0.41$, (Region I), the solutions correspond to

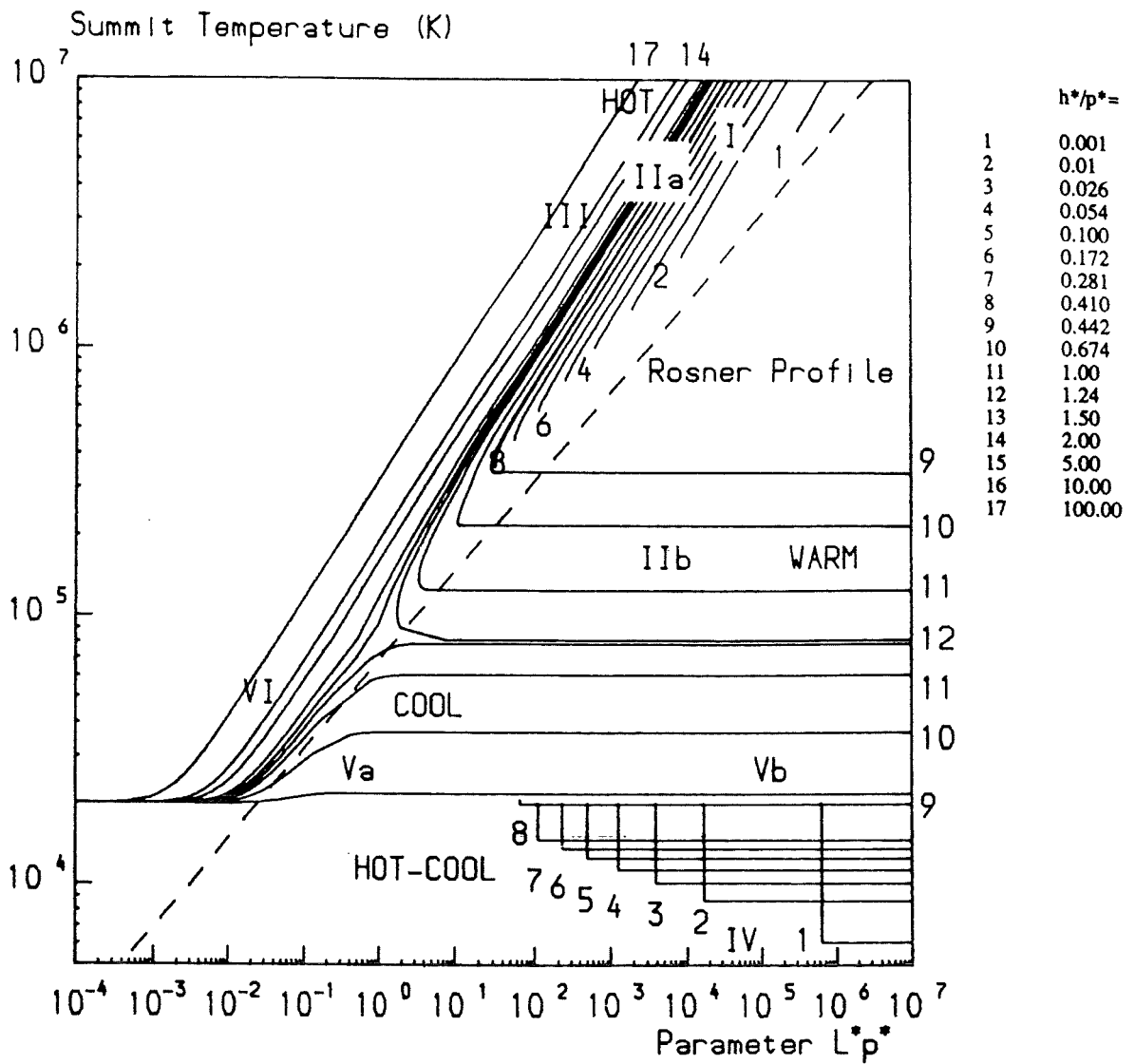


Figure 4.3a The summit temperature of a coronal loop as a function of the parameter L^*p^* for different values of the parameter h^*/p^* and for L^*p^* varying between 10^{-4} and 10^7 . Different categories of solution are marked. The broken line gives the summit temperature as deduced by Rosner et al (1978).

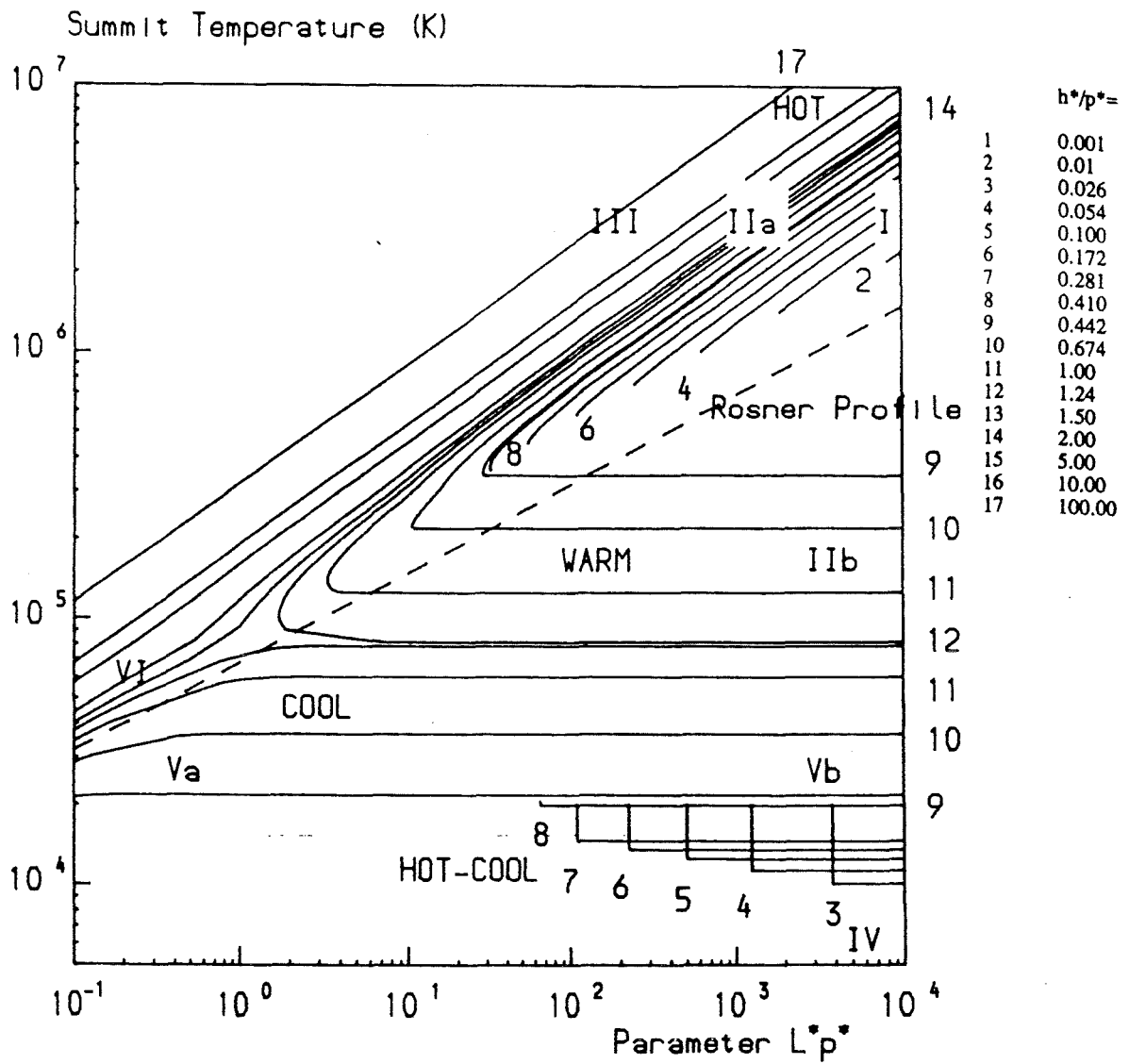


Figure 4.3b The summit temperature of a coronal loop as a function of the parameter L^*p^* for different values of the parameter h^*/p^* and for L^*p^* varying between 10^{-1} and 10^4 . Different categories of solution are marked. The broken line gives the summit temperature as deduced by Rosner et al (1978).

a footpoint given by A, C, F or H in Figure 4.1a, and a summit given by B, D, G or J. As the temperature gradient at $s^*=0$ is increased, (and the footpoint moves from A and towards H), the summit temperature increases (as the summit moves from B towards J), and the length of the contour increases. This corresponds to an increase in summit temperature as the loop length is increased.

Region IV contains the hot-cool solutions. It can be seen that changing the summit temperatures does not have much effect on the value of the parameter L^*p^* except near the saddle point. The maximum summit temperature of a hot-cool solution is equal to the footpoint temperature and the minimum temperature is that of the saddle point.

Near the saddle point, equation (4.25) has been used to calculate the value of L^*p^* . The scale is such that there appears to be little change in L^*p^* as the summit temperature is reduced until T^* equals T_c , giving the appearance of a right-angled bend in the curves at the bottom right hand corner of Figure 4.3a. For example, in the case where $h^*/p^* = 0.001$ (line 1), when $T^* = 0.2$, $L^*p^* = 619793$ and when $T^* - T_c = 10^{-6}$, i.e. the temperature is 0.1K above that of the saddle point L^*p^* increases to 619866.

For $0.41 < h^*/p^* < 1.25$, (Region II, between lines 8 and 12), the hot solution corresponds to starting the integration at point M and continuing as far as point J. As point M recedes from point K, point J recedes from point G and the contour length increases. The graph shows that longer loops have higher summit temperatures. As mentioned earlier,

infinite values of L^*p^* are found when point M is close to point K. On the graph this is shown by the data in region IIb. The temperatures in this region are lower, within the 'warm' range.

Thus as the summit temperature of a loop is decreased keeping h^*/p^* constant, the parameter L^*p^* decreases. This decrease does not continue indefinitely though. There is a lower limit to L^*p^* below which a hot (or warm) solution does not exist.

The hot solutions for $h^*/p^* > 1.25$ are shown in Region III. Again, the summit temperature increases with increasing h^*/p^* and L^*p^* .

Cool solutions are found for values of h^*/p^* greater than 0.41. Those where h^*/p^* is also less than 1.25 are shown in Region V. Those in Va are short loops, but when the contour terminates close to the X-point, the parameter L^*p^* is greatly increased. Those solutions are shown in Region Vb.

The solutions for $h^*/p^* > 1.25$ are shown in Region VI. As can be seen from Figure 4.1b, there is no topological difference between the cool and hot solutions for this value of h^*/p^* and the solutions in Region VI join onto those in Region III.

Figure 4.3a shows the solutions for L^*p^* in the range 10^{-4} to 10^7 while Figure 4.3b deals with the restricted range 10^{-1} to 10^4 . Figure 4.3c presents the way the

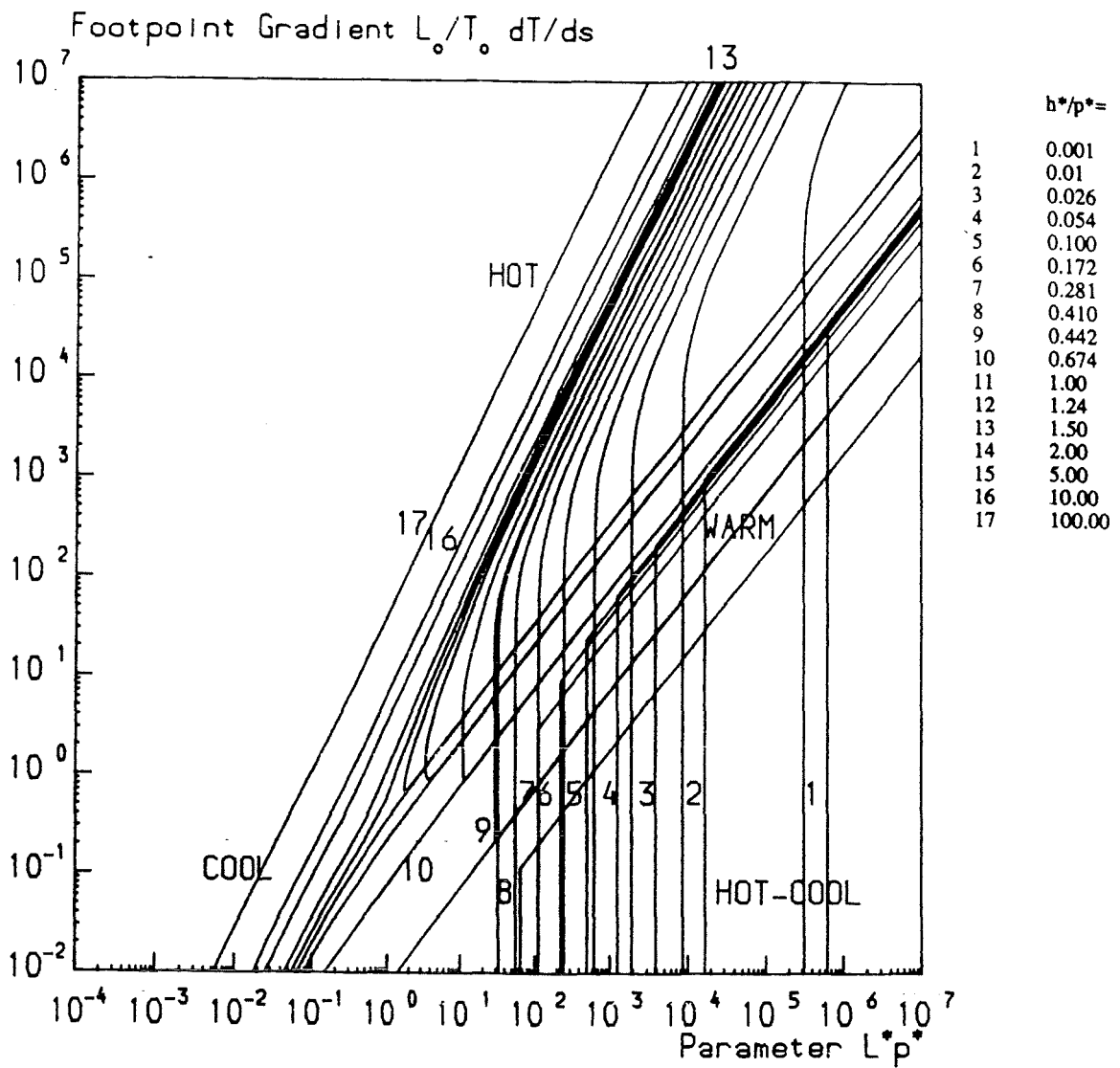


Figure 4.3c The dimensionless footpoint temperature gradient $L_0/T_0 \frac{dT}{ds}$ as a function of L^*p^* for different values of h^*/p^* .

footpoint temperature gradient varies with the parameters h^*/p^* and L^*p^* . Plotted is the dimensionless temperature gradient

$$\frac{L_o}{T_o} \frac{dT}{ds} = \frac{L^* p^*}{L' p'} \frac{dT^*}{dS} \quad (4.26)$$

It would have been more difficult to plot dT/ds , since the value of L_o (the loop half-length) is not unique for a particular value of L^*p^* . It is necessary for the footpoint temperature gradients to be positive but too high a value may make the solutions unrealistic if the heat flux becomes too large to be absorbed by the lower atmosphere. The largest temperature gradients occur for the hottest solutions.

The Rosner scaling law (Rosner et al, 1978), with constants to match the non-dimensionalisation used here becomes

$$T^*(1) = \left[\frac{L^* p^*}{3.12} \right]^{1/3} \quad (4.27)$$

On both Figure 4.3a and Figure 4.3b, this profile is shown by a broken line.

Figure 4.4 shows the same data as for Figure 4.3, plotted on the same axes but for constant values of L^*h^* instead of h^*/p^* . For values of h^*/p^* less than 100 this has been achieved by interpolation; for higher values it has been done analytically. These higher values realistically correspond to low values of p^* rather than high values of h^* . Again different regimes of solutions can be found.

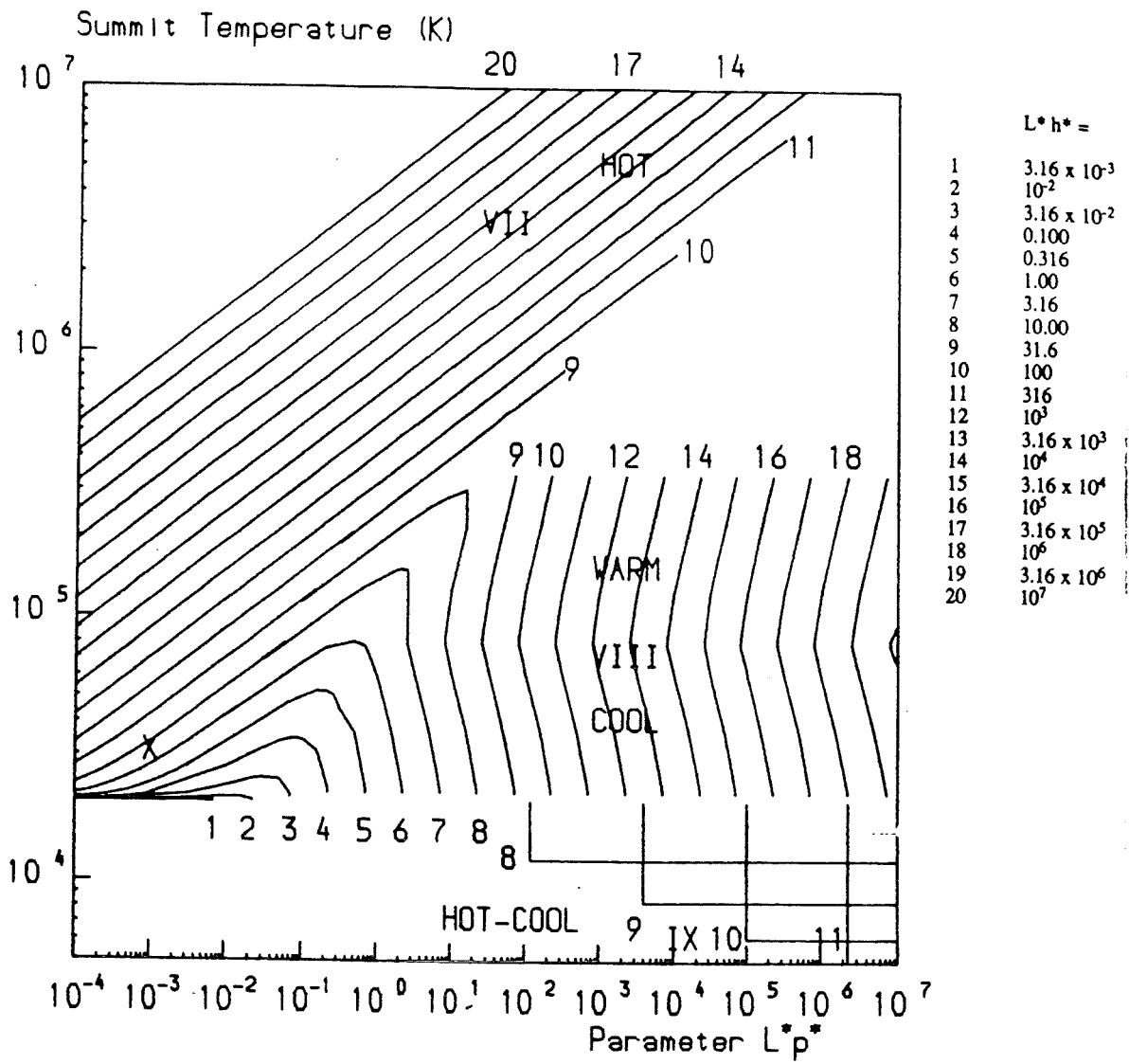


Figure 4.4a The summit temperature of coronal loops as a function of the parameter h^*/p^* for different values of the parameter L^*h^* and for L^*p^* varying between 10^{-4} and 10^7 .

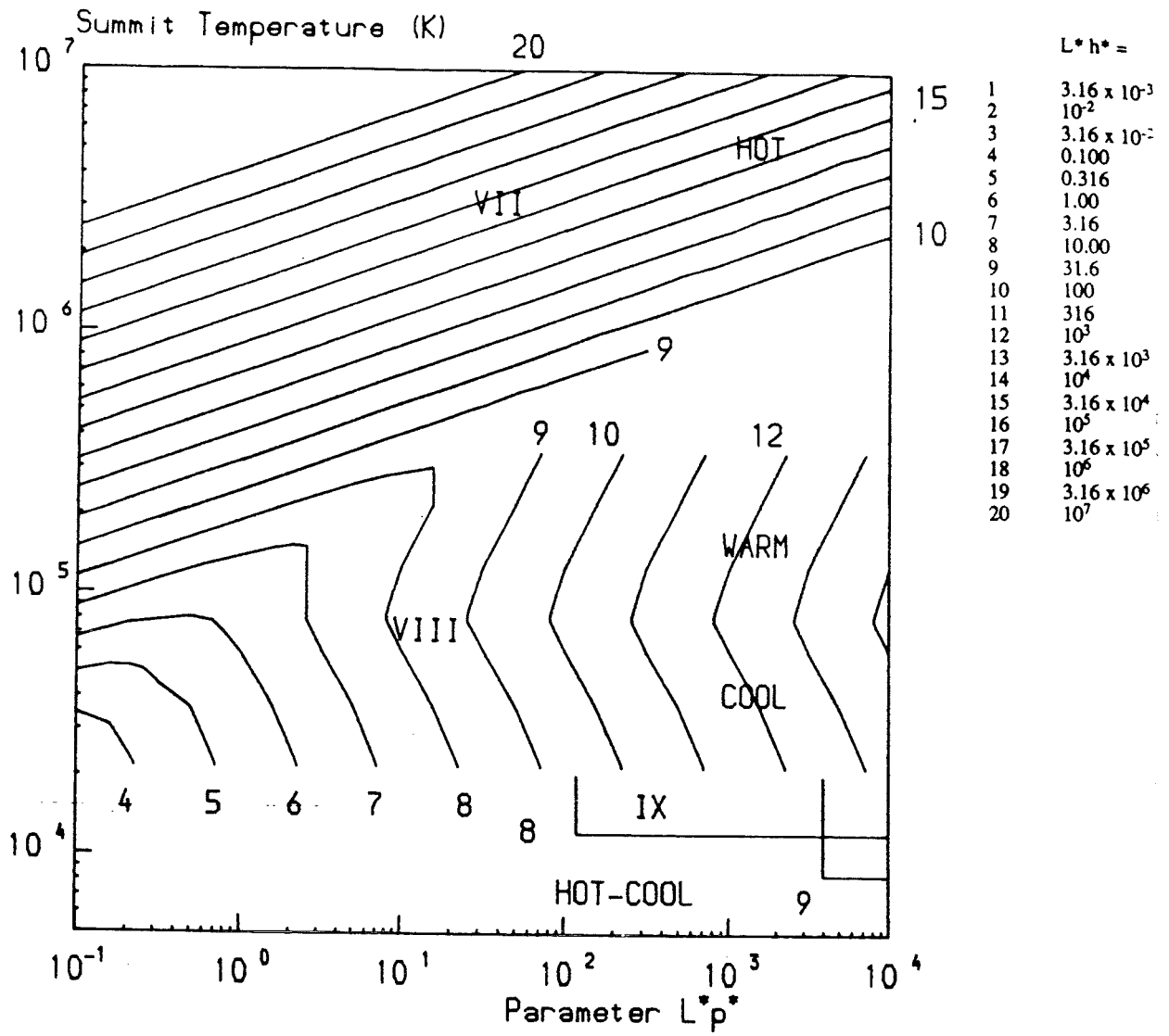


Figure 4.4b The summit temperature of coronal loops as a function of the parameter h^*/p^* for different values of the parameter L^*h^* and for L^*p^* varying between 10^{-1} and 10^4 .

When L^*h^* is greater than about 30, (Region VII), hot solutions exist with the summit temperature greater than about 400 000 K. There is, however, no topological difference between those solutions and cooler solutions with the same L^*h^* ; if a loop is cooled with L^*h^* remaining constant, this is allowable if the parameter L^*p^* reduces. L^*p^* and the summit temperature cannot increase indefinitely however, as this would lead to a negative temperature gradient at the footpoints. For high L^*p^* , however, another set of cooler solutions exists. This is shown in region VIII.

For values of L^*h^* in excess of 10, solutions exist which are hot along part of their lengths but cool at the summit (i.e. at a temperature of less than 20 000 K). Region IX shows these.

For all values of L^*h^* , solutions exist which are cool along their whole lengths (Region X). For higher values of L^*h^* , this requires extremely short loops.

Figure 4.4a shows the solutions for L^*p^* in the range 10^{-4} to 10^7 while Figure 4.4b deals with the restricted range 10^{-1} to 10^4 .

Figure 4.5 deals with the special case where $T'(0) = 0$ i.e. the footpoint temperature gradient is zero. There are two distinct branches to this curve - the hot solutions and the hot-cool solutions - for values of h^*/p^* less than 0.41. For values of h^*/p^* greater than this only the non-physical zero-length solution and the solution where the footpoint and summit are both represented by the saddle point T_c exist.

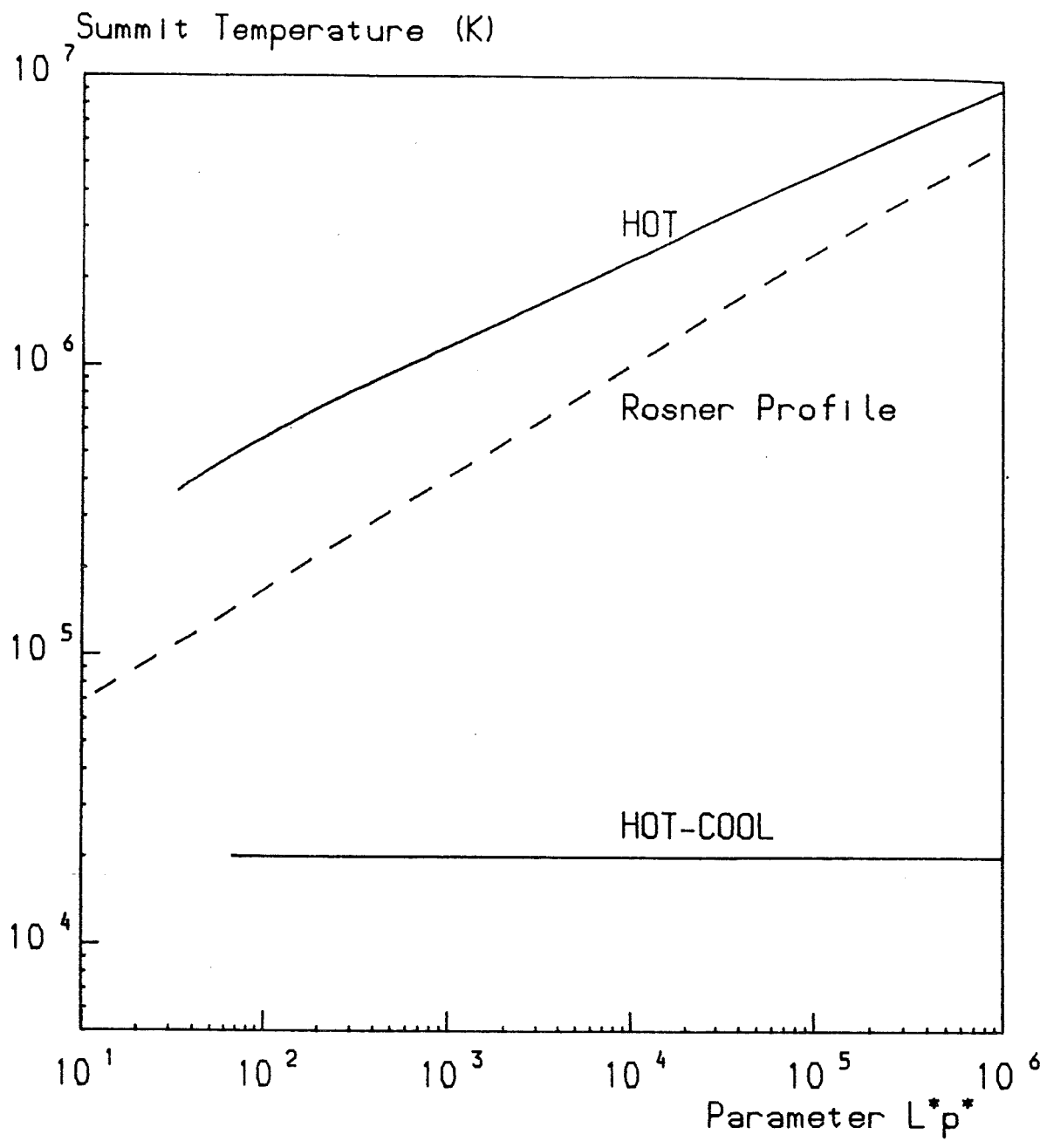


Figure 4.5 Thermally isolated coronal loops i.e. those with zero footpoint temperature gradients.

a) The loop summit temperature as a function of the parameter L^*p^* . Two distinct branches are found corresponding to hot loops and hot-cool loops. The summit temperature predicted by Rosner et al (1978) is shown by the broken line.

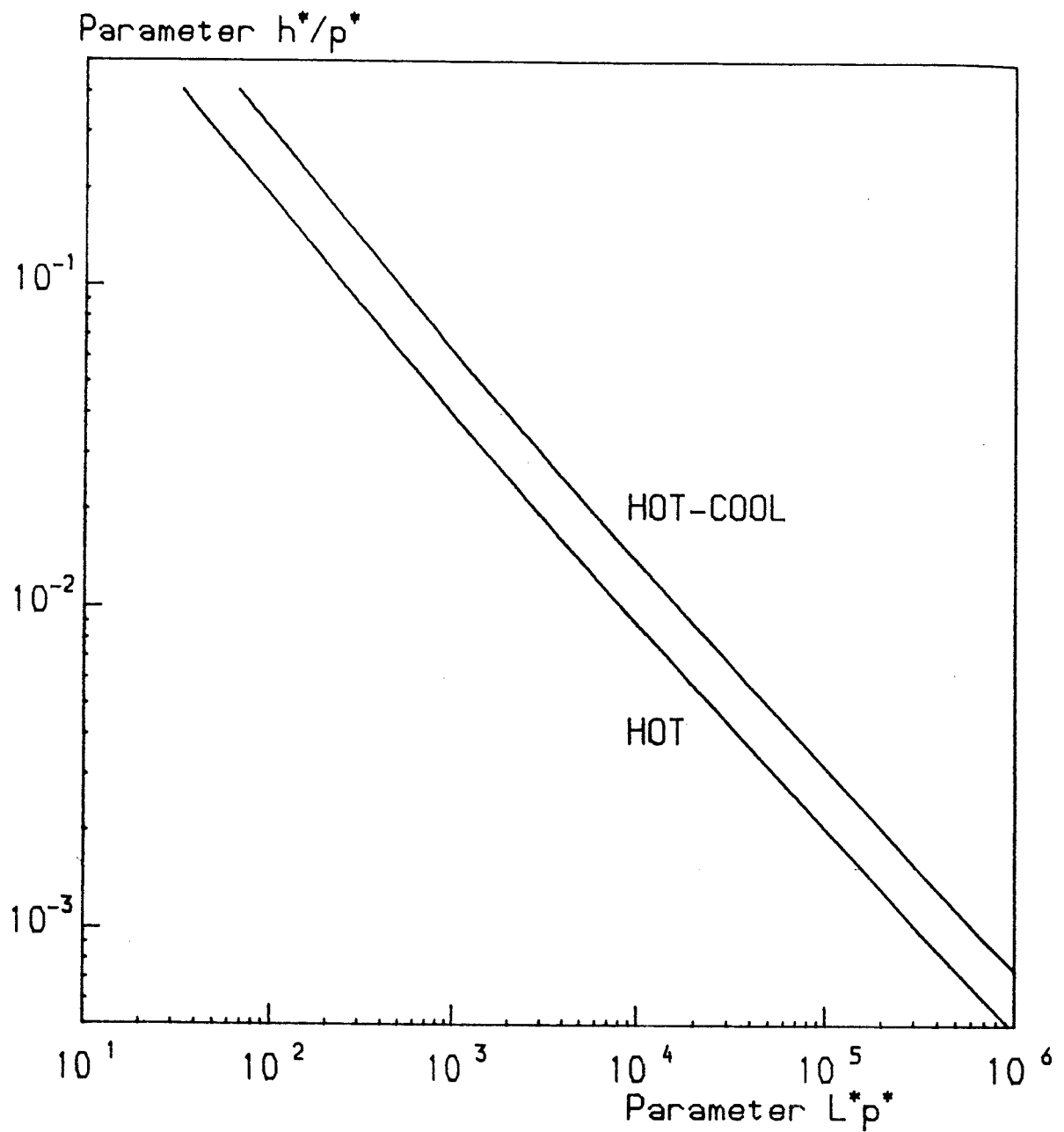


Figure 4.5 Thermally isolated coronal loops i.e. those with zero footpoint temperature gradients.
 b) The contours in (L^*p^*) (h^*/p^*) parameter space for which thermally isolated solutions exist.

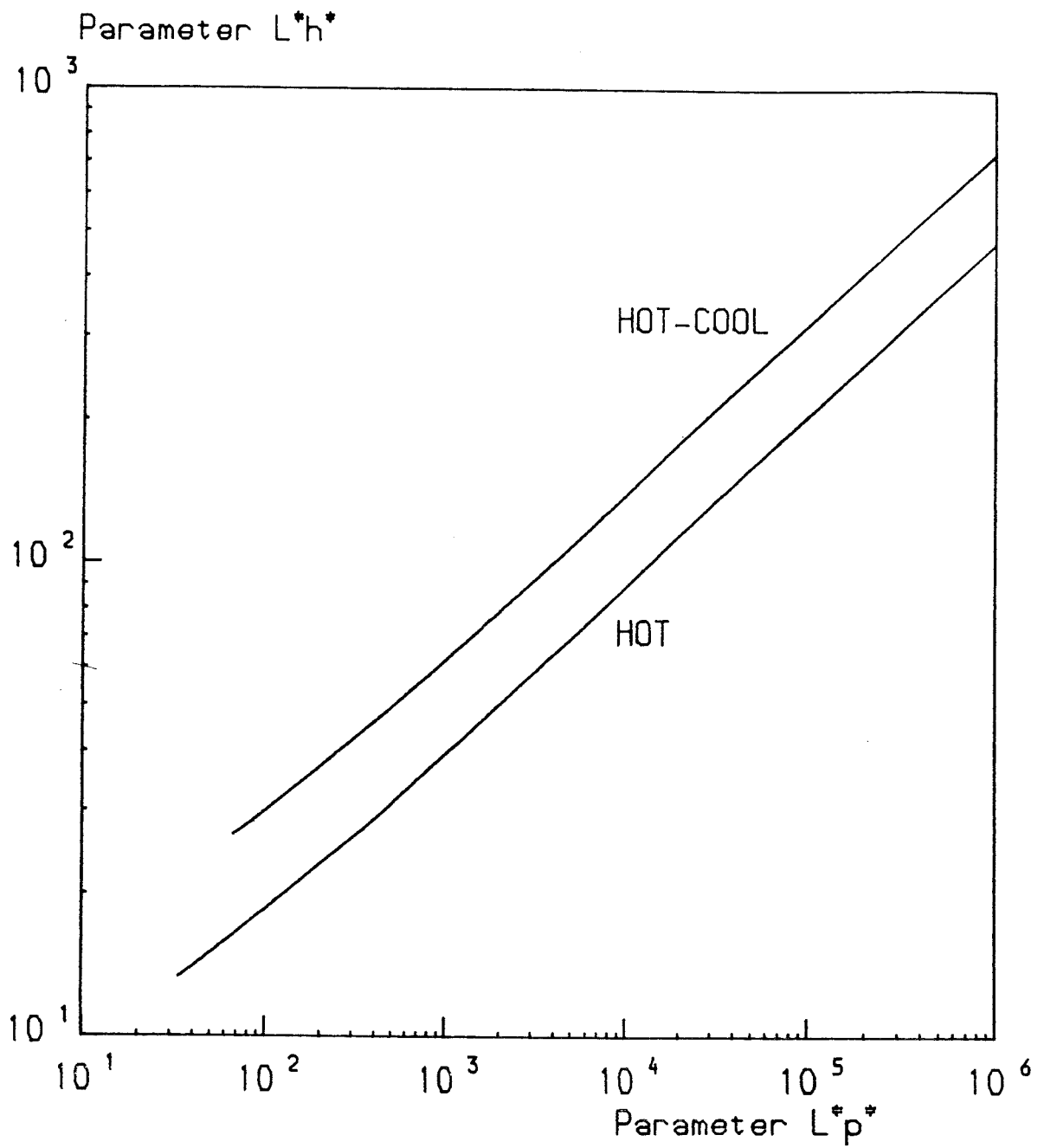


Figure 4.5 Thermally isolated coronal loops i.e. those with zero footpoint temperature gradients.
 c) The contours in (L^*p^*) (L^*h^*) space for which thermally isolated solutions exist.

Figure 4.5a shows the summit temperature varying with the parameter L^*p^* . For hot solutions, the temperature increases as L^*p^* increases. The Rosner profile is shown again by a broken line. Figure 4.5b shows how L^*p^* varies with h^*/p^* . As h^*/p^* is increased, solutions can only be found if L^*p^* is reduced. For a given value of h^*/p^* , L^*p^* is a factor of two greater for a hot-cool solution, than for a hot solution. Figure 4.5c shows the variation of L^*h^* with L^*p^* . These two parameters are positively correlated, with values of L^*h^* being higher for hot-cool solutions.

For every value of h^*/p^* less than 1.25, there exists a minimum value of L^*p^* for a hot solution. Figure 4.6 shows how this minimum L^*p^* varies with the corresponding value of the parameter h^*/p^* . When h^*/p^* is less than 0.41, the minimum L^*p^* occurs when the temperature gradient at the footpoint is zero. This is shown by the solid part of the curve.

When h^*/p^* is between 0.41 and 1.25, the minimum length occurs as a non-equilibrium point. Both hotter and cooler solutions have a higher corresponding value of L^*p^* . This is shown by the broken part of the curve.

Figure 4.7 shows how T varies with s^* for a typical hot loop, a hot-cool loop and a cool loop, respectively. Firstly it deals with a loop where $h^*/p^* = 0.1$ and $T' = 100$. This gives $L^*p^* = 248$. It can be seen that the temperature gradient is large near the footpoint and quickly reduces. If $h^*/p^* = 0.1$ and $T' = 100$, and a hot-cool solution is sought,

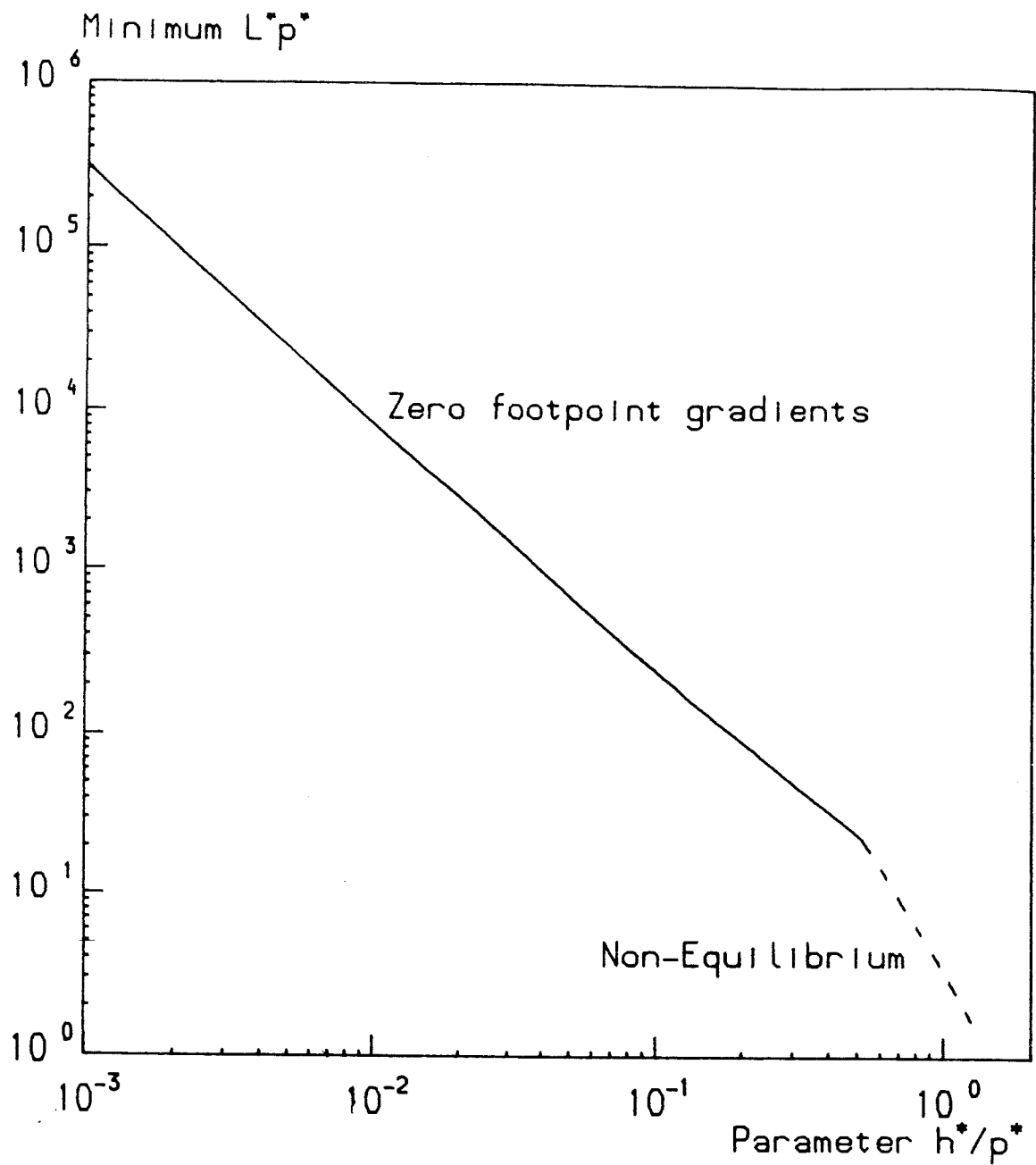


Figure 4.6 For every value of h^*/p^* less than 1.25 there is a minimum value of L^*p^* below which reasonable hot solutions cannot exist. This value is shown here. For h^*/p^* less than 0.41 negative footpoint temperature gradients would exist if L^*p^* were reduced below this value. For h^*/p^* greater than 0.41, non-equilibrium occurs.

this time $L^*p^* = 495$. Again there is a large temperature gradient near the footpoint and this time also near (but not at) the summit whereas the warm portion contains low temperature variations. Finally a completely cool loop is shown in with $h^*/p^* = 1.00$ and $T' = 100$ so $L^*p^* = 0.0156$. The change in temperature here is more gradual.

When $h^*/p^* < 0.41$ the phase plane has the form shown in Figure 4.1 with the footpoint lying along the line PQ. If the footpoint temperature gradient is negative, the footpoint lies along the section AH'. When the footpoint lies at C', a cool summit is found at E. As point C moves towards A, the length of this contour will tend towards zero as the summit moves towards the same point. As point C' moves towards point F', point E (the summit) moves towards the saddle point T_c and the length of the contour increases towards infinity. Thus for any value of L^*p^* , from zero to infinity, a solution can be found, but it is unrealistic since the footpoint temperature gradient is negative. When point H' is considered as the footpoint, no solution can be found.

Figure 4.8 shows the location of the different types of solution in the L^*p^* , h^*/p^* plane. In the regions marked I or III (these numbers correspond to those on Figure 4.3 one hot solution exists. The hot-cool solutions occur in the area marked I and IV. The region marked Va and VI is characterised by there being one cool solution, while the region marked II and Vb contains a hot, a warm, and a cool solution. There is no essential difference between the hot and cool solutions for h^*/p^* greater than 1.25 but the (broken) boundary has been drawn where the summit

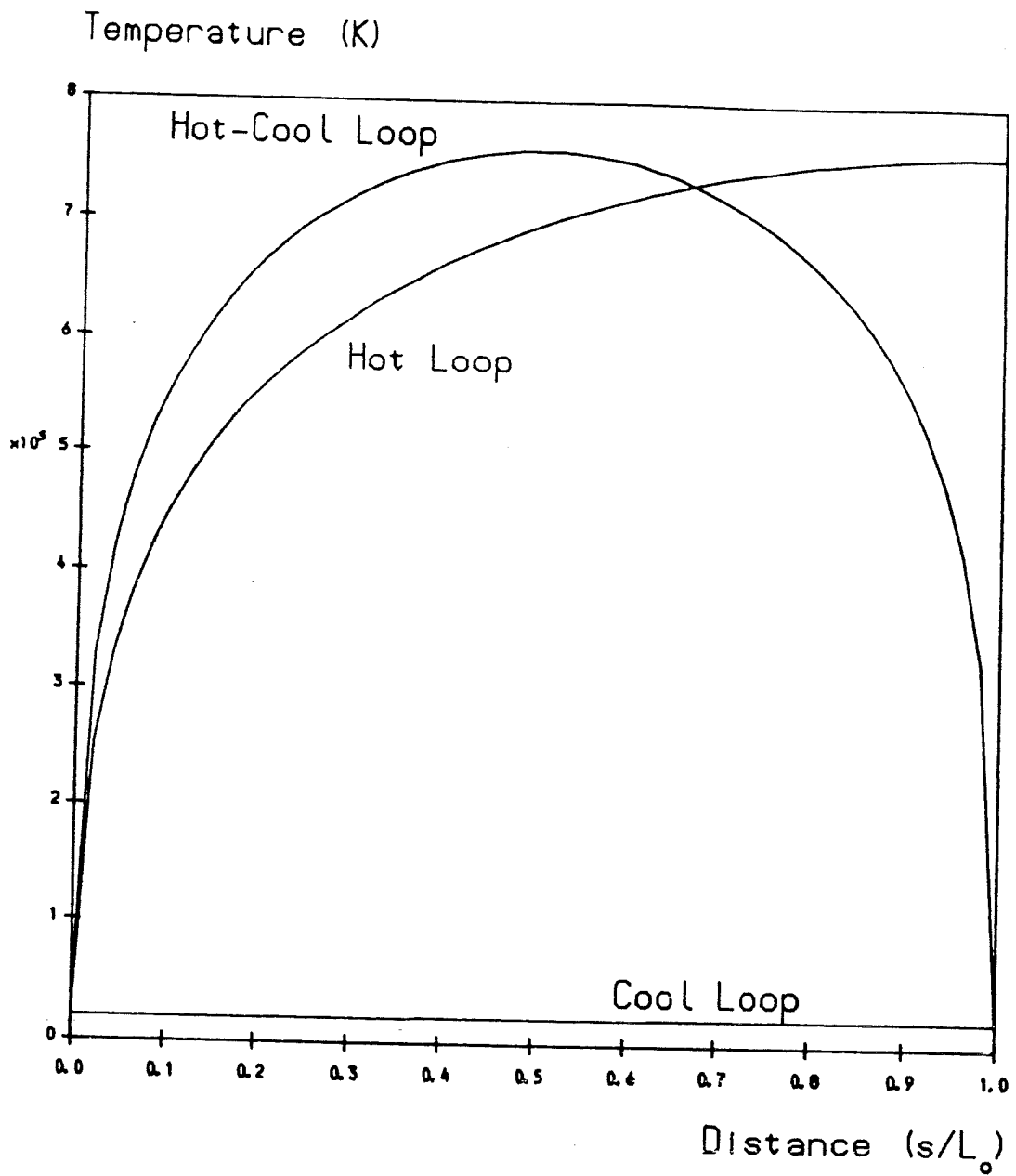


Figure 4.7 The variation of temperature along a hot loop, a cool loop and a hot-cool loop from the footpoint at $s = 0$ to the summit at $s = L_0$

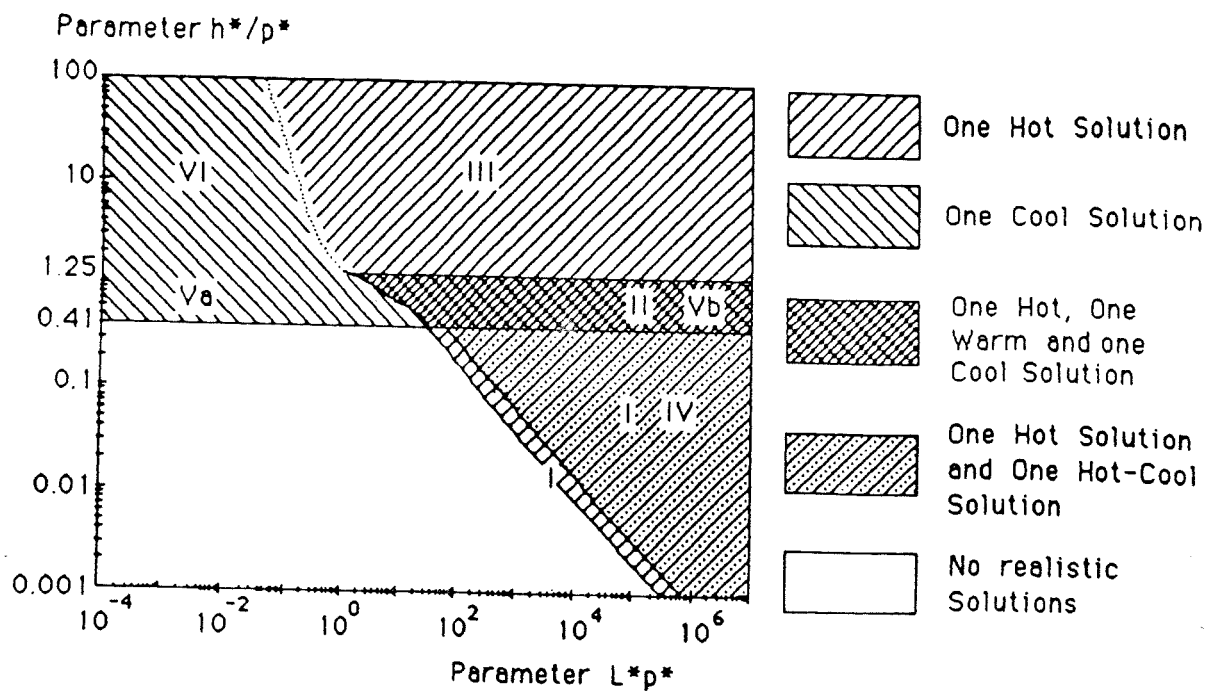


Figure 4.8 The areas of the (L^*p^*) (h^*/p^*) plane for which various different categories of solution exist.

temperature $T(1)$ equals $80\,000\text{ K}$ as this value divides the hot and warm solutions from the cool solutions for lower values of h^*/p^* . Additional unrealistic solutions with negative footpoint temperature gradients exist in both regions I, IV and the white region in the lower left-hand corner.

4.5 Conclusions

Quantitative solutions have been found to the equations derived by Hood and Anzer (1988) and new regimes of solution have been found. In particular, the cool solutions have been found for high values of heating, and the warm solutions have also been shown to be possible. The hot solutions, ranging in temperature from about $5 \times 10^5\text{ K}$ to above 10^7 K are consistent with temperatures known to exist in the corona. The cool solutions and hot-cool solutions represent potential areas for elementary loop structures within prominences (Ballester and Priest, 1989).

The observed differential emission measure shows the existence of hot material both at temperatures in excess of about $5 \times 10^5\text{ K}$ and also cool material at temperatures less than $8 \times 10^4\text{ K}$; these temperatures are consistent with the hot and cool loops referred to above. The emission measure gives evidence of much less material at temperatures between $8 \times 10^4\text{ K}$ and $5 \times 10^5\text{ K}$, the temperatures associated with the summits of the warm loops. The summits of certain of the warm loops will be at temperatures within this 'forbidden' range. Of course, hot (and hot-cool) loops will contain portions at temperatures

associated with warm loops but at such points the temperature gradients are relatively high and the relevant temperatures occur only over a short length of loop.

The hot loops are consistent with the temperatures of loops found by Sheeley et al (1977). The cool loops are consistent with the observations of Foukal (1975) of cool material (at temperatures less than 8×10^4 K along the whole of a loop). They are also of relevance for fibrils and active-region prominences where the magnetic field lies mainly along the plane of the prominence.

The hot-cool loops correspond to threads in quiescent prominences inclined to the plane of the prominence. The cool summit corresponds to the cool material of the prominence and the hot legs to the hotter surrounding corona.

The warm loops do not appear to correspond to any particular structure observed in the corona. A stability analysis may show these equilibria to be unstable.

It is instructive to compare the results with those found by Hood and Priest (1979). The Figure in Hood and Priest corresponding to Figure 4.3 here is shown as Figure 4.9. In it H corresponds to the h^*/p^* here and γ to $(L^*p^*)^2$. The temperature $T(1)$ is given in units of 10^6 K.

There are similarities between the two figures; both show hot solutions which have increased temperature with increased length and increased heating. The results by the present analysis give cooler summits for shorter loops while

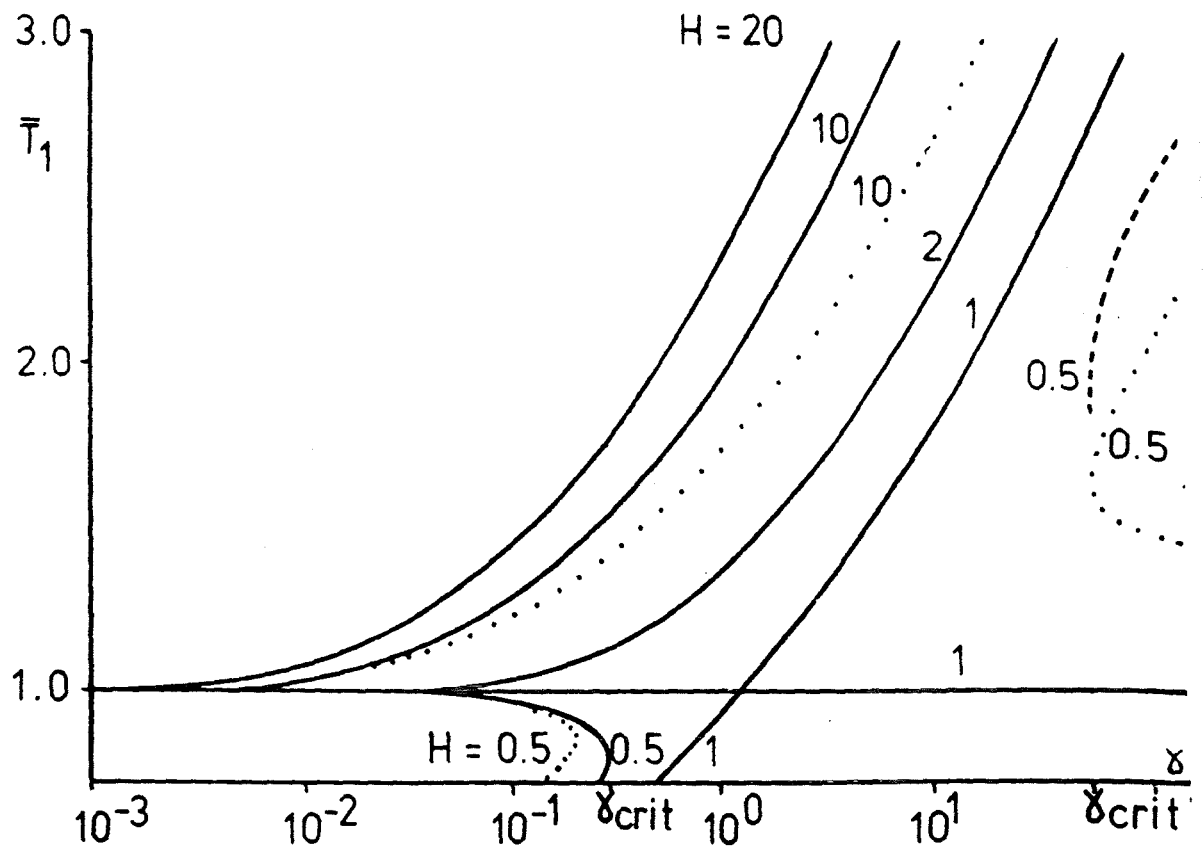


Figure 4.9 The loop summit temperature T_1 (in units of 10^6 K) as a function of the two dimensionless combinations $\gamma = L^2 p^2 [= \rho_0^2 \chi_0 T_0^{\alpha_0 - 2} L^2 / (\kappa_0 k^2 T^{7/2})]$ and $H = h/p [= hk / (\rho_0 \chi_0 T_0^{\alpha_0 - 1})]$. From Hood and Priest (1979)

for longer loops the summit temperatures are roughly equal. Figure 4.9 therefore corresponds to the region in Figure 4.3 above a temperature of 10^6 K.

At temperatures about 10^5 K there are dissimilarities between the two figures. For very short loops (low L^*p^*) the summit temperature approaches the footpoint temperature of 10^6 K for the Hood case, but in the present case it approaches the relevant footpoint temperature which is lower by a factor of 50.

The present analysis produces new features at lower temperatures. There are solutions with cool summits but hotter parts at other points along the loop for low heating rates. There are also loops with large values of L^*p^* for temperatures between 20 000 K and 400 000 K. In the Hood case the only cool solution is that for large L^*p^* when $h^*/p^* = 1$.

At present in order to isolate the essential effects, the analysis has been carried out with the neglect of gravity and with constant cross-sectional area, so that the magnetic field is uniform along each loop. Further work will include the relaxation of these assumptions.

CHAPTER FIVE - THERMAL EQUILIBRIA OF CORONAL MAGNETIC ARCADES WITH AXES ON PHOTOSPHERE

5.1 Introduction

In Chapter 4, see also Steele and Priest (1989b), equations of thermal equilibrium along coronal loops were solved. Coronal loops often form arcades and the thermal structure of such an arcade can be found by solving the equations of thermal equilibrium along each loop. It is intended to carry out such an analysis in this chapter.

5.2 Thermal Structure of Cylindrically Symmetric Arcades

A magnetic arcade consists of a large number of field lines and so an arcade can be thought of as comprising a continuum of such loops and the thermal structure of an arcade can be found by solving for the thermal structure of each individual loop. This procedure is valid as the thermal conductivity along the magnetic field is far greater than that across the field (Spitzer, 1962).

Coronal arcades can be of many configurations but one possible equilibrium is a cylindrically symmetric one with the axis on the photosphere and there being zero shear (Figure 5.1). This being the case, the field is constant along each field line and the analysis of Steele and Priest (1989b) applies.

A cylindrically symmetric magnetostatic equilibrium obeys the equation

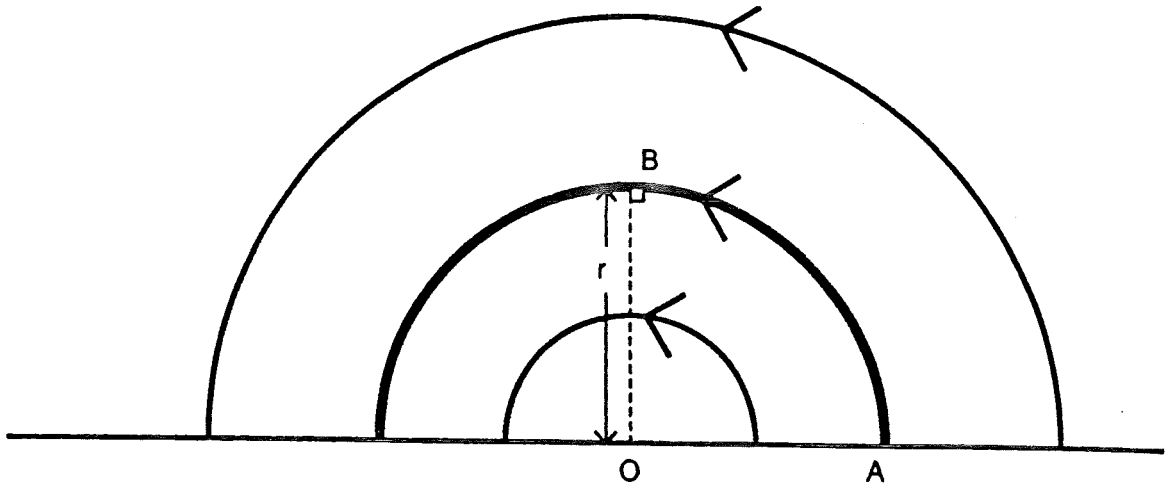


Figure 5.1 The form of the arcade considered. The axis is at point O and three loops are shown. The loop highlighted has footpoint at A and summit at B and lies a distance r from the axis.

$$\frac{d}{dr} \left(p + \frac{B_{\theta}^2}{2\mu} \right) + \frac{B_{\theta}^2}{\mu r} = 0 \quad (5.1)$$

where there are no shear or radial components to the field,
i.e.

$$\frac{d B_{\theta}^2}{dr} + 2 \frac{B_{\theta}^2}{r} = -2\mu \frac{dp}{dr} \quad (5.2)$$

Multiplying by r^2 ,

$$\frac{d}{dr} (B_{\theta}^2 r^2) = -2\mu r^2 \frac{dp}{dr} \quad (5.3)$$

i.e.

$$B_{\theta}^2 r^2 = -2\mu \int r^2 \frac{dp}{dr} \quad (5.4)$$

Now, considering the particular equilibrium (Figure 5.2a)

$$p = p_e + (p_c - p_e) \exp(-r^2/a^2) \quad (5.5)$$

where

$$\frac{dp}{dr} = -\frac{2r}{a^2} (p_c - p_e) \exp(-r^2/a^2) \quad (5.6)$$

and (5.4) becomes

$$B_{\theta}^2 r^2 = -\frac{4\mu}{a^2} (p_c - p_e) \int r^3 \exp(-r^2/a^2) dr \quad (5.7)$$

Putting $U = -r^2/a^2$ and thus $dU = -2r/a^2 dr$
the integral in (5.7) becomes

$$\int \frac{a^4}{2} U \exp(U) dU = \frac{a^4}{2} [U \exp(U) - \exp(U) + c]$$

and so

$$B_{\theta}^2 r^2 = 2(p_c - p_e) \mu (-r^2 \exp(-r^2/a^2) - a^2 \exp(-r^2/a^2) + c)$$

and

$$B_{\theta}^2 = -2(p_c - p_e) \mu \left(1 + \frac{a^2}{r^2}\right) \exp\left(-\frac{r^2}{a^2}\right) + \frac{c}{r^2} \quad (5.8)$$

In order to prevent a singularity at the origin, c is set equal to $c = 2(p_c - p_e) \mu a^2$ and so

$$B_{\theta}^2 = \frac{2(p_c - p_e) \mu a^2}{r^2} - 2(p_c - p_e) \mu \left[1 + \frac{a^2}{r^2}\right] \exp\left(-\frac{r^2}{a^2}\right) \quad (5.9)$$

as plotted in Figure 5.2b.

For this particular function p , the parameters L^*p^* and h^*/p^* will vary as follows.

$$\frac{h^*}{p^*} = \frac{h^*/p_e^*}{1 + (p_c^*/p_e^* - 1) \exp(-r^2/a^2)} \quad (5.10)$$

where $p_e^* = p_e/p_o$, $p_c^* = p_c/p_o$.

This parameter increases with r and then tends towards the constant value h^*/p_e^* .

$$L^* = \frac{L_o}{L_{\infty}} = \frac{\pi r}{L_{\infty}} \quad (5.11)$$

where L_{∞} is a standard loop length (see Chapter 4).

$$L^*p^* = \frac{r \pi p_e^*}{L_{\infty}} \left[1 + \left(\frac{p_c^*}{p_e^*} - 1\right) \exp\left(-\frac{r^2}{a^2}\right)\right] \quad (5.12)$$

This function can change from an increasing to a decreasing function of r depending on the value of p_c^*/p_e^* . For small values of p_c^*/p_e^* the function will be monotonically increasing but for larger values it will decrease for an interval. The borderline between the two

cases will be characterised by a stationary point of inflexion.

$$f = r p_e^* \left[1 + \left(\frac{\dot{p}_c}{\dot{p}_e} - 1 \right) \exp \left(- \frac{r^2}{a^2} \right) \right] \quad (5.13)$$

$$\frac{df}{dr} = p_e^* \left[1 + \left[\left(\frac{\dot{p}_c}{\dot{p}_e} - 1 \right) \left(1 - 2 \frac{r^2}{a^2} \right) \exp \left(- \frac{r^2}{a^2} \right) \right] \right] \quad (5.14)$$

$$\frac{d^2f}{dr^2} = (\dot{p}_c - \dot{p}_e) \left[- \frac{6r}{a^2} + \frac{4r^3}{a^4} \right] \exp \left(- \frac{r^2}{a^2} \right) \quad (5.15)$$

which is equal to zero at the point of inflexion, giving

$$\left(\frac{r}{a} \right)^2 = \frac{3}{2}$$

For this value of r/a , the first derivative should equal zero,

$$\dot{p}_e - 2 \left(\dot{p}_c - \dot{p}_e \right) \exp \left(- \frac{3}{2} \right) = 0$$

thus

$$\frac{\dot{p}_c}{\dot{p}_e} = \frac{1 + 2 \exp \left(- \frac{3}{2} \right)}{2 \exp \left(- \frac{3}{2} \right)} \approx 3.24 \quad (5.16)$$

When $p_c^*/p_e^* < 3.24$, L^*p^* is monotonically increasing; otherwise it decreases for a certain range of r .

Each contour in L^*p^* , h^*/p^* space as a function of r can be described by three parameters, namely a , h^*/p_e^* and p_c^*/p_e^* .

Note 1: The third parameter p_c^*/p_e^* can be replaced by a parameter giving the field strength at $r = a$. When $r = a$,

$$B_\theta^2(a) = 2(p_c - p_e) \mu (1 - 2 \exp(-1))$$

and so

$$\frac{p_c^*}{p_e^*} = 1 + 1.892 \frac{B_\theta^2(a)}{\mu p_e^*} \quad (5.17)$$

If $B_\theta^2(a) = 0$, (corresponding to $p_c^*/p_e^* = 1$) the field strength is zero everywhere and no arcade exists.

Note 2: It has been assumed that $p_e^* = 1$. This is done without loss of generality due to the non-dimensionalisation used.

Figure 5.2 shows how the various quantities vary with distance from the axis. Figure 5.2a shows that the pressure is p_c on the axis and reduces to p_e at infinite distances. The magnetic field profile is shown in Figure 5.2b. The field tends to zero both on the axis and at great distances and the maximum at $r/a = 1.34$ increases with the pressure ratio p_c/p_e (from zero when $p_c/p_e = 1$).

The variation of h^*/p^* with r and p_c/p_e is displayed in Figure 5.2c. At large axial distances it tends towards h^*/p_e^* while, as r tends to zero, h^*/p^* approaches h^*/p_c^* . Again this quantity is displayed for different values of the parameter p_c^*/p_e^* but the case $p_c^*/p_e^* = 1$ (which would give a constant value of h^*/p_e^*) is excluded.

Figure 5.2d shows L^*p^* varying with r for various values of p_c^*/p_e^* . Again $p_c^*/p_e^* = 1$ is excluded. For values of p_c^*/p_e^* less than 3.24 L^*p^* increases monotonically with r but for higher values there is a range of r where L^*p^* is a decreasing function.

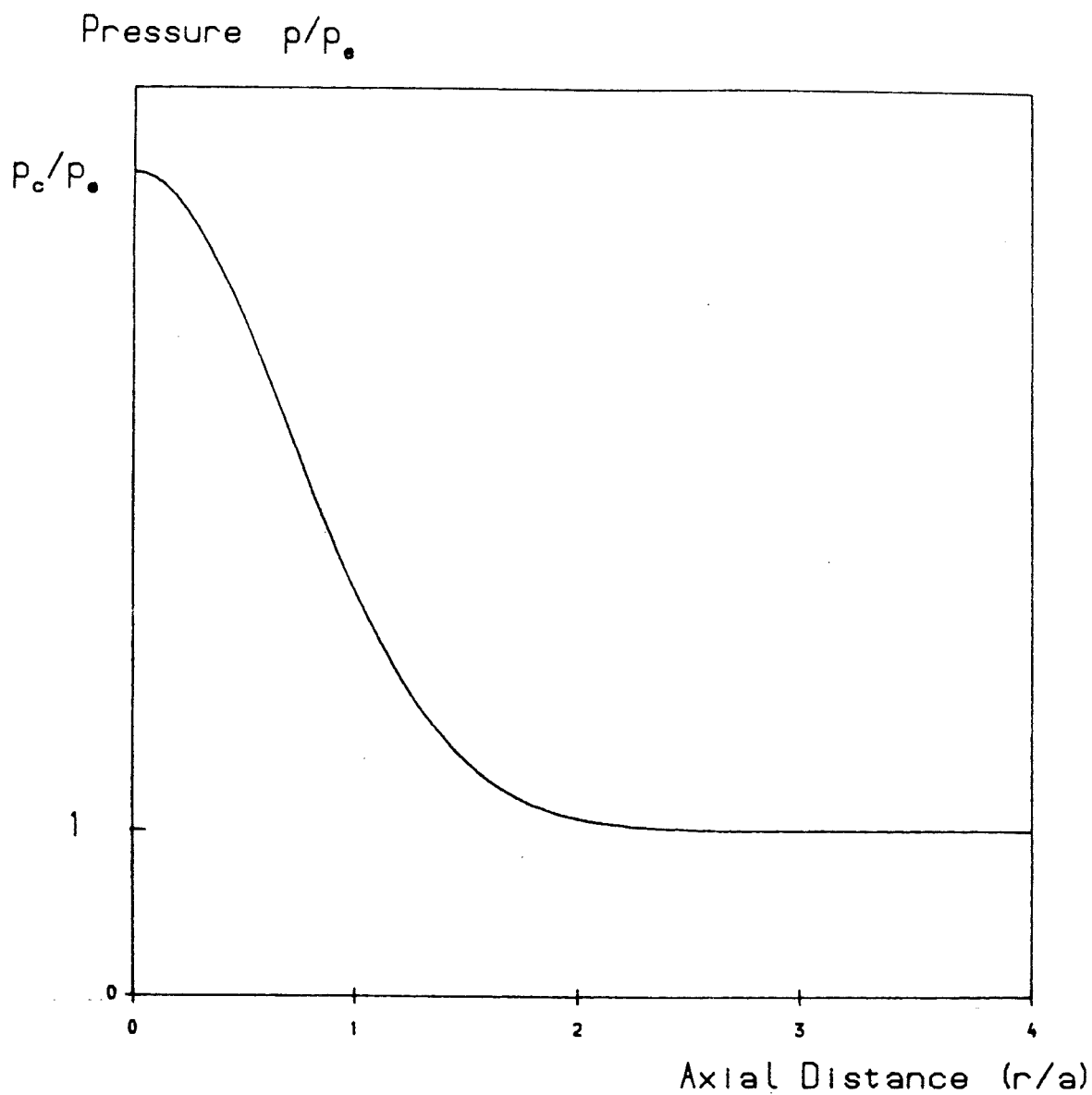


Figure 5.2a The variation of the plasma pressure within the cylindrically symmetric magnetic arcade referred to in section 5.2. It can be seen that the pressure is p_c on the axis and reduces to p_e at large axial distances.

Field $B / (2 \mu p_e)^{1/2}$

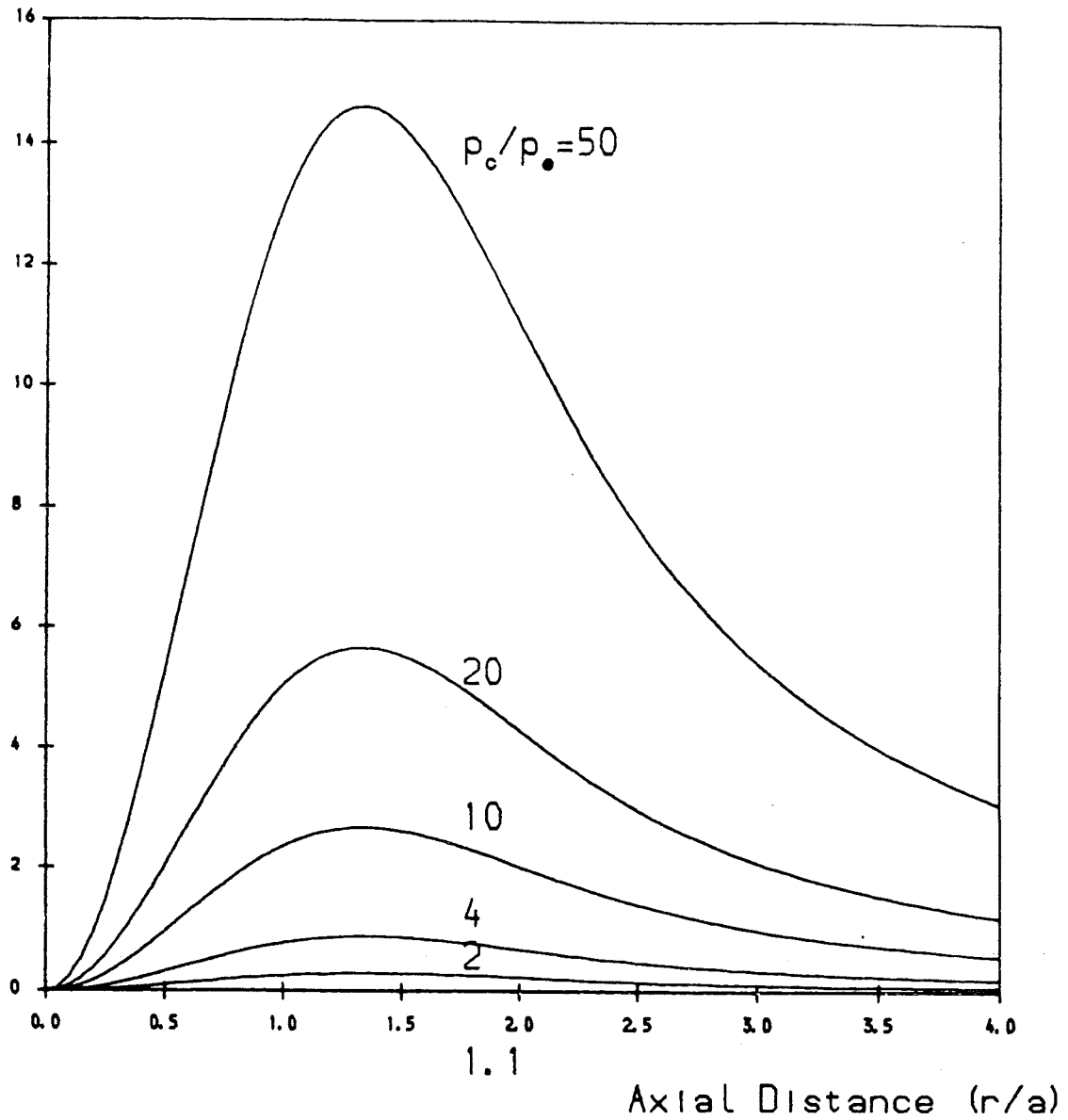


Figure 5.2b The value of the magnetic field within the arcade as a function of the axial distance for different values of the parameter p_c/p_e . The field is zero, both on the axis and at large distances. The case where $p_c/p_e = 1$ is not included as it would give a zero magnetic field.

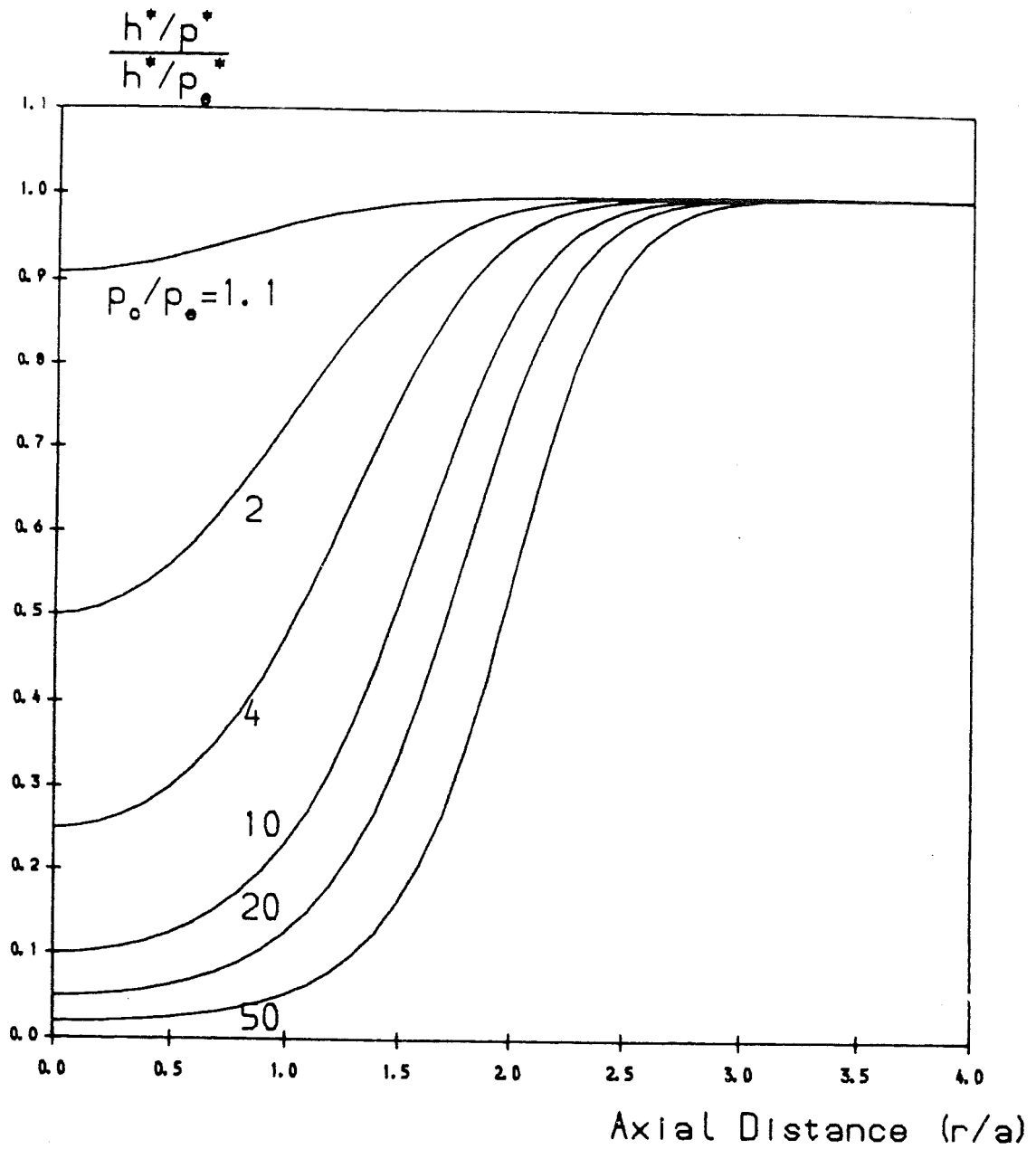


Figure 5.2c The variation with axial distance of the quantity h^*/p^* for different values of p_c/p_e . Again the case where $p_c/p_e = 1$ is excluded. The quantity h^*/p^* increases monotonically with axial distance.

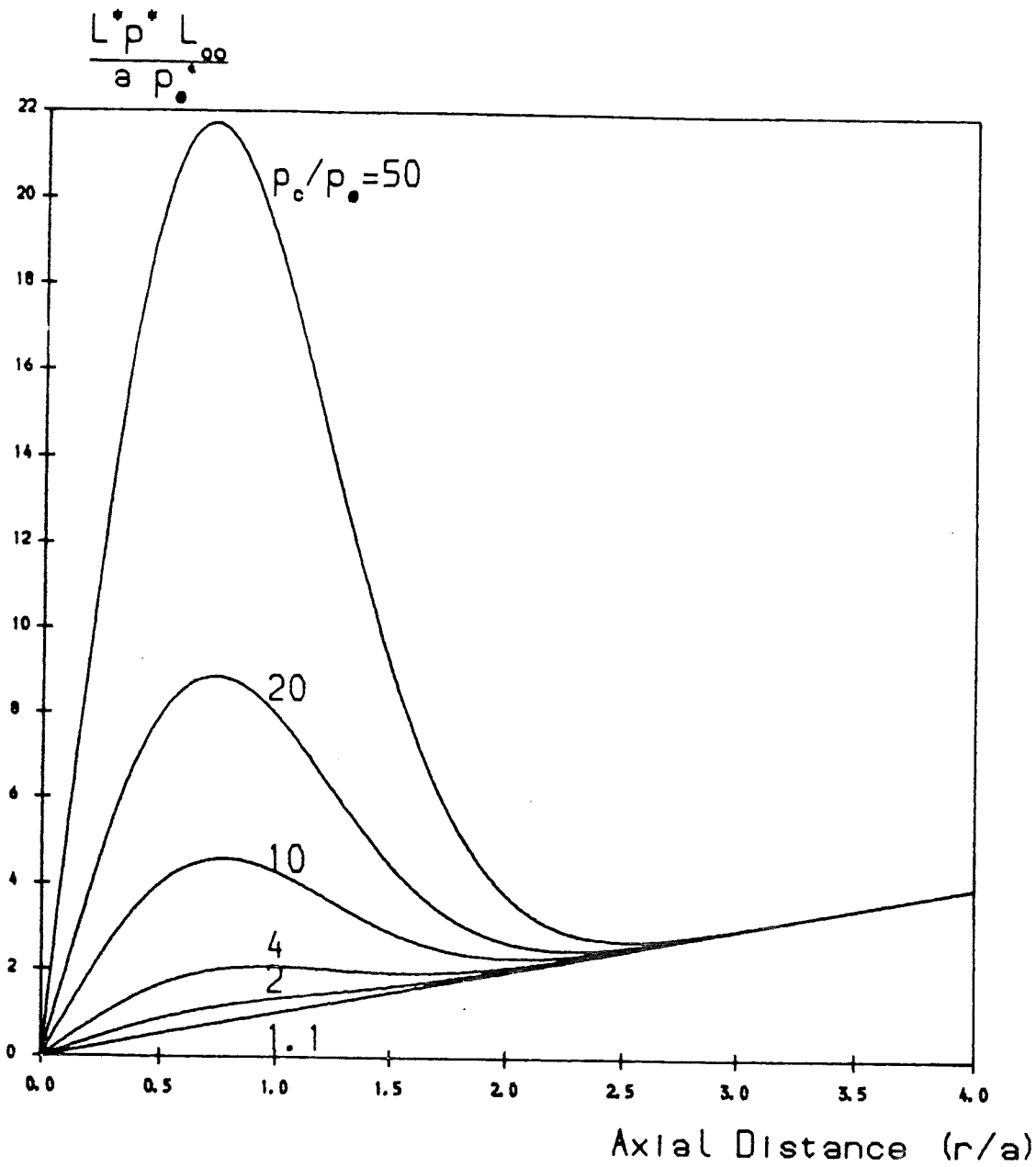


Figure 5.2d The variation with axial distance of the quantity L^*p^* for different values of p_c/p_e . L^*p^* is monotonically increasing with axial distance for low values of p_c/p_e , but there is a range of r/a where it decreases for higher values of p_c/p_e .

Figure 5.2e shows how the plasma beta, the ratio of plasma pressure to magnetic pressure (Priest 1982), varies with axial distance for the various values of the parameter p_c^*/p_e^* . The plasma beta is given by

$$\beta = \frac{1 + (p_c/p_e - 1) \exp(-r^2/a^2)}{(p_c/p_e - 1) (a^2/r^2 - (1 + a^2/r^2) \exp(-r^2/a^2))} \quad (5.18)$$

Realistic coronal values (less than of order unity) are found when p_c/p_e is greater than 4.

Figure 5.3 shows several contours in two-dimensional (L^*p^*) (h^*/p^*) space. Table 5.1 gives the relevant values of the various parameters. In contours 1 to 10, parameter 'a' is assigned one of the values 5×10^6 or 5×10^7 . These are chosen to give arcades 10Mm and 100Mm across measured with respect to $r=a$. The contours show a maximum r/a of 10. Contour 11 is less realistic with its small value for a, but has been included to show the effects of crossing the boundary between the regime of cool solutions and the regime where no solutions are realistic.

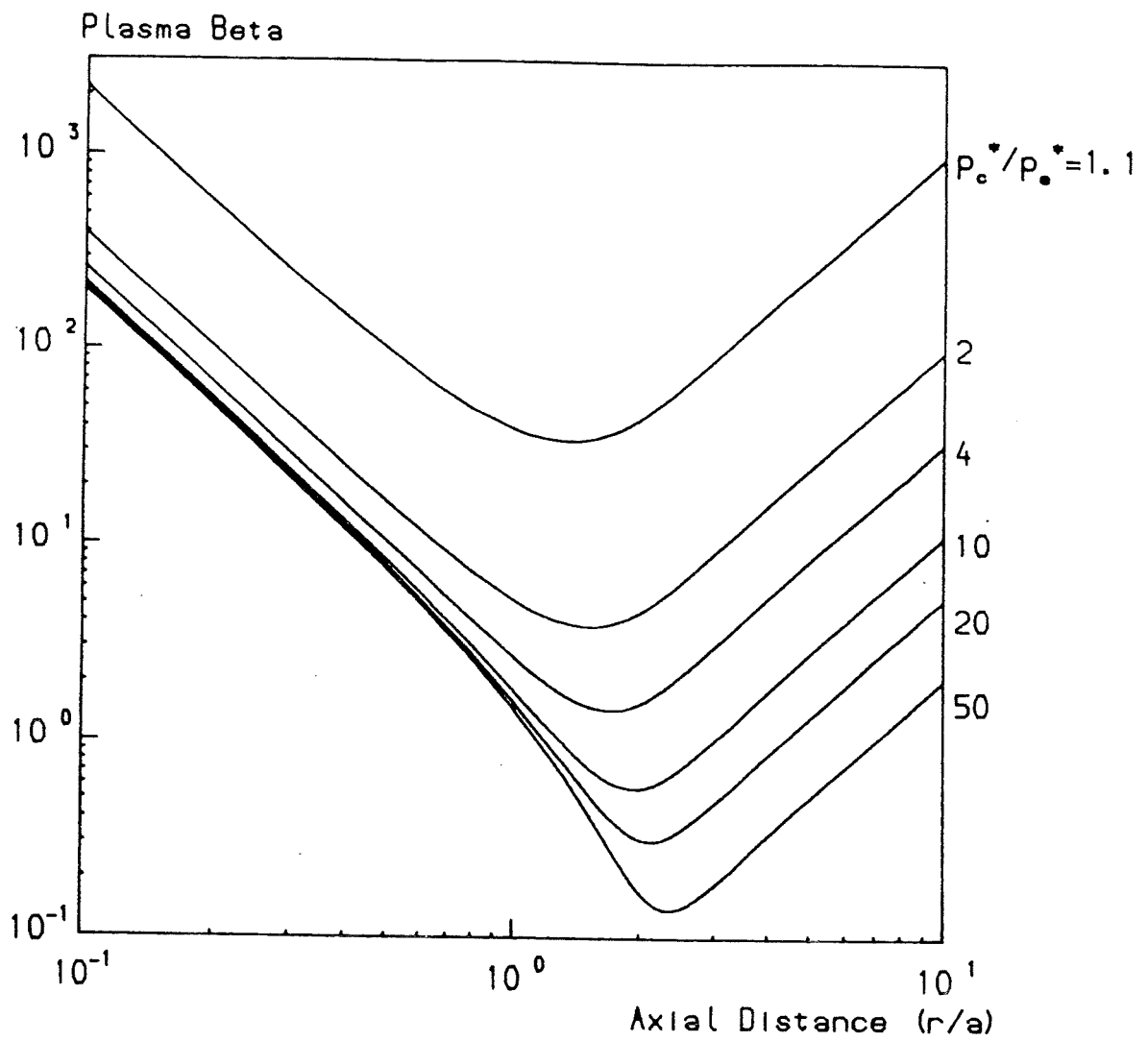


Figure 5.2e The variation of the plasma beta (the ratio of plasma to magnetic pressure) within the arcade for various values of p_c/p_e .

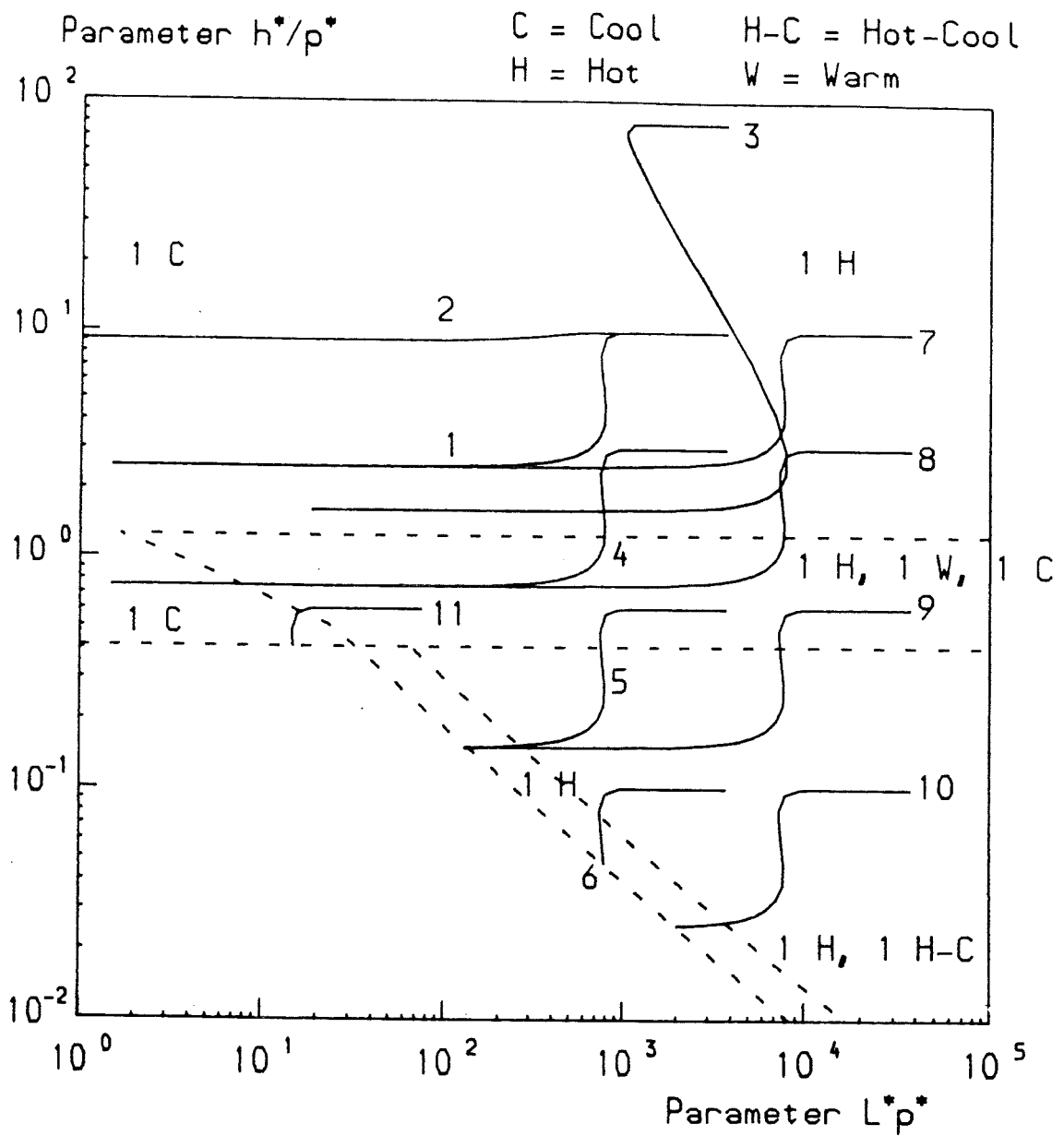


Figure 5.3 The areas of the (L^*p^*) - (h^*/p^*) plane which the various contour referred to in section 5.2 pass through. It can be seen that most contours cross a boundary beyond which new regimes of solution appear or old regimes of solution are no longer possible.

Table 5.1

	a	h^*/p_e^*	p_c^*/p_e^*
Contour 1	5×10^6	10	4
Contour 2	5×10^6	10	1.1
Contour 3	5×10^6	80	50
Contour 4	5×10^6	3	4
Contour 5	5×10^6	0.6	4
Contour 6	5×10^6	0.1	4
Contour 7	5×10^7	10	4
Contour 8	5×10^7	3	4
Contour 9	5×10^7	0.6	4
Contour 10	5×10^7	0.1	4
Contour 11	1×10^5	0.6	4

5.3 Results

The variation of the summit temperature with axial distance within an arcade is shown in Figure 5.4. For some regions of Figure 5.3 more than one solution exists; these multiple solutions have been shown.

Figure 5.4a shows the temperature profiles for each of the contours 1, 2, 3 and 5. Consider first contour 1. Since $h^*/p^* > 1.25$ for the whole contour, the hot and cool parts of the contour join continuously. The temperatures of the summits are monotonically increasing as one recedes from the axis. A slight kink in the graph around $r/a = 1$ reflects the change in h^*/p^* while L^*p^* remains roughly constant. The shortest loops ($r \ll a$) have summit temperatures close to the footpoint temperatures but the longer loops have much higher summit temperatures.

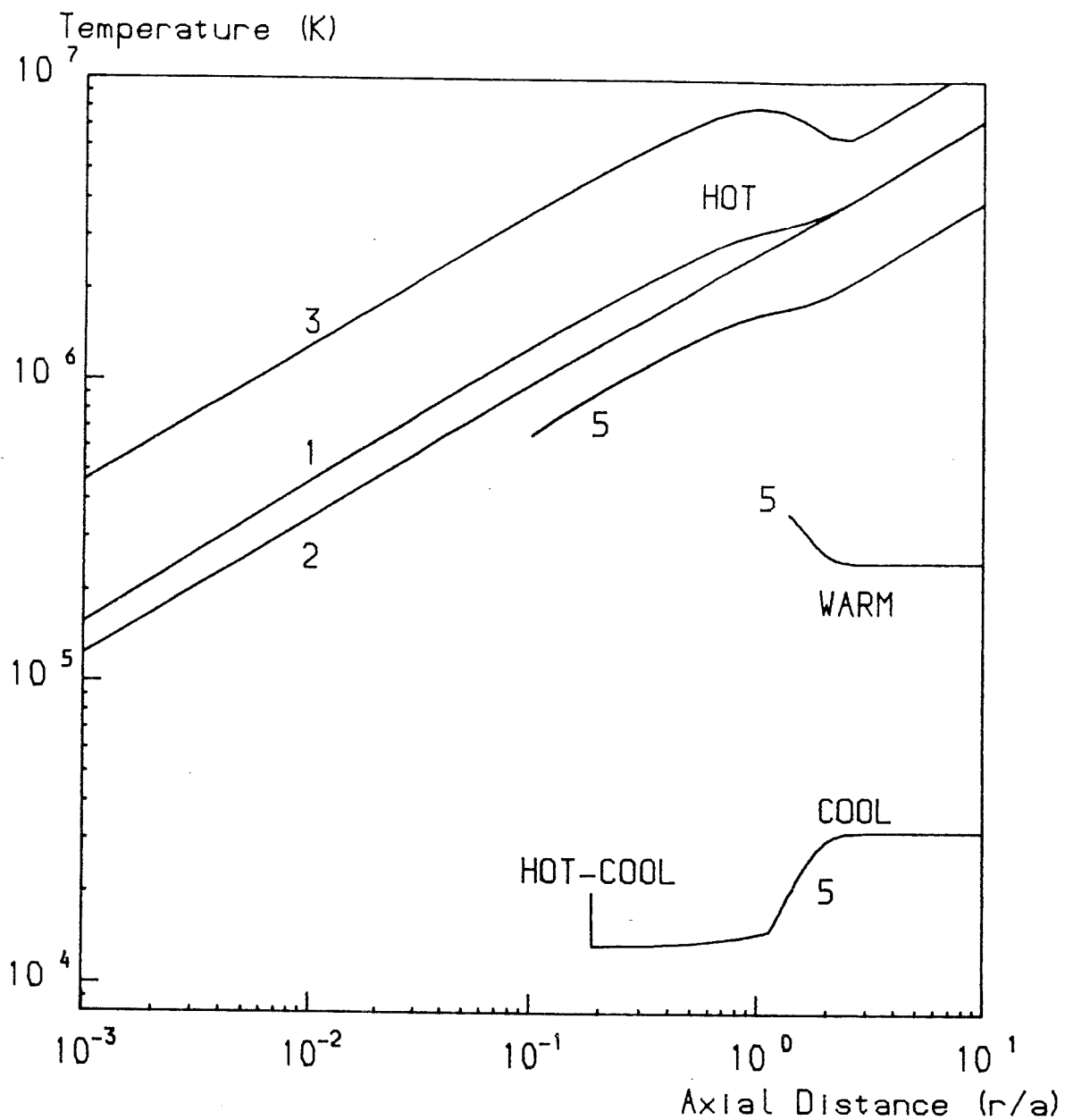


Figure 5.4a The variation of the summit temperature with height for the arcades generated by the contours 1, 2, 3 and 5 referred to in section 5.2. The division of the arcades into hot, warm, cool and hot-cool loops is noted.

Contour 2 is very similar to contour 1 except that the kink is almost absent - a result of the parameter h^*/p^* being roughly constant.

For contour 3 the variation of h^*/p^* within the arcade has been made very large. The result is that the temperature along the line of the loop summits is no longer monotonically increasing but a temperature reversal is found.

Contour 5 features temperature discontinuities and multiple solutions. For r/a larger than about 1.4, three solutions exist - hot, warm, and cool. For values of r/a lower than 1.4 warm and cool solutions no longer exist but a hot-cool solution is present. Figure 5.4a suggests that the cool solutions join smoothly onto the hot-cool solutions at a temperature of 20 000 K, but it must be remembered that the transition is only smooth at the extreme summits and that the hot-cool loop is much hotter than the cool loop at other points. At still lower values of r (i.e. $r/a < 0.2$) only the hot solution is present and when r/a falls below 0.1 there are no realistic solutions. Solutions do exist if the footpoint temperature gradient is allowed to be negative but they are not realistic since the base temperature gradient is thought to be greater than or equal to zero.

The temperature profiles generated by contours 4, and 6 are displayed in Figure 5.4b. As h^*/p^* is not always greater than 1.25 for contour 4, the hot and cool solutions no longer join up continuously. For r/a greater than about 0.9 only the one solution (hot) exists but for r/a in the range 5×10^{-3} to

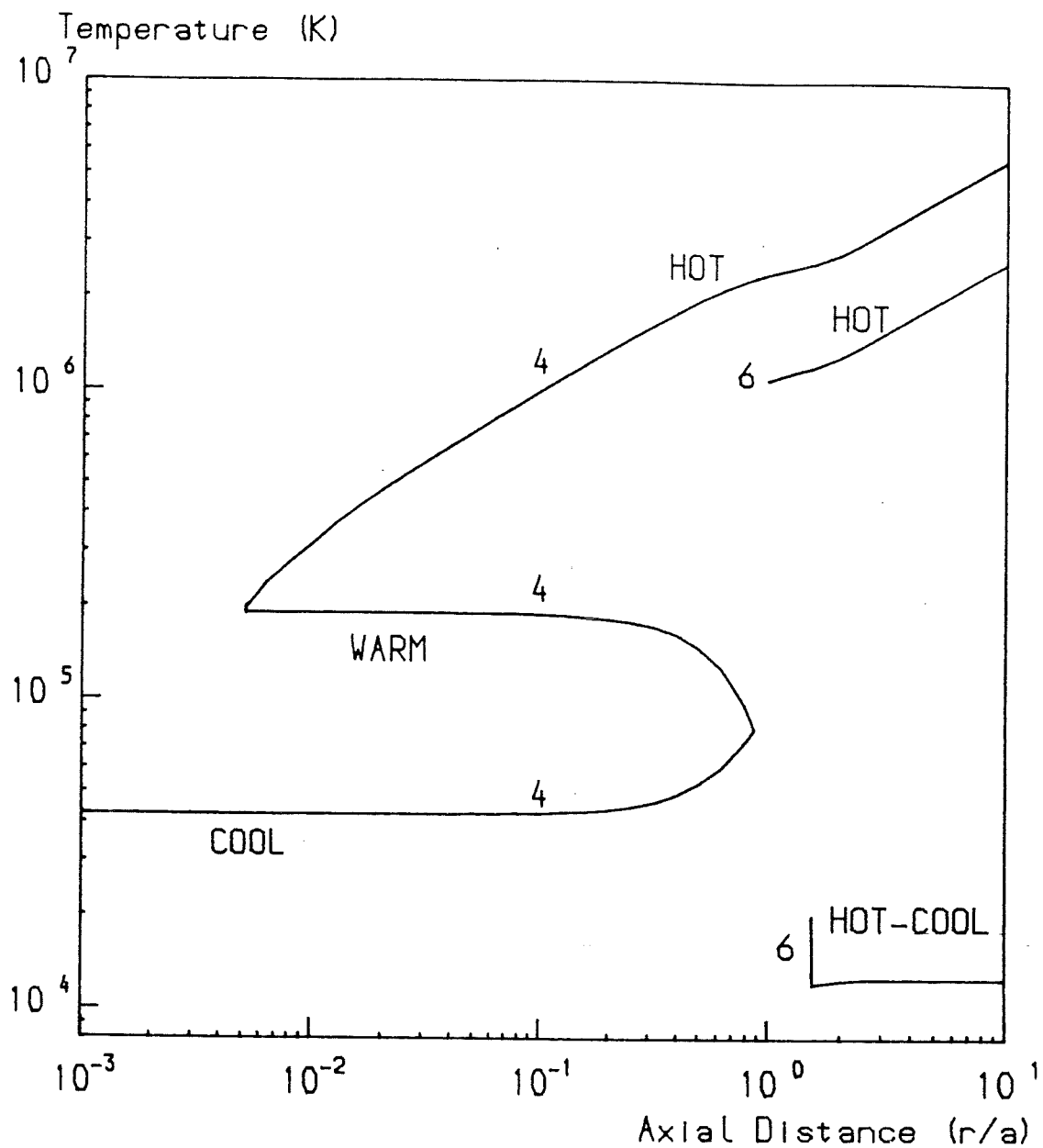


Figure 5.4b The variation of the summit temperature with height for the arcades generated by the contours 4 and 6 referred to in section 5.2. The division of the arcades into hot, warm, cool and hot-cool loops is noted.

0.9, three solutions exist, namely a hot solution, a warm solution and a cool solution (although the observed differential emission measure would suggest that warm loops are rare). When r/a is less than 5×10^{-3} the only solution is a cool solution. The hot and warm solutions merge as r/a is reduced to 5×10^{-3} and non-equilibrium is reached.

The temperature profile generated by contour 6 is similar to that produced by contour 5 except that h^*/p^* is always less than 0.41 and the part of Figure 5.4a containing the warm and cool solutions is absent.

Figure 5.4c displays the temperature profiles generated by contours 7, and 9. On contour 7, h^*/p^* is always greater than 1.25 and so the hot and cool solutions join up. This profile is similar to that generated by contour 1. The temperature profile generated by contour 9 is similar to that generated by contour 5. When r/a exceeds 1.4, three solutions exist, namely hot, warm and cool. In the range $0.02 \leq r/a \leq 1.4$ only two solutions exist, a hot solution and a hot-cool solution. Again, it is only vertically above the axis that the cool and hot-cool solutions join smoothly. The hot-cool solutions cease to exist (with positive footpoint temperature gradients) when r/a falls below 0.02 and the hot solutions suffer the same fate when $r/a < 0.01$.

The profiles generated by contours 8, 10 and 11 are shown on Figure 5.4d. The profiles for contours 8 and 10 show similarities to those generated by contours 4 and 6 respectively in Figure 5.4b. One difference is that the minimum radius for hot and warm solutions is less than

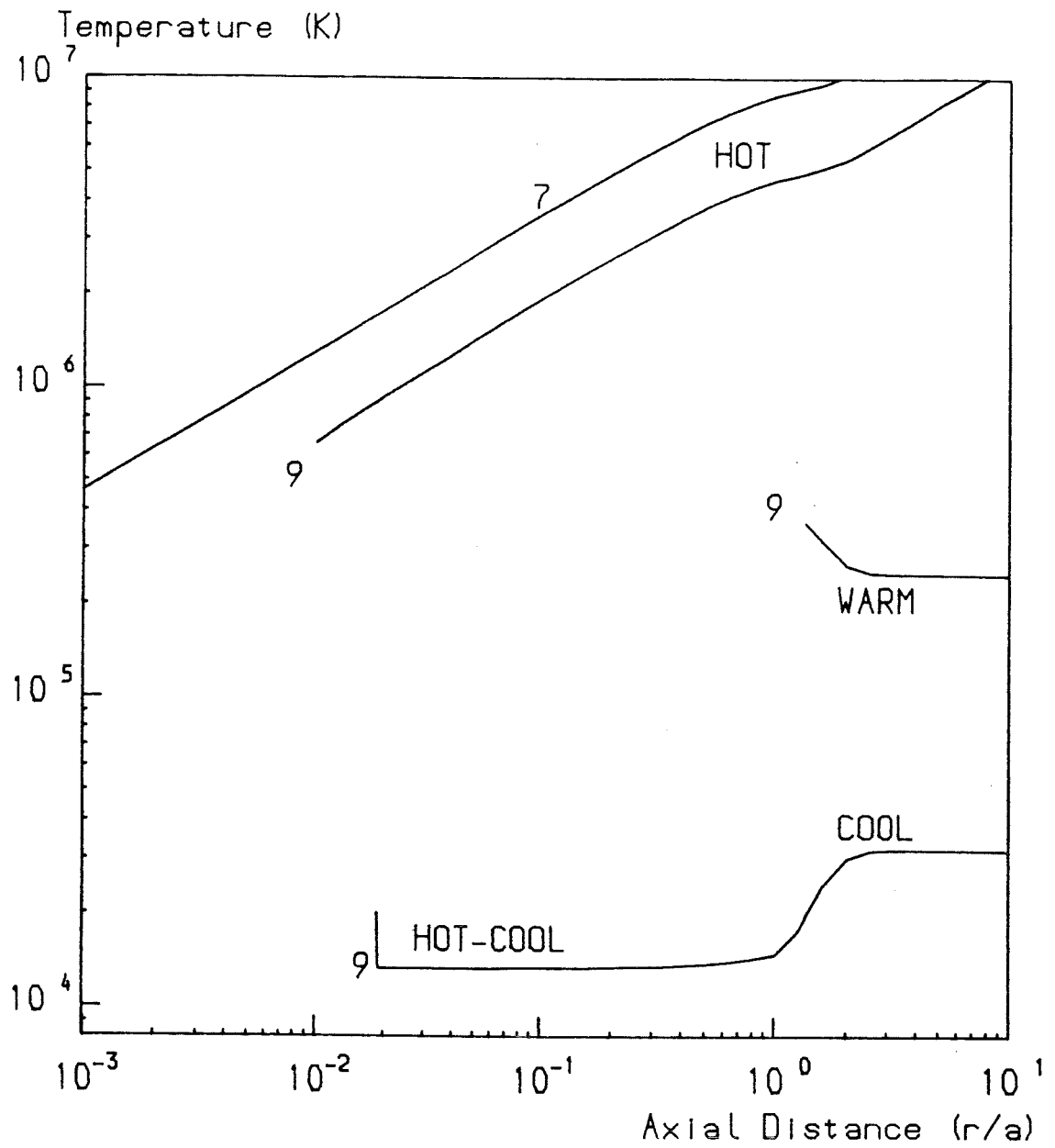


Figure 5.4c The variation of the summit temperature with height for the arcades generated by the contours 7 and 9 referred to in section 5.2. The division of the arcades into hot, warm, cool and hot-cool loops is noted.

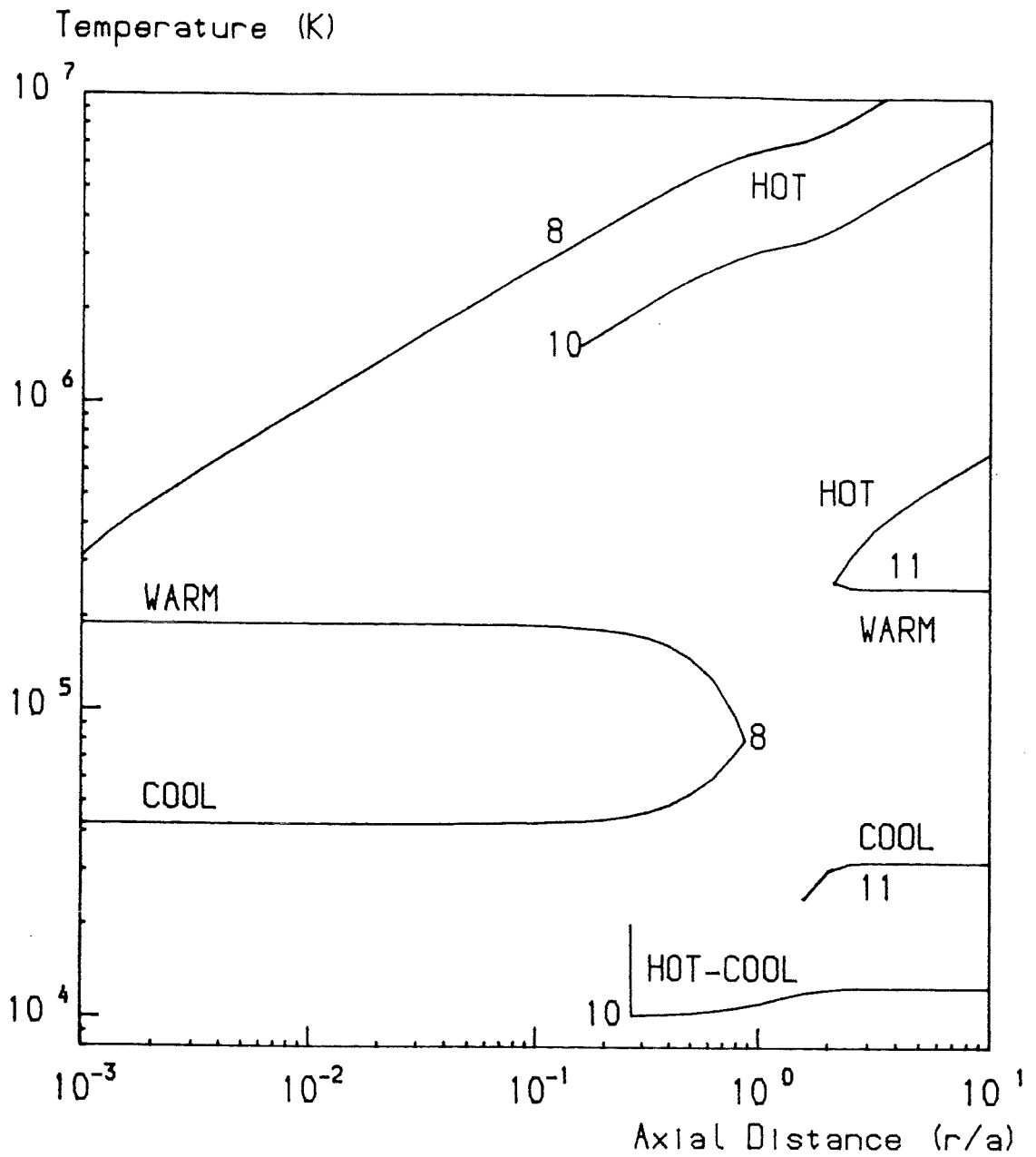


Figure 5.4d The variation of the summit temperature with height for the arcades generated by the contours 8, 10 and 11 referred to in section 5.2. The division of the arcades into hot, warm, cool and hot-cool loops is noted.

$10^{-3}a$ for contour 8. Considering contour 11, for radii (r) larger than $2.2a$ three solutions exist but as the axis is approached ($1.6 \leq r/a \leq 2.2$) only the cool solution exists (cf contour 4). Reducing r further (i.e. $r/a \leq 1.6$) causes the remaining solution to disappear. This contour uses an unrealistically low value of 'a' but it is included to highlight an interesting region of parameter space.

At various points in Figure 5.4, the summit temperature is found to change suddenly and non-continuously as solutions of a different regime are found or the existing regime no longer produces solutions. This can occur when h^*/p^* crosses one of the critical values 0.41 or 1.25 or, for a particular value of h^*/p^* , L^*p^* crosses a particular value - the minimum L^*p^* for a hot or hot-cool solution.

Dealing with the first case, for large L^*p^* (greater than about unity) $h^*/p^* = 1.25$ is the maximum value of that parameter for which warm or cool solutions may occur (Regions II, Vb on Figure 4.8. For L^*p^* less than about 30, $h^*/p^* = 0.41$ separates the area where cool solutions may occur (region Va) from the area where no realistic solutions may exist, while for larger L^*p^* (i.e. L^*p^* greater than about 30) it represents the boundary between the regimes of warm and cool solutions (region Vb) and that of hot-cool solutions (region IV). On both sides of this boundary hot solutions exist when L^*p^* is larger than 30. The value of r for which $h^*/p^* = 1.25$ is referred to as r_1 and the value of r giving $h^*/p^* = 0.41$ is denoted by r_2 .

The value of r/a corresponding to this boundary is

given by

$$\frac{r}{a} = \left[\log_e \frac{\frac{\dot{p}_c}{\dot{p}_e} - 1}{\frac{\dot{h}^*}{\dot{p}_e} \cdot \frac{1}{c} - 1} \right]^{\frac{1}{2}} \quad (5.19)$$

where c is set equal to 0.41 (for r_2) or 1.25 (for r_1) as required. This critical radius is dependent on the parameters \dot{h}^*/\dot{p}_e^* and \dot{p}_c^*/\dot{p}_e^* and is displayed in Figure 5.5a for $c=0.41$ (r_2 , full lines) and $c=1.25$ (r_1 , broken lines). There can only be a critical radius when $c < \dot{h}^*/\dot{p}_e^* < c \dot{p}_c^*/\dot{p}_e^*$, the critical radius tending to zero or infinity as those limits are approached.

For L^*p^* greater than about unity, r_1 divides the area of cool or warm solutions from the area where only hot solutions exist. For $L^*p^* \geq 30$, r_2 divides the area of cool or warm solutions from that of hot-cool solutions; for $L^*p^* \leq 30$ it divides the area of cool solutions from the area where no realistic solutions exist.

The minimum r/a for a hot (or hot-cool) solution (corresponding to the contour crossing a diagonal line in Figure 5.3) cannot be expressed as a simple function of the parameters. It depends on all three parameters a , \dot{h}^*/\dot{p}_e^* and \dot{p}_c^*/\dot{p}_e^* but the exact value must be calculated numerically. The minimum r for a hot-cool solution will henceforth be referred to as r_3 while the minimum length for a hot solution will be known as r_4 . The hot (or hot-cool) loop of minimum loop radius r_4 or r_3 has zero temperature gradients

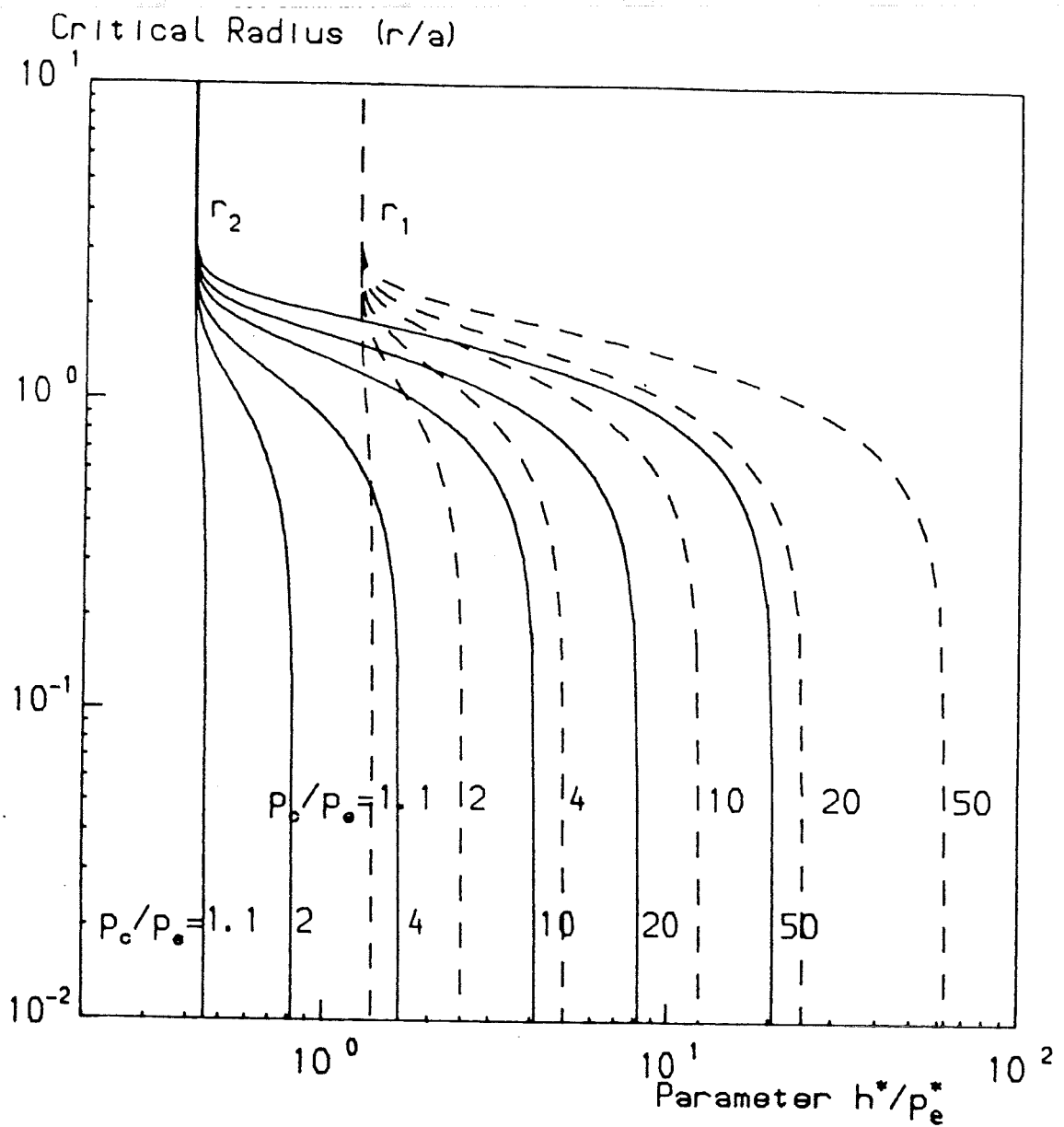


Figure 5.5a The variation of r_1 and r_2 with p_c/p_e , h^*/p_e^* and a where r_1 is the maximum axial distance at which warm or cool loops can exist ; when $r = r_1$, h^*/p^* is equal to the critical value 1.25. r_2 is the axial distance of the boundary where, for large L^*p^* , the cool or warm loops are separated from the hot-cool loops, the hot-cool loops lying nearer the axis. Hot loops can exist on both sides of this boundary. For low L^*p^* r_2 is the minimum axial distance for cool loops. When $r = r_2$, h^*/p^* equals the critical value 0.41

at the footpoints and is referred to as 'thermally isolated' (Basri et al (1979), Vernazza, Avrett and Loeser (1981)).

The values of r_3 and r_4 are displayed on Figures 5.5b and 5.5c, respectively. In each case r_3 (or r_4) is plotted as a function of h^*/p_e^* with the full curves representing $a = 5 \times 10^6$ m and the broken curves $a = 5 \times 10^7$ m. Curves for six values of p_c^*/p_e^* (1.1, 2, 4, 10, 20, 50) are shown.

The critical radius, r_4 , shown in Figure 5.5c refers to the point of loss of hot solutions as r/a is decreased in contours 4, 5, 6, 9, 10, and 11, i.e. r_4 separates the regime of hot solutions from the regime of no realistic solutions. The radius r_3 , shown in Figure 5.5b, refers to the loss of hot-cool solutions as r/a is decreased using contours 5, 6, 9 and 10. Thus r_3 separates the regime of hot solutions and hot-cool solutions from that of hot-solutions only.

The reason for the curves stopping at low values of r/a in Figures 5.5b and 5.5c is that for particular values of a and p_c^*/p_e^* , if h^*/p_e^* is raised high enough, hot solutions (or cool solutions onto which the hot solutions join smoothly) exist for all values of r/a and hot-cool solutions for none (contours 1, 2, 3, 7). It can be seen that as h^*/p_e^* is increased, r_{crit} decreases and hot (or hot-cool) solutions can be found for a wider range of r/a . Where it exists, the minimum radius for a hot-cool solution is about twice that for a hot solution.

Instead of plotting r_4/a as a function of h^*/p_e^* it is instructive to plot r_4 as a function of a for different values

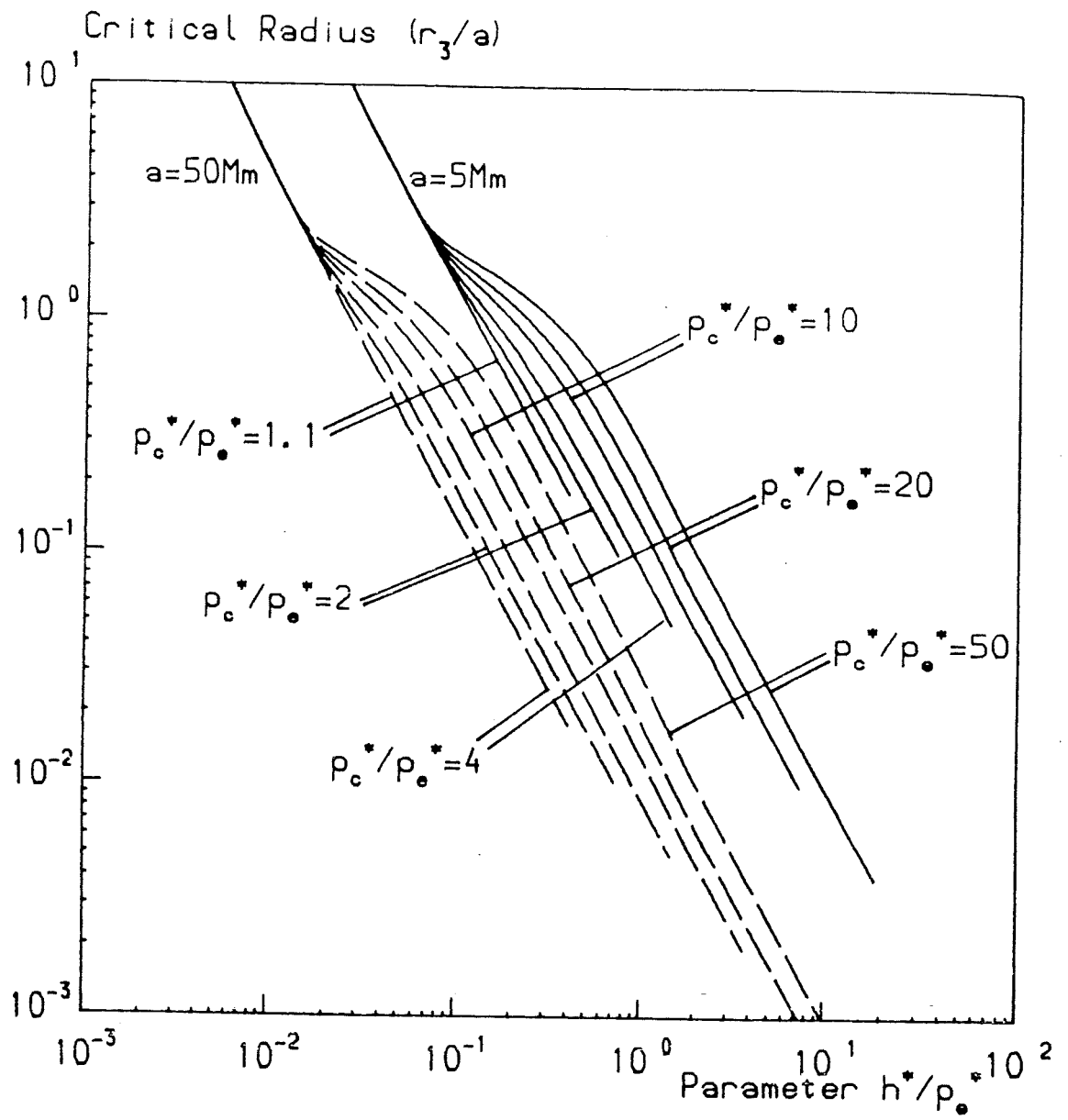


Figure 5.5b The variation of r_3/a with h^*/p_e^* where r_3 is the minimum axial distance for which hot-cool loops can exist for h^*/p_e^* less than 0.41.

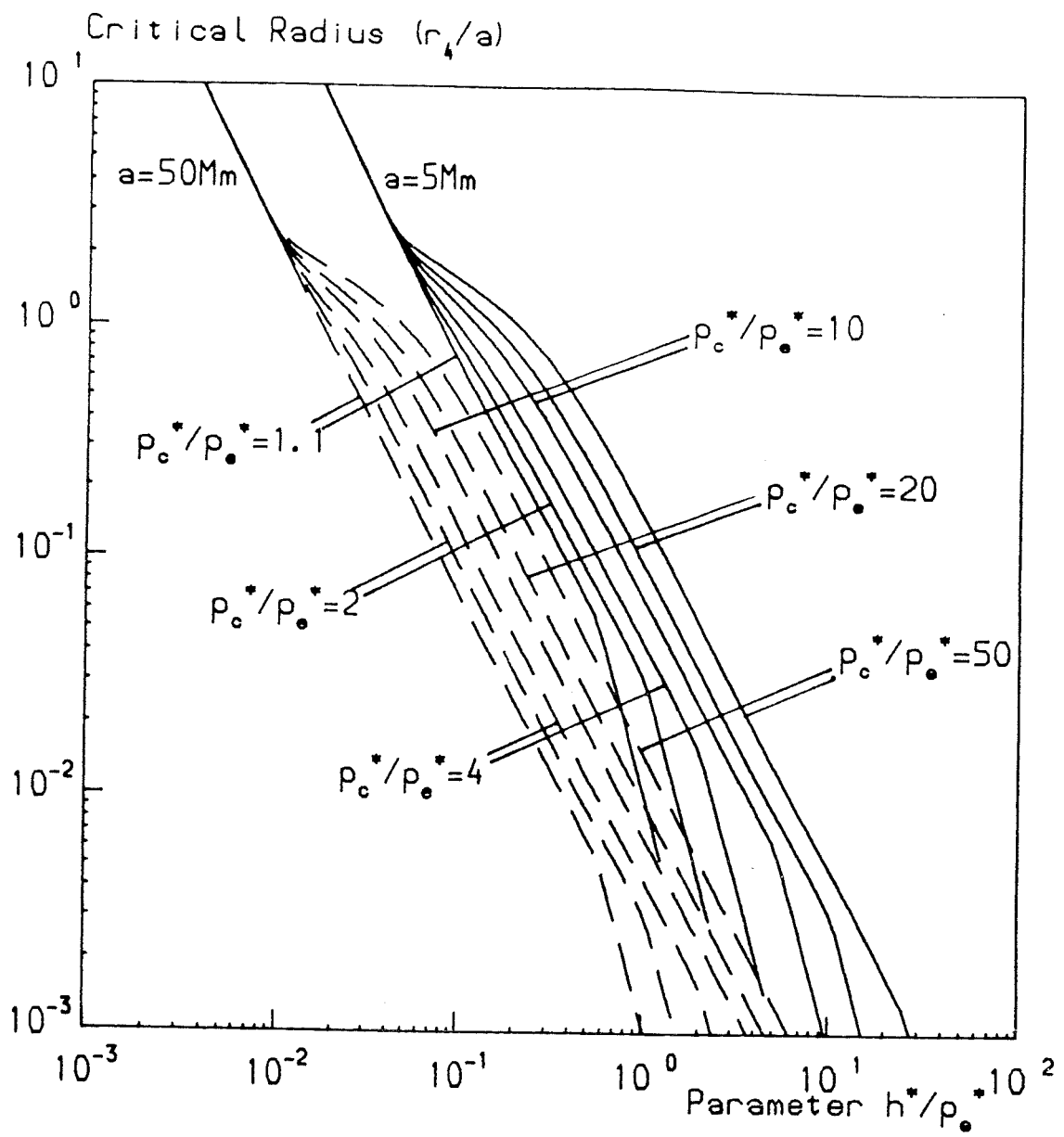


Figure 5.5c The variation of r_4/a with h^*/p_0^* where r_4 is the minimum axial distance for which hot loops can exist for h^*/p_0^* less than 1.25.

of the parameters h^*/p_e^* and p_c^*/p_e^* (Figure 5.5d). As can be seen from Figure 5.5c, r_4 is more dependent on h^*/p_e^* than it is on p_c^*/p_e^* . However from Figure 5.5d it can be seen that r_4 is almost independent of a for values of a in excess of 10^6 m. For extremely low values of h^*/p_e^* and higher values of p_c^*/p_e^* (contours 6, 10) the variation with a becomes more significant when a is in the range 10^6 m to 10^7 m. The case where $h^*/p_e^* = 3.0$ and $p_c^*/p_e^* = 1.1$ is not included as h^*/p_e^* is never less than 1.25 and there is no lower limit to the radius of hot loops.

Figure 5.6 shows the how the temperature (plotted on the vertical axis) varies in two dimensions within the various arcades.

Figure 5.6a shows the temperature profile for contour 1. It can be seen that for all loops, the hottest part is at the summit and also that on receding from the axis the temperature increases. On the vertical axis, the temperature increases only slowly around $r/a = 1$, corresponding to the 'kink' found at this distance in Figure 5.4a. Figure 5.6b shows the same information for contour 2. This plot is very similar to 5.6a except that the temperature varies in a more uniform manner on the vertical axis.

Figure 5.6c which refers to contour 3, is quite different. A temperature reversal has been shown to exist on the vertical axis (Figure 5.4a). When investigated in two dimensions, this reveals itself as a thermal island, an area where the temperature decreases in all directions.

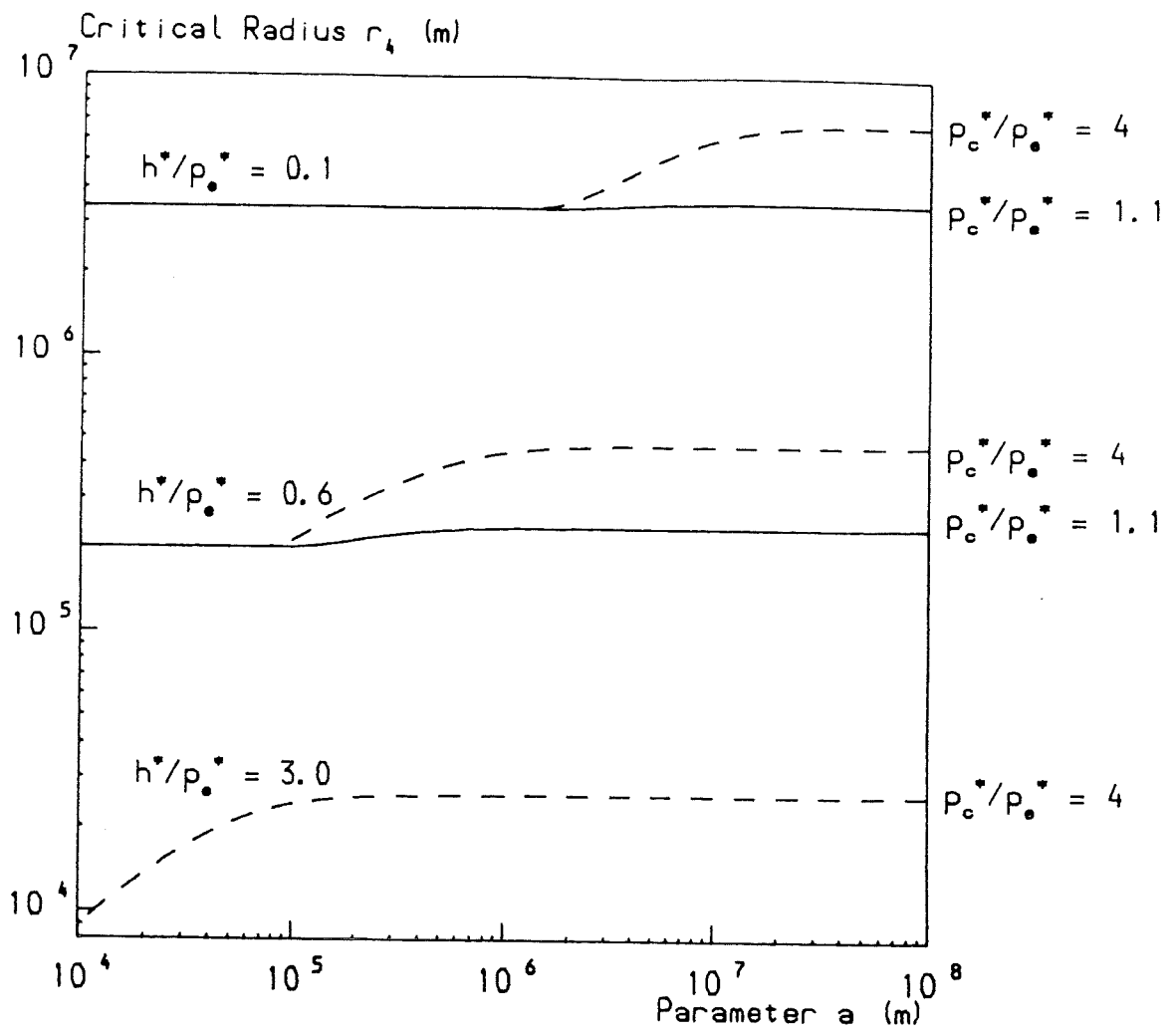


Figure 5.5d The variation of r_4 with a for various values of the parameters h^*/ρ_e^* and ρ_c^*/ρ_e^* . The curves for $\rho_c^*/\rho_e^* = 1.1$ are shown in full and those for $\rho_c^*/\rho_e^* = 4$ are shown in broken.

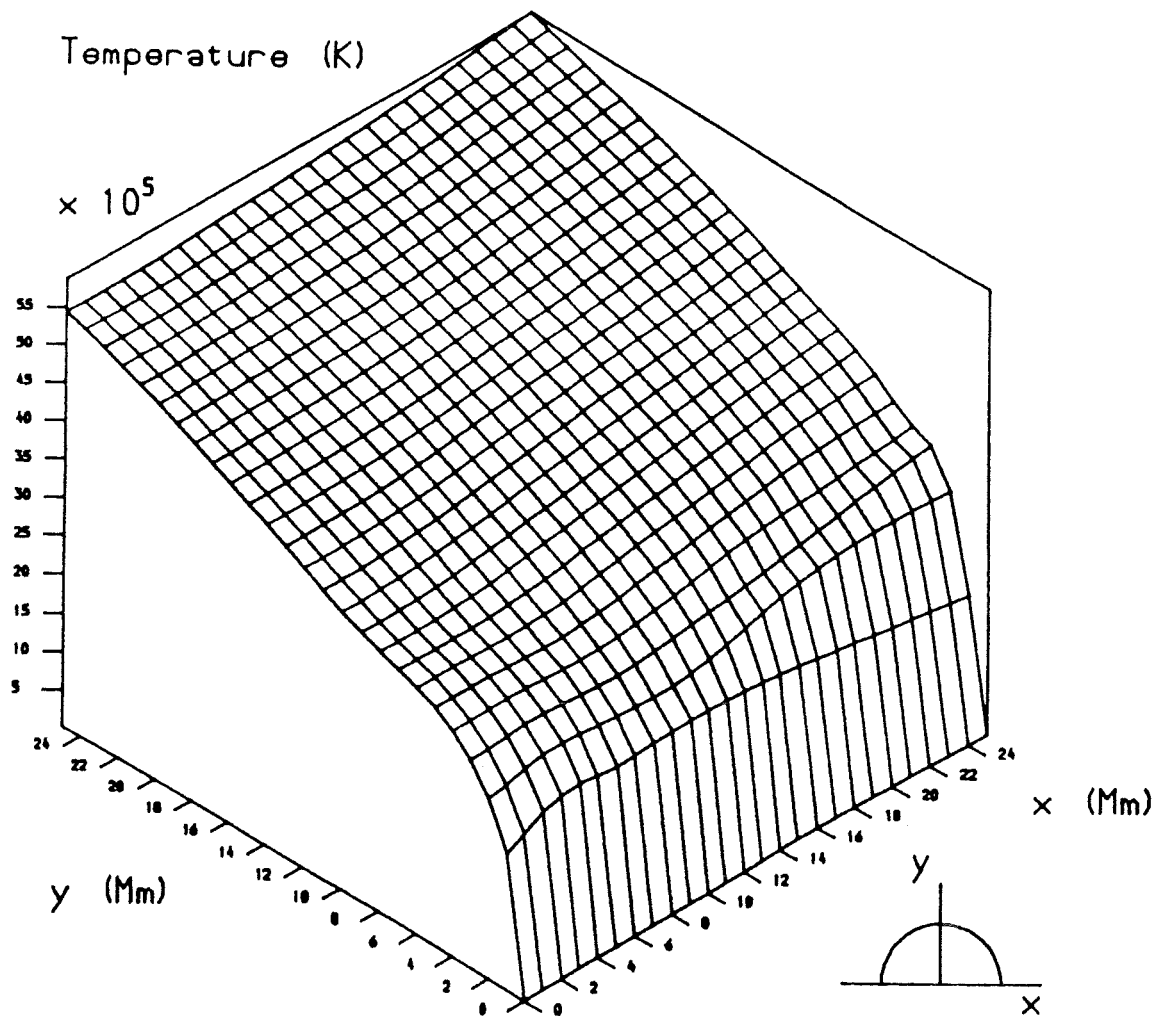


Figure 5.6a The temperature profile in two-dimensional space, for the arcade generated by contour 1.

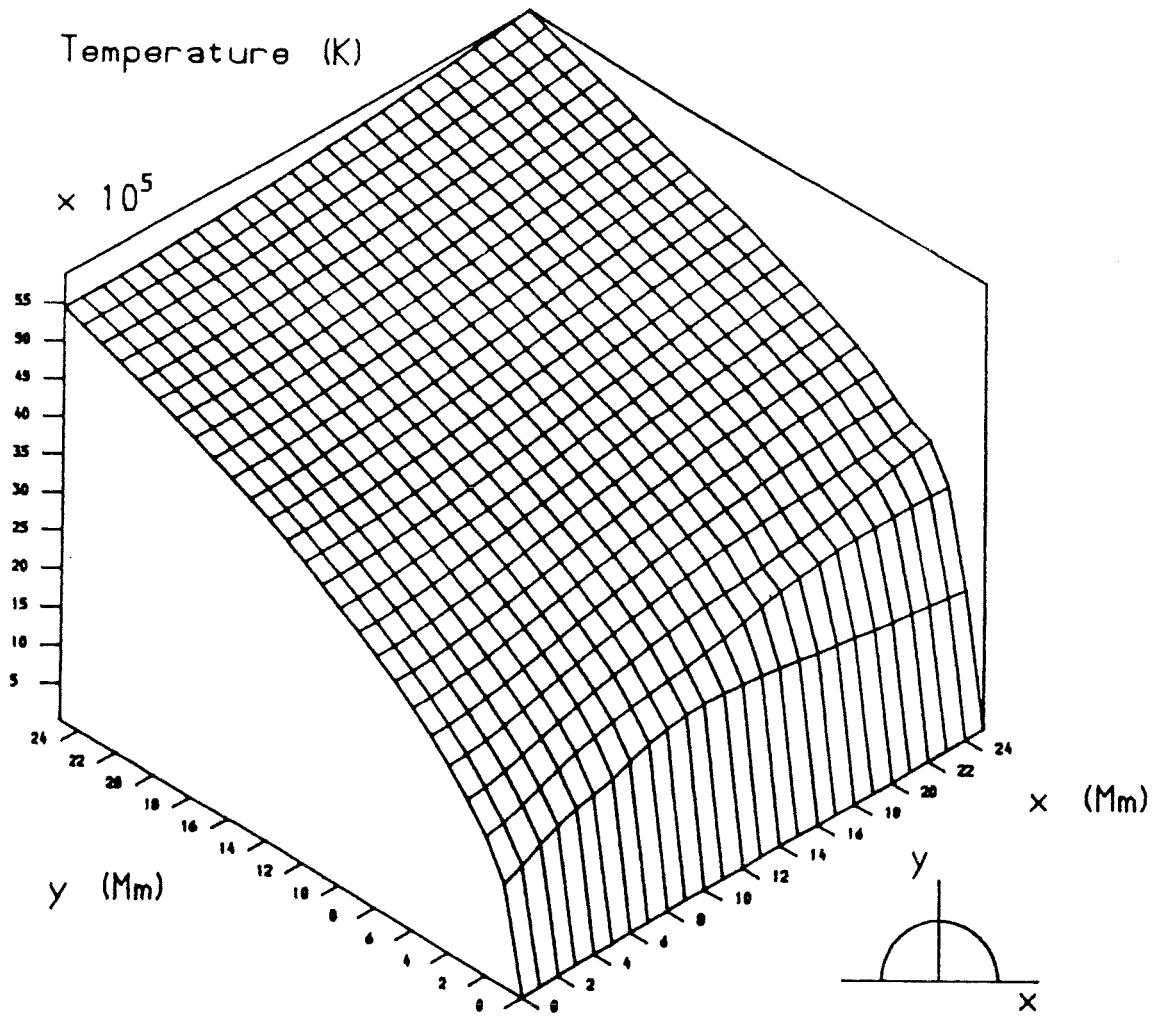


Figure 5.6b The temperature profile in two-dimensional space, for the arcade generated by contour 2.

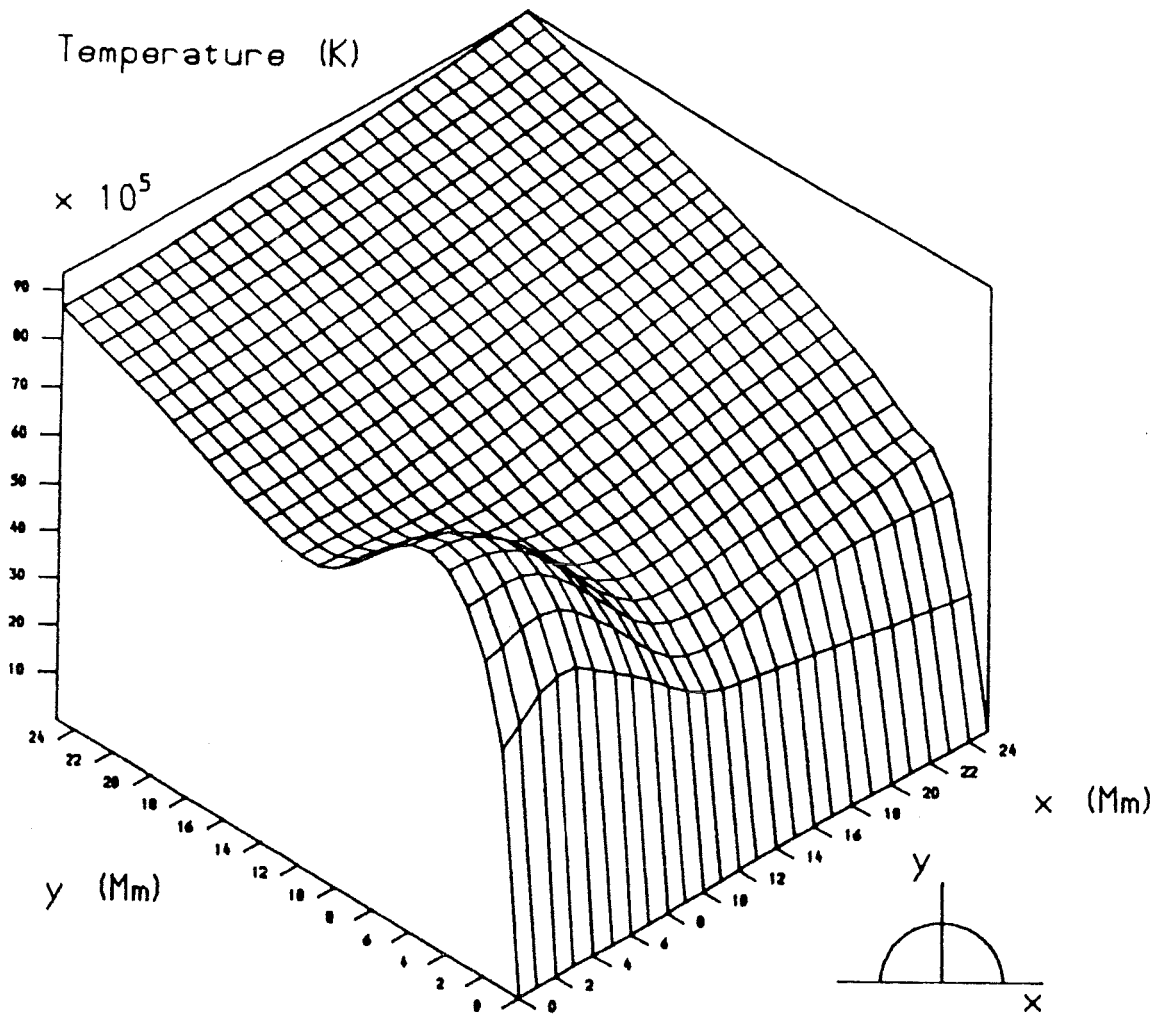


Figure 5.6c The temperature profile in two-dimensional space, for the arcade generated by contour 3.

When a , p_c^*/p_e^* and h^*/p_e^* take on the values which generate contour 4, there are several different possibilities. For r/a greater than 0.9 only hot solutions exist and for r/a less than 0.005 only cool solutions exist. However, in the intermediate region the loops can be either hot, warm or cool. If the loops in this intermediate region are cool, then Figure 5.6d applies. For $r/a > 0.9$ the temperature increases with height above the photosphere and the picture is similar to that shown in Figure 5.6a. A temperature discontinuity occurs when $r/a = 0.9$ for all parts of the loop except those closest to the footpoints. Inside this area the plasma is at a much cooler temperature which does not vary much from point to point. The situation when the loops in the intermediate area are warm is illustrated in Figure 5.6e. The region $r/a > 0.9$ is unchanged from Figure 5.6d but closer to the axis the picture changes. Most of the area $r/a < 0.9$ lies at the temperature of the neutral point T_c (between 20 000 K and 80 000 K). Near the footpoints the temperature is (equal to 20 000 K) and near the summits the temperature is higher.

For contour 5 there are again several possibilities. When $r/a > 1.4$, the loops can be hot, warm or cool. However, if it assumed that the temperature in this external region is at the hot coronal value the hot solution is the most meaningful. For r/a lying in the range 0.2 to 1.4 the solutions can be either hot, or hot-cool. Figure 5.6f shows the temperature profile when hot loops exist in the external region and hot-cool loops exist in the intermediate area. It can be seen that there is a temperature discontinuity at $r/a = 1.4$ for all parts of the loop except

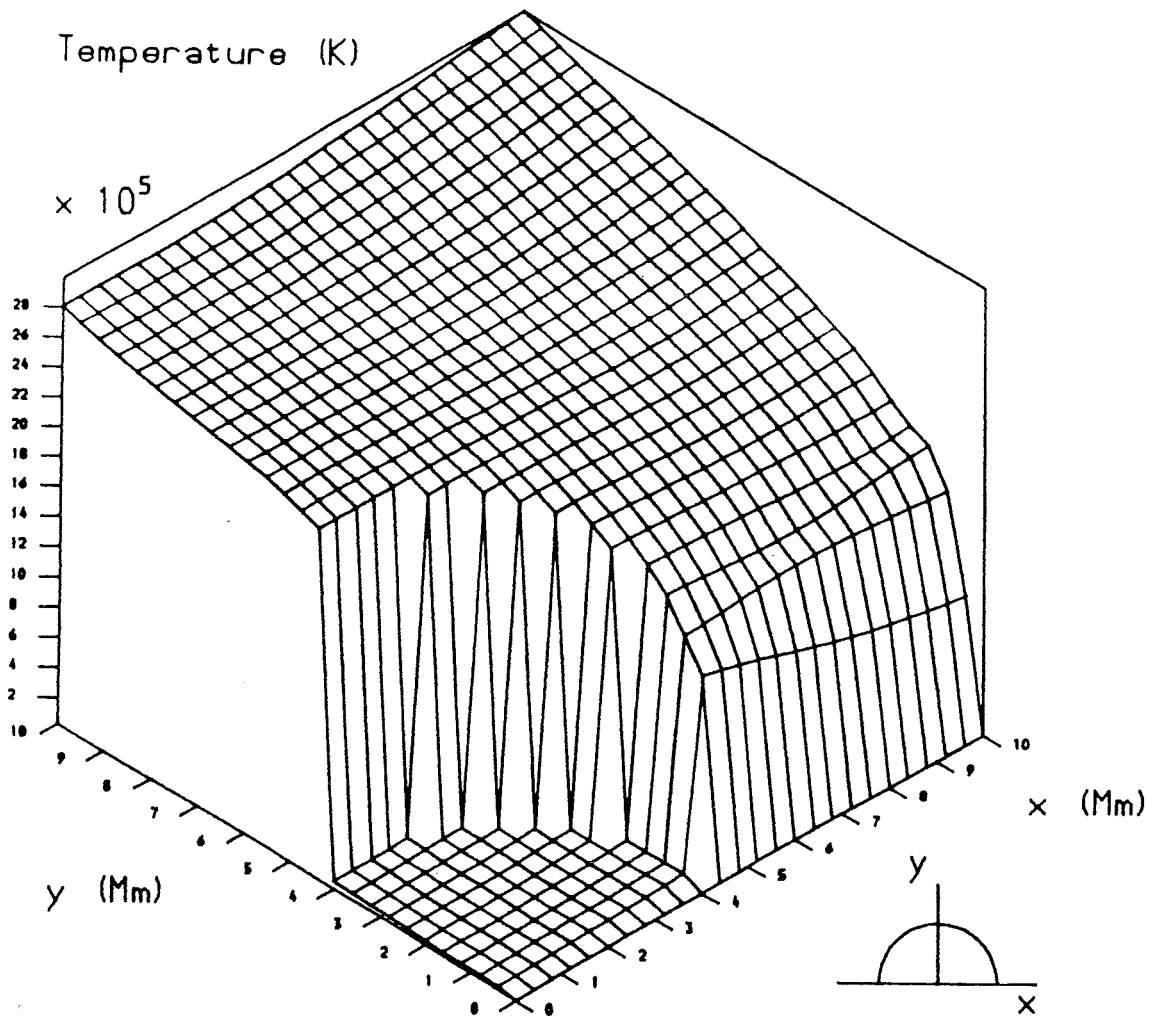


Figure 5.6d The temperature profile in two-dimensional space, for the arcade generated by contour 4 with cool loops in the region $0.005 < r/a < 0.9$.

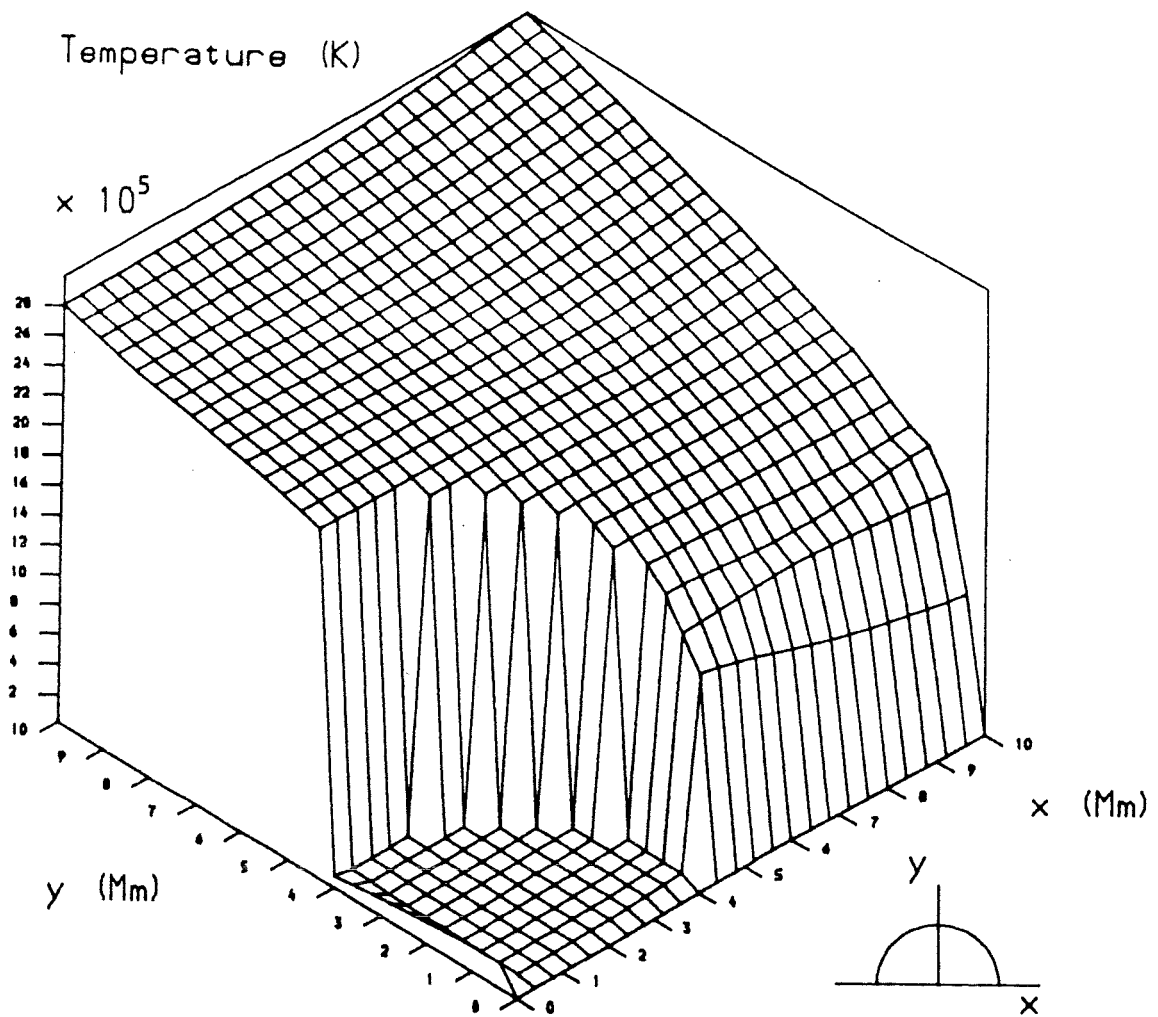


Figure 5.6e The temperature profile in two-dimensional space, for the arcade generated by contour 4 with warm loops in the region $0.005 < r/a < 0.9$.

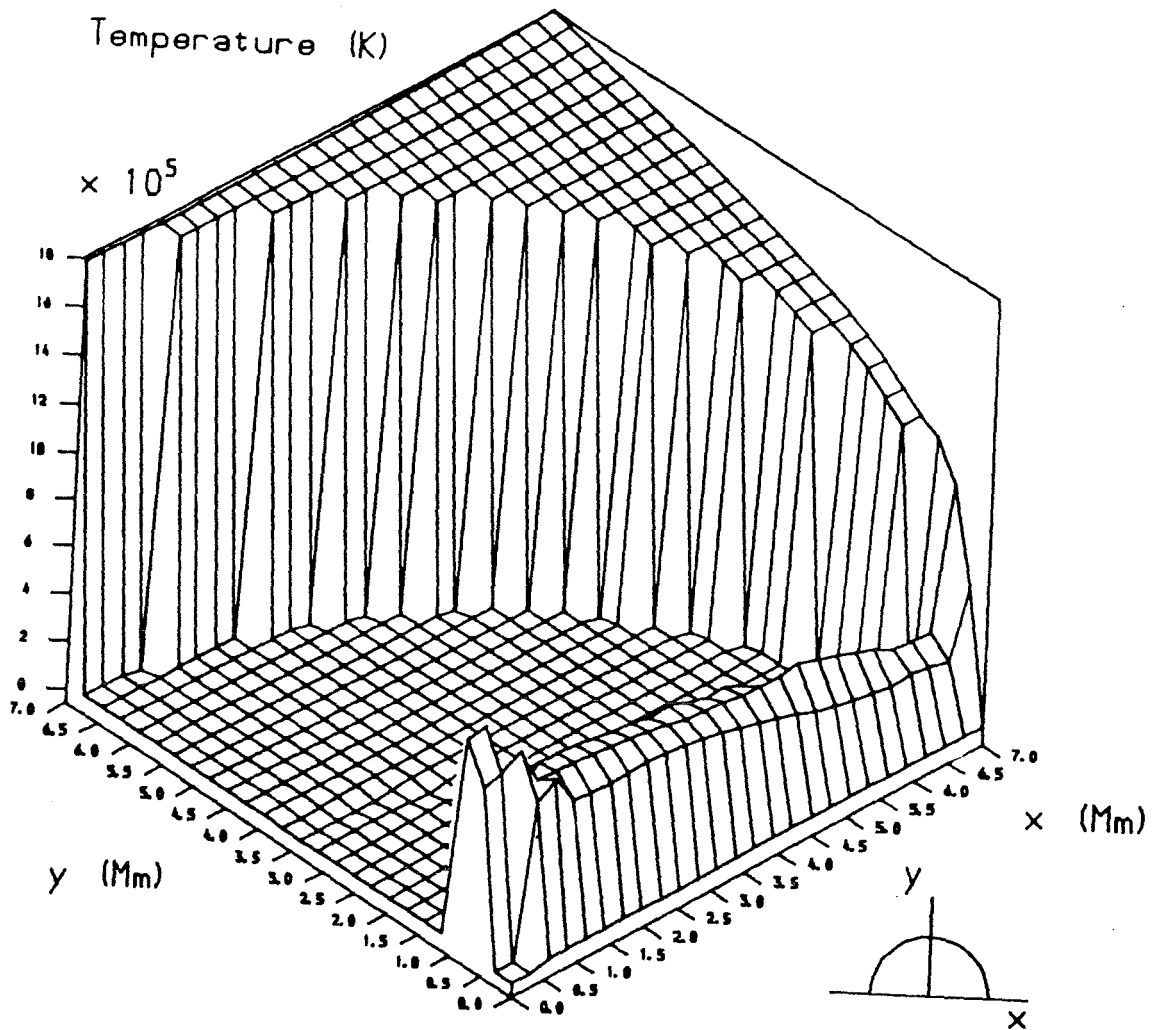


Figure 5.6f The temperature profile in two-dimensional space, for the arcade generated by contour 5 with hot loops for $r/a > 1.4$ and hot-cool loops when $0.2 < r/a < 1.4$.

the part near the footpoints. Outside this discontinuity, the temperature is monotonically increasing with height. When $r/a < 1.4$, the loop temperature increases with height in the vicinity of the footpoint but soon decreases to temperatures roughly comparable with those of the footpoints. The reason for the summit temperature for those hot-cool loops being prevalent over a regime that extends far from the summit is that for all those loops except those with the minimum length for a hot-cool loop, the contour on the phase plane passes very close to the neutral point T_c , and thus this temperature extends over a longer portion of loop. When r/a lies between 0.1 and 0.2, hot solutions exist and there is a temperature discontinuity on the boundary between them and the hot-cool loops. This discontinuity is most marked near the loop summits where the hot-cool loops are much cooler, but nearer the footpoints the hot-cool loops are at temperatures not markedly different from those of the hot-loops. From Figure 5.6f it can be seen that solutions do not exist nearer the axis than about $r/a = 0.1$; a value of zero has been shown for the temperature. The area between $r/a = 0.2$ and $r/a = 1.4$ is a candidate for prominence formation (e.g. Ballester and Priest 1989). A drawback is that the temperature to either side of the loop summits is of a similar temperature to that of the summits. This suggests that any prominence forming would be a wide structure rather than a long thin filament.

Figure 5.6g considers the case where instead of there being hot solutions for $r/a > 1.4$, there are warm solutions instead. Of course, such warm solutions will not match smoothly onto the hot corona but this case is included to

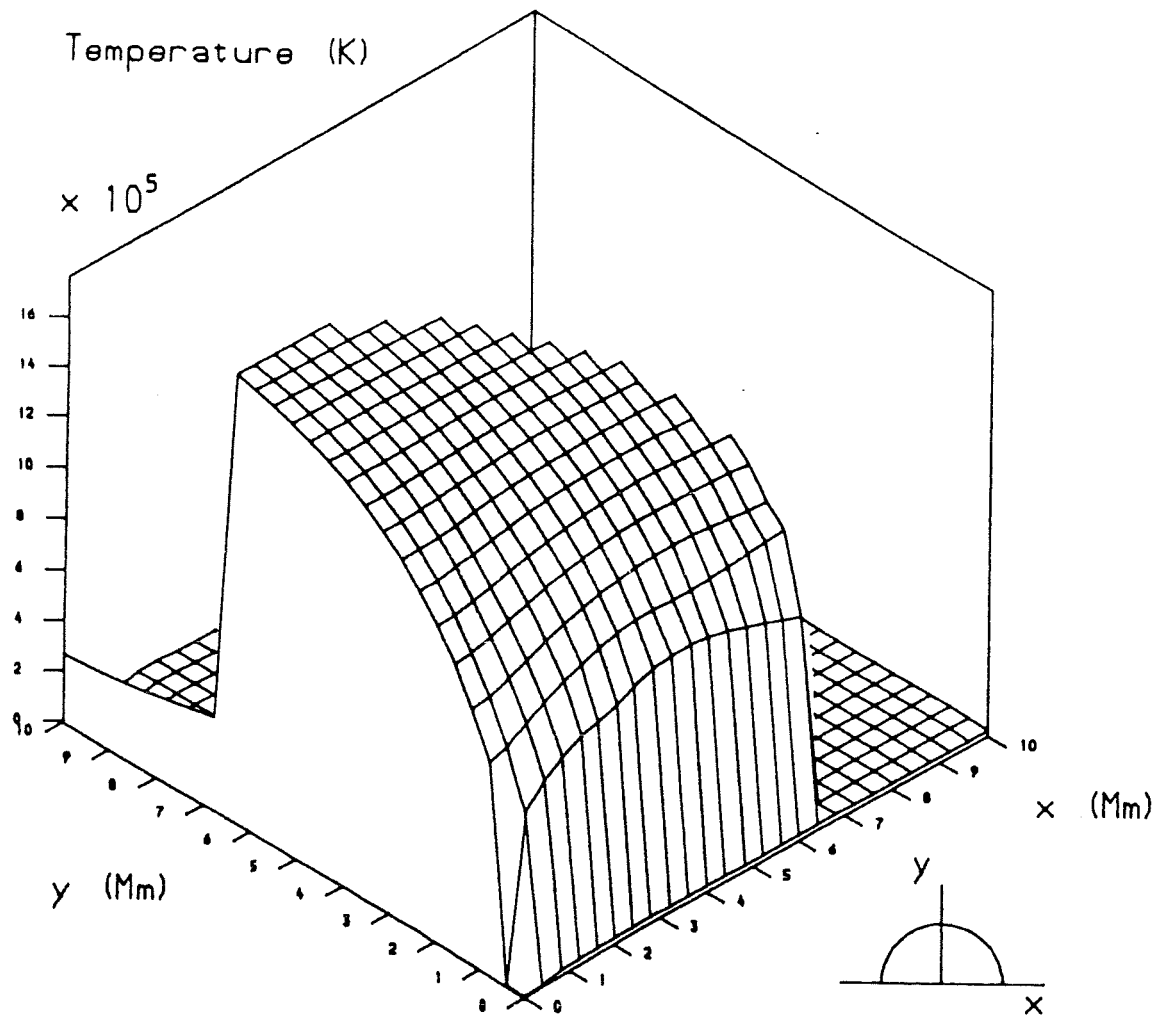


Figure 5.6g The temperature profile in two-dimensional space, for the arcade generated by contour 5 with warm loops for $r/a > 1.4$ and hot loops for $0.1 < r/a < 0.9$.

highlight an interesting region of parameter space. It is also assumed that for $0.1 < r/a < 1.4$ the loops are hot. In this region the temperature increases with height above the photosphere. In the outer region however, the temperature is between 20 000 K and 80 000 K except near the footpoints (where it is equal to 20 000 K) and the summits (where it is higher).

Contour 6, like contour 5 gives both hot and hot-cool solutions over a particular range of r (in this case $r/a > 1.6$) but unlike contour 5 there is no outer region giving a choice between hot, warm and cool solutions. For smaller r ($0.9 < r/a < 1.6$) only hot solutions exist and for $r/a < 0.9$ no realistic solutions exist. The hot solutions can match smoothly onto an outer hot corona and Figure 5.6h gives the temperature profile for an arcade which contains hot loops for $r/a > 0.9$. For the area where $r/a > 0.9$, the temperature increases with height. Where $r/a < 0.9$, the temperature function has been set equal to zero as no equilibrium exists.

Figure 5.6i which refers to contour 7 is very similar to Figure 5.6a. As the temperature profiles for contours 8, 9, and 10 would be very similar to those for contours 4, 5, and 6, respectively, they are not shown.

The temperature profile when the parameters p_c^*/p_e^* and h^*/p_e^* take on the profiles that are generated by contour 11 is given in Figure 5.6j. There are three ranges of r which give different results here. When $r/a > 2.1$, the temperature increases as one moves away from the axis, both in a vertical and a horizontal direction. At $r/a = 2.1$, a

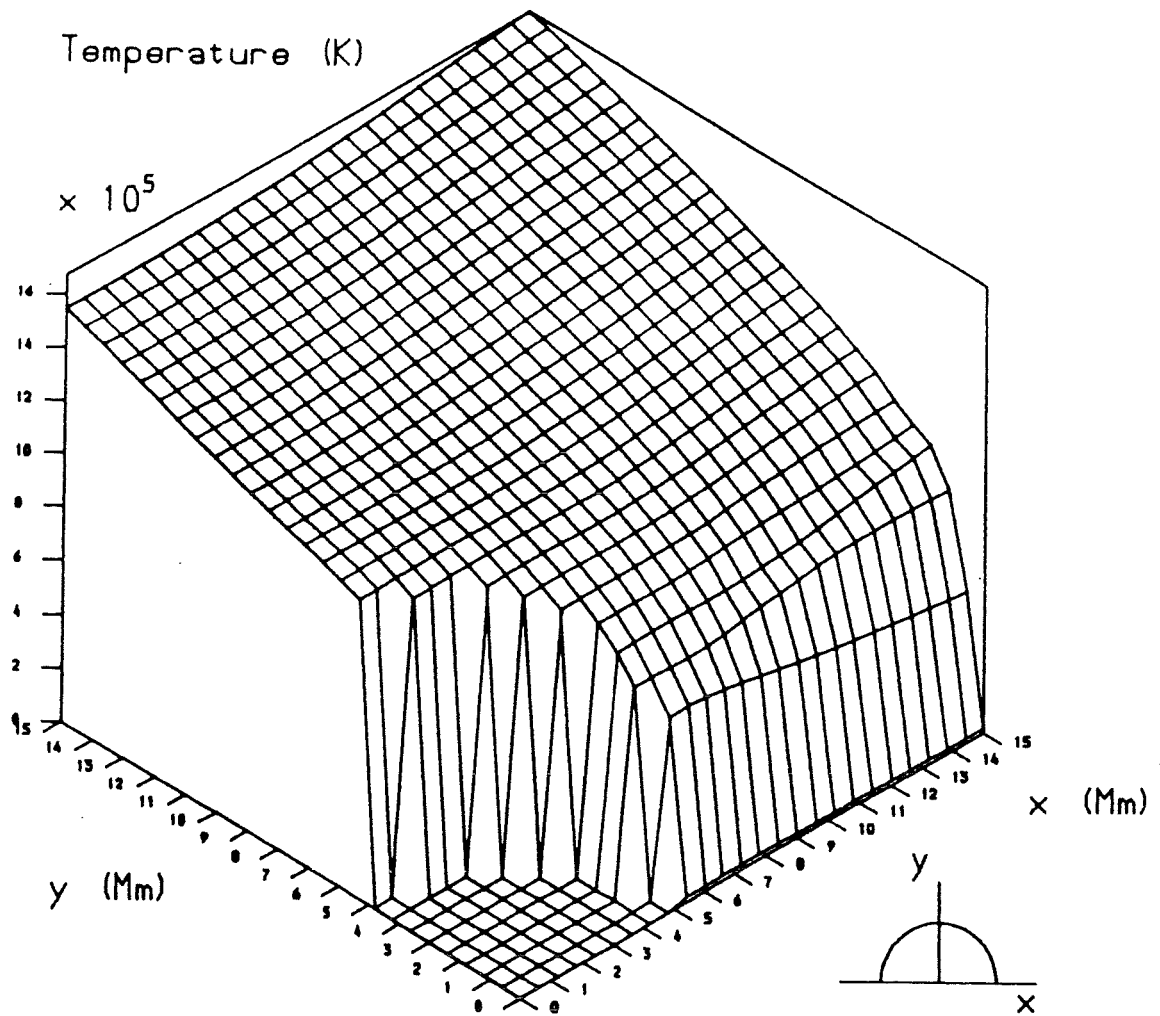


Figure 5.6h The temperature profile in two-dimensional space, for the arcade generated by contour 6 with hot loops for $r/a > 0.6$.

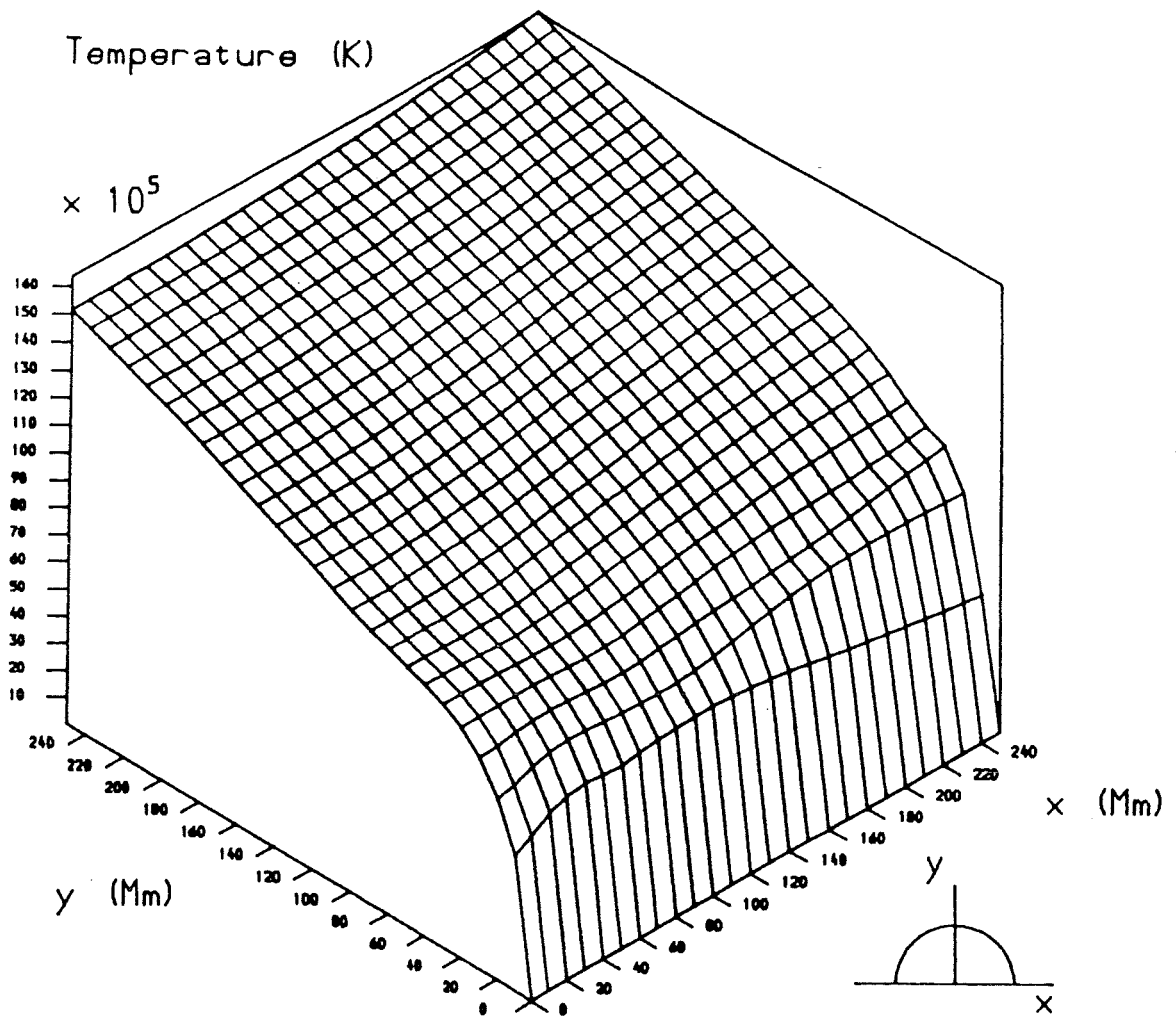


Figure 5.6i The temperature profile, in two-dimensional space, for the arcade generated by contour 7.

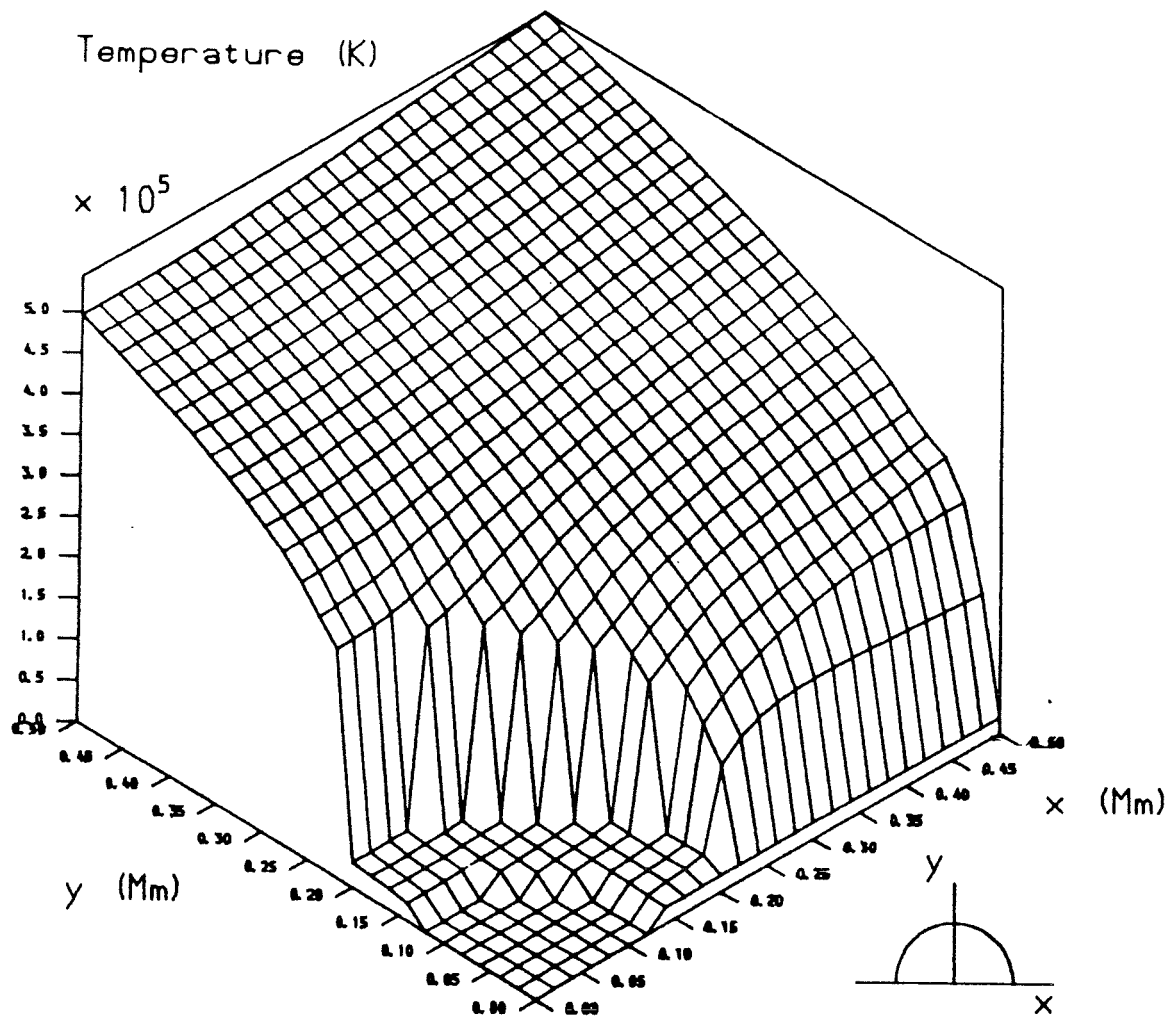


Figure 5.6j The temperature profile in two-dimensional space, for the arcade generated by contour 11 with hot loops when $r > 2$ and cool loops when $1.3 < r/a < 2$.

temperature discontinuity occurs and for r/a in the range 1.3 to 2.1 the temperature is roughly constant along each loop. For $r/a < 1.3$ no realistic solutions exist and so the temperature function has been set equal to zero.

For most of the cases above it has been assumed that the arcade joins onto the hot corona for large r , and this has been achieved by making use of the hot solutions. Some of the temperature profiles shown denote temperatures in excess of that of the solar corona (e.g. Figure 5.6i where the outermost fields have temperatures of $6-8 \times 10^6$ K but those occur for large r where the simple form taken for the magnetic field (5.9) no longer applies.

For small r , many of the contours enter a region where no realistic solutions exist and the temperature function has been set equal to zero. It is not obvious what happens in this area. It is possible that what goes on affects the area outside.

5.4 Variation of Parameters

So far several discrete contours have been considered but it is instructive to consider what would happen if a contour were to gradually change its shape. It is assumed that as the situation changes the pressure and magnetic field are still described by equations (5.5) and (5.9). The contour shape and position depend on the three parameters a , h^*/p_e^* and p_c^*/p_e^* . If a were to increase or decrease the whole contour would move to the right or left respectively (e.g. starting with contour 1 and increasing a gives contour

7). An increase in h^*/p_e^* can be caused either by an increase in h^* or a decrease in p_e^* . For h^* to increase or decrease would cause the whole contour to move up or down (e.g. differences between contours 1, 4, 5 and 6). (Of course, as h^* represents the unknown heating function, it is not obvious how such a change would occur). For p_e^* to change with p_c^* remaining constant would change the two parameters h^*/p_e^* and p_c^*/p_e^* and the right hand end of the contour would move up or down as p_e^* is decreased or increased. A change in p_e^* would mean a change in the plasma pressure in the corona. Finally, an increase in p_c^* with p_e^* remaining constant shifts the left hand end of the contour downwards (e.g. contour 2 changing to contour 1).

In most cases a slight change in the contour will only affect the thermal structure to a minor extent but there are a small number of cases where a small change in the contour can drastically affect the thermal structure.

Varying a will not cause any major changes in the thermal structure except in a few cases where a is unrealistically small.

Starting from contour 4 with warm solutions between r/a equal to 0.005 and 0.9, and decreasing a will initially cause only minor changes. One effect is that the region of warm solutions decreases and when a has decreased by a factor of about 100 the region of warm solutions disappears and only cool solutions remain.

Something similar happens to contour 5 (with hot-cool

loops present for r/a between 0.2 and 1.4) as a is decreased. If a is decreased by a factor of 10, the hot-cool solutions can no longer be present. If the energy is not available to heat the plasma to the temperature of hot loops, then non-equilibrium will occur.

Both the cases mentioned above, however, occur only when a is too small to be physically realistic.

Changes to h^*/p^* caused by changes in h , p_c^* or p_e^* can also lead to solutions being lost. Starting with contour 5 or 9 with hot-cool loops present, and increasing h^*/p^* near the axis, either by increasing h^* or by decreasing p_c will cause the left hand end of the contour to approach the line $h^*/p^* = 0.41$. When h^*/p^* reaches this value, the hot-cool solutions can no longer be present. If the energy is not available to heat the plasma to the temperature found at the top of the corresponding hot loop, no equilibrium exists.

Similarly, starting with contour 4 or contour 8, with warm (or cool) solutions present and increasing h^*/p^* near the axis towards and past 1.25 (or decreasing it towards and past 0.41) causes the warm (or cool) loops no longer to be possible. Again if the energy is not available to form a hot loop, an equilibrium is not possible.

Other possibilities exist for perturbations to the contours causing non-equilibrium but those would entail starting from contour 5 or 9 with warm solutions for large r/a . An increase or decrease in h^*/p^* for large r/a so that it is no longer in the range 0.41 to 1.25, will cause warm

solutions no longer to be present. However, as these warm loops do not join onto the hot corona, and warm loops are thought to be unlikely due to the minimum in the differential emission measure, it is hard to see this configuration occurring to start with.

5.6 Conclusions

The thermal structure of cylindrically symmetric arcades have been found by solving the equations of thermal equilibrium along each loop in the arcade. Assuming that the plasma pressure and magnetic field are as given by equations (5.5) and (5.9), there are three parameters which determine the possible thermal structures.

Arcades divide into several forms. For high values of the coronal heating (or low plasma pressure in the arcade), the temperature increases with height and with distance from the main axis of the arcade. If the variation of plasma pressure in the arcade is high enough, a thermal island (an area where the temperature decreases in all directions) can form. In all cases mentioned above the temperature varies continuously at all points.

When the coronal heating is lower, (or the pressure higher) a thermal discontinuity must occur. At large axial distances hot loops are present and close to the axis cool loops are present (see contours 4 and 8). A discontinuity can occur either very close to the axis or at a greater distance from it or there can be a discontinuity at each of the two aforementioned points. The loops in the annulus between the

two potential discontinuities will be hot, cool or warm respectively. If the loops are cool, the plasma vertically above the main axis will be at temperatures between 20 000 K and 80 000 K, temperatures not significantly different from those of prominences and at heights consistent with those of prominences.

When the coronal heating term is reduced further no equilibrium solutions exist near the axis (subject to the constraint that the footpoint temperature gradient is not negative). This is consistent with the findings of Priest and Smith (1979) that equilibria cannot be found for the whole arcade when the pressure is too high or the coronal heating too low. Contours 5 and 9 are the relevant ones. It is not obvious what happens in this area close to the axis. It is possible that the loops in the area are thermally active. The possibility exists for the lack of equilibrium to change the structure in the outer regions but this possibility will be ignored. The inner region is small (about 1 Mm across or smaller for values of h^*/p_e^* greater than about 0.5 and p_c^*/p_e^* less than about 4) compared to the size of the arcade.

Hot loops can exist at all distances from the axis in excess of the radius of the area for which equilibrium solutions do not exist. This would give a thermal structure similar to those at a higher h^*/p_e^* except for the central area. Instead of there being hot loops everywhere there is an annulus where hot-cool loops can exist instead. This would give plasma at temperatures less than 20 000 K above the main axis, a situation not inconsistent with a prominence.

The problem regarding a prominence in this case and the previous case is that the summit temperature is prevalent over a large proportion of the loop and not just a small part at the summit. This discounts the possibility of a cool thin prominence surrounded by hot material on both sides. However, if a condensation were to occur at the cool summit and a dip were to occur, the resulting configuration would be a variation on the Kippenhahn-Schluter (1957) type of prominence but with cool rather than hot material at the sides.

An alternative is that the arcade contains cool loops (contours 4 or 8) or hot-cool loops (contours 5 or 9) for a particular value of z (the longitudinal coordinate) and hot loops for values of z slightly greater and less. This would give a prominence aligned parallel to the field lines.

For even smaller values of the parameter h^*/p_e^* (contours 6 and 10) the internal region where no equilibria are possible expands (see Figure 5.5d). Another change is that the external region where hot-cool solutions are no longer possible is not present. As the temperature at large distances from the arcade has to join onto the temperature of the hot corona, it is difficult to see the hot-cool loops being present unless at some arbitrary distance from the axis there is a changeover from hot-cool to hot loops.

It is possible to change the thermal structure of the arcade by varying one or more of the parameters a , h^*/p_e^* and p_c^*/p_e^* . In certain areas it is possible for the contour

to evolve to a configuration where cool, warm or hot-cool loops no longer become possible. If there is not enough energy to heat the plasma to the temperature of the corresponding hot loop, no equilibria can exist and the plasma will enter some other configuration. It is possible that plasma may then condense to form a prominence.

CHAPTER SIX - THERMAL EQUILIBRIUM OF ISOBARIC CORONAL ARCADES

6.1 Introduction

An arcade whose pressure is uniform will be considered in this chapter. The magnetic field in such an arcade will be described by

$$\frac{d}{dr} \left(\frac{B_{\theta}^2}{2\mu} \right) + \frac{B_{\theta}^2}{\mu r} = 0 \quad (6.1)$$

(assuming again that there are no shear or radial field components), i.e.

$$B_{\theta} \propto 1/r \quad (6.2)$$

There will be a singularity at the origin unless it is excluded from the region of interest. One way to exclude the origin is to place it a depth d below the photosphere (Figure 6.1).

As the pressure is uniform in the arcade, the parameter h^*/p^* will be uniform (if it is independent of the field strength B). The parameter L^*p^* will increase with the length of the relevant loop. The half-length of a loop with footpoint at A and summit at B (a height y_s above the photosphere) is given by

$$L_o = (d + y_s) \tan^{-1} \left[\sqrt{\frac{y_s^2}{d^2} + 2 \frac{y_s}{d}} \right] \quad (6.3)$$

so that the parameter L^*p^* varies as

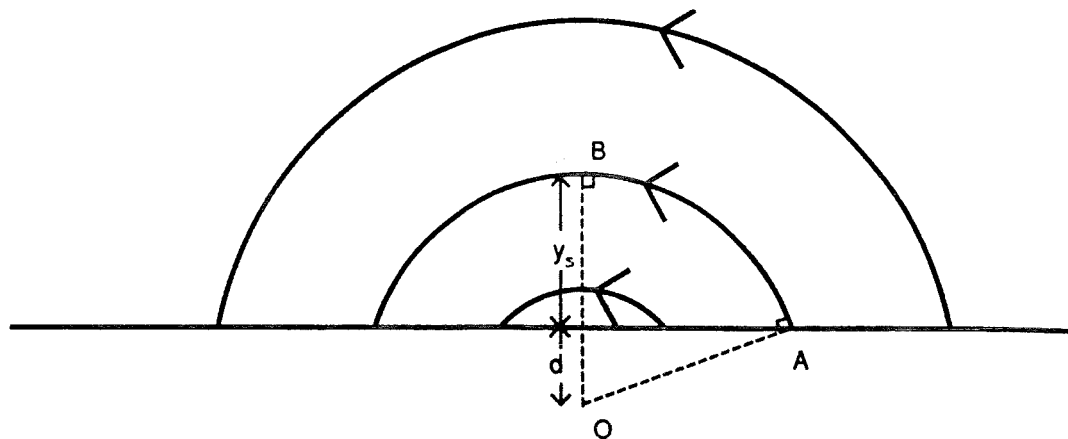


Figure 6.1 The form of the magnetic arcade considered. The axis is at O , a depth d below the horizon and a typical loop has footpoint at A and summit at B , a distance y_s above the photosphere

$$L^*p^* = \frac{L_o}{L_\infty} p^*$$

$$= \frac{d}{L_\infty} \left(1 + \frac{y_s}{d}\right) \tan^{-1} \left[\sqrt{\frac{y_s^2}{d^2} + 2 \frac{y_s}{d}} \right] \quad (6.4)$$

The contour in $(L^*p^*)-(h^*/p^*)$ space will then be represented by a straight horizontal line. The exact position of the contour (as a function of y_s/d) depends on the two parameters h^*/p^* and $d p^* / L_{oo}$.

Figure 6.2 shows L^*p^* as a function of y_s/d for various values of $d p^* / L_{oo}$. In the limits as y_s/d is large or small, L^*p^* is given by

$$L^*p^* = \frac{d}{L_\infty} p^* \sqrt{2} \left(\frac{y_s}{d}\right)^{1/2} \propto y_s^{1/2} \quad y_s \ll d \quad (6.5)$$

$$L^*p^* = \frac{y_s p^*}{L_\infty} \frac{\pi}{2} \propto y_s \quad y_s \gg d \quad (6.6)$$

6.2 Results for Uniform Heating

The types of loops within the arcade depend on the parameter h^*/p^* . If h^*/p^* is greater than 1.25 hot loops exist for large y_s/d but as y_s/d is reduced these join smoothly onto cool loops. When h^*/p^* lies between 0.41 and 1.25, for large y_s/d , loops can be hot, warm or cool but for small y_s/d only cool loops exist. When h^*/p^* is less than 0.41, for large y_s/d there is a choice between hot loops and hot-cool loops. As y_s/d is reduced, however, first the hot loops and then the hot-cool loops are lost and there are no realistic solutions (i.e. no solutions with non-negative footpoint temperature gradients).

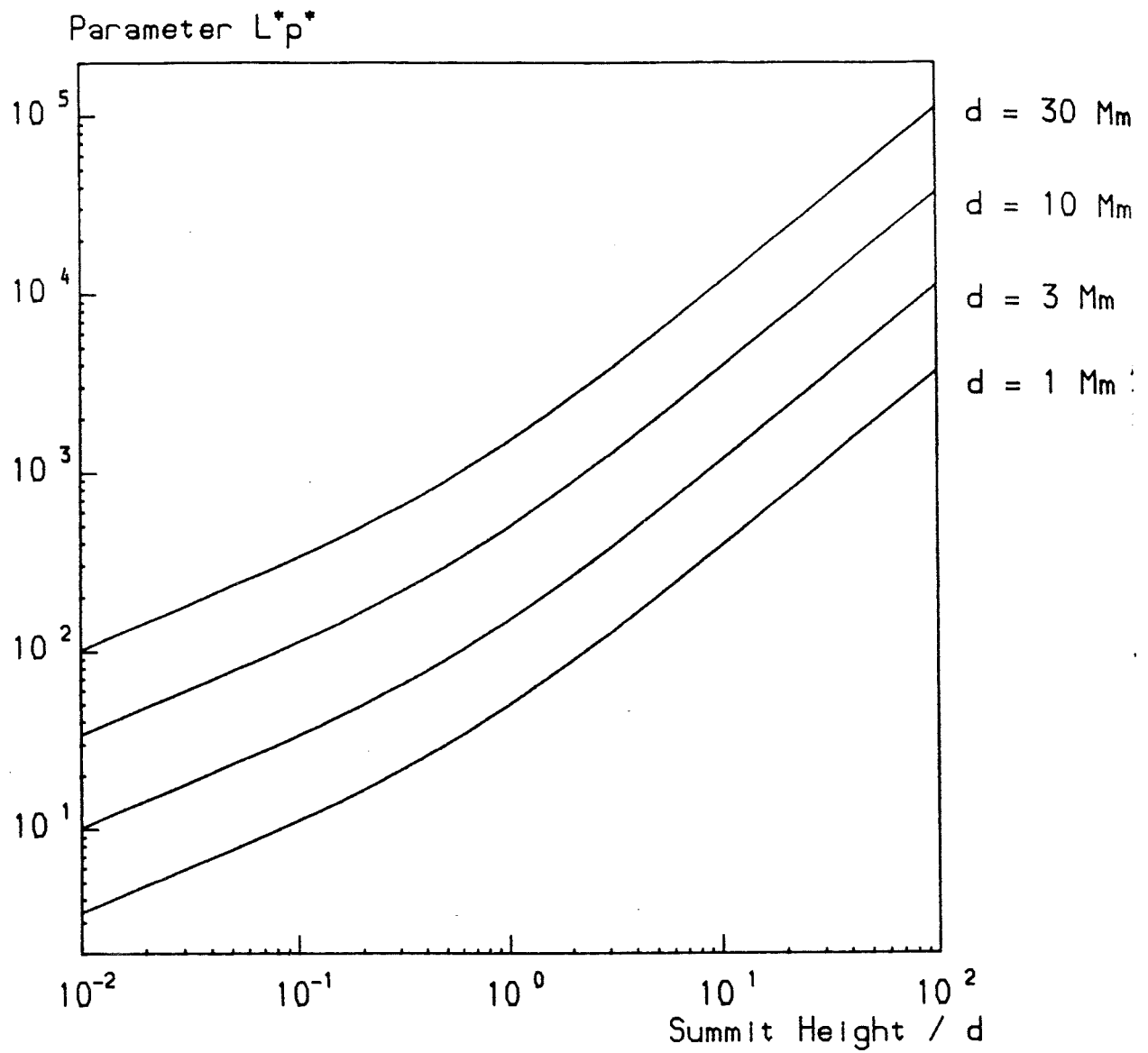


Figure 6.2 The variation of the parameter L^*p^* with the ratio of the loop summit height to the depth, d , of the axis below the photosphere for different values of d .

Six contours are chosen in the $(L^*p^*)-(h^*/p^*)$ plane. Table 6.1 gives the details.

Table 6.1

Contour	h^*/p^*	d (Mm)	p^*	$d p^* / L_{\infty}$
1	2.0	1	1	23.7
2	0.8	1	1	23.7
3	0.2	1	1	23.7
4	2.0	10	1	237
5	0.8	10	1	237
6	0.2	10	1	237

Figure 6.3 shows how the summit temperature of the loop varies with summit height above the solar photosphere. Contours 1, 2 and 3 are shown in Figure 6.3a and contours 4, 5 and 6 are on Figure 6.3b.

It can be seen that for the arcades generated by contours 1 and 4 there exist hot loops well away from the point on the photosphere directly above the axis. As the origin is approached, the loop summits are at lower temperatures. When h^*/p^* is greater than 1.25, the hot loops join smoothly onto the cool loops near the photosphere.

For the arcades generated by contours 2 and 5, for loops whose summits are well above the photosphere, there are three possibilities, a hot loop, a cool loop and a warm loop. As the height of the summit is decreased (keeping the same value of the depth d, of the axis, hot and warm solutions cease to exist. This happens about 30 km above

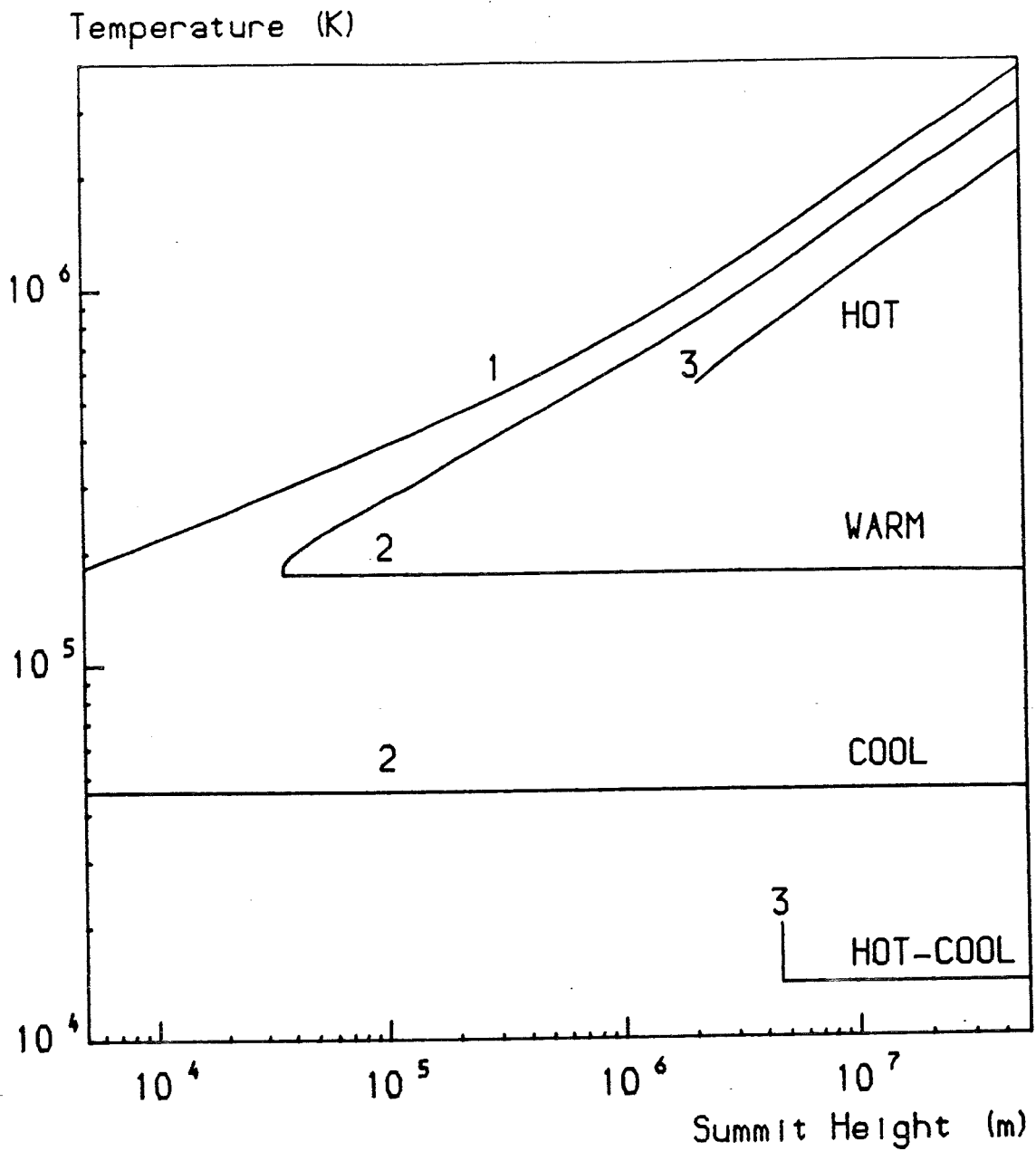


Figure 6.3a The variation of the summit temperature with summit height for the arcades generated by contours 1, 2 and 3 in section 6.2. The division of the arcades into hot, warm, cool and hot-cool loops is noted.

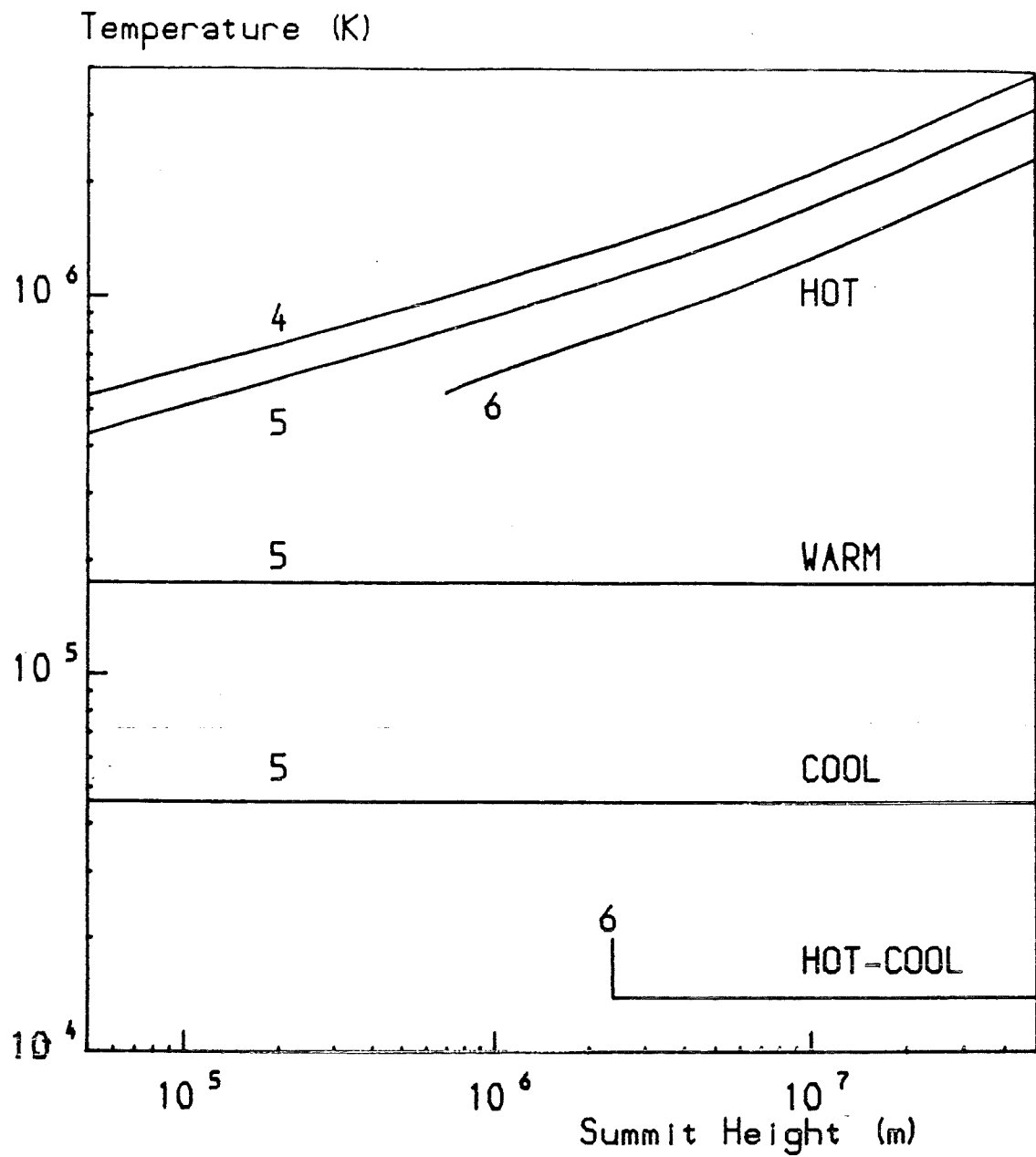


Figure 6.3b The variation of the summit temperature with summit height for the arcades generated by contours 4, 5 and 6 in section 6.2. The division of the arcades into hot, warm, cool and hot-cool loops is noted.

the photosphere for contour 2 and at a lower height for contour 5. For loops whose summits are closer to the photosphere, only cool loops exist.

For contours 3 and 6, where h^*/p^* is less than 0.41, both hot and hot-cool loops may exist with summits greater than a certain height above the photosphere. This height is about 4.5 Mm for contour 3 and about 2.4 Mm for contour 6. Below this summit height, only cool loops exist and below a further summit height, no static loops at all may exist. This further summit height is about 2Mm for contour 3 and about 0.6 Mm for contour 6.

At various points on Figure 6.3, the summit temperature is observed to change suddenly and discontinuously as solutions of a different regime are found or the existing regime no longer produces solutions. This occurs when the contour crosses a diagonal line (representing the minimum L^*p^* for a hot or hot-cool loop for a particular value of h^*/p^*) in the (L^*p^*) - (h^*/p^*) plane.

The minimum summit height for hot-cool loops is referred to as y_3 and applies when $h^*/p^* < 0.41$ (contours 3,6). Hot loops may occur both when y_s is greater than y_3 and when y_s is slightly less than y_3 . The minimum summit height for hot loops is referred to as y_4 and applies when $h^*/p^* < 1.25$ (contours 2, 3, 5 and 6). The heights y_3 and y_4 depend on the two parameters $d p^* / L_{00}$ and h^*/p^* and must be calculated numerically.

Figure 6.4a shows y_3 as a function of h^*/p^* for four

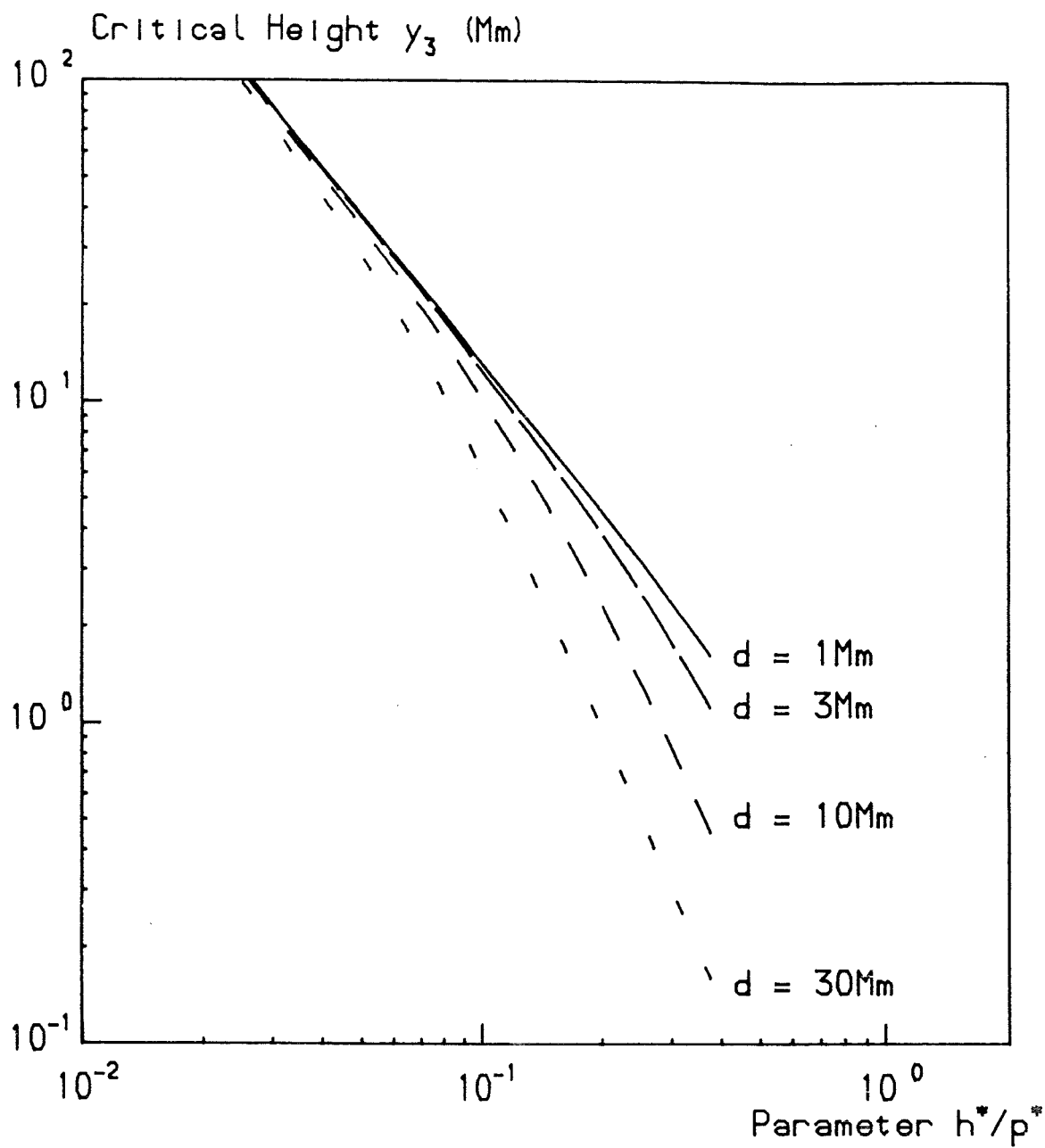


Figure 6.4a The variation with the parameter h^*/p^* and depth d of the critical height y_3 , the minimum summit height for hot-cool loops.

values of d . For small values of h^*/p^* , y_3 is almost independent of d . It is interesting to note that for high h^*/p^* , y_3 increases as d decreases.

Similar behaviour is found for y_4 (Figure 6.4b). For h^*/p^* less than 1.25, y_4 is a decreasing function of h^*/p^* and for larger values of h^*/p^* , y_4 is meaningless. Again, y_4 is not highly dependent on d especially for low values of h^*/p^* .

Surface plots have been drawn showing how the temperature varies in two dimensions (Figure 6.5). Figure 6.5a deals with contour 1. Here as $h^*/p^* > 1.25$ the temperature varies smoothly throughout the arcade, and, except near the photosphere, it is generally increasing with distance from the axis. Of course, the temperature will not increase indefinitely as one travels out as the form assumed for the magnetic field no longer applies at large distances.

Figure 6.5b deals with contour 2 for hot loops with summit height > 30 km and cool loops beneath. The cool loops all have almost the same summit temperature and hence almost the same thermal structure throughout. Apart from very close to the footpoints there is a discontinuity at the interface between the hot and cool solutions. The temperature profile for the area of hot solutions is similar to that for contour 1 although the temperatures are somewhat lower.

Instead of there being hot loops in the region far away from the axis the equations admit both warm and cool loops.

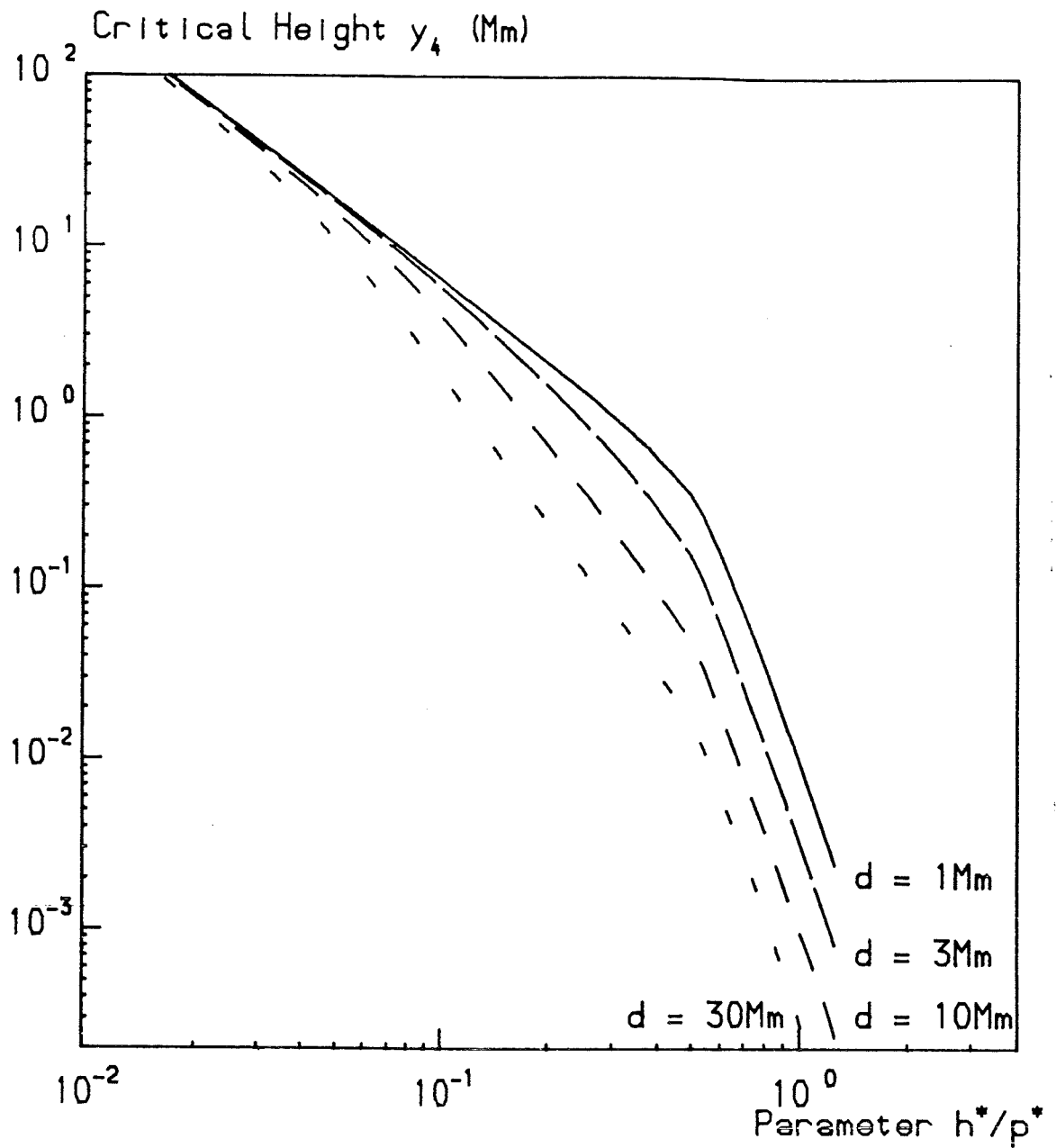


Figure 6.4b The variation with the parameter h^*/p^* and depth d of the critical height y_4 , the minimum summit height for hot loops.

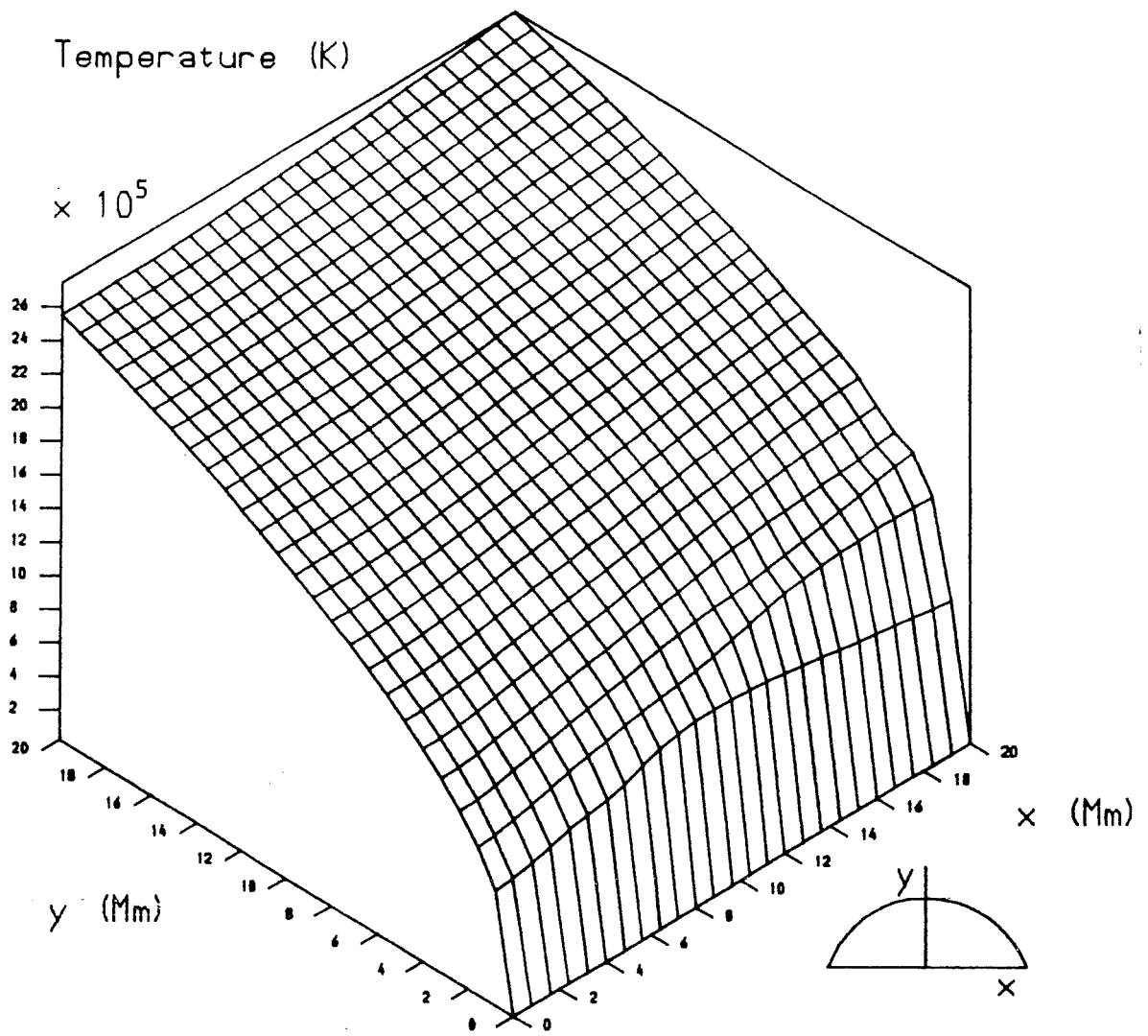


Figure 6.5a Temperature profile in two dimensional space for the arcade generated by contour 1.

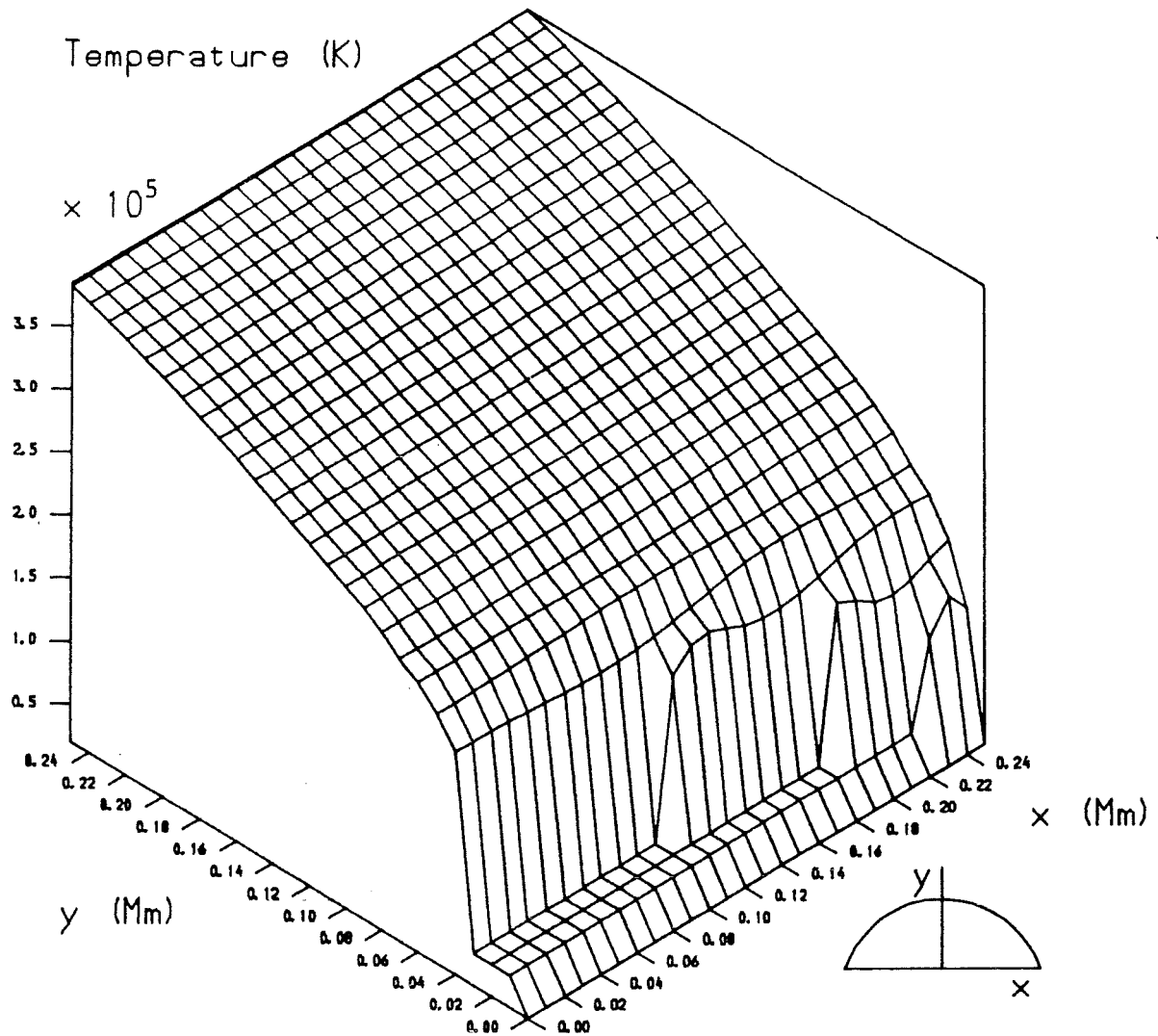


Figure 6.5b Temperature profile in two dimensional space for the arcade generated by contour 2 with hot loops at greater summit heights and cool loops at lesser summit heights.

The objection to both cases is that the warm or cool loops cannot join onto the hot corona unless a discontinuity occurs at some large distance.

For contour 3, there is a minimum summit height (about 2 Mm) beneath which equilibria cannot be found. For summit heights between 2 Mm and 4.5 Mm only hot loops are possible. Loops with summit heights greater than 4.5 Mm can be either hot or hot-cool. Figure 6.5c shows how the temperature varies in an arcade described by contour 3 with the loops being hot for all summit heights greater than about 2 Mm. In a small area near the point on the photosphere directly above the axis, no equilibrium solutions exist.

Figure 6.5d deals with the case where the loops with summit heights greater than about 4.5 Mm are hot-cool. Close to the point on the photosphere directly above the axis no equilibria exist. This area is surrounded by hot loops which in turn are surrounded by loops with hot regions near, but not at, the footpoints and with cool regions near and at the summits. The overall effect is that the atmosphere above about 4.5 Mm is 'cool' while nearer the photosphere it is 'hot'. Of course, for the temperature to join onto that of the hot corona, there must be a discontinuity in the temperature.

Figure 6.5e is concerned with contour 4. It is very similar to contour 1 except that for the shorter loops the temperatures are lower than those generated by contour 1.

Figure 6.5f deals with contour 6 and is similar to

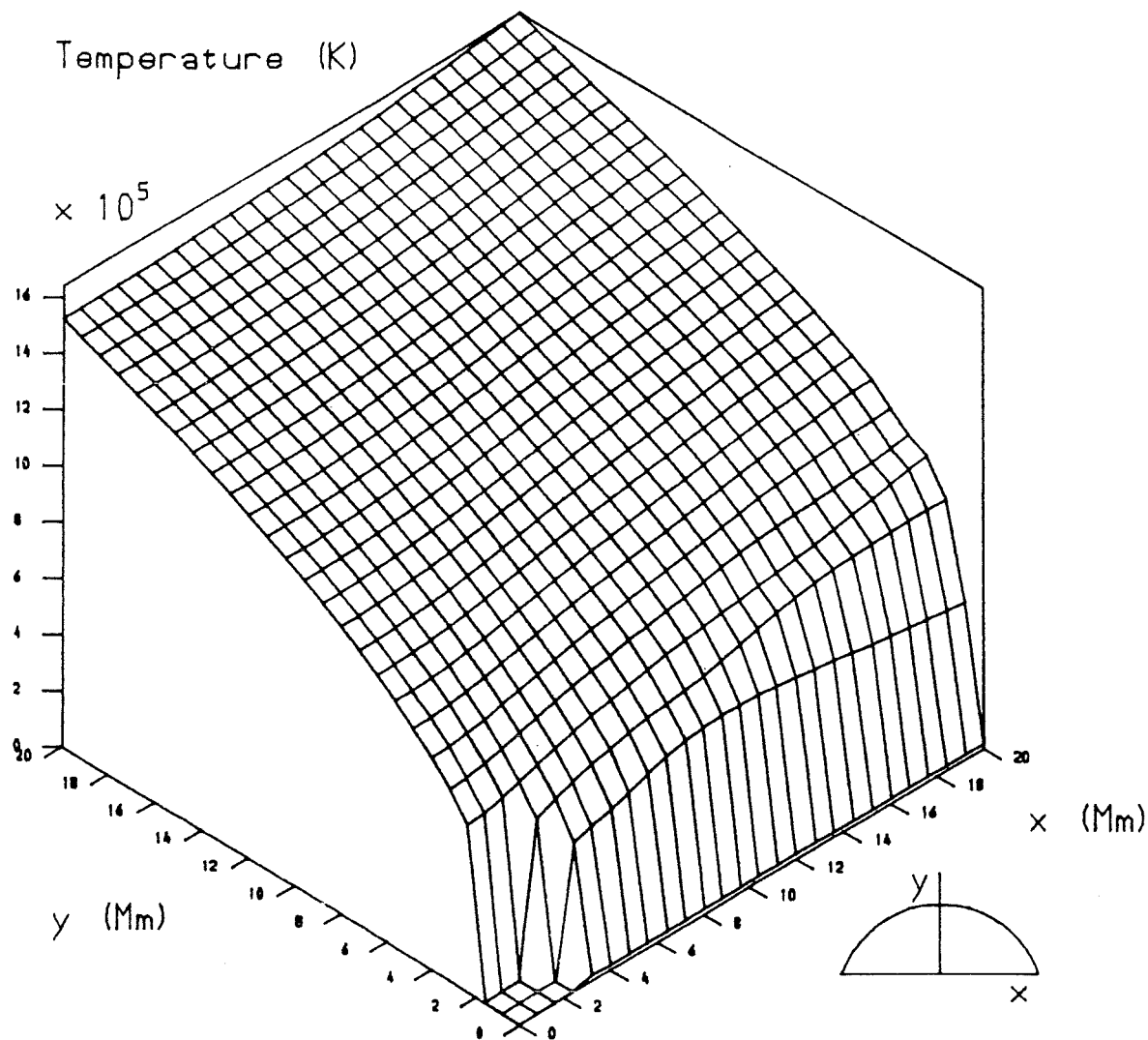


Figure 6.5c Temperature profile in two dimensional space for the arcade generated by contour 3 with hot loops present at all axial distances which admit equilibrium solutions.

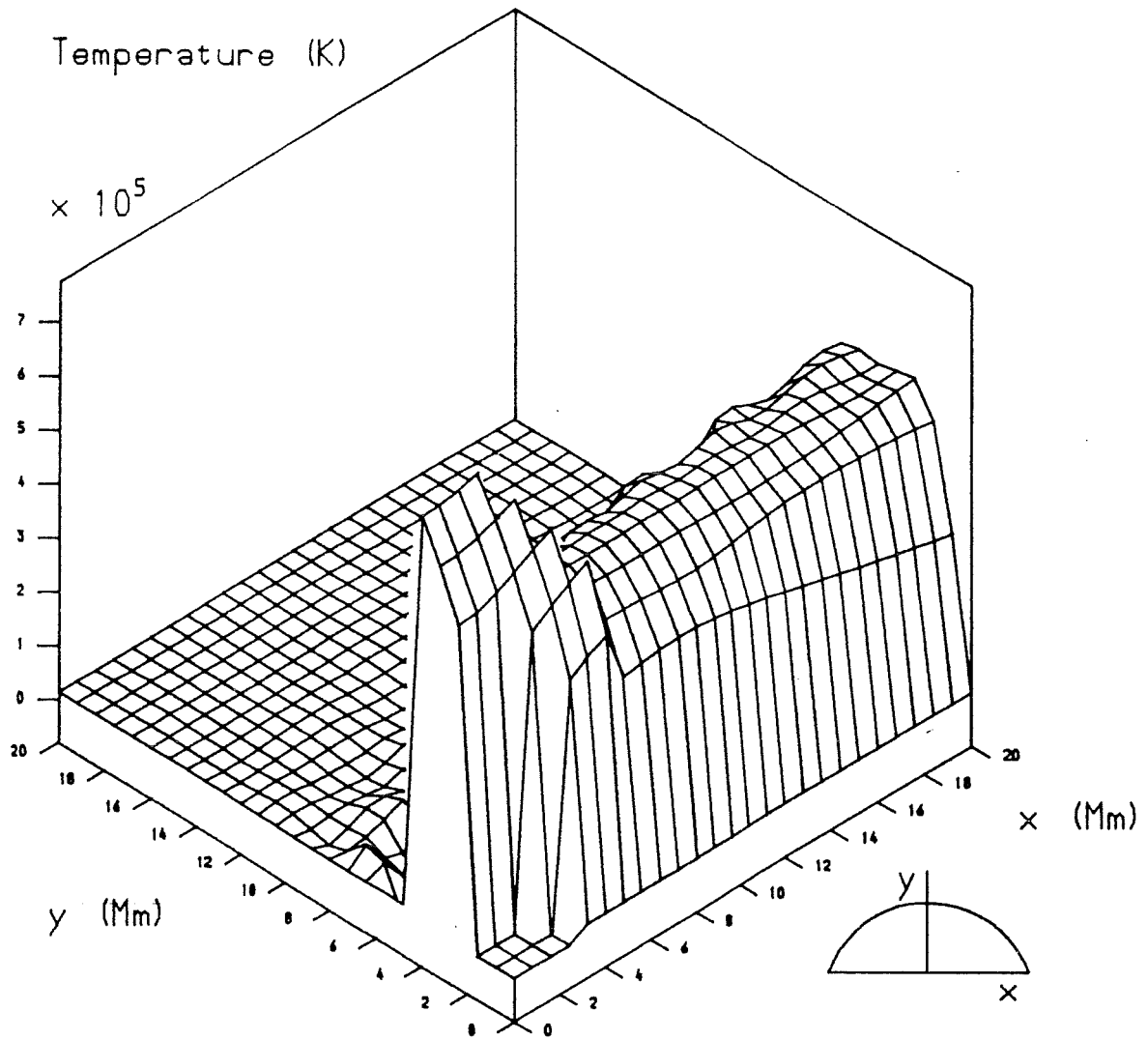


Figure 6.5d Temperature profile in two dimensional space for the arcade generated by contour 3 with hot-cool loops in the region far from the axis.

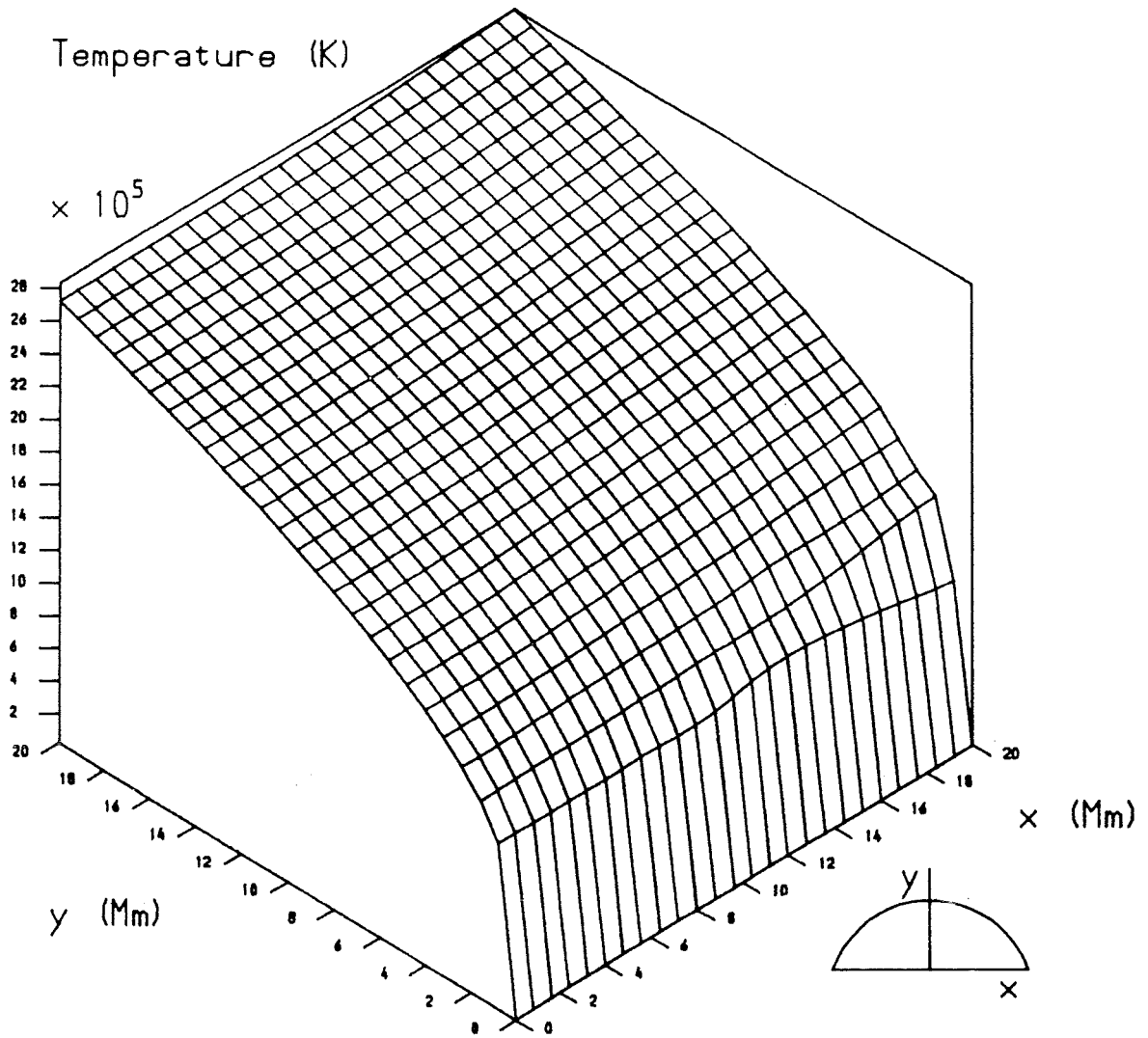


Figure 6.5e Temperature profile in two dimensional space for the arcade generated by contour 4.

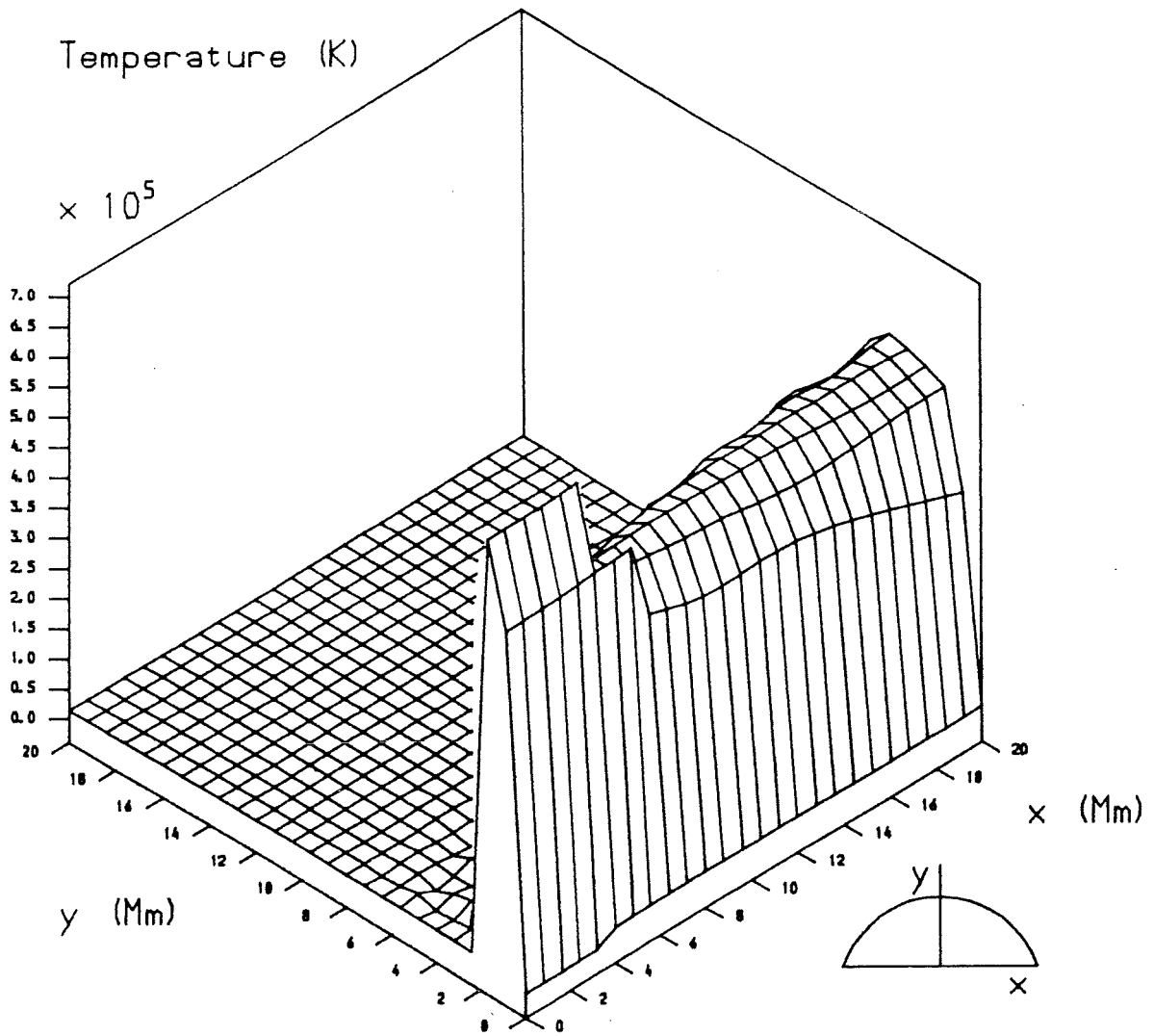


Figure 6.5f Temperature profile in two dimensional space for the arcade generated by contour 6 with hot-cool loops in the region far from the axis.

Figure 6.5d except that the small area near the photosphere is too small to show up on the scale used here.

Figures 6.5b, 6.5c, 6.5d and 6.5f feature discontinuities in the temperature as kinds of solutions no longer exist when certain regions of the arcade are entered. These discontinuities occur along circular arcs centred on the axis beneath the photosphere.

6.3 Results for Magnetic Heating

Sakurai and Levine (1981) have suggested that the coronal heating parameter h^* is proportional to B^2 . This implies

$$\frac{h^*}{p^*} = \left(\frac{h}{p}\right)_o \left(\frac{d}{d + y_s}\right)^2 \quad (6.7)$$

where $(h/p)_o$ is the value of h^*/p^* at the point on the photosphere directly above the axis and y_s is the height of the highest point on the loop.

As the loop summit height is increased, the parameter h^*/p^* decreases. For small and large y_s ,

$$\frac{h^*}{p^*} = \left(\frac{h}{p}\right)_o \quad y_s \ll d \quad (6.8)$$

$$\frac{h^*}{p^*} = \left(\frac{h}{p}\right)_o \left(\frac{d}{y_s}\right)^2 \quad y_s \gg d \quad (6.9)$$

The contours in the (L^*p^*) - (h^*/p^*) plane representing arcades are different from those in the case where the heating is independent of the field strength. Table 6.II shows the values of $(h/p)_o$ and d for five arcades and the contours are illustrated in Figure 6.6.

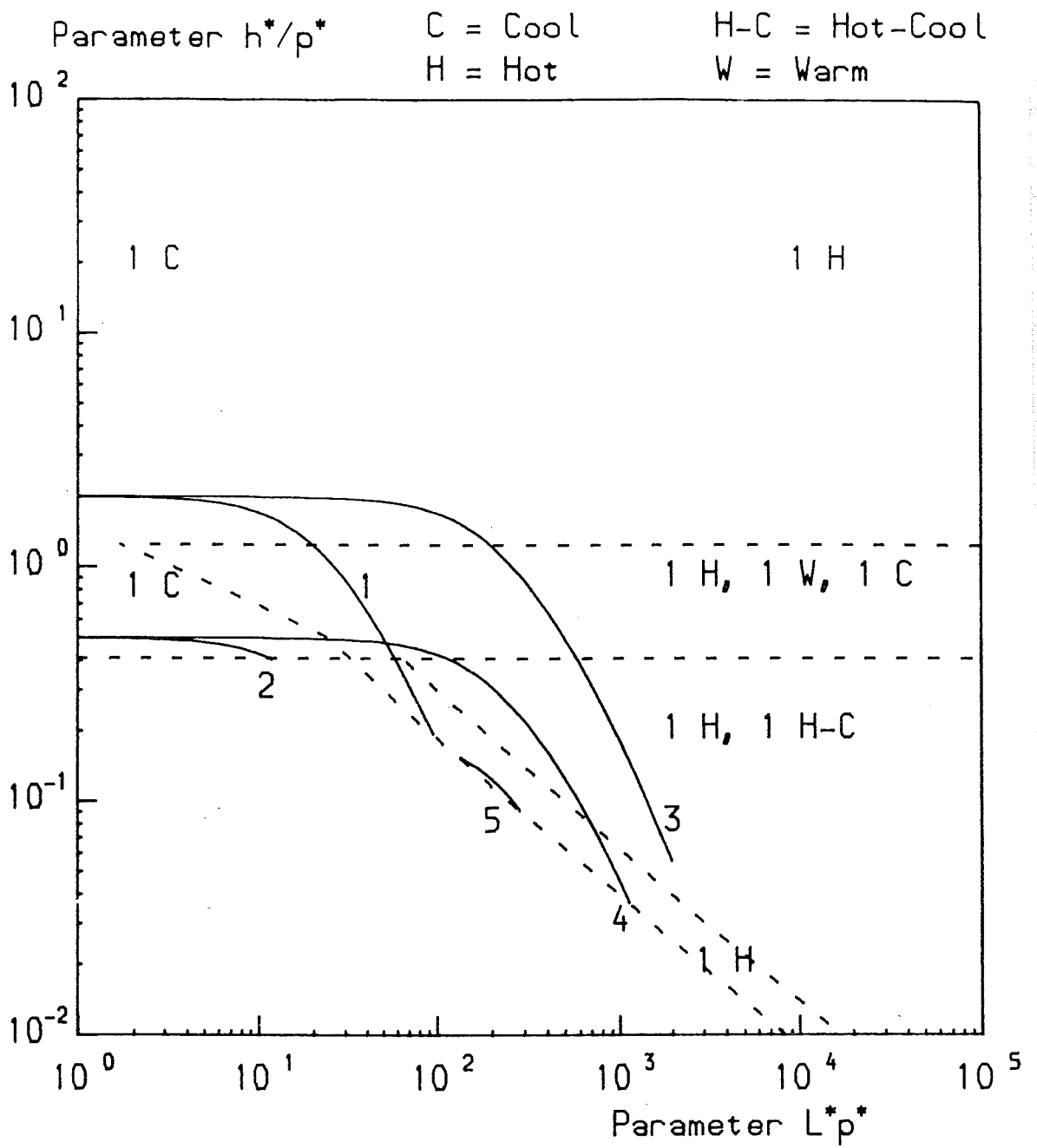


Figure 6.6 Five contours in the $(L^*p^*)(h^*/p^*)$ plane which represent the different contours of section 6.3

Table 6.11

Contour	$(h/p)_o$	d (Mm)	p^*	$d p^* / L_{o0}$
1	2.0	1	1	23.7
2	0.5	1	1	23.7
3	2.0	10	1	237
4	0.5	10	1	237
5	0.2	10	1	237

The case was also considered where $(h/p)_o = 0.2$ and $d = 1$ Mm. The resultant contour, however, is always in the region where no realistic solutions are possible.

Contours 1 to 5 pass through areas where solutions of the various kinds are possible. Figure 6.7 shows how the summit temperature varies within the arcade for contours 1 and 2 (Figure 6.7a) and contours 3, 4 and 5 (Figure 6.7b). For all arcades there is a finite upper limit to the size of the area within which realistic solutions are possible. Obviously, in practice, a more complex background field will modify the solutions, especially at large distances.

For loops in the arcade described by contour 1, where summits are within 2 Mm of the photosphere hot loops are always possible. These are of decreasing summit temperature with decreasing height. For loops whose summits lie between 0.2 Mm and 1 Mm above the photosphere, warm and cool solutions are possible. The warm loops have summit temperatures increasing with summit height while for the

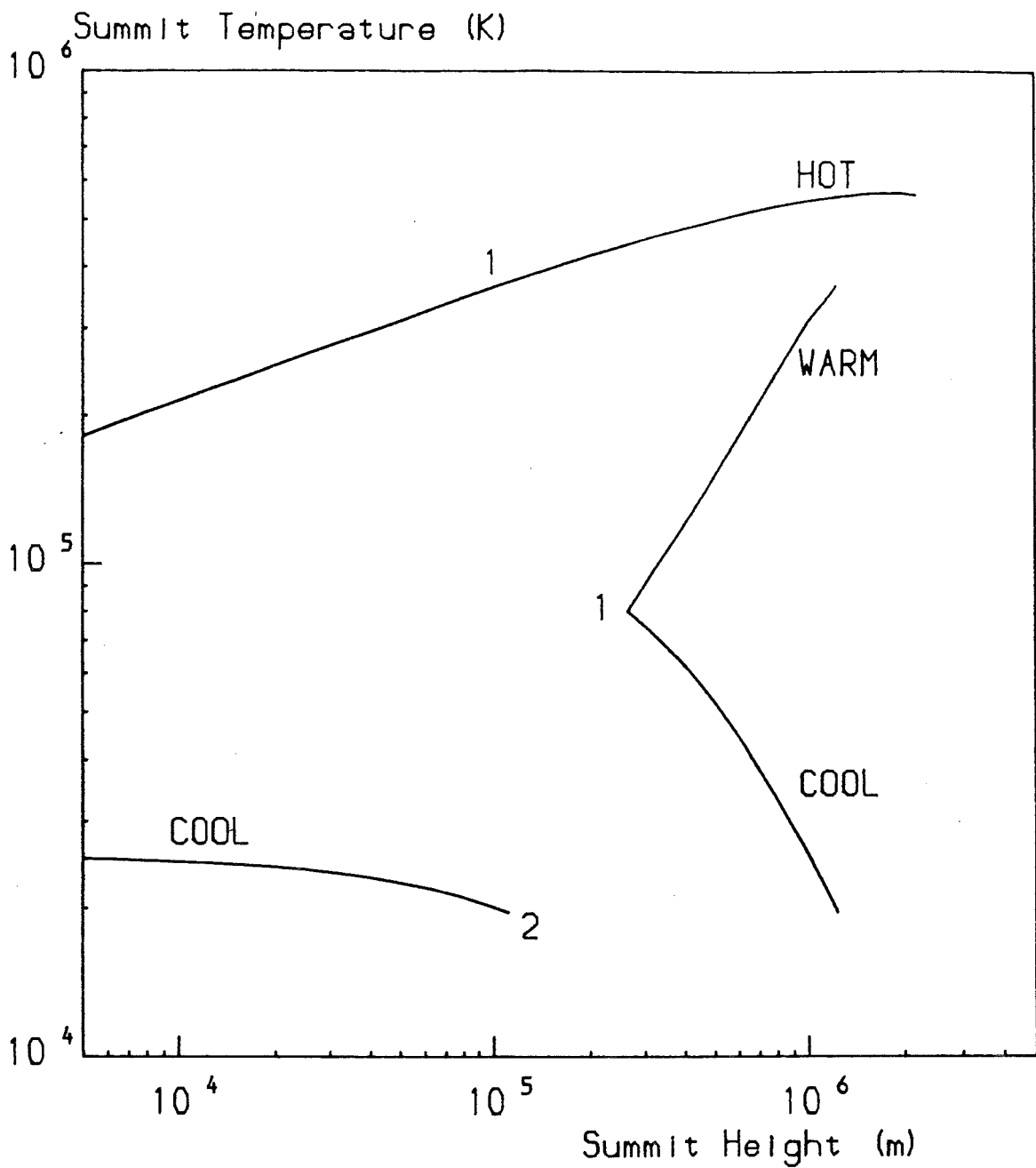


Figure 6.7a The variation of loop summit temperature with summit height for contours 1 and 2 of section 6.3. The division of the arcade into hot, warm and cool loops is noted.

cool loops, as the summit height increases, the summit temperature decreases.

Realistic solutions are only possible within 0.1 Mm of the surface when the arcade is that generated by contour 2. These cool solutions have summit temperatures slightly greater than the footpoint temperatures. As the summit height increases, the summit temperature decreases until the limiting case where the loop is isothermal with a temperature of 20 000 K. If the summit height is increased further, no realistic solutions can be found.

When contour 3 is the relevant one hot loops can exist for summit heights up to greater than 50 Mm. These hot loops have temperatures which increase with summit height. Between 2 Mm and 10 Mm warm and cool loops may also exist and above 10 Mm hot-cool loops may exist.

Contour 4 also features loops of the four different kinds. At summit heights greater than 20 Mm no realistic solutions exist but as the summit height is reduced, hot loops appear at 20 Mm and hot-cool loops at 15 Mm. As the summit height is reduced further the summit temperature of the hot-cool loops increases until at 1 Mm the summit temperature is equal to the footpoint temperature. At lower summit heights, hot-cool solutions cannot be found but both warm and cool loops are possible. From Figure 6.7b it would appear that the transition between the hot-cool and cool loops is a smooth one but this is only the case at the summit. Nearer the footpoints the hot-cool loop is at a much greater temperature than the cool loop.

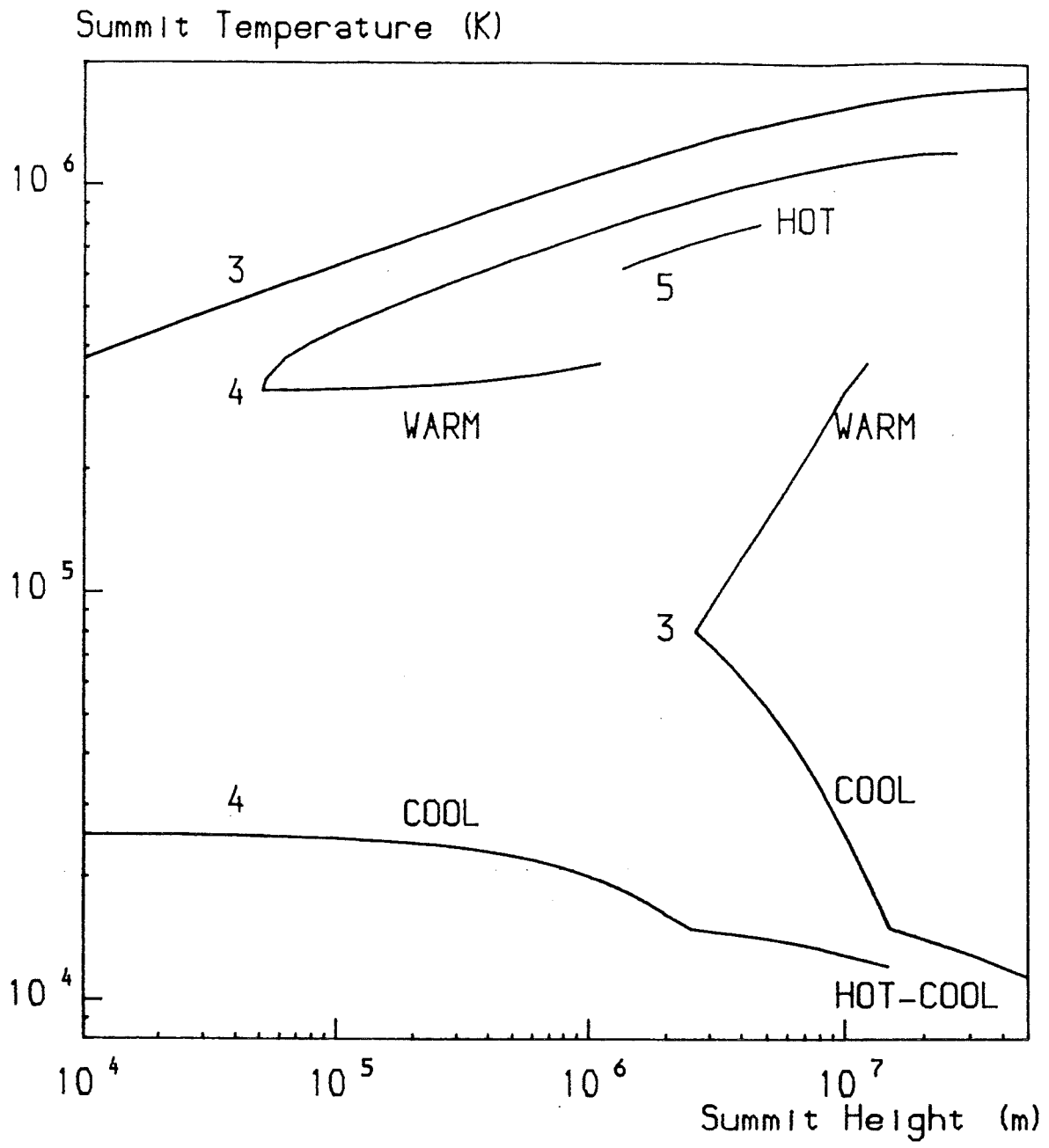


Figure 6.7b The variation of loop summit temperature with summit height for contours 3, 4 and 5 of section 6.3. The division of the arcade into hot, hot-cool, warm and cool loops is noted.

For contour 5, only for a very limited range of summit heights, (1 to 4 Mm) are any solutions possible. These solutions which do exist are of the hot type with summit temperature increasing slightly with height. Nearer the axis and further from it no realistic equilibria exist.

Figure 6.7 features discontinuities as the contour crosses boundaries between the areas of the different forms of solution; these boundaries are denoted by broken lines in Figure 6.6. The variation with the parameters of the heights at which these discontinuities occur is shown in Figure 6.8.

The quantity y_1 denotes the summit height where $h^*/p^* = 1.25$. Above this, for $L^*p^* \geq 1$, hot, warm and cool loops may exist while below this only hot loops may exist. Similarly y_2 denotes the summit height where $h^*/p^* = 0.41$. For $L^*p^* \geq 30$, above the summit height y_2 hot and hot-cool loops may exist (the hot-cool loops only exist when $h^*/p^* \geq 60$) and below this summit height hot, warm and cool loops may exist.

For $h^*/p^* < 0.41$, y_3 is the minimum L^*p^* for hot-cool loops and is denoted by the right of the two diagonal broken lines on Figure 6.6. Contours entering the area of hot-cool loops cross this line either once or twice. When $(h/p)_0$ and/or d are sufficiently high the contour enters (when the summit height is y_2) from the area above of hot, warm and cool solutions, otherwise it enters (when the summit height is y_3) from the area of hot solutions to the left. In either case as r is increased the contour leaves the area of

hot-cool loops (when the summit height is y_3) by travelling downwards into the area of hot loops only. Thus either one or two values of y_3 exist, one being the maximum summit height for hot-cool loops and the other, when it exists, being the minimum height.

Similar behaviour is found for y_4 , the value of the loop summit height corresponding to the minimum L^*p^* for a hot solution and represented by the left of the two diagonal broken lines on Figure 6.6. If $(h/p)_o$ and/or d are large enough, one value of y_4 is found corresponding to the maximum size of the arcade, otherwise two values are found corresponding to the minimum summit height for hot solutions and the maximum size of the arcade.

The critical heights y_1 and y_2 are given by

$$\frac{y_{\text{crit}}}{d} = \sqrt{\frac{(h/p)_o}{c}} - 1 \quad (6.10)$$

where c is set equal to 1.25 (for y_1) and 0.41 (for y_2). Figure 6.8a shows y_1/d (in full) and y_2/d (in broken) as functions of $(h/p)_o$. Such discontinuities only occur when $(h/p)_o > c$, otherwise values of h^*/p^* less than the critical value c exist for all values of the loop summit height.

Figure 6.8b shows y_3 as a function of $(h/p)_o$ for different values of d . When d is low, only one value of y_3 exists, the maximum summit height at which hot-cool loops may occur. As $(h/p)_o$ is reduced this maximum height also reduces. There is, however, a minimum value of $(h/p)_o$ at which a value of y_3 can be found, corresponding to the contour touching the corner of the region of hot-cool

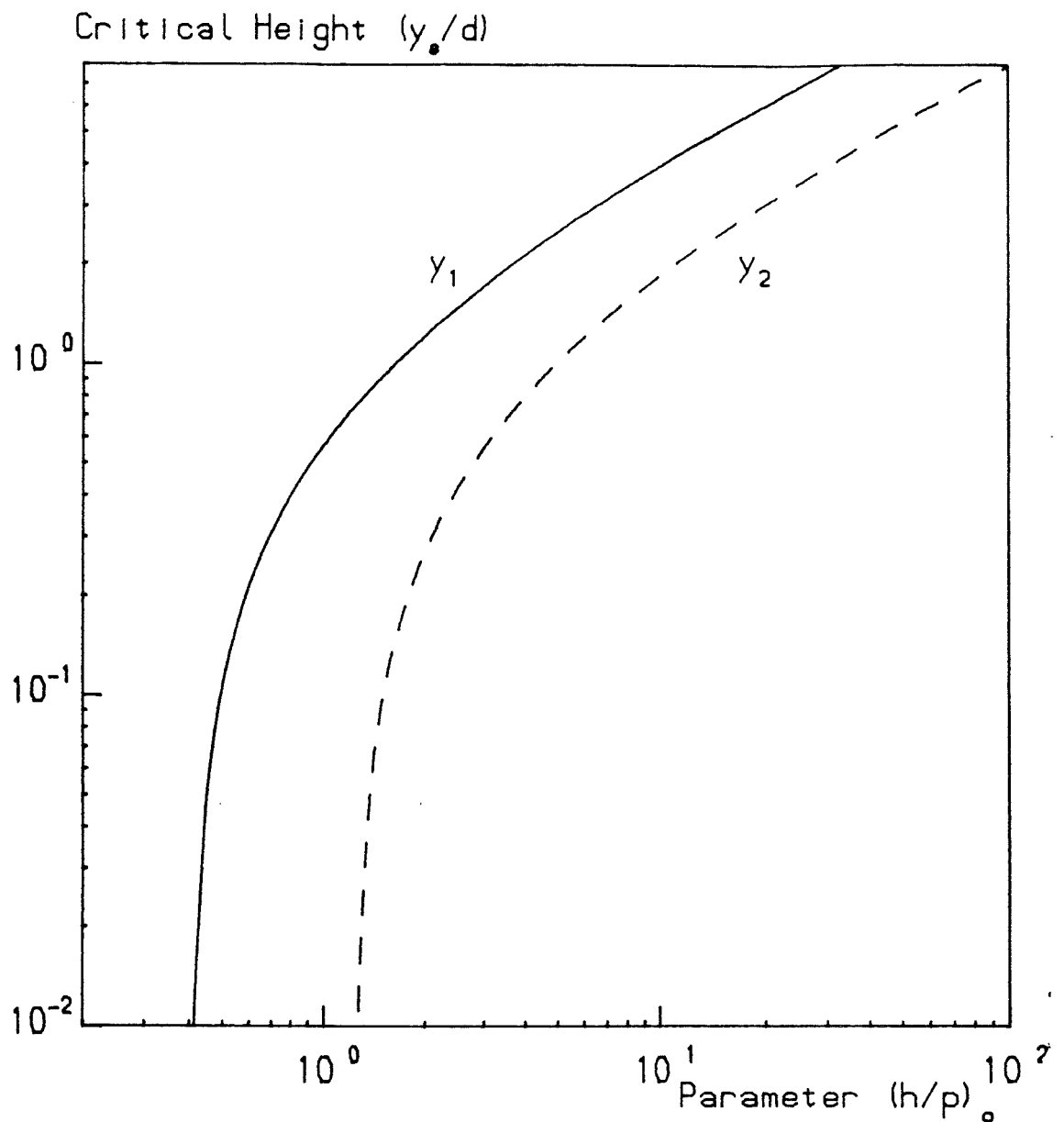


Figure 6.8a The variation of the ratios y_1/d and y_2/d with the parameter $(h/p)_0$: when $y_s = y_1$, h^*/p^* is equal to the critical value 1.25; when $y_s = y_2$, h^*/p^* is equal to the critical value 0.41.

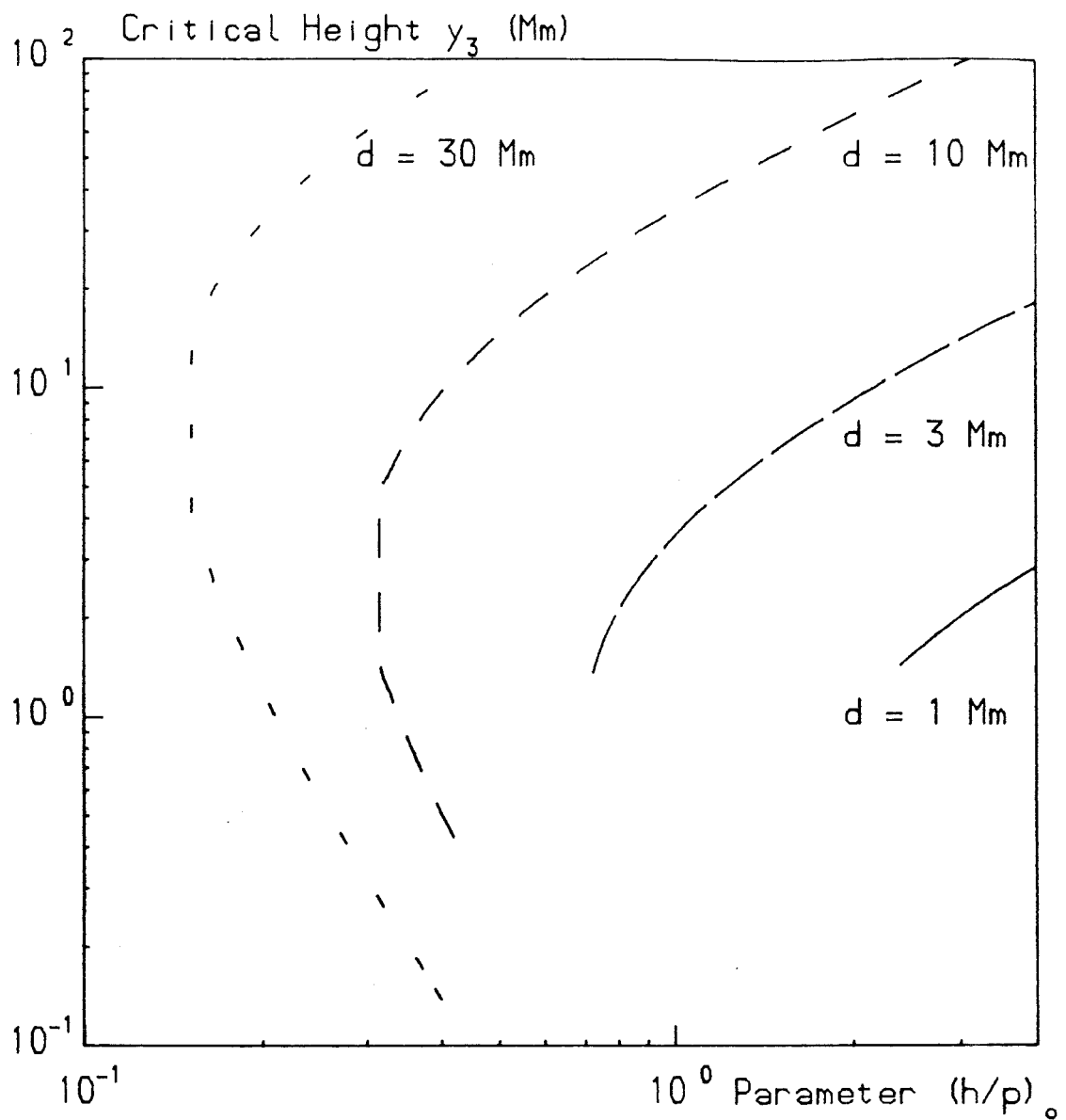


Figure 6.8b The variation of the critical height y_3 with the parameter $(h/p)_0$ for different values of the axial depth d . When one value of y_3 is recorded for a particular combination of $(h/p)_0$ and d , it is the maximum summit height for hot-cool loops; when two values are recorded these are the minimum and maximum heights for hot-cool loops.

solutions.

For larger d , the situation again depends on $(h/p)_0$. If $(h/p)_0$ is sufficiently large, one value of y_3 exists (corresponding to the maximum summit height for hot-cool loops). Reducing $(h/p)_0$ two values of y_3 exist, minimum and maximum heights for hot-cool loops. Reducing $(h/p)_0$ still further, no hot-cool loops can be found and no values of y_3 are recorded. Contours 3 and 4 exhibit one value of y_3 corresponding to the maximum summit height for hot-cool loops.

Figure 6.8c gives the corresponding plot for y_4 instead of y_3 . For high $(h/p)_0$, one value of y_4 is found corresponding to the maximum size of the arcade. As $(h/p)_0$ is reduced, a second value of y_4 appears, the minimum summit height for hot loops. Reducing $(h/p)_0$ further eliminates all hot solutions and there are therefore no values of y_4 . Contours 1 and 3 admit one value of y_4 , corresponding to the maximum arcade size. Contours 4 and 5 give two values of y_4 , the minimum and maximum summit heights for hot loops.

Figure 6.9 shows how the temperature varies in two dimensions within the arcade. For each contour several different profiles can be drawn as for some ranges of axial distance r , there is a choice between different types of solution. A sample of all the possibilities has been produced.

Figure 6.9a deals with contour 1 where the loops are hot out as far as the limit where no equilibrium solutions exist. The temperature varies smoothly everywhere except

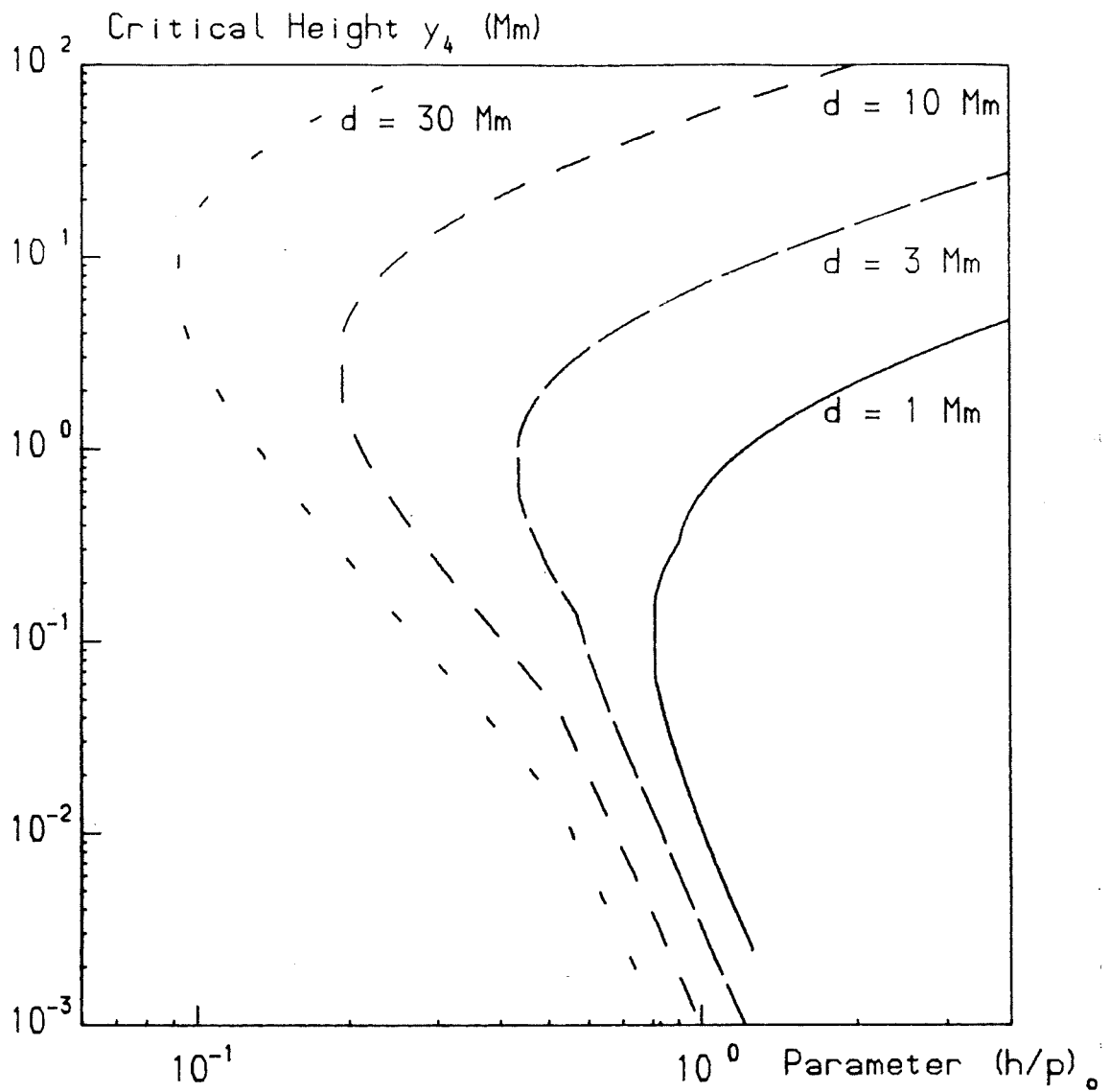


Figure 6.8c The variation of the critical height y_4 with the parameter $(h/p)_0$ for different values of the axial depth d . When one value of y_4 is recorded for a particular combination of $(h/p)_0$ and d , it is the maximum summit height for hot loops; when two values are recorded these are the minimum and maximum heights for hot loops.

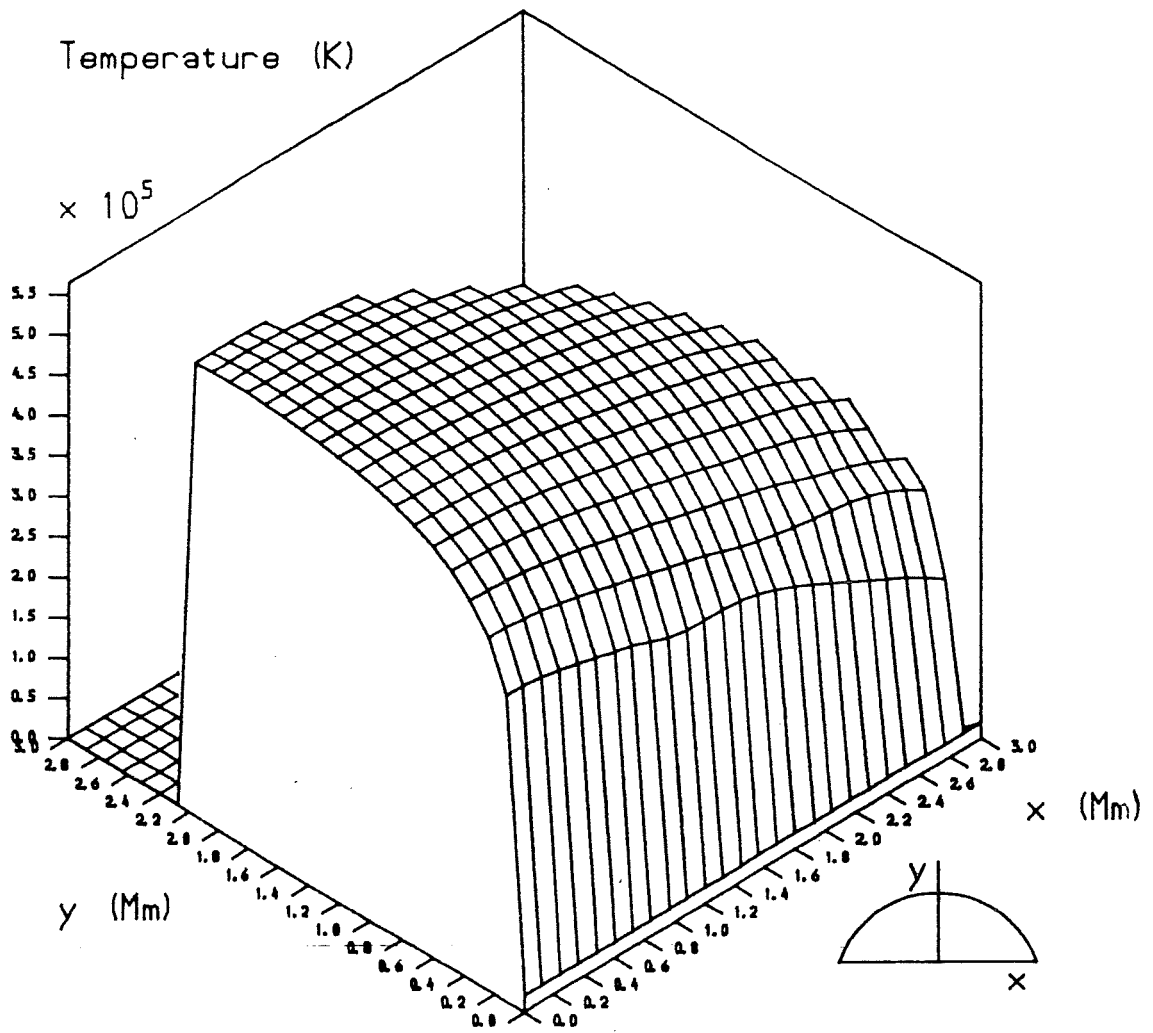


Figure 6.9a Temperature profile in two dimensions for the arcade generated by contour 1 where loops are hot out as far as the limit where no equilibria exist.

near the boundary between the region of hot loops and the region where no equilibria exist. The field is weaker here than it is closer to the axis and (as is the case with the outer boundaries of all arcades mentioned here) the background field may radically affect the situation.

Figure 6.9b also features contour 1 but this time cool loops exist with summit heights between 0.2 Mm and 1 Mm. In addition to the discontinuity at the outer boundary of the arcade, there are discontinuities at either edge of the area of cool loops. Moving out from the axis in the area of cool loops, the temperature reduces slightly.

Figure 6.9c is relevant to contour 2. Close to the axis, cool loops exist; further away no solutions can be found with positive footpoint temperature gradients. Close to the axis, the summit temperature is about 2.4×10^4 K while, as one recedes towards the axial radius beyond which no solutions exist, the summit temperature drops to 2×10^4 K to equal the footpoint temperature. When observing Figure 6.9c it must be remembered that the footpoints corresponding to the summits near the maximum height for cool solutions are at values of x much greater than can be displayed and to infer that the summits near the maximum height possible correspond to the footpoints for the largest values of x shown is incorrect.

Two temperature profiles are shown for contour 3. That on Figure 6.9d has warm solutions for loops with summit heights between 3 and 10 Mm and hot loops at axial distances greater and less than this. It can be seen that

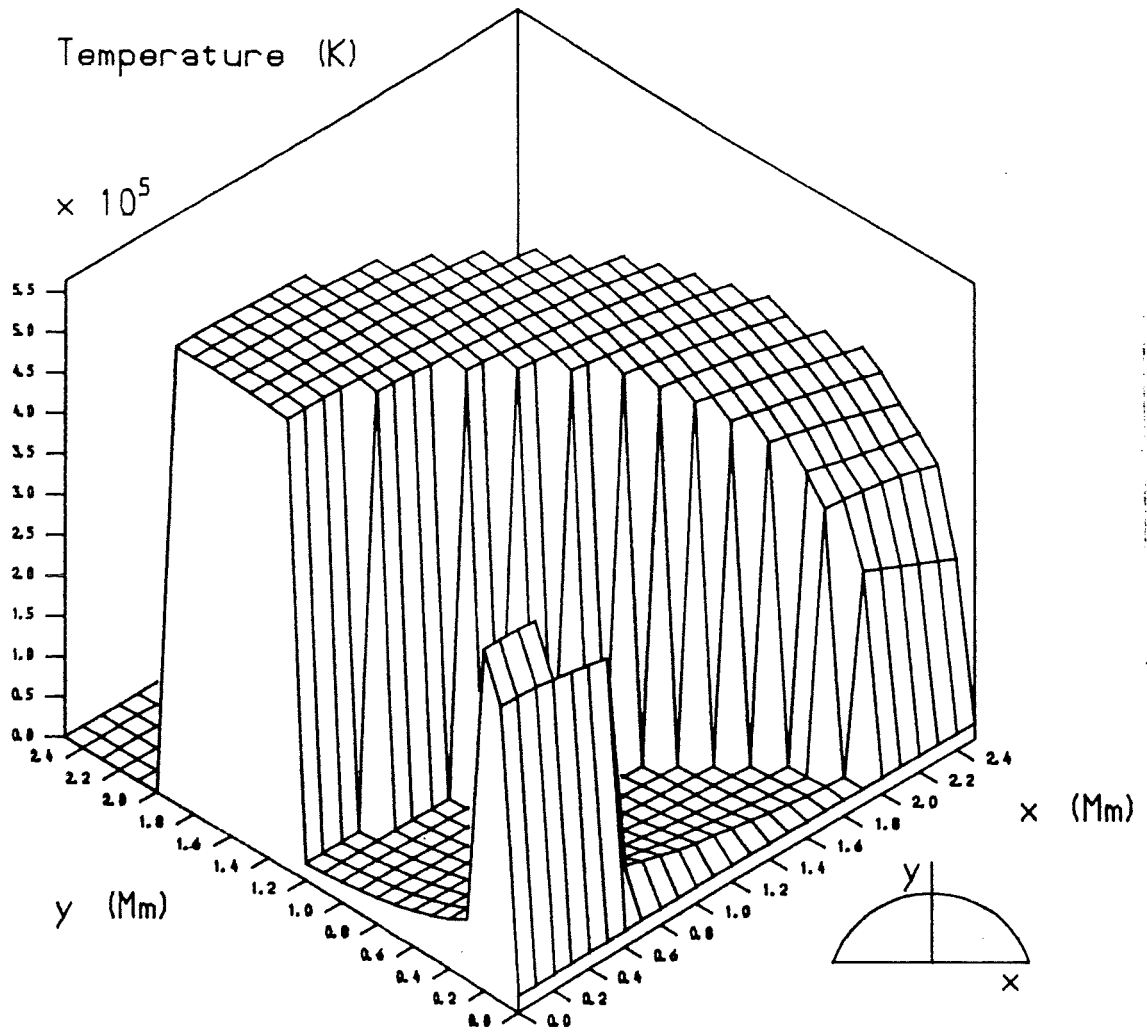


Figure 6.9b Temperature profile in two dimensions for the arcade generated by contour 1 where loops are hot out as far as the limit where no equilibria exist except for an annulus of cool loops.

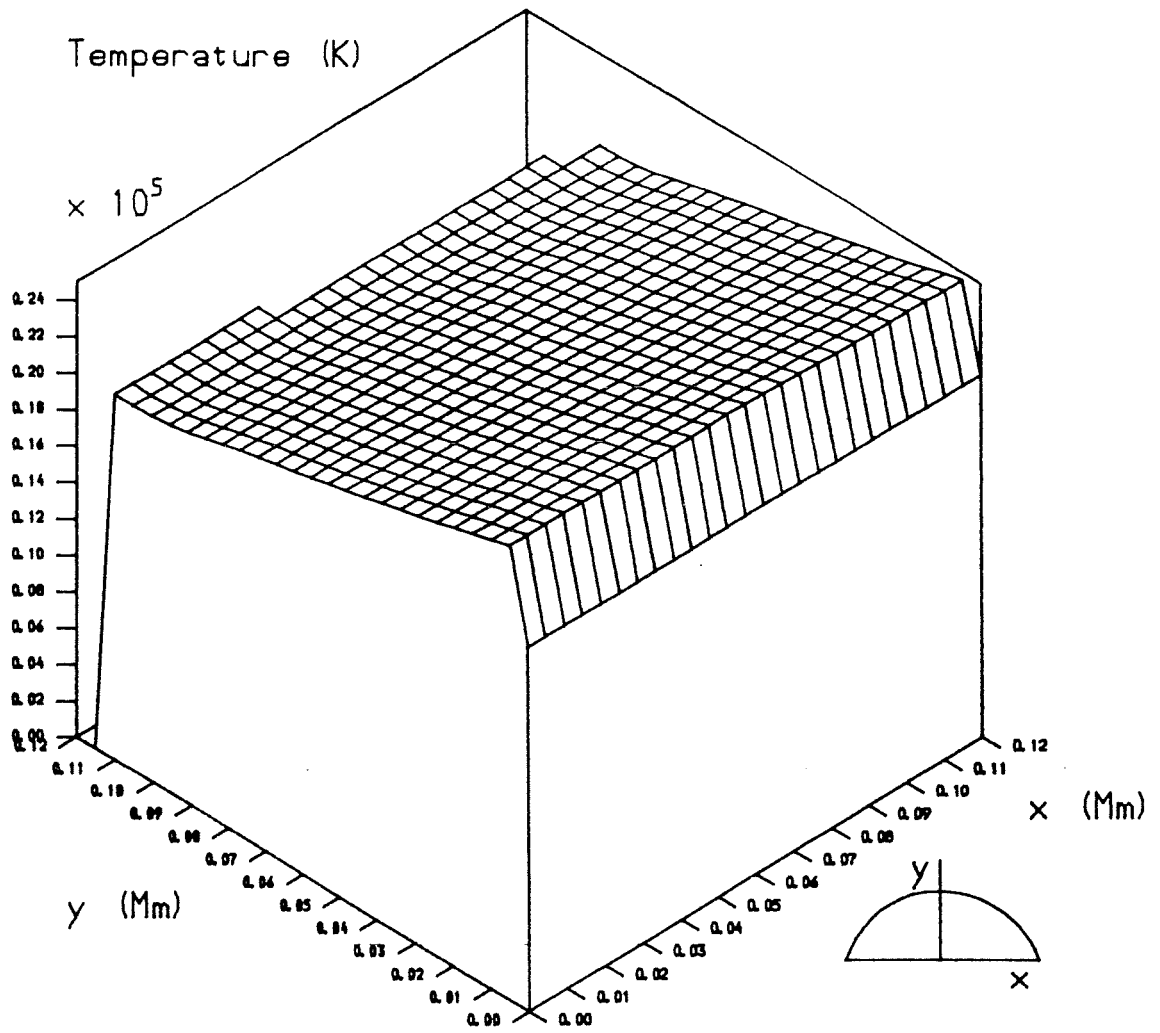


Figure 6.9c Temperature profile in two dimensions for the arcade generated by contour 2.

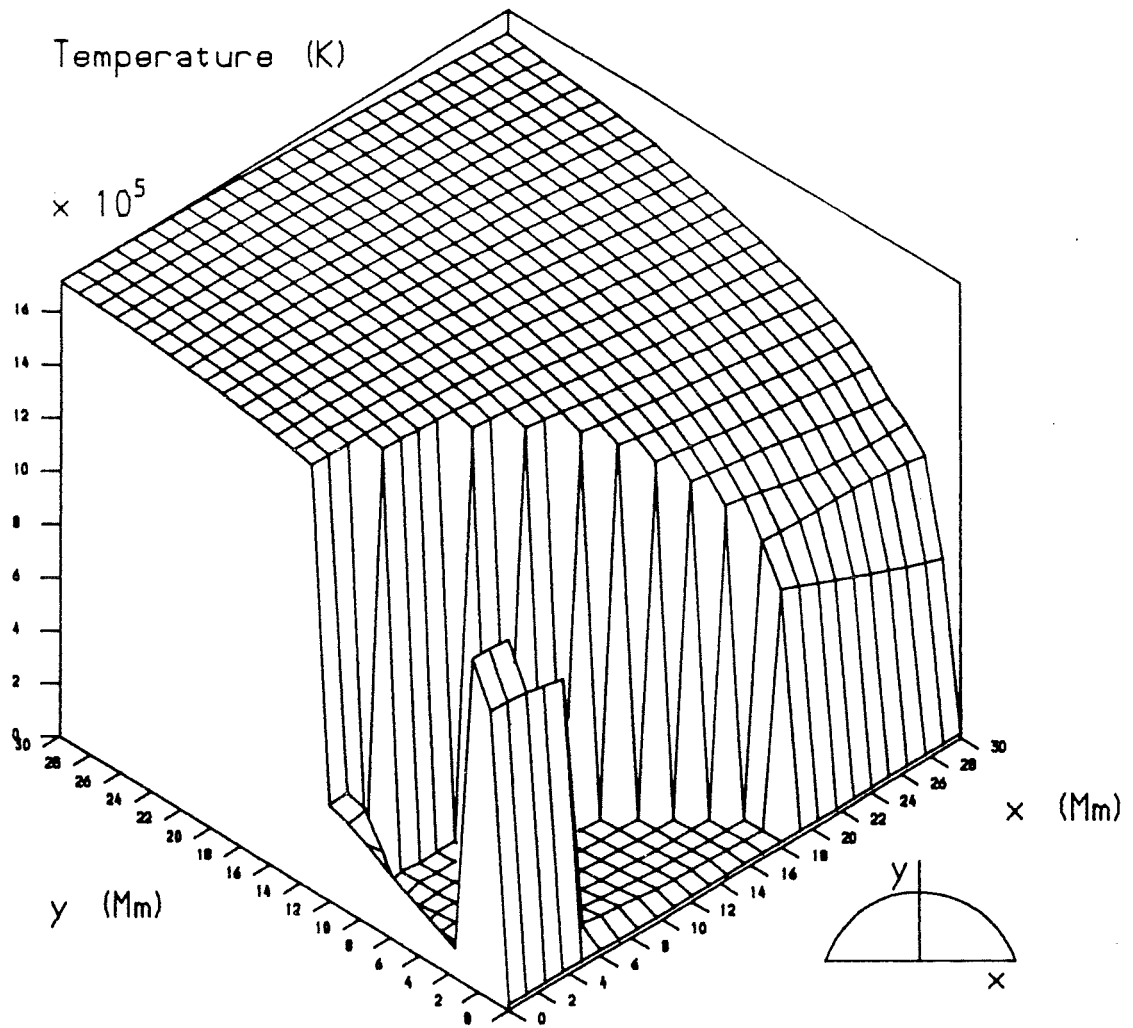


Figure 6.9d Temperature profile in two dimensions for the arcade generated by contour 3 where an annulus of warm loops exists with hot loops at greater and smaller axial distances.

much of the warm region is at temperatures between 20 000 K and 80 000 K with cooler footpoints and hotter summits.

Figure 6.9e gives the temperature profile when the loops with summits lower than 3 Mm are hot, with cool loops in the surrounding region. Outside the area of cool loops, hot-cool loops exist. It can be seen that near the summits the cool and hot-cool regimes join smoothly but near the footpoints the transition is not so smooth.

Figure 6.9f is relevant to contour 4. For summit heights between 15 and 26 Mm hot loops exist; closer to the axis lie hot-cool loops. Within 1 Mm of the point on the photosphere directly above the axis lie warm loops with a small region of cool loops inside these. The region of warm and cool loops, however, is too small to be well represented on Figure 6.9f.

Figure 6.9g shows the only solutions which can be found for contour 5, an annulus of hot loops with areas of no solution both inside and outside.

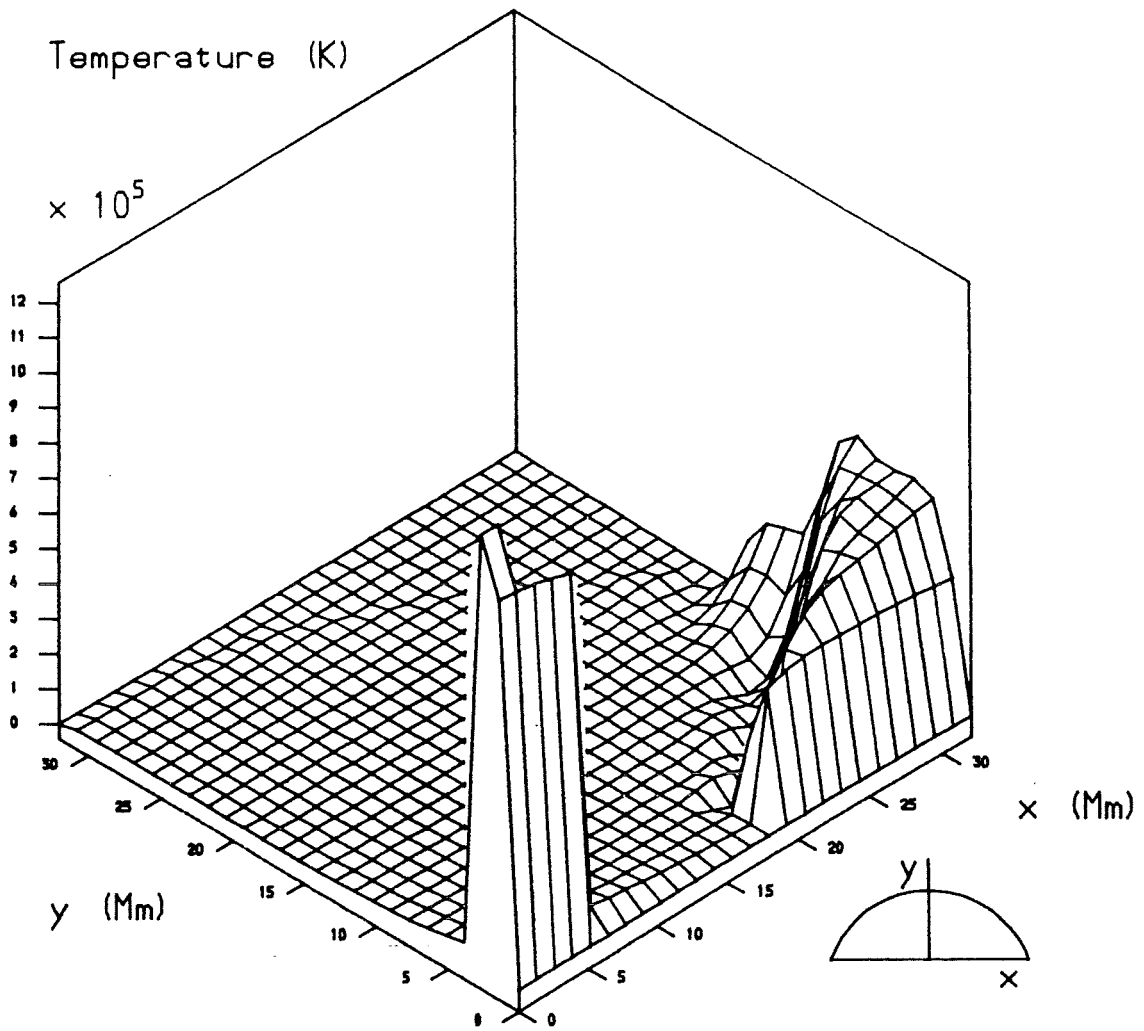


Figure 6.9e Temperature profile in two dimensions for the arcade generated by contour 3 where hot loops exist close to the axis. At greater axial distances cool and hot-cool loops exist followed by a region where no equilibria exist.

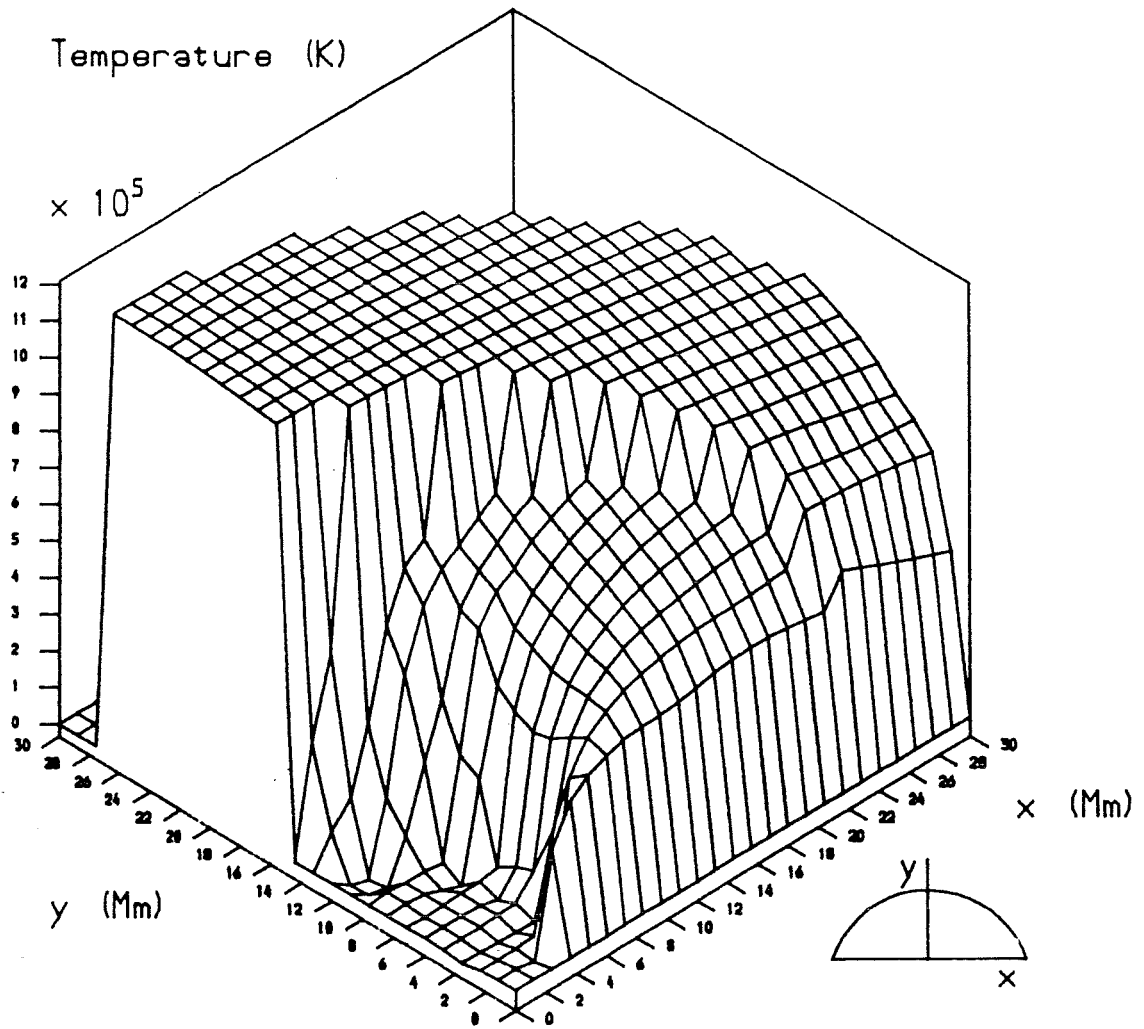


Figure 6.9f Temperature profile in two dimensions for the arcade generated by contour 4 where moving out from the axis, cool loops, warm loops, hot-cool loops and hot loops exist followed by an area where no equilibria exist.

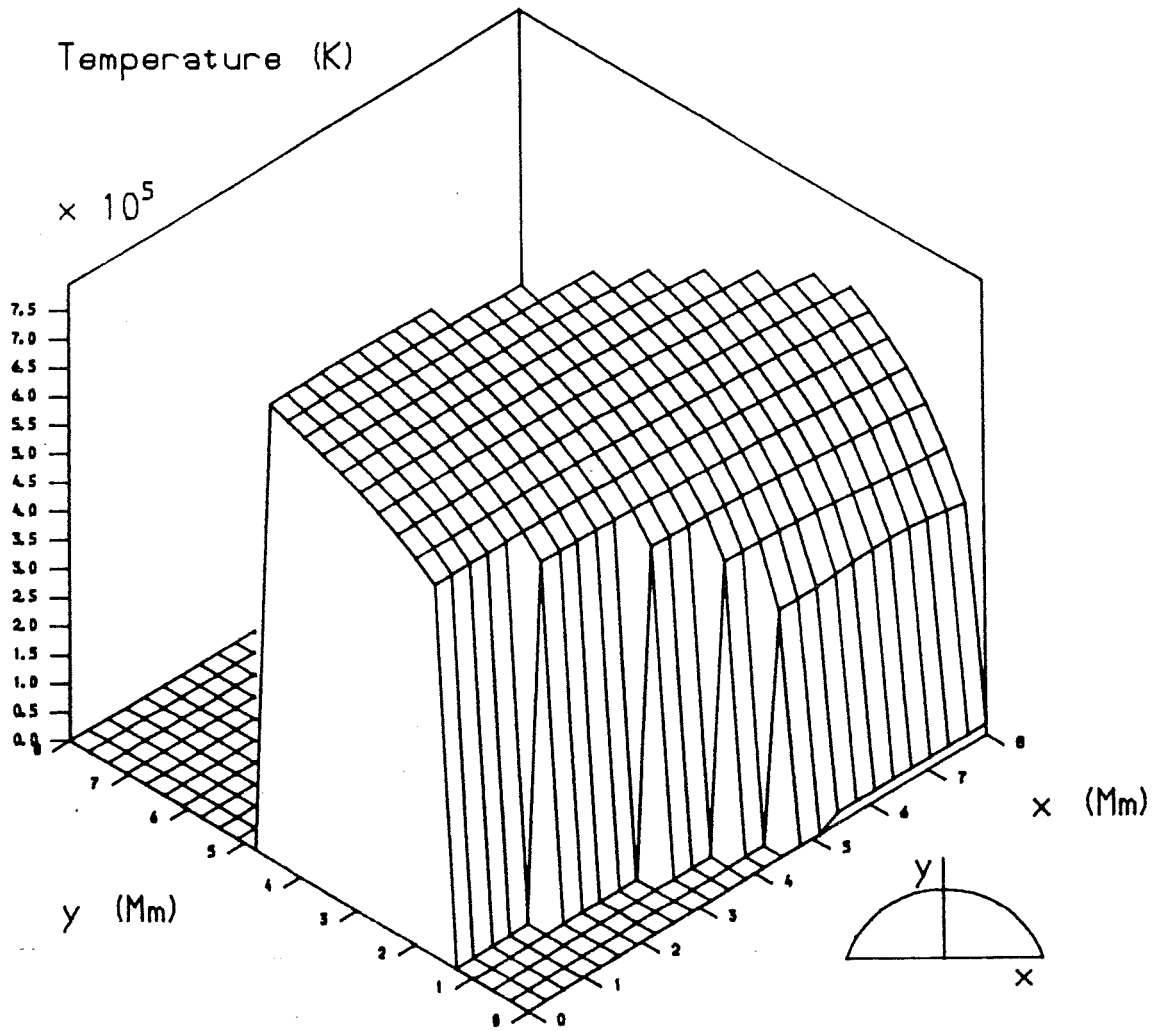


Figure 6.9g Temperature profile in two dimensions for the arcade generated by contour 5. An annulus of hot loops exists with no equilibria closer to or further from the axis.

6.4 Effects of Shearing the Arcade

It is instructive to consider next the effects of shearing the arcade whose axis lies beneath the photosphere. The footpoints on one side of the axis are moved in a direction parallel to the axis while their counterparts on the other side of the axis are moved in the opposite direction.

6.4.1 Uniform Heating

It will be assumed that the arcade remains in cylindrical symmetry with its axis still a depth d below the photosphere. This being so, the field components will satisfy

$$\frac{d}{dr} (B_{\phi}^2 + B_z^2) + \frac{2B_{\phi}^2}{r} = 0 \quad (6.11)$$

It is assumed that the field component normal to the surface remains unaffected by the shear. For the unsheared arcade this quantity is

$$B_n = B_{\phi} \cos \phi = \frac{k}{r} \frac{x}{r} = \frac{k}{r} \sqrt{1 - \frac{d^2}{r^2}} \quad (6.12)$$

at a distance x perpendicular to the axis.

The ϕ component of the perturbed field will thus satisfy

$$B_{\phi} \cos \phi = \frac{k}{r} \sqrt{1 - \frac{d^2}{r^2}} \quad (6.13)$$

i.e.

$$B_{\phi} = k/r \quad (6.14)$$

Thus the azimuthal field component is unchanged on shearing. The longitudinal field will thus be a constant and will be denoted by k_1/d .

The field line in ϕ, z space satisfies

$$\frac{r \, d\phi}{dz} = \frac{B_\phi}{B_z} = \frac{k/r}{k_1/d} \quad (6.15)$$

and so

$$\frac{dz}{d\phi} = \frac{k_1 r^2}{k d} \quad (6.16)$$

Thus

$$z = \frac{k_1 r^2}{k d} \left(\phi - \frac{\pi}{2} \right) + z_s \quad (6.17)$$

At the loop summit, $\phi = \pi/2$ and $z = z_s$. At the footpoints, $\sin \phi = d/r$ and

$$\begin{aligned} z &= \frac{k_1 r^2}{k d} \left(\sin^{-1} \frac{d}{r} - \frac{\pi}{2} \right) + z_s \\ &= \frac{k_1}{k} \frac{x^2 + d^2}{d} \left(\tan^{-1} \frac{d}{x} - \frac{\pi}{2} \right) + z_s \end{aligned} \quad (6.18)$$

The footpoints further from the axis are moved most, the increase of displacement with axial distance being greater than linear.

The half-length L_0 of the loop is given by considering the displacements in ϕ and z along the loop.

$$\begin{aligned} L_0 &= \sqrt{\left[\frac{k_1 r^2}{k d} \left(\sin^{-1} \frac{d}{r} - \frac{\pi}{2} \right) \right]^2 + r^2 \left(\sin^{-1} \frac{d}{r} - \frac{\pi}{2} \right)^2} \\ &= \left[\left[\frac{k_1 r^2}{k d} \right]^2 + r^2 \right]^{1/2} \left(\sin^{-1} \frac{d}{r} - \frac{\pi}{2} \right) \end{aligned} \quad (6.19)$$

In terms of y_s , the height of the summit above the photosphere, L_0 is given by

$$L_o = d \left[\frac{k_1^2}{k^2} \left(1 + \frac{y_s}{d}\right)^4 + \left(1 + \frac{y_s}{d}\right)^2 \right]^{1/2} \tan^{-1} \sqrt{\left(\frac{y_s}{d}\right)^2 + 2\frac{y_s}{d}} \quad (6.20)$$

The length of the loop of given summit height increases as shear is applied by increasing the parameter k_1/k . The parameter L^*p^* changes accordingly and so both the uniform heating and heating dependent on field cases change with shear.

The total magnetic field is given by

$$B = \sqrt{\frac{k^2}{r^2} + \frac{k_1^2}{d^2}} = \frac{k}{d} \sqrt{\frac{1}{\left(1 + \frac{y_s}{d}\right)^2} + \frac{k_1^2}{k^2}} \quad (6.21)$$

For the uniform heating case, shear causes L^*p^* to increase. When heating is proportional to B^2 , both parameters L^*p^* and h^*/p^* increase with shear.

The first sheared case to be considered is that where the coronal heating parameter h^* is assumed to be constant. The parameter h^*/p^* is therefore unaffected by the shearing process. The parameter L^*p^* becomes (on shearing).

$$L^*p^* = \frac{d}{L_\infty} \left[\frac{k_1^2}{k^2} \left(1 + \frac{y_s}{d}\right)^4 + \left(1 + \frac{y_s}{d}\right)^2 \right]^{1/2} \times \tan^{-1} \sqrt{\frac{y_s^2}{d^2} + 2\frac{y_s}{d}} p^* \quad (6.22)$$

Figure 6.10 shows how the quantity L^*p^* / d varies with y_s/d . As the shear (controlled by k_1/k) increases, so does L^*p^* particularly at large y/d . Nine values of k_1/k are used; these correspond to the values in table 6.III.

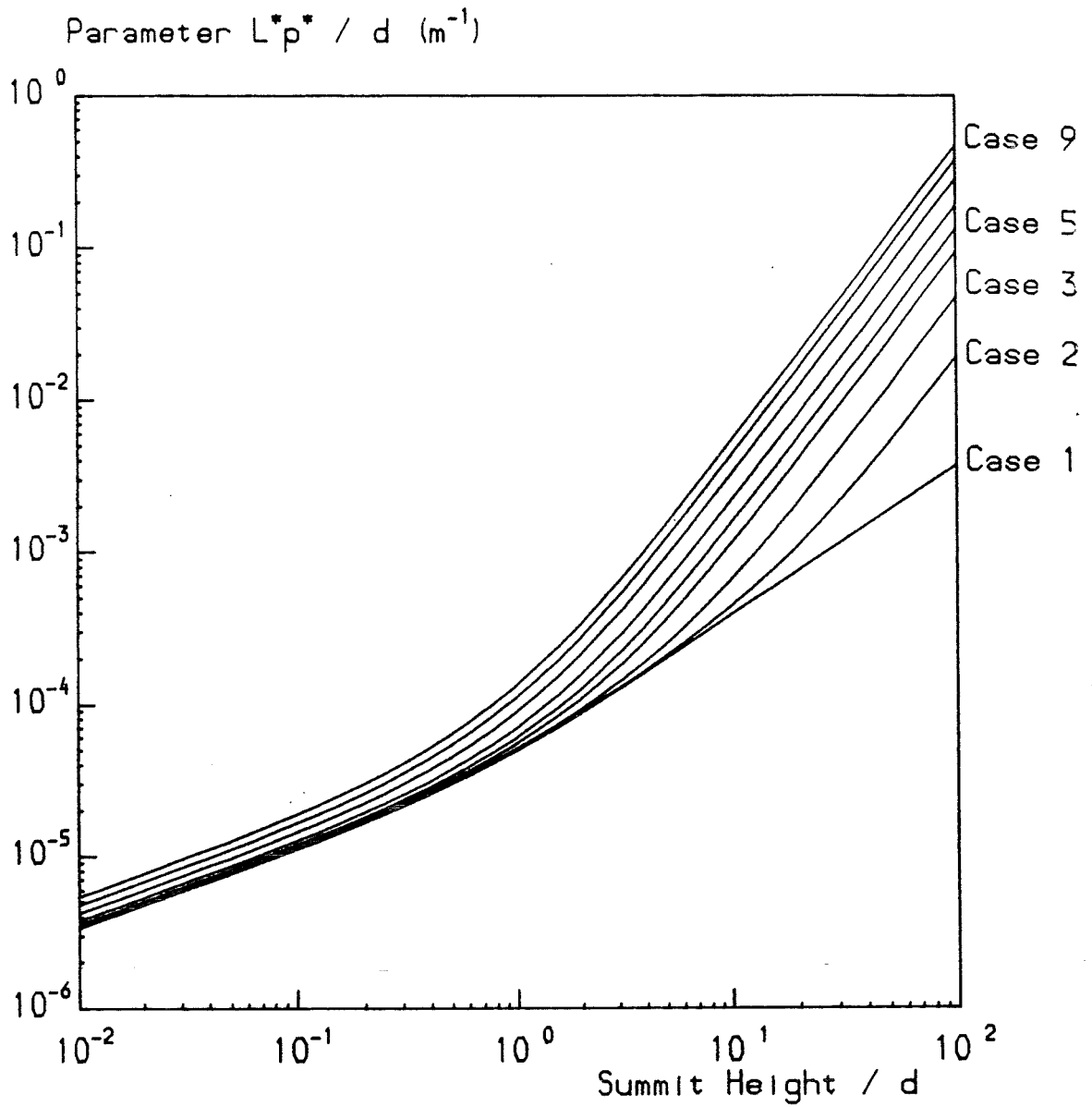


Figure 6.10 The variation of the parameter L^*p^*/d with loop summit height for varying amounts of shear. Case 1 represents the unshaped arcade. In this figure it is assumed that the coronal heating parameter is independent of magnetic field

Table 6.III

Case 1	$k_1/k = 0.0$ (Unsheared Case)
Case 2	$k_1/k = 0.05$
Case 3	$k_1/k = 0.125$
Case 4	$k_1/k = 0.25$
Case 5	$k_1/k = 0.35$
Case 6	$k_1/k = 0.5$
Case 7	$k_1/k = 0.75$
Case 8	$k_1/k = 1.0$
Case 9	$k_1/k = 1.25$

The effect is that the value of L^*p^* originally relevant at a particular summit height now refers to a lower height. Thus loops of the same temperature structure are found but these are closer to the photosphere. Figure 6.11a shows the effect of shearing the arcade generated by contour 1 and Figure 6.11b the effect of shearing the arcade generated by contour 2. In each case the thermal structure is moved towards lower heights. The same effect occurs for the remaining contours.

When $h^*/p^* < 1.25$, there exists a minimum summit height, y_4 for hot loops and when $h^*/p^* < 0.41$, there exists a minimum length, y_3 , for hot-cool loops. These are plotted on Figure 6.12 for a) $h^*/p^* = 0.2$ (y_3 and y_4) and b) $h^*/p^* = 0.5$ (y_4 only). The critical heights are shown in full for $d = 1$ Mm and in broken for $d = 10$ Mm.

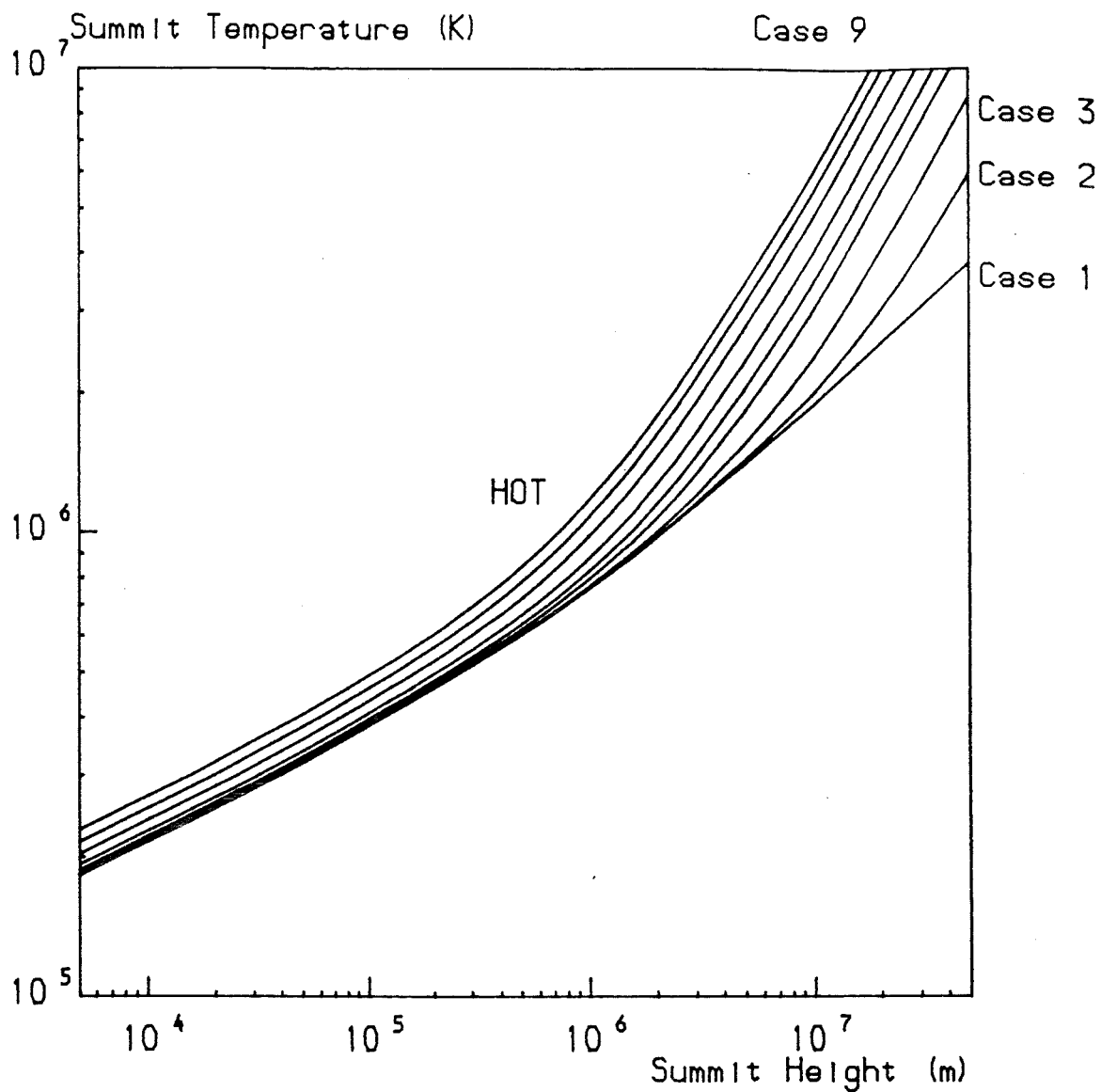


Figure 6.11a The effect on the summit temperature of shearing arcade 1 of section 6.3. It is assumed that the coronal heating parameter h^* is independent of magnetic field strength

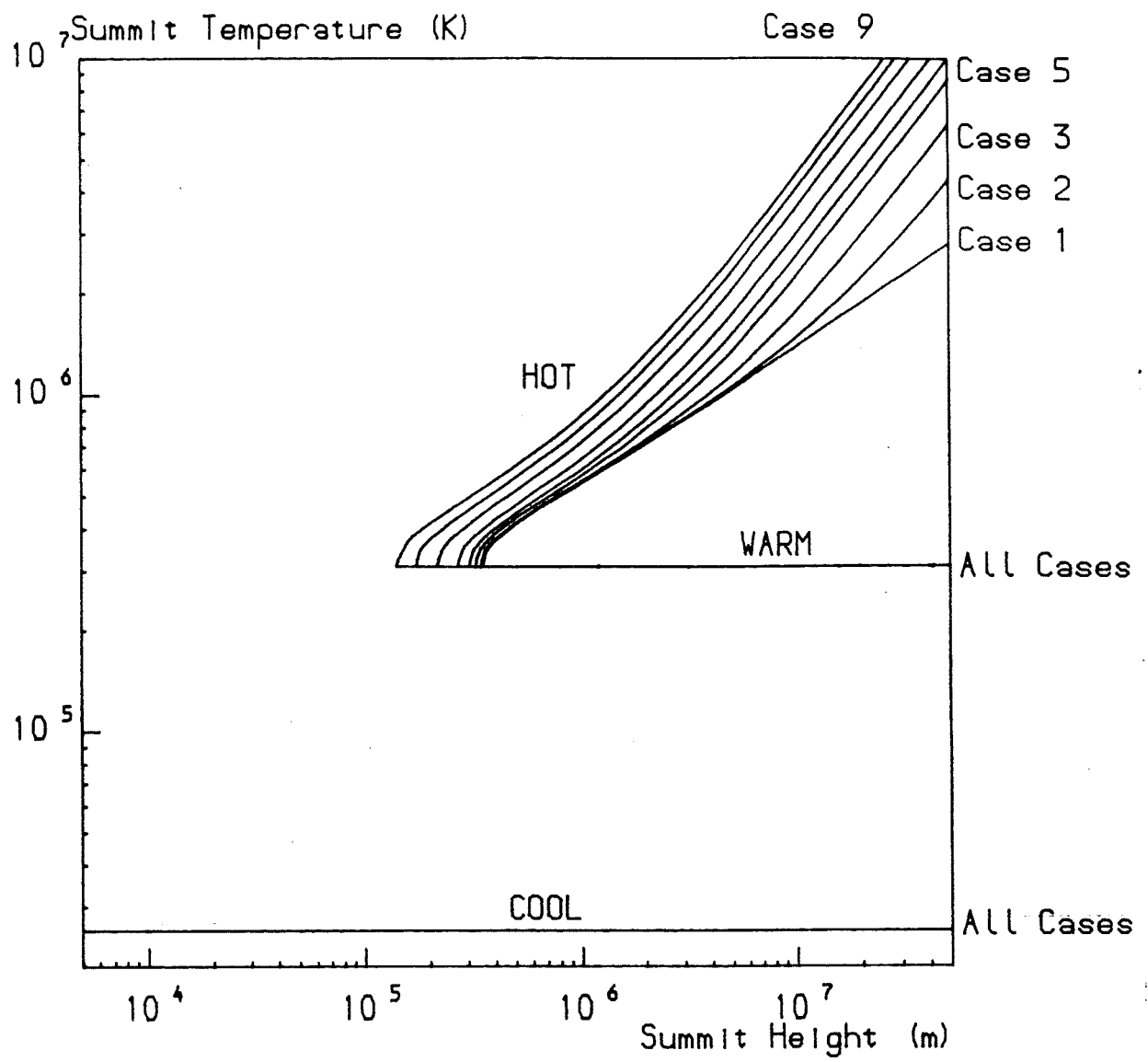


Figure 6.11b The effect on the summit temperature of shearing arcade 2 of section 6.3. It is assumed that the coronal heating parameter h^* is independent of magnetic field strength

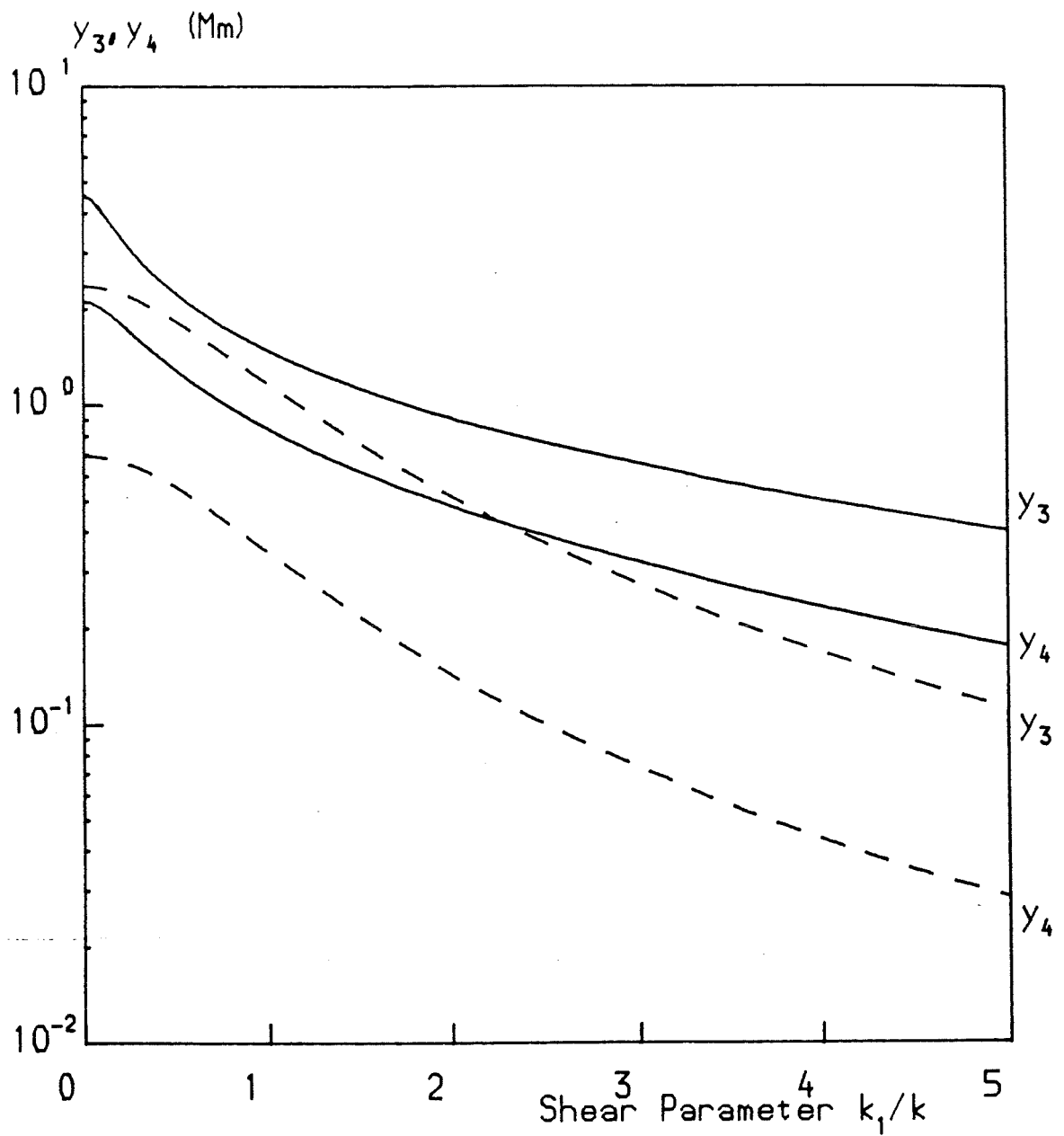


Figure 6.12a The minimum summit heights for hot loops (y_4) and hot-cool loops (y_3) as functions of the shear parameter k_1/k . The full lines denote an axial depth of 1 Mm and the broken lines an axial depth of 10 Mm. The value of $(h/p)_0$ is 0.2.

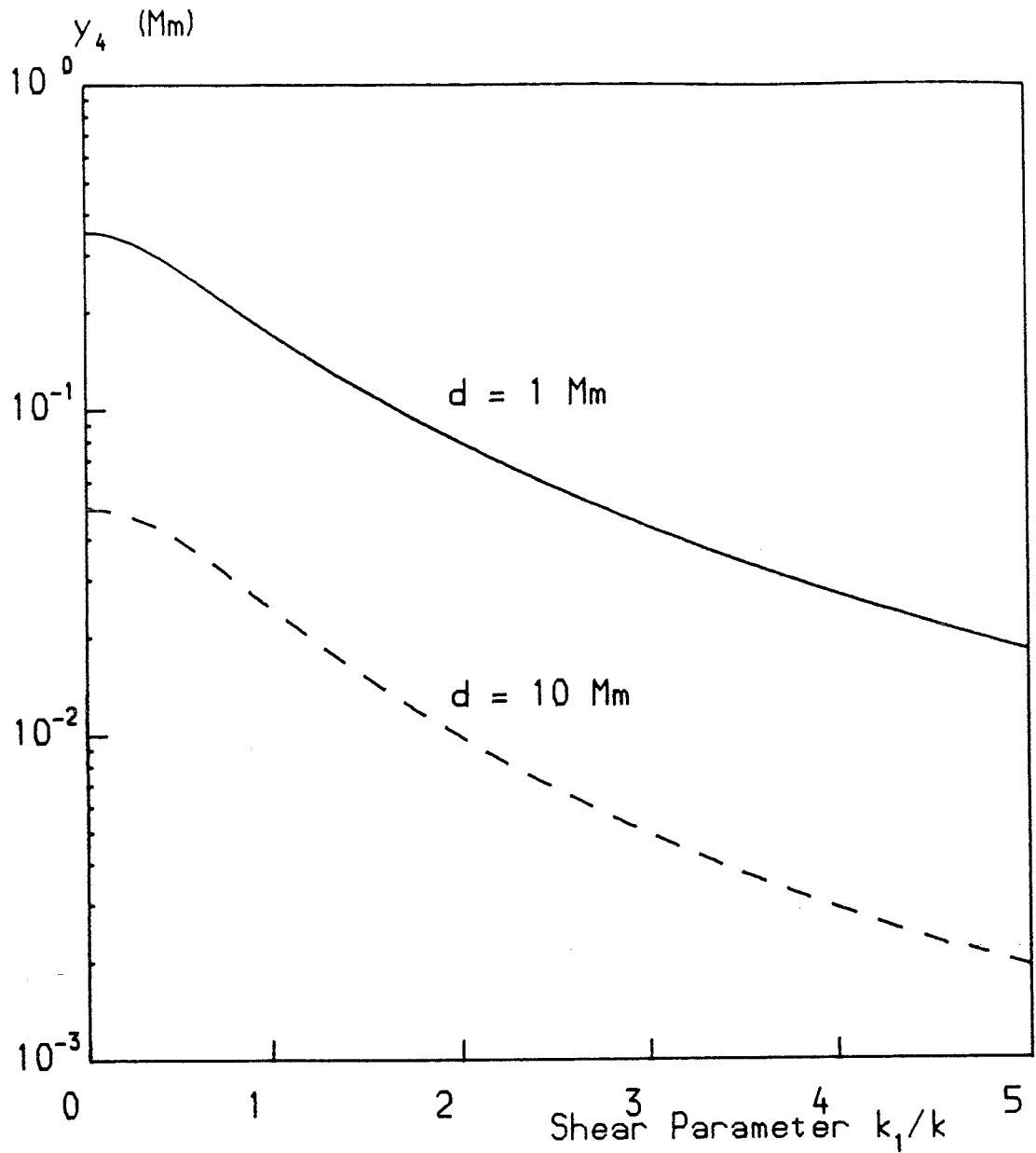


Figure 6.12b The minimum summit heights (y_4) for hot loops as a function of the shear parameter k_1/k . The full line denotes an axial depth of 1 Mm and the broken line an axial depth of 10 Mm. The value of $(h/p)_0$ is 0.5

6.4.2 Magnetic Heating

When the coronal heating parameter depends on the square of the magnetic field, both parameters L^*p^* and h^*/p^* increase on shearing. The parameter h^*/p^* becomes

$$\frac{h^*}{p^*} = \left(\frac{h}{p}\right)_0 \left[\frac{1}{\left(1 + \frac{y_s}{d}\right)^2} + \frac{k_1^2}{k^2} \right] \quad (6.23)$$

where $(h/p)_0$ is the value h^*/p^* takes in the unsheared case at the point on the photosphere directly above the axis. In the limit where $k_1 \gg k$, h^*/p^* reduces to

$$\frac{h^*}{p^*} = \left(\frac{h}{p}\right)_0 \frac{k_1^2}{k^2} \quad (6.24)$$

i.e. the heating parameter is independent of position within the arcade.

Six unsheared arcades are chosen, as determined by the values of d and $(h/p)_0$ in table 6.IV. Five of these arcades correspond to the five arcades from section 6.3; the sixth (arcade 3) was not included in that section as no equilibrium solutions existed.

Table 6.IV

Arcade	$(h/p)_0$	d	Figures
1	2	1 Mm	6.13a, 6.14a
2	0.5	1 Mm	6.13b, 6.14b
3	0.2	1 Mm	6.13c, 6.14c
4	2	10 Mm	6.13d, 6.14d
5	0.5	10 Mm	6.13e, 6.14e
6	0.2	10 Mm	6.13f, 6.14f

The nine values of k_1/k representing the amount of shear applied to the arcade are taken to be the same as in section 6.4.1. Figure 6.13 shows the effect of shearing the arcade on the contour in $(L^*p^*)-(h^*/p^*)$ parameter space while Figure 6.14 shows how the temperature profile is affected by the shear.

Figures 6.13a and 6.14a refer to arcade 1. The unsheared arcade can have hot loops up to summit heights of 2 Mm and warm or cool loops between summit heights of 0.3 Mm and 1.3 Mm. There is thus a finite upper limit to the size of the arcade. Of course as the field is weaker towards this outer limit the background field may well change the situation. On increasing the parameter k_1/k a second regime of hot loops appears at large summit heights (Case 3) and on increasing the shear still further this regime joins onto the existing regime (Case 4). Hot-cool loops appear at large summit heights (greater than 2.5 Mm for case 4). When case 6 is reached, the hot-cool loops are no longer present and the regions of warm and cool loops may extend out indefinitely. On reaching case 8, the warm and cool loops no longer exist as h^*/p^* is always greater than 1.25. The only loops possible now are hot loops. The temperatures of the hot loops are greater than the temperatures of the hot loops in the unsheared case.

The shearing of arcade 2 has several features in common with the shearing of arcade 1. On both cases the contours increase in both L^*p^* and h^*/p^* and the variation of h^*/p^* along the contour decreases. In both unsheared

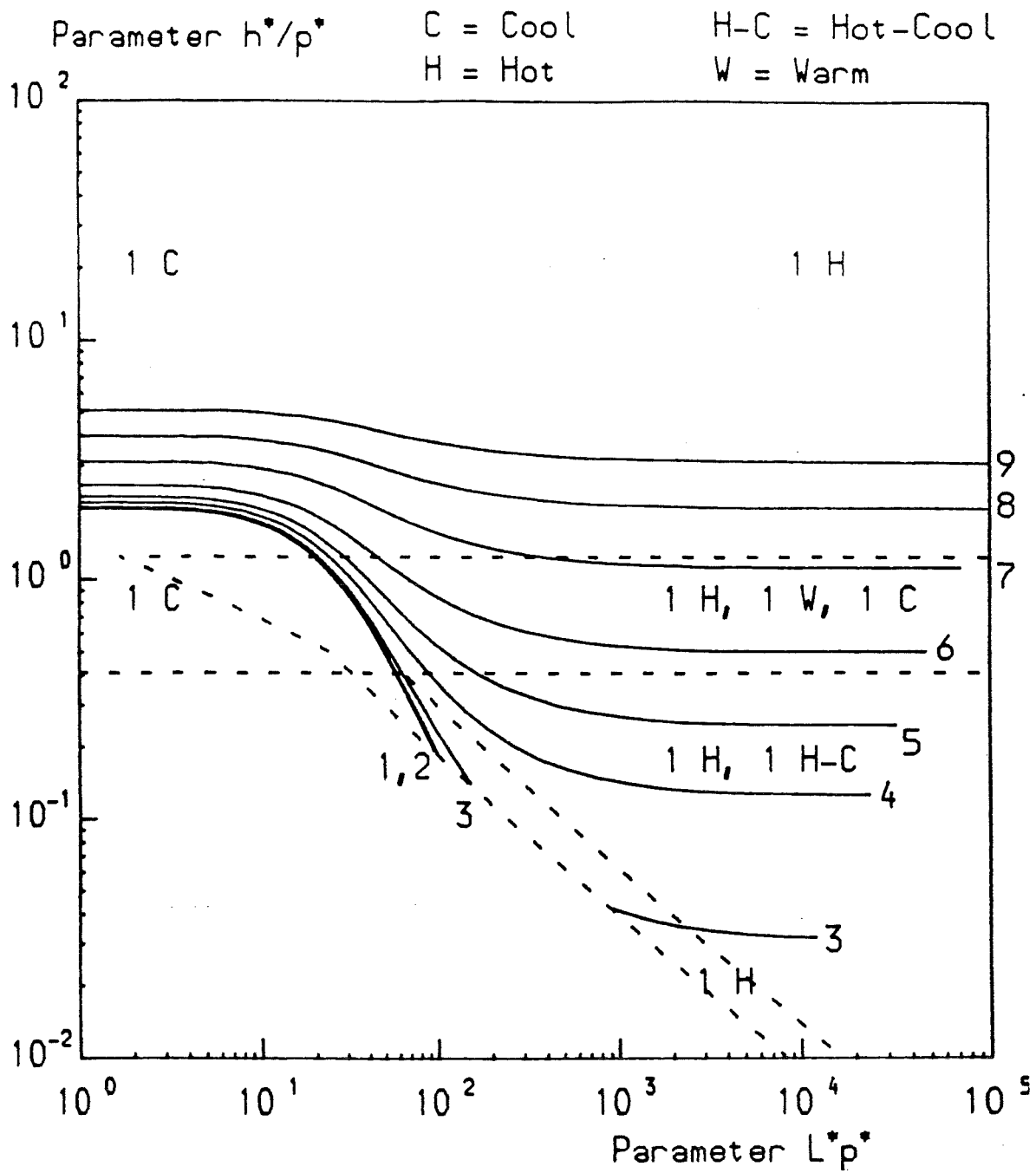


Figure 6.13a The effect on the contour in $(L^*p^*)-(h^*/p^*)$ space describing arcade 1 of section 6.4.2 of shearing the relevant arcade. The nine cases mentioned refer to the amounts of shear in Table 6.III.

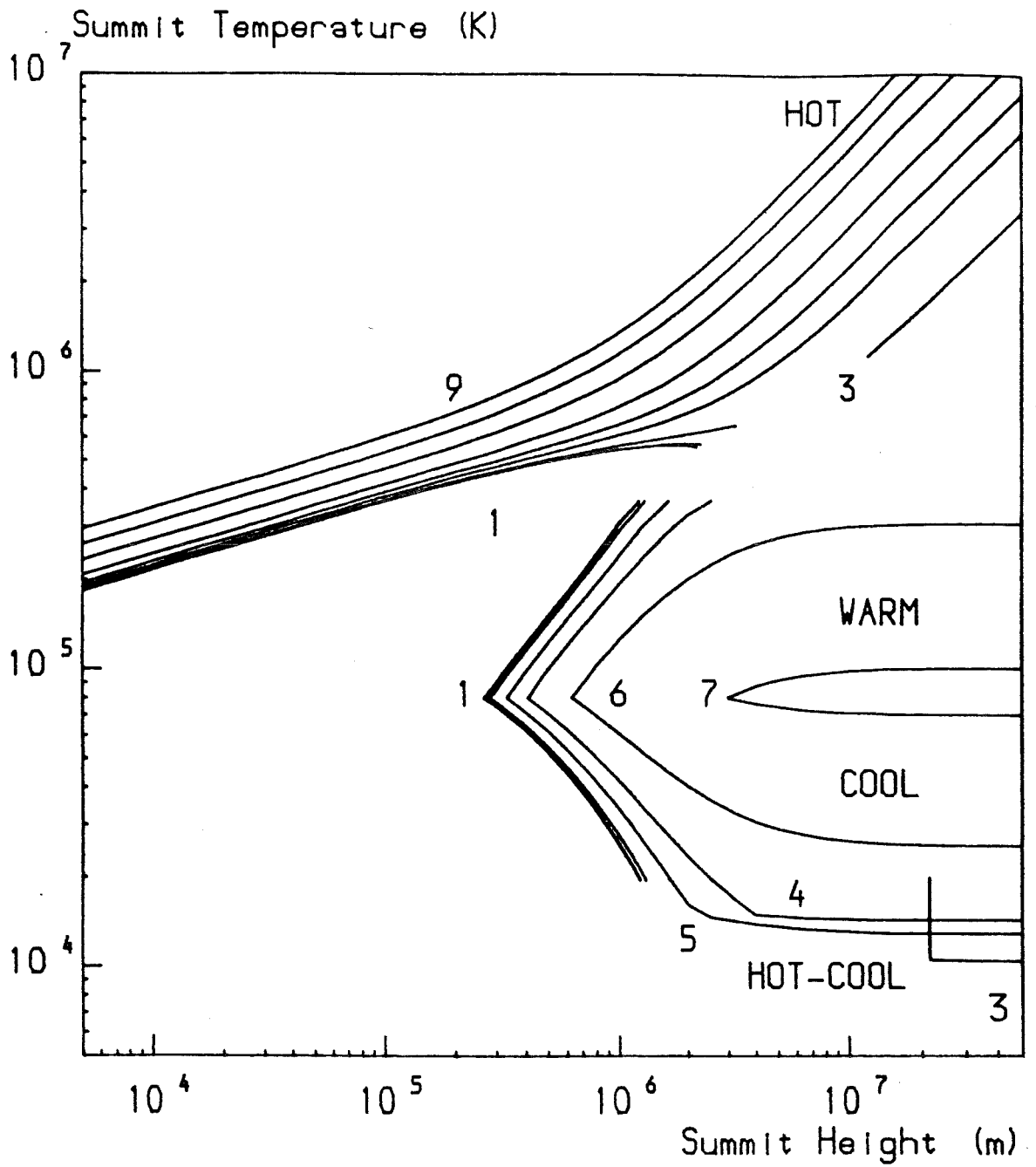


Figure 6.14a The loop summit temperature as a function of loop summit height for differing amounts of shear. The arcade sheared is arcade 1 of section 6.4.2.

cases there is an upper limit to the size of the arcade but shearing the arcade allows solutions at all summit heights. The unsheared version of arcade 2 consists of cool loops within 0.1 Mm of the photosphere and no loops at greater distances. On applying shear the region of cool loops expands slightly and firstly hot and then hot-cool loops appear at large summit heights (case 4). The regions of cool and hot loops expand towards each other until (case 7) there are solutions for all summit heights. There are now cool loops as high as 1 Mm and hot-cool loops beyond. There are also warm loops at summit heights between 0.03 and 1 Mm and hot loops at all summit heights in excess of 0.03 Mm. Increasing the shear further removes the hot-cool loops as h^*/p^* is always greater than 1.25 and also allows the hot loops to extend right down to join smoothly onto the cool loops near the photosphere.

In the unsheared case arcade 3 possesses no equilibrium solutions at all. On shearing, hot and hot-cool loops appear at large summit heights (e.g. 25 Mm and 35 Mm respectively for case 4). On increasing the shear further, the heights of the lower boundaries of the regimes of hot and hot-cool loops decrease. Eventually (case 9) for low L^*p^* , h^*/p^* gets larger than 0.41 and cool loops appear near the photosphere and warm loops for a range of r equal to the upper part of the range of cool loops. If the shear were to be increased further the hot-cool loops would disappear and subsequently the warm and cool loops would no longer exist and hot loops would stretch down to the photosphere.

Arcade 4 (Figures 6.13d, 6.14d) has many points in

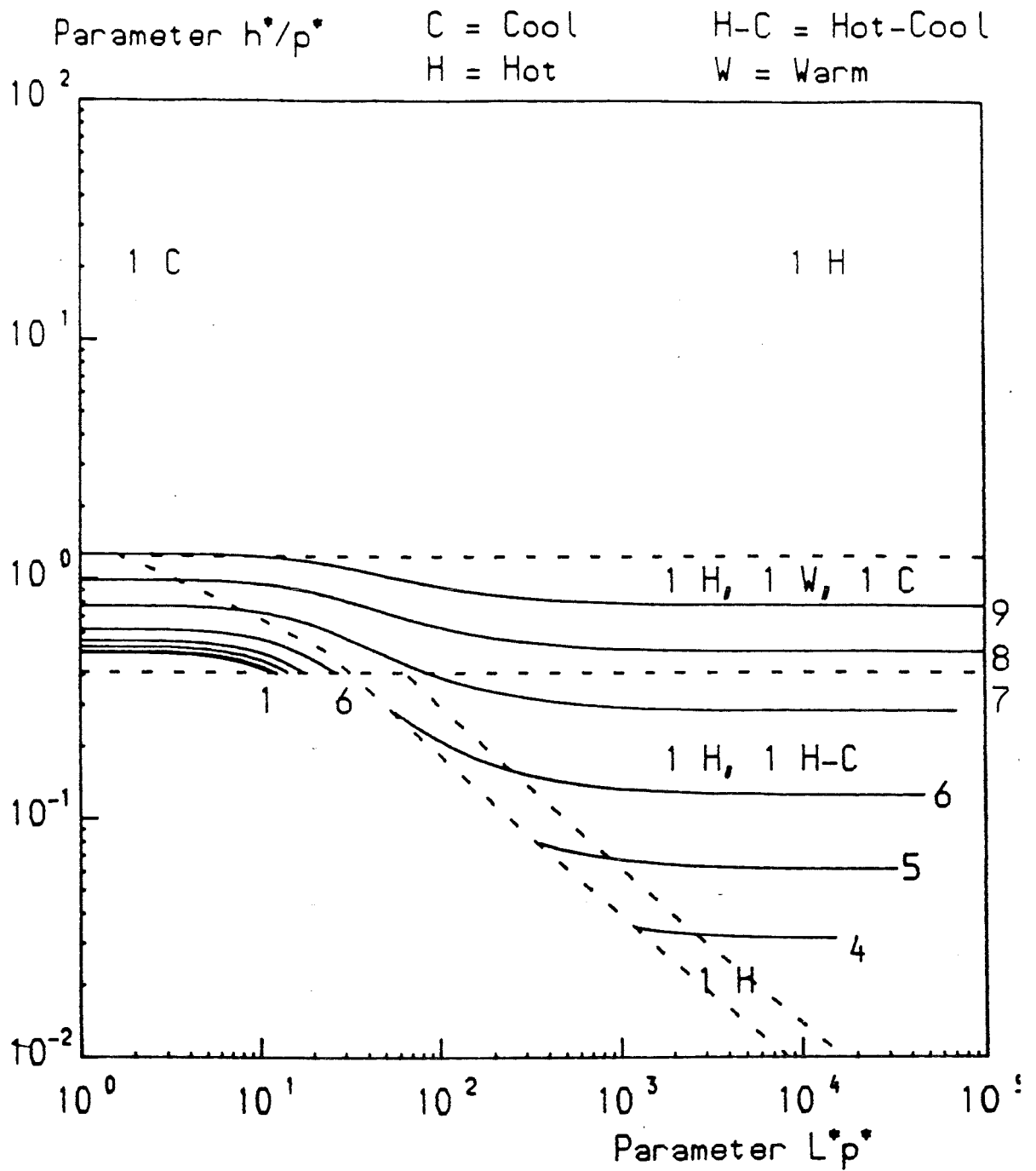


Figure 6.13b The effect on the contour in (L^*p^*) - (h^*/p^*) space describing arcade 2 of section 6.4.2 of shearing the relevant arcade. The nine cases mentioned refer to the amounts of shear in Table 6.III.

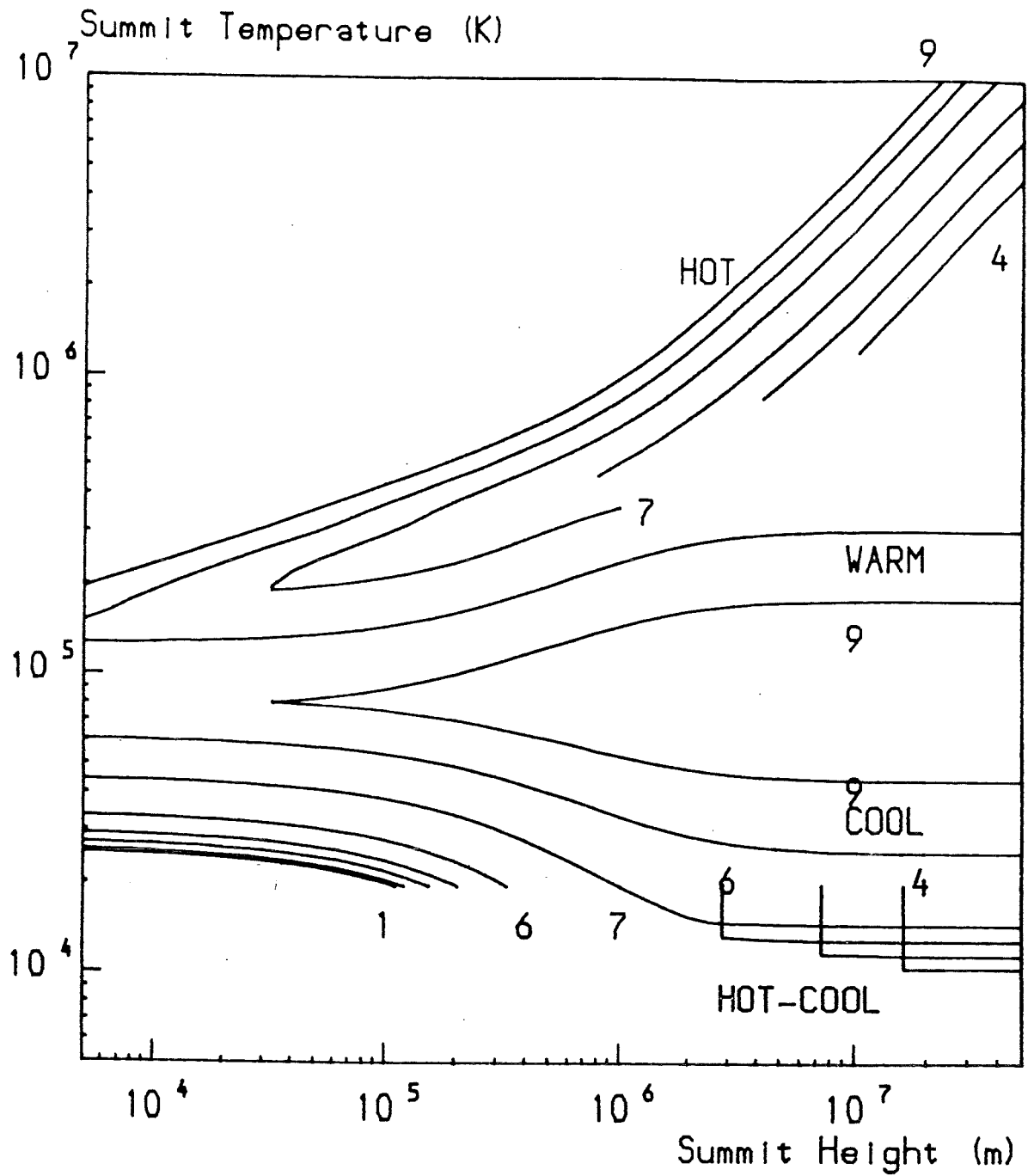


Figure 6.14b The loop summit temperature as a function of loop summit height for differing amounts of shear. The arcade sheared is arcade 2 of section 6.4.2.

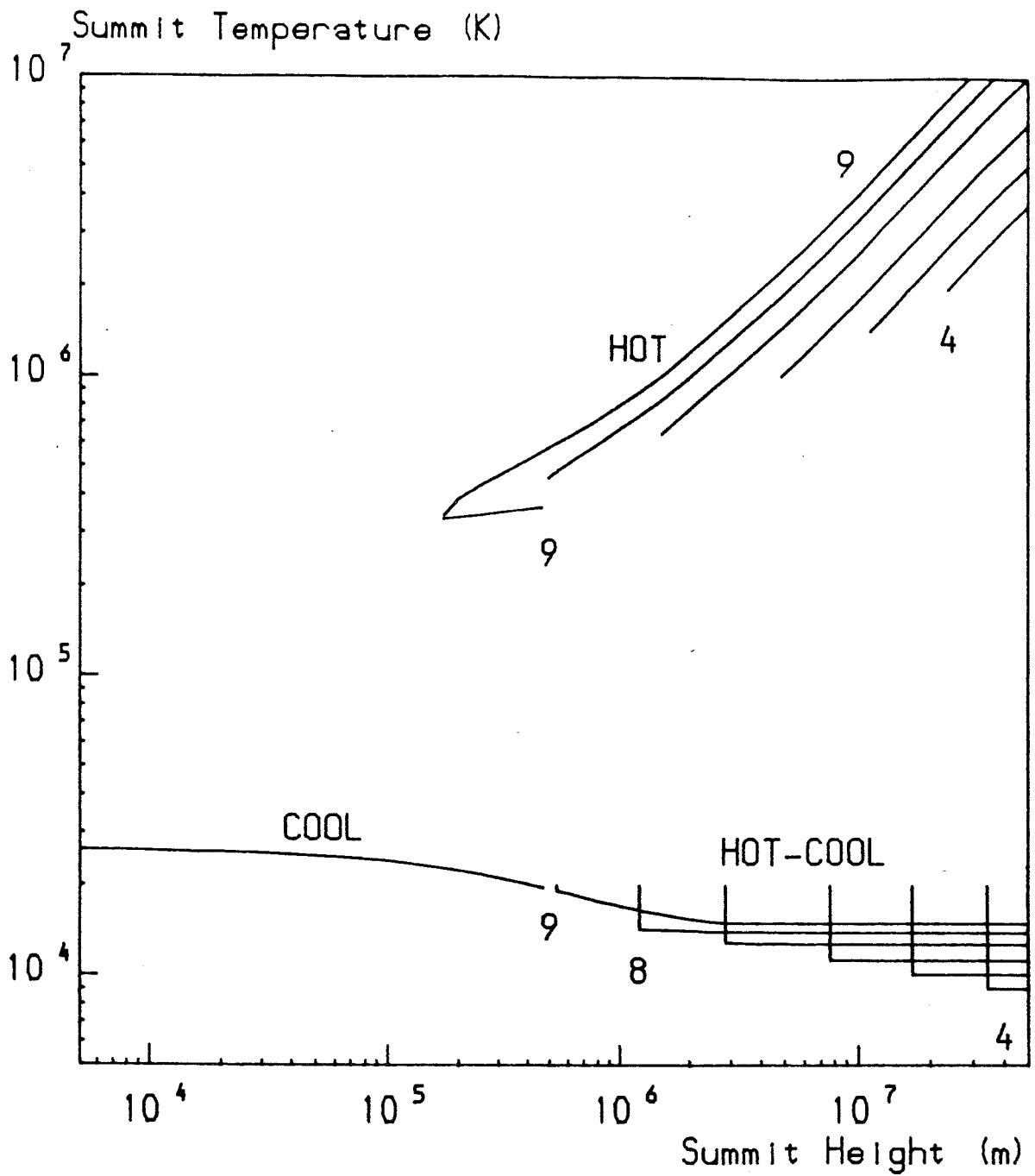


Figure 6.14c The loop summit temperature as a function of loop summit height for differing amounts of shear. The arcade sheared is arcade 3 of section 6.4.2.

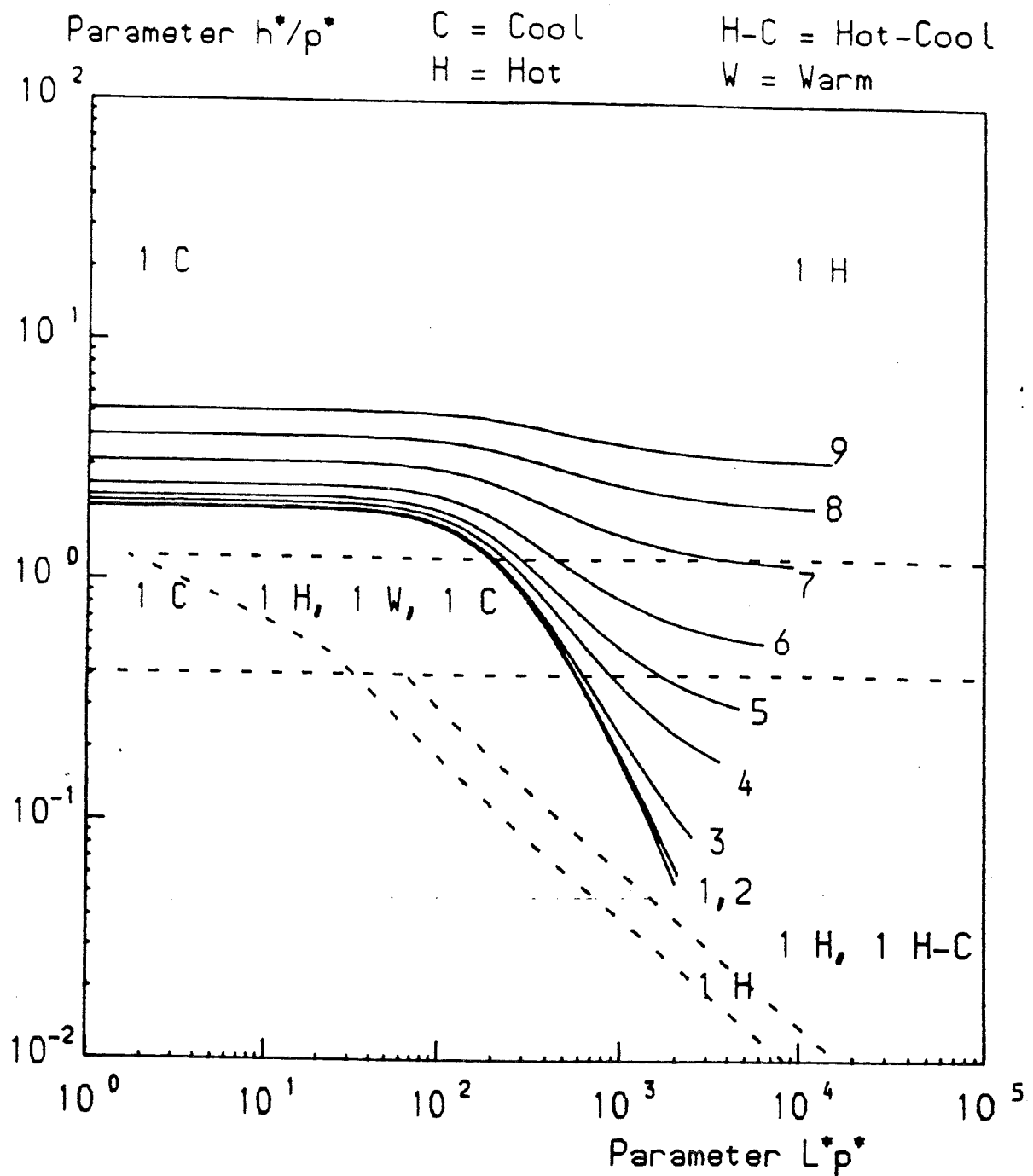


Figure 6.13d The effect on the contour in $(L^*p^*)-(h^*/p^*)$ space describing arcade 4 of section 6.4.2 of shearing the relevant arcade. The nine cases mentioned refer to the amounts of shear in Table 6.III.

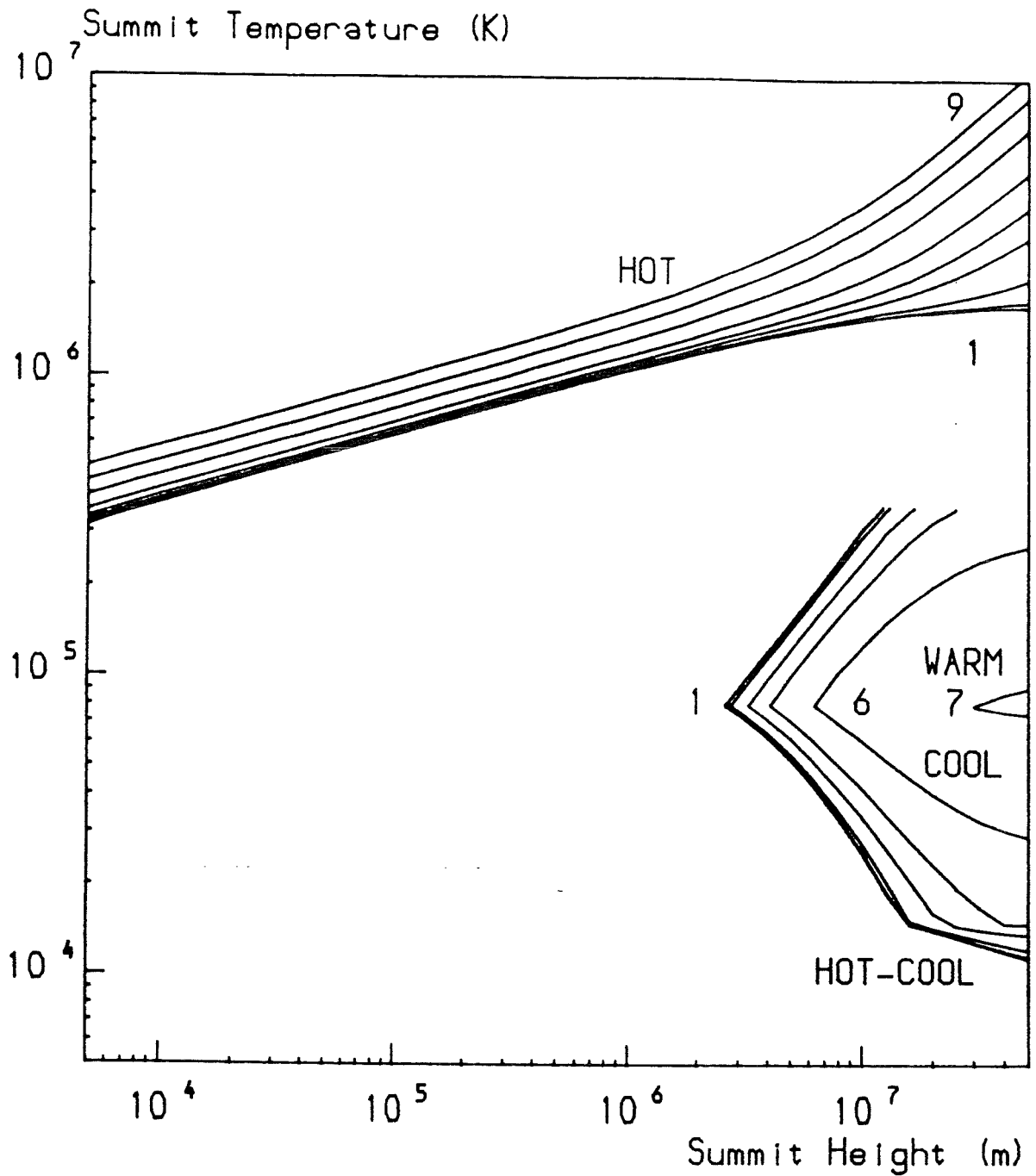


Figure 6.14d The loop summit temperature as a function of loop summit height for differing amounts of shear. The arcade sheared is arcade 4 of section 6.4.2.

common with arcade 1. It may seem strange that the contours for arcade 1 extend to larger values of L^*p^* but this is because of the term $(1 + y_s/d)^4$. There are two main differences between Figure 6.14a and Figure 6.14d apart from the fact that features occur at greater summit heights for Figure 6.14d. Due to the larger value of d , hot solutions exist for all values of the summit height and all values of the shear parameter k_1/k . Hot-cool solutions (in arcade 4) exist for cases 1 and 2 and those, together with the hot-cool solution for case 3 join smoothly (as far as the summit temperature is concerned) onto the corresponding cool solutions.

Similarly, the temperature profile for the shearing of arcade 5 has much in common with that for arcade 2. The effect of the increase in d is that the contours 1 to 6 no longer cross from the area of cool solutions to the area where no equilibria exist. Loops exist for all values of loop summit height (except for in the cases of very low shear where there is a finite upper limit to the size of the arcade). In the unsheared case (case 1) hot-cool loops exist between summit heights of 2 and 16 Mm and warm and cool loops when the summit height is less than 2 Mm, the cool loops extending down to the photosphere. Hot loops exist for summit heights between 0.1 Mm (the minimum summit height for warm loops) and 30 Mm. On shearing, the range of hot loops increases until there is no finite upper limit to the size of the arcade. The regions of warm and cool loops increase in size and the region of hot-cool loops moves outwards until (case 4) such loops can extend out indefinitely. On increasing the shear still further, (case 8)

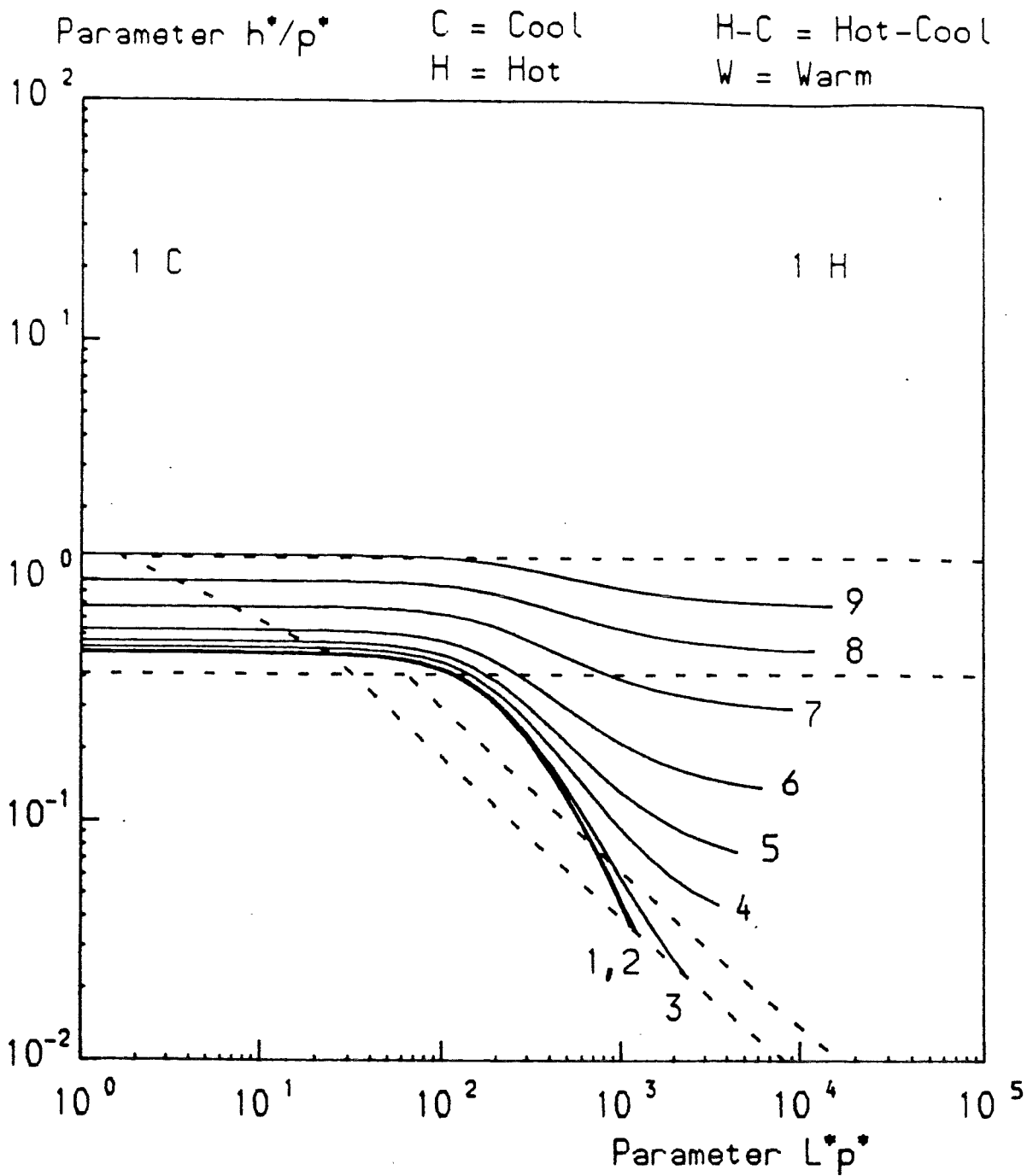


Figure 6.13e The effect on the contour in $(L^*p^*)-(h^*/p^*)$ space describing arcade 5 of section 6.4.2 of shearing the relevant arcade. The nine cases mentioned refer to the amounts of shear in Table 6.III.

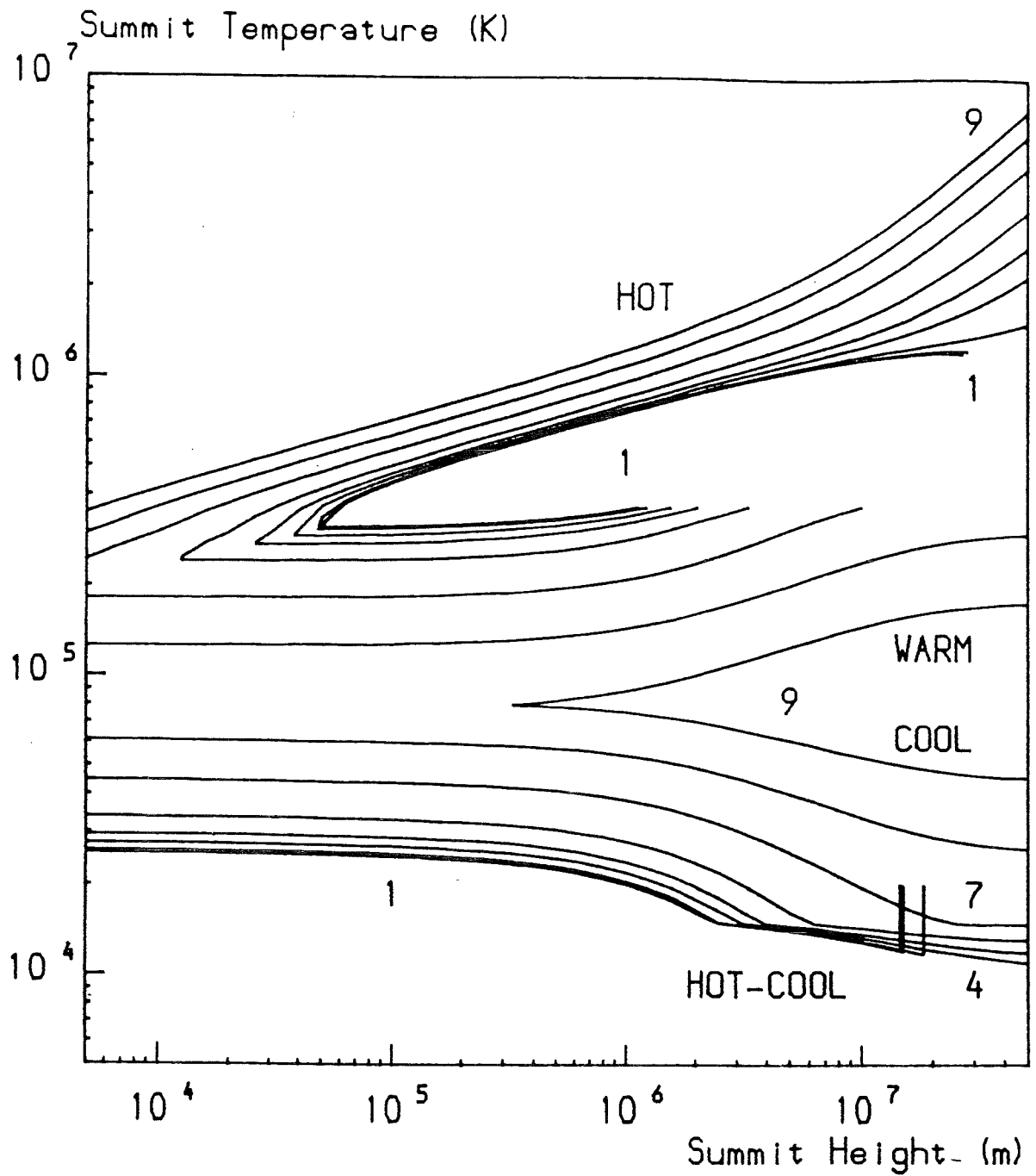


Figure 6.14e The loop summit temperature as a function of loop summit height for differing amounts of shear. The arcade sheared is arcade 5 of section 6.4.2.

the hot-cool loops no longer exist and the warm and cool loops extend out indefinitely. Further increasing the shear would cause the warm and cool solutions no longer to exist.

The unsheared case of arcade 6 consists merely of a small annulus (summit heights of 1 to 4 Mm) of hot loops. On applying shear this annulus expands both inwards and outwards. Also (case 4) another region of hot loops appears at large summit height and the two regions (case 5) join up. At this stage hot-cool loops appear. The hot-cool loops extend to lower summit heights until they join up (as far as summit temperatures are concerned) with cool loops near the photosphere. Also at this stage warm loops can exist for summit heights between the lower limit for hot loops and the upper limit for cool loops. If the shear were increased still further firstly the hot-cool loops and then the warm loops would disappear and there would be hot loops at large summit heights joining smoothly onto cool loops near the photosphere.

6.4.3 Sheared arcade with Constant Field Strength on Outer Field Line

The method of shearing described in sections 6.4.1 and 6.4.2 is a fairly simplistic model for the process. Regrettably it suffers from two shortcomings. As the arcade is sheared the footpoints at large distances move further than footpoints close to the axis and in the extreme case footpoints at infinity move an infinite distance. Also, as the shearing is carried out, the field at any point in the arcade increases (as the azimuthal component remains unchanged

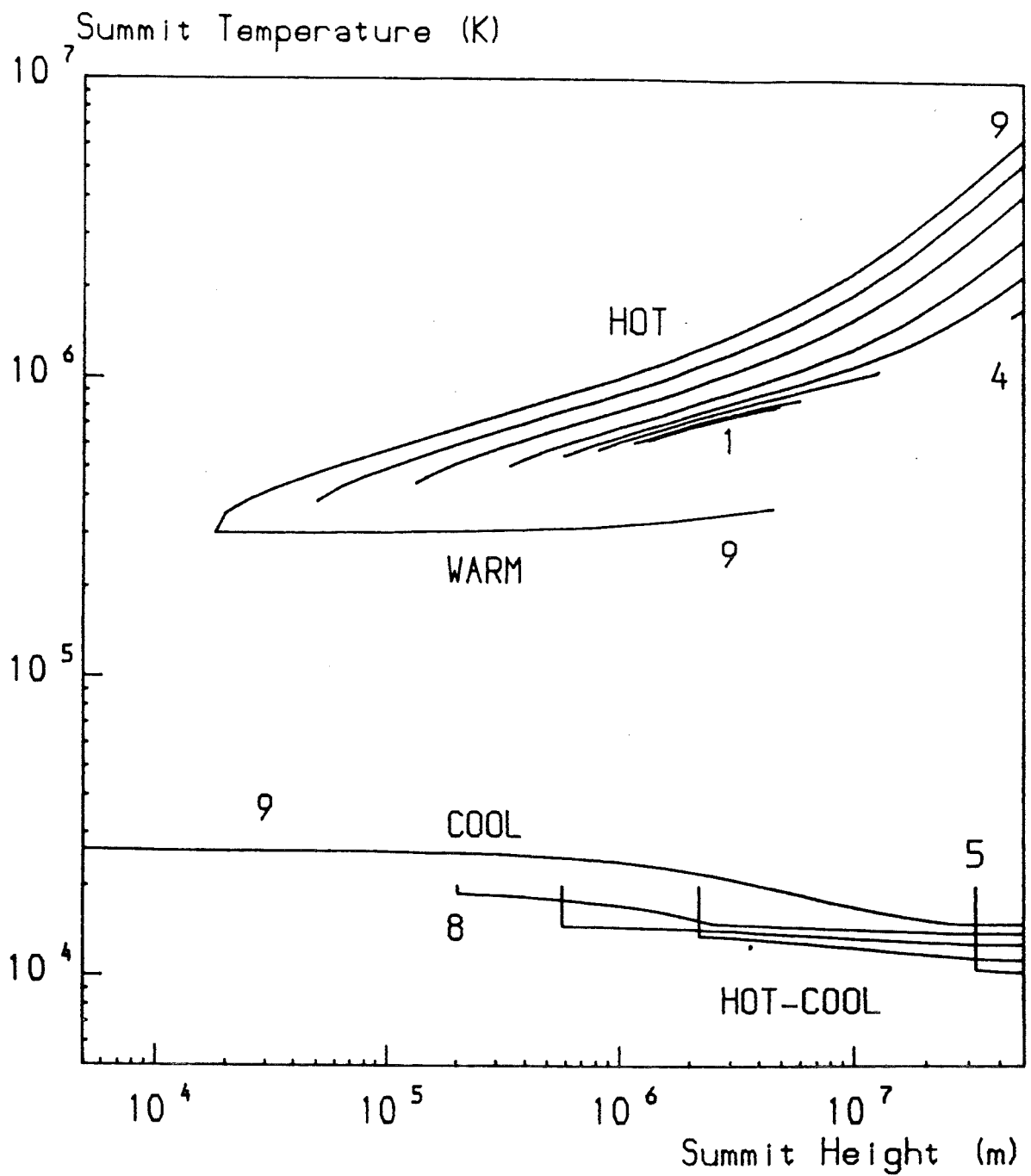


Figure 6.14f The loop summit temperature as a function of loop summit height for differing amounts of shear. The arcade sheared is arcade 6 of section 6.4.2.

and a longitudinal component appears). For pressure balance with the corona outside the arcade, the pressure of the corona must increase similarly. This is not the case for the analysis of section 6.4.1 and 6.4.2.

To prevent those difficulties, the arcade is given a finite size. It is assumed that loops have footpoints no further than a distance w to either side of the point on the photosphere directly above the axis. Loops therefore have heights above the photosphere up to $(w^2 + d^2)^{1/2} - d$. To preserve the pressure balance at the outer boundary of the arcade, the magnetic field of the outer field line is constrained to be constant. One way to do this is to scale the field by a constant value. This does produce difficulties (e.g. the flux through the surface decreases as shear is applied) but this method of shearing will be investigated.

The magnetic field in the arcade satisfies

$$B^2 = \frac{k^2}{r^2} + \frac{k_1^2}{d^2} \quad (6.25)$$

where k and k_1 are scaled by a common multiplier. For the unsheared case and the outer field line (satisfying $r^2 = d^2 + w^2$) the field is given by

$$B^2 = \frac{k_o^2}{w^2 + d^2} \quad (6.26)$$

where k_o is the value of k for the unsheared arcade. Equating

$$\frac{k^2}{w^2 + d^2} + \frac{k_1^2}{d^2} = \frac{k_o^2}{w^2 + d^2} \quad (6.27)$$

and, keeping k_1/k as a parameter,

$$\left(\frac{k}{k_0}\right)^2 = \frac{1}{1 + \left(1 + \frac{w^2}{d^2}\right) \left(\frac{k_1}{k}\right)^2} \quad (6.28)$$

and so

$$\left(\frac{B}{B_0}\right)^2 = \frac{\left(1 + \frac{y_s}{d}\right)^{-2} + \frac{k_1^2}{k^2}}{1 + \left(1 + \frac{w^2}{d^2}\right) \frac{k_1^2}{k^2}} \quad (6.29)$$

where y_s is the height of the loop summit above the photosphere and B_0 is the field strength at the point on the photosphere directly above the axis in the unsheared case. The parameter L^*p^* is the same as it was for the first method of shearing but as the field varies, the parameter h^*/p^* must be amended for the case where the heating parameter varies with the field strength. The parameter h^*/p^* is now given by

$$\frac{h^*}{p^*} = \frac{\frac{1}{\left(1 + \frac{y_s}{d}\right)^2} + \frac{k_1^2}{k^2}}{1 + \left(1 + \frac{w^2}{d^2}\right) \frac{k_1^2}{k^2}} \left(\frac{h}{p}\right)_0 \quad (6.30)$$

where $(h/p)_0$ is the value of the parameter h^*/p^* at the point on the photosphere directly above the axis. In the limit that k_1/k is large, h^*/p^* becomes

$$\frac{h^*}{p^*} = \frac{\left(\frac{h}{p}\right)_0}{1 + \frac{w^2}{d^2}} \quad (6.31)$$

i.e. the coronal heating parameter is constant. This is because the magnetic field is dominated by the constant longitudinal component.

The shear is again given by

$$z = \frac{k_1}{k} \frac{d^2 + x^2}{d^2} \left(\tan^{-1} \frac{d}{x} - \frac{\pi}{2} \right) + z_s \quad (6.32)$$

which is directly proportional to the parameter k_1/k and it is for this reason that the shear is increased by increasing k_1/k rather than k_1/k_0 . The two parameters are linked by

$$\left(\frac{k_1}{k_0} \right)^2 = \frac{\left(\frac{k_1}{k} \right)^2}{1 + \left(1 + \frac{w^2}{d^2} \right) \left(\frac{k_1}{k} \right)^2} \quad (6.33)$$

If the shear were to tend towards infinity, k_1/k would tend towards infinity similarly while k_1/k_0 would tend towards the constant value $1/(1 + w^2/d^2)$.

Figure 6.15 shows how the contour in the (L^*p^*) - (h^*/p^*) plane changes as the arcade is sheared. The parameters used were $d = 10$ Mm, $w = 50$ Mm, $(h/p)_0 = 2.0$. Nine values of the parameter k_1/k are chosen, the same values as in the previous section. Instead of the right hand end of the contour moving up as shear is applied, the left hand end moves down. As before the result when k_1/k is large is that h^*/p^* does not vary much within the arcade but the almost constant value of h^*/p^* is lower. The value of h^*/p^* at the outer boundary of the arcade remains constant as the magnetic field has been constrained to be constant, but on shearing the outer value of L^*p^* increases as the field lines are now longer. For larger values of the shear (Cases 6 to 9) for low summit heights, the contour passes through the area where no equilibria can be found.

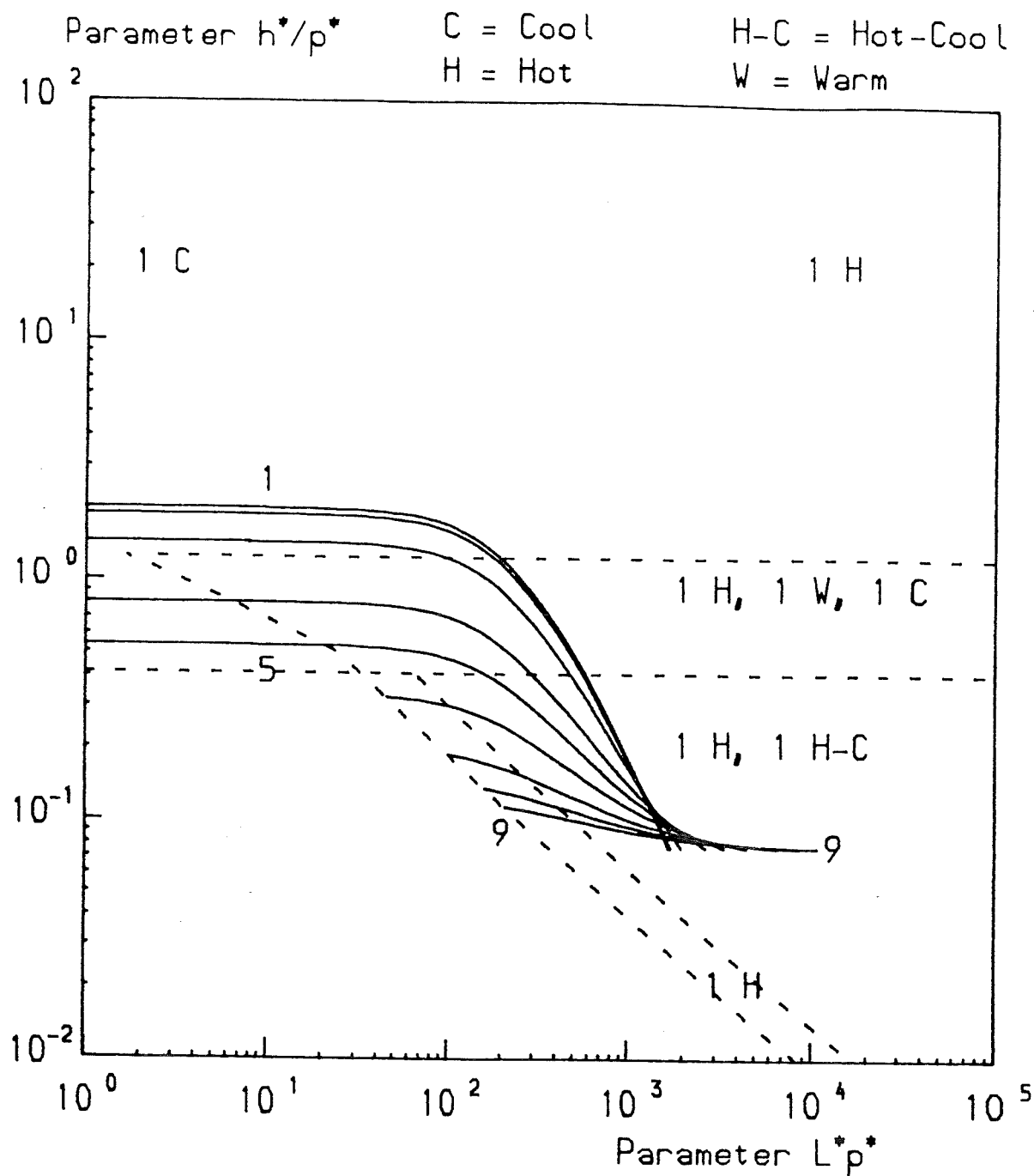


Figure 6.15 The contour on two dimensional (L^*p^*) (h^*/p^*) parameter space describing the arcade of section 6.4.3 and the effect on this contour of shearing the arcade. At the outer boundary, h^*/p^* remains constant as the outer field line is constrained to retain its field strength but closer to the axis the field strength is reduced. The parameter L^*p^* increases near the outer boundary as the loop lengths increase.

Figure 6.16 shows the effect of the shear on the profile of the summit temperature as a function of loop summit height. Case 1 represents the unsheared arcade where hot loops can exist for all values of the summit height up to the maximum summit height for the arcade. Warm or cool loops may exist for summit heights in the range 2 to 10 Mm and hot-cool loops above this. When shear is applied, the summit temperature for the hot loops increases for loops higher than about 10 to 20 Mm but decreases for lower lying loops. The regimes of warm and cool loops move towards lower summit heights as does the lower edge of the regime of hot-cool loops. When case 4 is reached, the cool loops may now reach down to the photosphere. A cool core has now formed to the arcade. The warm and hot loops cannot stretch this far down; both regimes having the same lower limit at the same summit temperature. Once case 6 is reached, the parameter h^*/p^* is always less than the critical value 0.41 thus eliminating the possibility of warm or cool loops. Low lying loops cannot now be in thermal equilibrium. Hot solutions may exist for all loops whose summits lie above a certain height (about 0.15 Mm for case 6 and increasing to about 1 Mm for case 9). Hot-cool loops may exist above another critical height (about 0.8 Mm for case 6 and increasing to about 4 Mm for case 9). Hot-cool loops close to the minimum summit height for such loops have summits at 20 000 K.

Summit Temperature (K)

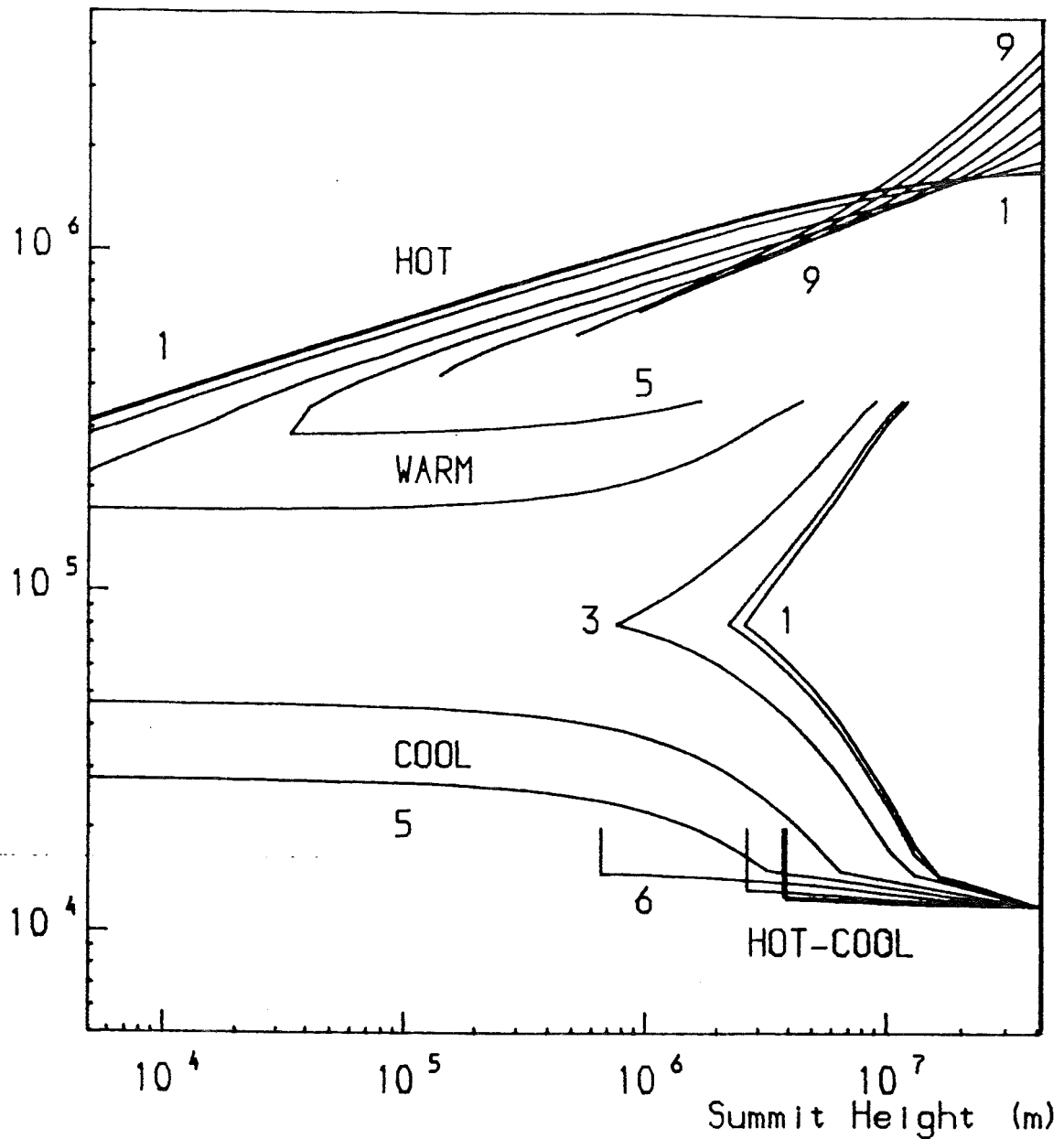


Figure 6.16 The loop summit temperature as a function of loop summit height for the arcade of section 6.4.3 and the effect on the profile of shearing the arcade. Case 1 is the unsheared arcade and case 9 is the most sheared. Shearing the arcade creates a cool core as near the axis hot loops do not exist for cases 5 to 9.

6.4.4 Sheared Arcade with constant Field Strength on Outer Field Line and Constant Flux through Base

A third method of shearing the arcade is similar to the second method in that the field strength of the outer field line retains its value but the magnetic flux through the base of the arcade is assumed to remain constant. Originally the axis is at O (Figure 6.17) a depth d below the axis and the field line with footpoints at A and C (a distance w to either side of the point E on the photosphere directly above the axis) passes through B at its summit. On shearing the axis may move, say to O', a distance D below the photosphere, and the loop summit is now at B'. It is assumed that the magnetic flux passing through AE is conserved. Cylindrical symmetry is assumed.

For the unsheared arcade, the field is $B_\theta = k/r$. The field line ABC has strength $k/(d^2 + w^2)^{1/2}$ and the flux through AE (a unit width in the longitudinal direction) is

$$\begin{aligned} F &= \int_{x=0}^w B_\theta \cos \theta \, dx = \int_{x=0}^w \frac{k}{r} \frac{x}{r} \, dx = \int_{x=0}^w \frac{kx}{x^2 + d^2} \, dx \\ &= \frac{k}{2} \log_e \left(1 + \frac{w^2}{d^2} \right) \end{aligned} \quad (6.34)$$

The sheared arcade is assumed to satisfy

$$\frac{d}{dR} (B_\theta^2 + B_z^2) + \frac{2B_\theta^2}{R} = 0 \quad (6.11)$$

where R is measured from O', a distance D beneath the photosphere.

It is assumed that B_z is constant with R for a

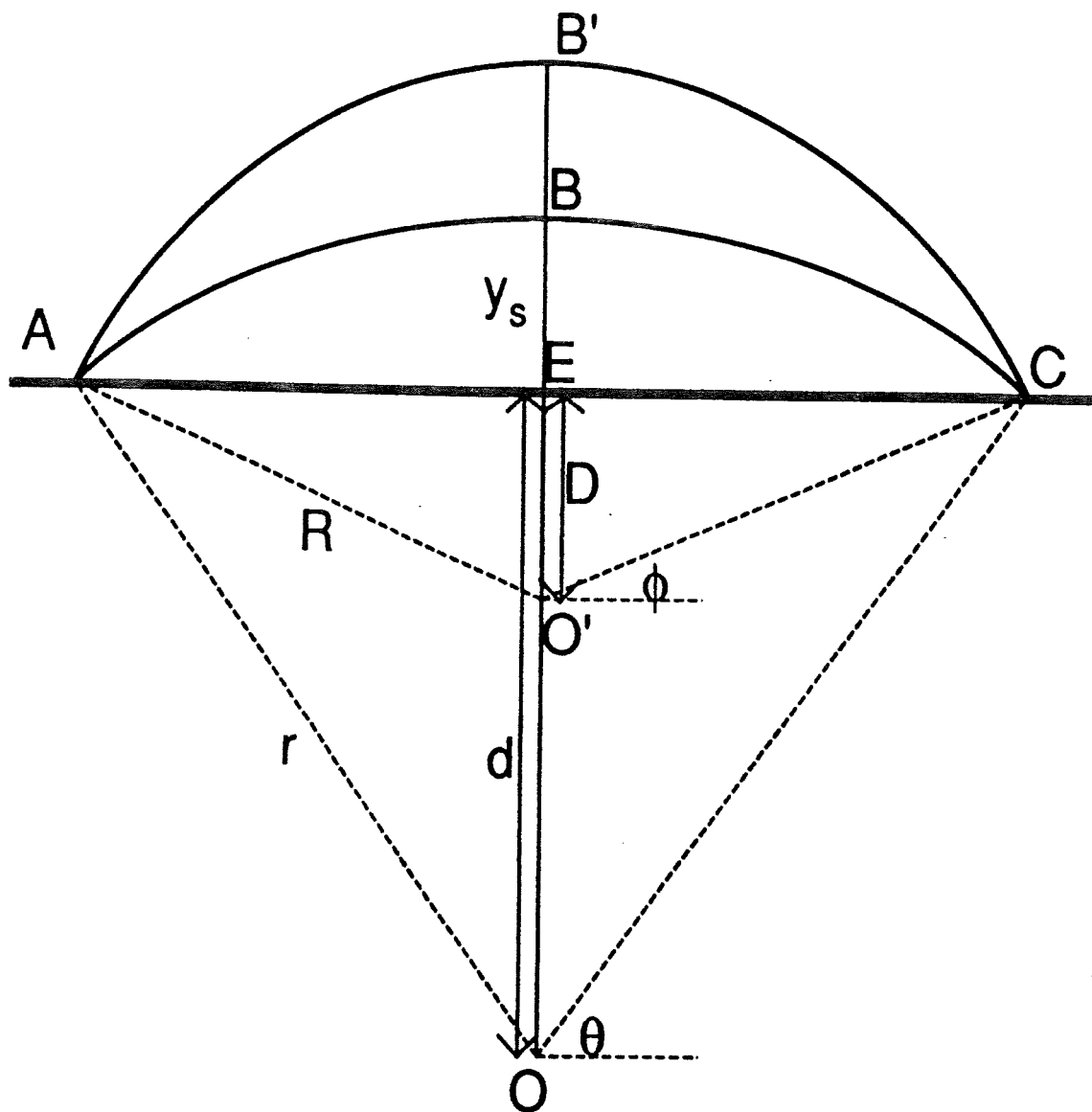


Figure 6.17 A cross-section through the arcades of section 6.4.4. Originally a loop is described by ABC of radius r with centre O a depth d below the photosphere but on shearing, to conserve the magnetic flux through AE, the axis moves upwards to O', a depth D below the photosphere and the loops are of radius R and described by AB'C.

particular arcade and shear and so B_ϕ satisfies $B_\phi = K/R$ for some constant K .

The flux through AE is given by

$$F = \int_{x=0}^w \frac{Kx}{R} dx = \int_{x=0}^w \frac{Kx dx}{x^2 + D^2} = \frac{K}{2} \log_e \left(1 + \frac{w^2}{D^2} \right) \quad (6.35)$$

and so K is given by

$$K = k \frac{\log_e \left(1 + \frac{w^2}{d^2} \right)}{\log_e \left(1 + \frac{w^2}{D^2} \right)} \quad (6.36)$$

The value K_1/D of B_z can be found by constraining the strength of the outer field line to be constant i.e. when $R^2 = D^2 + w^2$, $B_z^2 + B_\phi^2 = k^2/(w^2 + d^2)$; thus

$$K_1^2 = \frac{k^2 D^2}{w^2 + d^2} - \frac{K^2 D^2}{w^2 + D^2} \quad (6.37)$$

The sheared field is given by

$$B_\phi = \frac{K}{R} = \frac{k}{R} \frac{\log_e \left(1 + \frac{w^2}{d^2} \right)}{\log_e \left(1 + \frac{w^2}{D^2} \right)} \quad (6.36)$$

$$B_z = \frac{K_1}{D}$$

$$= k \sqrt{\frac{1}{w^2 + d^2} - \frac{1}{w^2 + D^2} \left[\frac{\log_e \left(1 + \frac{w^2}{d^2} \right)}{\log_e \left(1 + \frac{w^2}{D^2} \right)} \right]^2} \quad (6.39)$$

A field line is described by

$$\frac{R d\phi}{dz} = \frac{B_\phi}{B_z} = \frac{K/R}{B_z} \quad (6.40)$$

and so

$$\frac{dz}{d\phi} = \frac{B_z R^2}{K} \quad (6.41)$$

and

$$z = \frac{B_z R^2}{K} \left(\phi - \frac{\pi}{2} \right) \quad (6.42)$$

At the footpoints $\sin \phi = D/R$ and so

$$z = z_0^{-1} (x^2 + D^2) \left(\tan^{-1} \frac{D}{x} - \frac{\pi}{2} \right) \quad (6.43)$$

where

$$\begin{aligned} z_0^{-1} &= \sqrt{\frac{1}{w^2 + d^2} \frac{\log_e (1 + w^2/D^2)}{\log_e (1 + w^2/d^2)} - \frac{1}{w^2 + D^2}} \\ &= \frac{1}{D} \frac{K_1}{K} \end{aligned} \quad (6.44)$$

For a given amount of shear, the displacement of the footpoints increases with distance from point E on the photosphere directly above the axis.

The parameters h^*/p^* and L^*p^* can now be calculated. The heating parameter h^*/p^* depends on the magnetic field which is given by

$$\begin{aligned} B^2 &= \frac{k^2}{R^2} \left[\frac{\log_e (1 + w^2/d^2)}{\log_e (1 + w^2/D^2)} \right]^2 + \frac{k^2}{w^2 + d^2} \\ &\quad - \frac{k^2}{w^2 + D^2} \left[\frac{\log_e (1 + w^2/d^2)}{\log_e (1 + w^2/D^2)} \right]^2 \\ &= \frac{k^2}{w^2 + d^2} \end{aligned}$$

$$+ k^2 \left[\frac{1}{(D + y_s)^2} - \frac{1}{w^2 + D^2} \right] \left[\frac{\log_e (1 + w^2/d^2)}{\log_e (1 + w^2/D^2)} \right]^2 \quad (6.45)$$

where y_s is the height above the photosphere of the relevant loop. At point E, the point on the photosphere directly above the axis, and for the unsheared arcade, B is given by

$$B^2 = \frac{k^2}{d^2} \quad (6.46)$$

and so

$$\frac{h^*}{p^*} = \left(\frac{h}{p} \right)_0 \left[\frac{1}{1 + \frac{w^2}{d^2}} + \left[\frac{d^2}{(D + y)^2} - \frac{d^2}{w^2 + D^2} \right] \left[\frac{\log_e (1 + \frac{w^2}{d^2})}{\log_e (1 + \frac{w^2}{D^2})} \right]^2 \right] \quad (6.47)$$

where $(h/p)_0$ is the value of the parameter h^*/p^* for the unsheared arcade at the point on the photosphere directly above the axis.

The length L_0 of the loop is calculated by considering the changes in z and ϕ along the loop

$$L_0 = \left(\sin^{-1} \frac{D}{R} - \frac{\pi}{2} \right) x$$

$$\left[\left[\frac{1}{w^2 + d^2} \left[\frac{\log_e (1 + \frac{w^2}{D^2})}{\log_e (1 + \frac{w^2}{d^2})} \right]^2 - \frac{1}{w^2 + D^2} \right] (x^2 + D^2)^2 + R^2 \right]^{1/2}$$

$$= \left(\sin^{-1} \frac{D}{D+y} - \frac{\pi}{2} \right) x$$

$$\left[\left[\frac{1}{w^2 + d^2} \left[\frac{\log_e \left(1 + \frac{w^2}{D^2} \right)}{\log_e \left(1 + \frac{w^2}{d^2} \right)} \right]^2 - \frac{1}{w^2 + D^2} (x^2 + D^2)^2 + (D + y)^2 \right] \right]^{1/2} \quad (6.48)$$

and the parameter L^*p^* is given by

$$L^*p^* = \frac{L_o}{L_\infty} p^* \quad (6.49)$$

Two arcades are sheared using the method described above. Arcade 1 is the arcade sheared in section 6.4.3 (i.e. $w = 50$ Mm, $d = 10$ Mm, $(h/p)_o = 2.0$) and Arcade 2 is described by $w = 50$ Mm, $d = 10$ Mm, $(h/p)_o = 0.5$. As a means of increasing K_1/K , the value of z_o^{-1} is increased leading to a decrease in D , i.e. the axis moves closer to the surface. The following values of $d z_o^{-1}$ are used and the corresponding values of D/d are displayed in Table 6.V.

Table 6.V

	$d z_o^{-1}$	D/d
Case 1	0.0	1.000
Case 2	0.1	0.806
Case 3	0.2	0.482
Case 4	0.3	0.251
Case 5	0.4	0.122
Case 6	0.5	0.057
Case 7	0.6	0.026
Case 8	0.7	0.012
Case 9	0.8	0.005

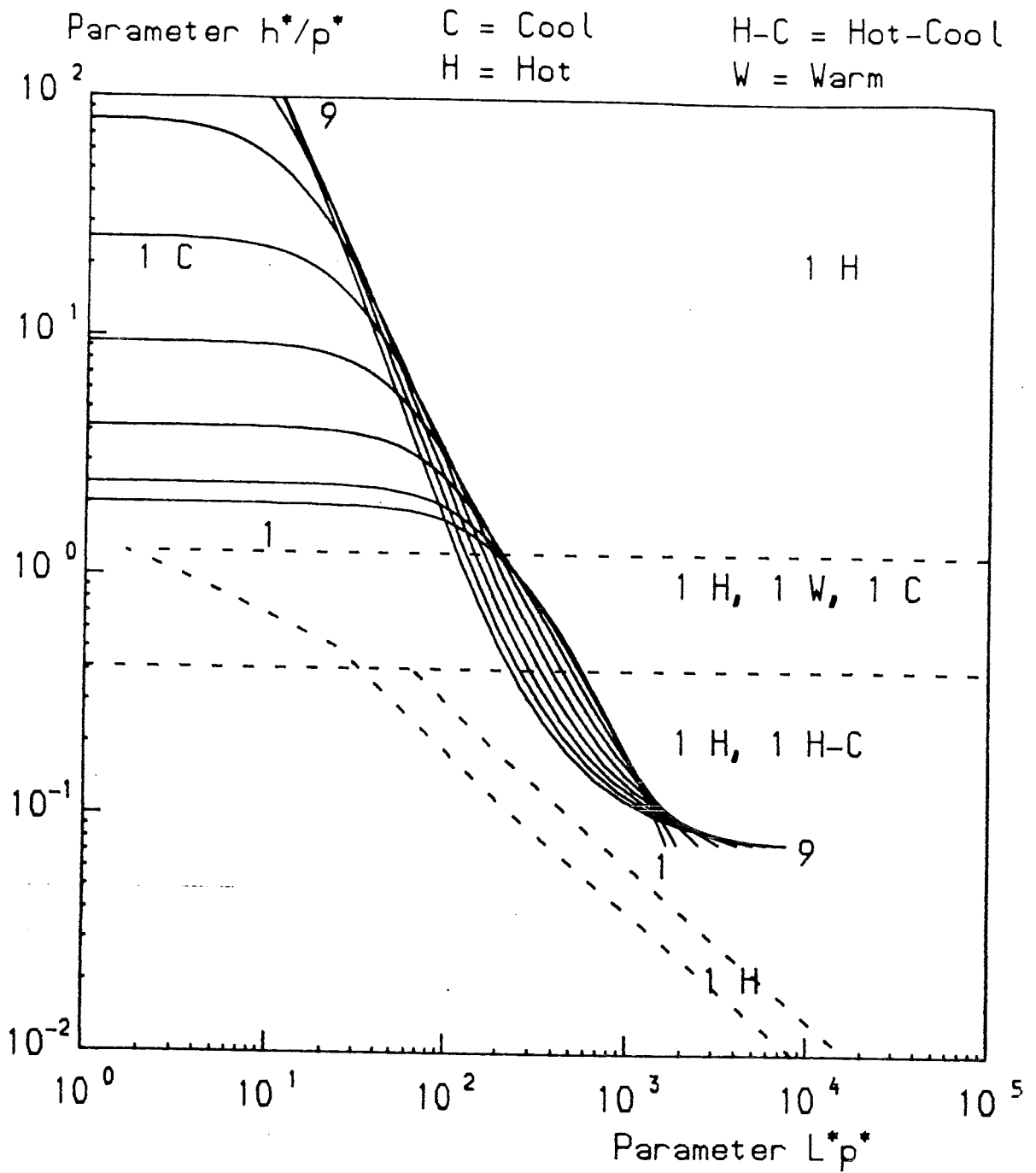


Figure 6.18a The contour describing arcade 1 of section 6.4.4 and the effect on it of shearing the arcade. The contour continues to pass through the same regions of the L^*p^* h^*/p^* plane. Case 1 is the unsharred arcade and subsequent cases denote increased amounts of shear.

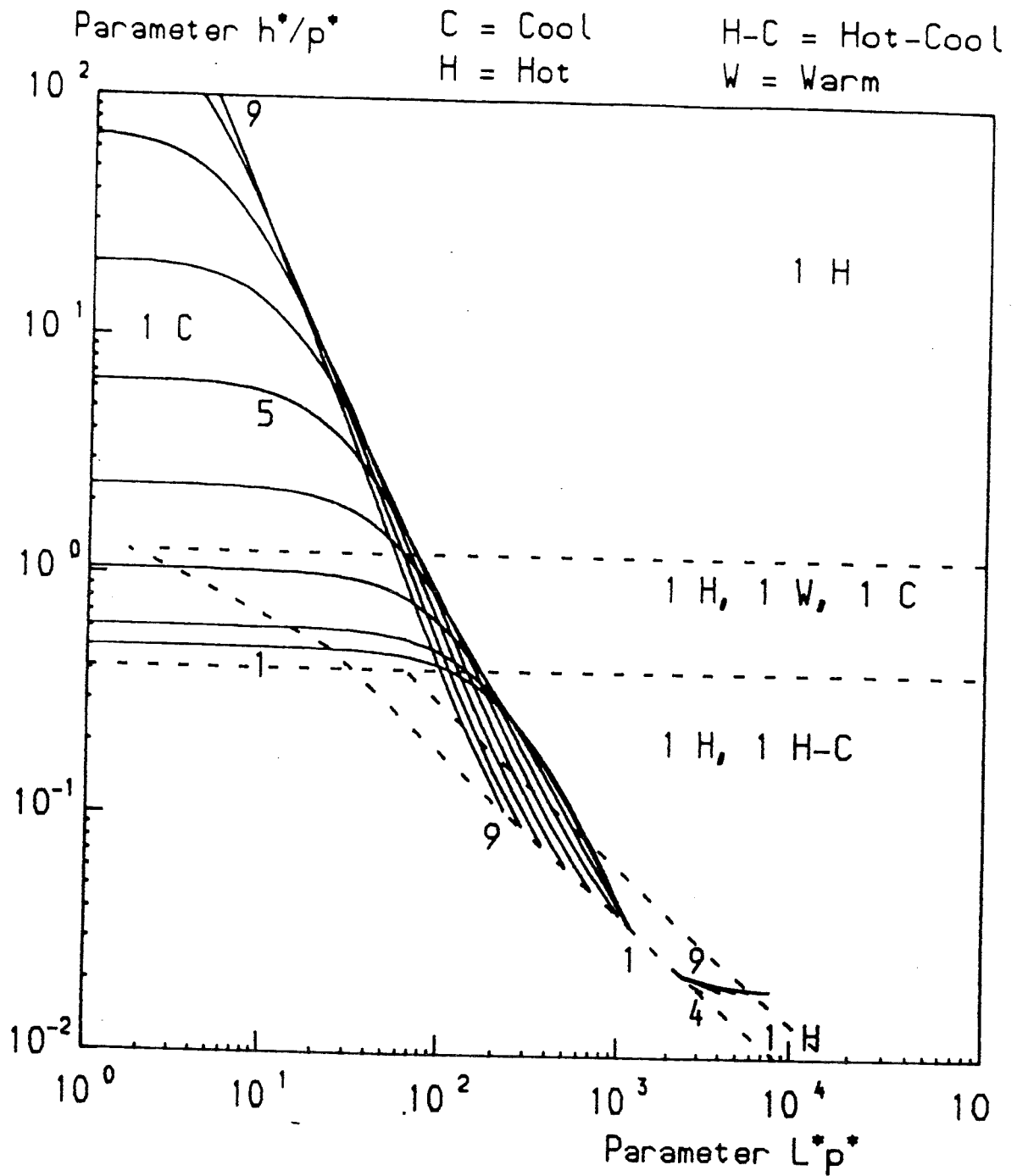


Figure 6.18b The contour describing arcade 2 of section 6.4.4 and the effect on it of shearing the arcade. Once case 4 is reached, hot loops can exist down to the photosphere without a discontinuity. Also, a further regime of equilibria exists at the outer boundary of the arcade, separated from the inner equilibria by a region of non-equilibrium.

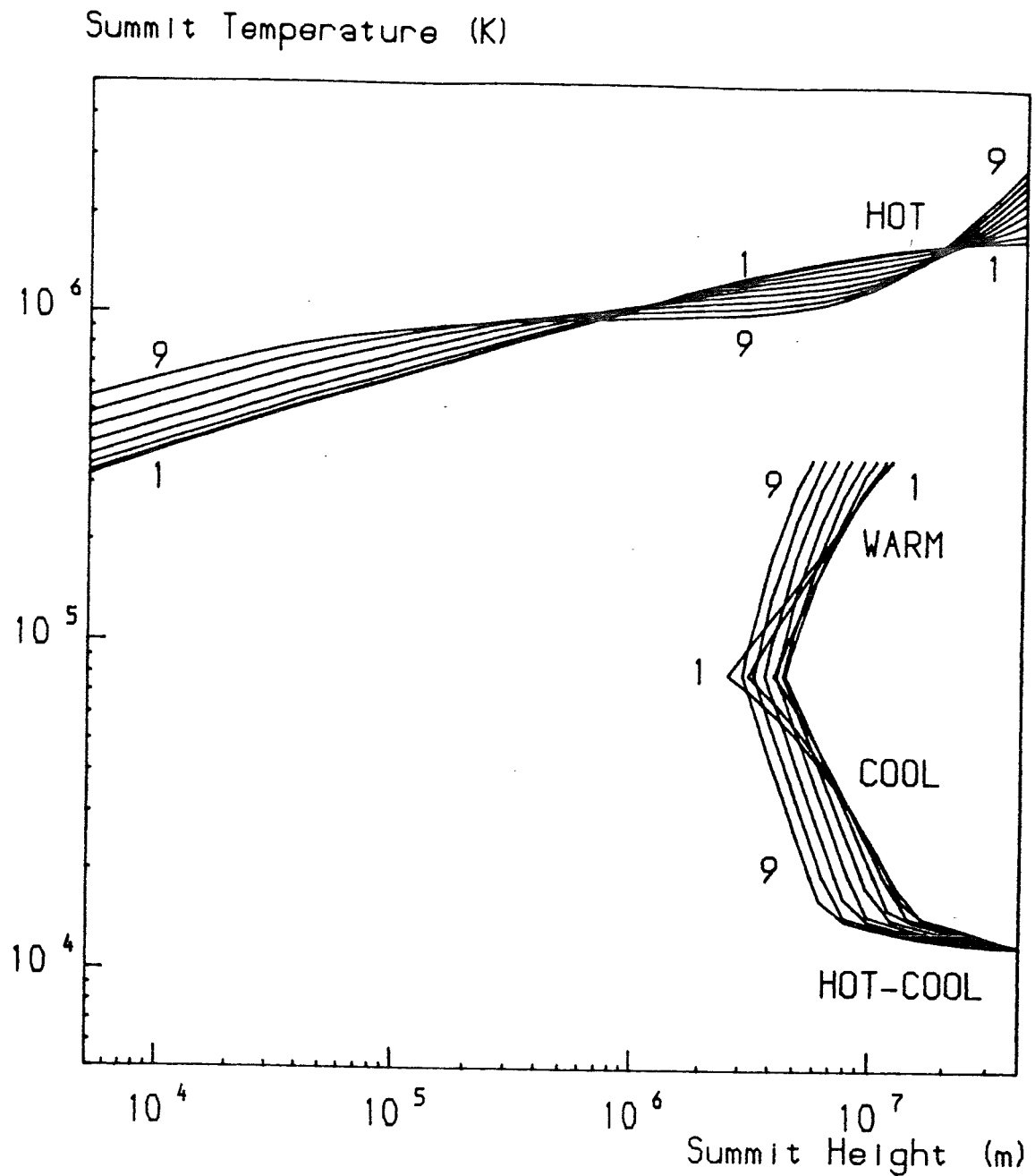


Figure 6.19a The loop summit temperature for arcade 1 of section 6.4.4 as a function of loop summit height and how this profile changes as shear is applied. The basic characteristics of this profile do not change although the minor details do.

Figure 6.19b shows the corresponding figure for arcade 2. One point to notice is that for cases 1 and 2 there is a lower limit to the summit heights of hot (and warm) loops. When the shear is greater than or equal to that for case 4, hot loops (or cool loops onto which the hot loops join smoothly) exist all the way down to the surface. In this case therefore, shearing the arcade removes a cool core. Thus a way of creating a cool core is to unshear the arcade. Near the outer edge of the arcade, equilibrium solutions cannot always be found. For cases 1 to 3, no equilibria exist in the extreme outer part of the arcade while for cases 4 to 9 there is an annulus where no equilibria can exist but either side of this, hot loops may exist. The loops outside this annulus have hotter summits than those beyond the inner edge of the annulus. When the shear is great enough, (cases 8 and 9) hot-cool loops can exist outside the annulus.

6.5 Conclusions

In this chapter several forms of isobaric arcade with their axes below the photosphere have been considered. The first case studied has a coronal heating parameter h^* that is assumed to be independent of the magnetic field of the arcade. Here the situation depends strongly on the parameter h^*/p^* , which is directly proportional to the ratio of coronal heating to pressure in the arcade. There are two critical values of h^*/p^* , 0.41 and 1.25. When h^*/p^* is greater than 1.25, the temperature varies continuously within the arcade. Hot loops exist well away from the photosphere - these join smoothly onto cool loops near the photosphere.

Summit Temperature (K)

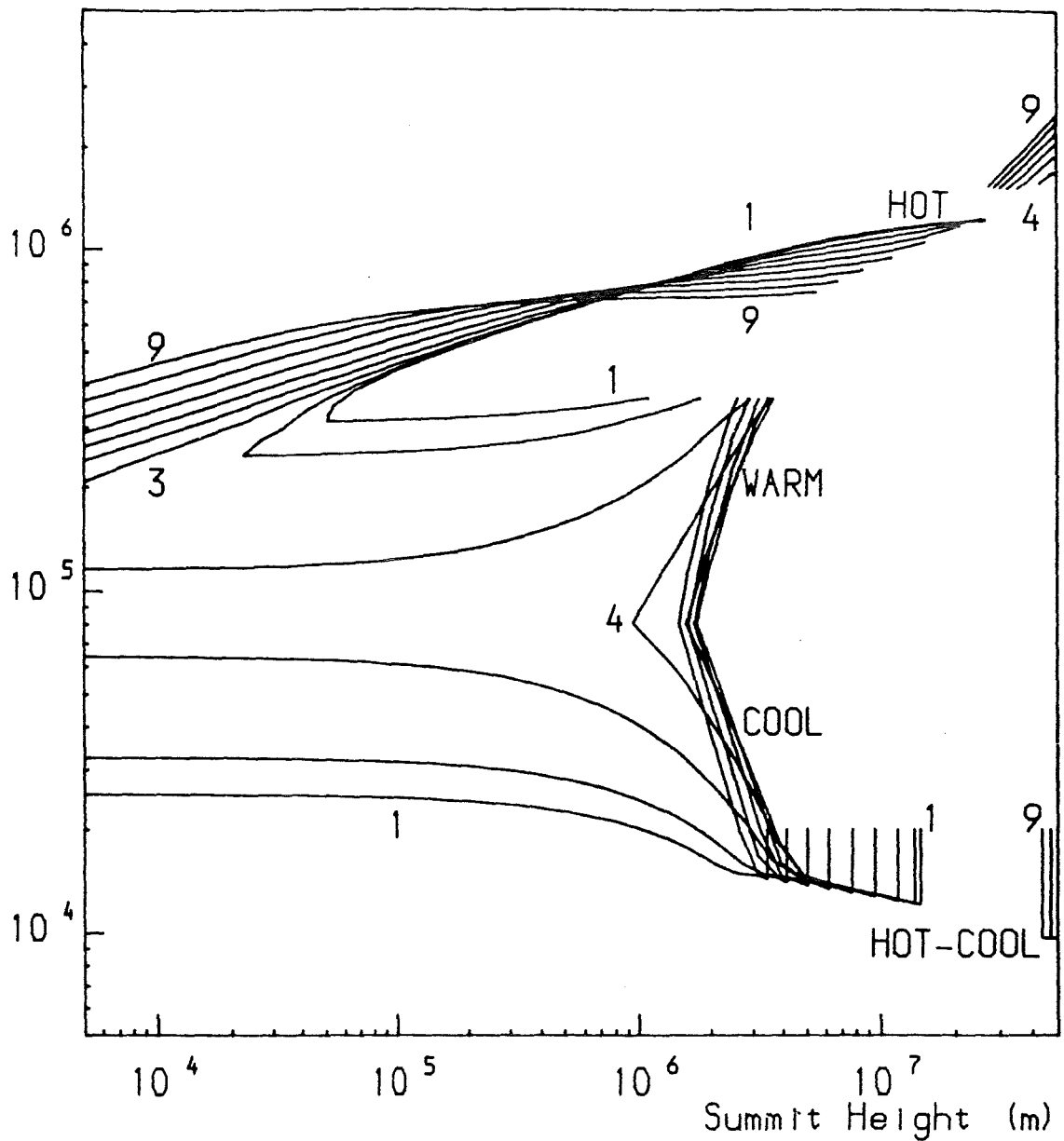


Figure 6.19b The loop summit temperature for arcade 1 of section 6.4.4 as a function of loop summit height and how this profile changes as shear is applied. Once case 4 is reached, the hot loops join smoothly down to the photosphere and further hot loops appear outside the original outer limit of equilibria. Once case 8 is reached, hot-cool loops may appear in this regime as well.

When h^*/p^* lies between 0.41 and 1.25 it is only cool loops that can exist near the photosphere. Higher up cool loops, warm loops and hot loops may all exist. If cool or warm loops exist, there must be a temperature discontinuity near the outermost part of the arcade as the surrounding corona is hotter. Of course, in the outermost part of the arcade, the situation is influenced by the background field which is stronger than the weak outer arcade field. When warm or hot loops exist in the part of the arcade away from the photosphere, there must be a temperature discontinuity between these loops and the cool loops below.

When h^*/p^* is less than 0.41 no equilibria at all may exist near the photosphere. For higher loops hot solutions exist and for higher loops still both hot and hot-cool solutions are possible. If it is hot-cool loops that exist in this area, temperature discontinuities must exist at both the inner and outer edges of the regime of hot-cool loops.

In addition to the parameter h^*/p^* , the thermal structure of the arcade is influenced by d , the depth of the axis below the photosphere. This depth d does not influence the types of thermal structure that occur - it merely influences the summit heights at which they occur. The greater the axial depth d , the less the summit height at which a particular feature occurs.

Instead of the coronal heating parameter being independent of magnetic field strength, it may vary as the square of the field strength. This imposes an upper limit to

the loop summit height at which equilibria can exist.

The thermal structure depends on the depth d of the axis below the photosphere and on $(h/p)_0$, the value of h^*/p^* at the point on the photosphere directly above the axis.

For small values of $(h/p)_0$ i.e. less than 0.41, no equilibrium solutions at all exist near the photosphere. For large d an annulus of hot loops may exist (with perhaps an annulus of hot-cool loops embedded in it if d is sufficiently large), otherwise no equilibria exist in the whole arcade.

When $(h/p)_0$ lies between 0.41 and 1.25 several possibilities exist. Cool loops exist in the region near the photosphere. For low d , these are the only equilibria. When d is higher, the contour describing the arcade passes through areas of cool loops, cool, warm or hot loops, (possibly hot-cool loops depending on the value of d) and hot loops before entering a region of parameter space where no equilibria are possible.

If $(h/p)_0$ is greater than 1.25, the situation does not change greatly. The contour in parameter space now enters the region where cool, warm or hot loops are possible from an area of hot loops instead of cool loops.

Several scenarios have been proposed to model the shearing of an arcade. In the most simple model, both the loop length and magnetic field increase. In the case where coronal heating is independent of magnetic field the existing thermal structure remains but is moved to lower summit

heights.

When coronal heating is dependent on magnetic field strength, both h^*/p^* and L^*p^* increase for each loop in the arcade. This has the effect of allowing equilibria for loops for all summit heights where previously there had been an upper limit to the summit height for which equilibria existed.

This simple shearing model suffers from certain deficiencies. As the shear increases with horizontal distance from the axis, at infinite distance, infinite shear would occur. Also as the magnetic field increases, the arcade is no longer in pressure balance with the surrounding corona.

One solution is to limit the size of the arcade and to conserve pressure balance by scaling the field accordingly. This has the effect of creating a cool core to the arcade and further shear causes there to be no equilibria at all near the photosphere.

The final method investigated of shearing the arcade is to limit the size of the arcade and conserve pressure balance and at the same time conserve flux through the base. This is achieved by allowing the axis to approach the photosphere. This need not cause a fundamental change to the thermal structure of the arcade but in one case studied, shearing had the effect of removing a cool core.

As in Chapter 5, the formation of cool or hot-cool loops is relevant to the formation of prominences.

CHAPTER SEVEN - CONCLUSIONS AND SUGGESTIONS FOR FURTHER WORK

Several projects have been carried out involving equilibria in the solar corona. In these cases, the aim has been to model some fundamental aspects of the equilibrium. In all cases it is possible to refine the model by adding further effects but it is vital to produce and understand simple models before adding refinements.

The model of the erupting coronal mass ejection (Chapter 2) breaks new ground in several ways. The CME is modelled as a bubble rather than a loop, utilising a three-dimensional nature. Before the eruption, the configuration is in a stable equilibrium, a necessity for a quiescent prominence; previous models have had the system erupting from a neutrally stable equilibrium. In the model of Chapter 2, reconnection accelerates the eruption but the reconnection itself is initiated by the eruption, unlike previous models (e.g. Anzer and Pneuman, 1982) where the opposite occurs.

A great many assumptions have been made in constructing the model and generalisation would include the removal of at least some of these assumptions. These include the following :

- 1) It has been assumed that the mass of the prominence remains constant whereas downflows (Engvold, 1976; Cui Lian Shu, 1985) and even upflows (Martres et al, 1981; Malherbe et al, 1983) have been observed. Flows, and in particular downflows can be modelled a) by assuming that

the prominence mass varies as a simple power law function of its height and b) by solving the equation of motion of a particle in the prominence once eruption begins.

2) The existing procedure for modelling reconnection beneath the prominence has been to assume a profile for the magnetic flux in the region as a function of the prominence height. While the profile chosen satisfies several physical requirements, the model could be improved by adapting specialist reconnection models or by using a profile for the flux beneath the prominence which agrees more closely with those found from numerical experiments.

3) So far, the presence of plasma in the cavity and plasma and magnetic field above the bubble have been ignored. Again, this is a reasonable preliminary assumption but a more comprehensive model could be set up that takes these effects into account.

4) Until now only the points at the extreme top of the prominence and bubble have been considered, making this a one-dimensional model (although it reflects in many ways the three-dimensional nature of the system). A two-dimensional model would therefore be more general although a more numerical approach may be required.

5) One topic not considered until now is the physics of coronal mass ejection legs and so it is possible to model changes in the structure of the legs during the eruption.

6) Another important topic is that of global reconnection of the outer field lines of the system, as opposed to the local reconnection already modelled, since this process must occur at some point to prevent an unobserved build up of interplanetary magnetic flux.

The analysis of perturbations to a cylindrically symmetric equilibrium with its axis on the photosphere (Chapter 3) confirms and extends the work of Priest (1988a). Priest found that when such an equilibrium is perturbed by an increase to the base pressure, neighbouring equilibria cannot be found if the field lines are constrained to remain cylindrically symmetrical.

The present treatment has found that if the constraint of cylindrical symmetry is removed, in general neighbouring equilibria are not possible but if the perturbation to the base pressure is such that the pressure is redistributed rather than there being a net change in the total pressure then a neighbouring equilibrium can indeed be found.

Again certain assumptions are made and generalisation of the project includes the relaxation of these assumptions.

It is assumed so far that the plasma pressure above and to either side of the area of magnetic field remains fixed when the arcade is perturbed. If the pressure were allowed to vary it is likely that the constraint would be modified as it depends on the outer boundary condition (3.21). If, however, any change takes place quasistatically the outer boundary condition would remain unchanged.

Magnetic field was assumed to be absent in the external region so a further development would be the addition of such a field either by considering an infinite arcade or by adding a helmet streamer above the existing field region. A further departure from the existing model would be to

consider an initial state which is not in a cylindrically symmetric equilibrium or a perturbation to the base pressure which is not laterally symmetric.

Chapter 4 concerned finding numerical solutions to the equations studied by Hood and Anzer (1988). In addition to actually finding numerically how the temperature varies along a coronal loop, several new regimes of solution have been found, notably the cool solutions for high values of the coronal heating and also the warm solutions.

For the whole of Chapter 4 it is assumed that the loops concerned are of constant cross-sectional area (and hence constant magnetic field along the loop). Another assumption made is that the effects of gravity can be neglected. Again, further work would include the relaxation of these assumptions. Area variation can be included, as can gravity and it is also possible to include a term to take into account rotational forces in loops which exist on stars which rotate quickly. Loops can be considered where the summit boundary condition is that the temperature gradient is a finite value. One possibility here is that the heating term can be ignored. Another development is the analysis of the stability of the various equilibria found in the present work.

Chapters 5 and 6 which deal with arcades consisting of an assembly of coronal loops are based on the work of chapter 4. Here, the thermal structures several forms of arcade are found. In a large proportion of the arcades, there are regions where more than one possible equilibrium exists;

which equilibrium exists in practice will depend on the amount and distribution of energy available and on the stability of the relevant equilibria. In other regions of some of the arcades, (including the outer regions of the arcades where the coronal heating is directly proportional to the square of the magnetic field strength), no equilibria exist subject to the condition that the footpoint temperature gradients are non-negative.

Shearing of certain arcades has been carried out; depending on the shear model used this either creates new equilibria or destroys existing equilibria.

All of the developments mentioned for Chapter 4 can be carried out for Chapters 5 and 6. Allowing the cross-sectional area of a loop to change with space as one moves along the loop allows the analysis of arcades which are not cylindrically symmetrical. In addition, there are several further modifications that can be carried out. So far two general forms of arcade have been considered, namely an arcade incorporating pressure variation which has its axis on the solar photosphere (Chapter 5) and an isobaric arcade with its axis below the photosphere (Chapter 6). The two approaches could be combined i.e. one could consider an arcade with its axis below the photosphere and with pressure variation. There are also various cases that have not been considered e.g. the effects of constraining the heating term to be dependent on the magnetic field strength, or of shearing the arcade have not been considered for the form of arcade considered in Chapter 5.

It is an aim of the thermal analysis of arcades to produce a model for the formation of a prominence as this is a process which is not well understood. In some cases found in Chapters 5 and 6, 'cool' material (at temperatures around 20 000 K) exists at heights consistent with those of prominences. In other cases, as the parameters describing the arcade are changed, equilibria can cease to exist and it would be interesting to set up a system of equations to follow the time evolution of the system.

Although a large number of modifications have been suggested to the models produced in this thesis, it must be remembered that it is necessary to produce a simple model of a phenomenon and to understand the basic processes before adding refinements. The purpose of this thesis has been to produce such basic models.

References

- Amari, T., and Aly, J.J. :1988, *Astron. Astrophysics.*, **208**,
361
- Antiochos, S.K. :1979, *Astrophys J.*, **232**, L125
- Antiochos, S.K. and Noci, G. :1986, *Astrophys J.*, **301**, 440
- Antiochos, S.K., Shoub, E.C., An, C.-H., and Emslie, A.G. :1985,
Astrophys. J., **298**, 876
- Anzer, U. :1968, *Solar Phys.*, **3**, 298
- Anzer, U. and Pneuman, G.W. :1982, *Solar Phys.*, **79**,129
- Anzer, U., and Priest, E.R., :1985, *Solar Phys.*, **95**, 263
- Anzer, U., and Poland, A.I. :1979, *Solar Phys.*, **61**, 95
- Athay, R.G. :1966, *Astrophys. J.*,**145**, 784
- Athay, R.G. :1984, *Astrophys. J.*, **287**, 412
- Ballester, J.L., and Priest, E.R. :1988a, *Dynamics and Structure
of Solar Prominences*, Universitat de les Iles Balears.
eds. J.L. Ballester and E.R. Priest, p. 137
- Ballester, J.L., and Priest, E.R. :1988b, *Dynamics and Structure
of Solar Prominences*, Universitat de les Iles Balears
- Ballester, J.-L. and Priest, E.R. :1989, *Astron. Astrophys.*, in
press.
- Basri, G.S., Linsky, J.L., Bartoe, J.-D.F., Breuckner, G. and Van
Hoosier, M.E. :1979, *Astrophys. J.*, **230**, 924
- Birn, J. and Schindler, K. :1981, Chap. 6 of *Solar Flare MHD*,
(ed. E. R. Priest), Gordon and Breach
- Bonnet, R.M., and Tsiropoula, G. :1981, *Solar Phys.*, **75**, 139
- Browning, P.K. and Priest, E.R. :1986, *Solar Phys.*, **106**, 335
- Cox, D.P., and Tucker, W.H. :1969, *Astrophys. J.*, **157**, 1157
- Craig, I.J.D., McClymont, A.N., and Underwood, J.H. :1978,
Astron. Astrophys., **70**, 1

- Craig, I.J.D., and McClymont, A.N. :1987, *Astrophys. J.*, **318**,
421
- Craig, I.J.D., Robb, T.D., and Rollo, M.D. :1982, *Solar Phys.*,
76, 331
- Crifo, F., Picat, J.T., and Cailloux, M., :1983 *Solar Phys.*, **83**,
143
- Cui Lain-Shu, Hu Ju, Ji Guo-Ping, Ni Xiang-Bin, Huang
You-Ran, Fang Cheng: 1985, *Chin. Astron. Astrophys.*, **9**,
49
- De Haan, D.B. :1939, *Nouvelles Tables d'Integrales Definite*, G.E.
Strecht and Co., New York
- De Moulin, P. and Priest, E.R. :1988, *Astron. Astrophys.*, **206**,
336
- Dollfus, A. :1971, in C.J. Macris (ed.), *Physics of the Solar
Corona*, D Reidel, p.97
- Dungey, J.W. :1953, *Mon. Not. Roy. Astron. Soc.*, **113**, 180
- Dupree, A.K., and Goldberg, L., :1967, *Solar Physics.*, **1**, 229
- Engvold, O. :1976, *Solar Phys.*, **49**, 283
- Fisher, R.R. :1972, *Solar Phys.*, **24**, 385
- Fisher, R.R. :1984, *Adv. Space Res.*, **4**, 163
- Foukal, P.V. :1975, *Solar Phys*, **43**, 327
- Foukal, P.V. :1976, *Astrophys. J.*, **210**, 578
- Foukal, P.V. :1981, *Astrophys. J.*, **245**, 304
- Gosling, J.T., Hildner, E., MacQueen, R.M., Munro, R.H., Poland
A.I., and Ross, C.L. :1976, *Solar Phys.*, **48**, 389
- Habbal, S. and Rosner, R. :1979 *Astrophys. J.*, **234**, 1113
- Harrison, R.A. :1986, *Astron. Astrophys.*, **162**, 283
- Heyvaerts, J., Lasry, J.M., Schatzman, M. and Witomsky, G. :
1982, *Astron. Astrophys.*, **111**, 104
- Hildner, E. :1971, Ph.D. Thesis, Univ. of Colorado
- Hildner, E. :1974, *Solar Phys.*, **35**, 123

- Hildner, E., Gosling, J.T., MacQueen, R.M., Munro, R.H., Poland, A.I., and Ross, C.L. :1976, *Solar Phys.*, **48**, 127
- Hildner, E. et. al. :1986, *Proc. Solar Max. Mission Workshop*, Chap 6
- Hood, A.W. :1983, *Solar Phys.*, **87**, 279
- Hood, A.W. :1985, in E.R. Priest (ed.) *Solar System Magnetic Fields*, D. Reidel Publ. Co., Dordrecht, Holland, Ch. 4
- Hood, A.W. and Anzer, U. :1988, *Solar Phys.*, **115**, 61
- Hood, A.W. and Priest, E. R. :1979, *Astron. Astrophys.*, **77**, 233
- Hood, A.W., and Priest, E.R. : 1980, *Solar Phys.*, **66**, 113
- Howard, R.A., Sheeley, N.R., Koomen, M.J., and Michels, D.J. :1985, *J. Geophys. Res.*, **90**, 8173
- Hundhausen, A.J., MacQueen, R.M., and Sime, D.G. :1984, *Trans AGU*, **65**, 1069
- Hundhausen, A.J., Sawyer, C.B., House, L., Illing, R.M.E., and Wagner, W.J. : 1984a, *J. Geophys. Res.*, **89**, 2639
- Hundhausen, A.J. et. al. :1984b, Chap 6 of "*Solar Terrestrial Physics ; Present and Future*", (eds. D. Butler and K. Papadopolous), NASA Ref. Publ. 1120
- Jackson, B.V. :1981, *Solar Phys.*, **73**, 133
- Jackson, B.V., and Hildner, E. :1978, *Solar Phys.*, **60**, 155
- Kippenhahn, R., and Schluter, A. :1957, *Z. Astrophys.*, **43**, 36
- Kuperus, M., and Raadu, M. :1974, *Astron. Astrophys.*, **31**, 189
- Kuperus, M., and Van Tend, W. :1981, *Solar Phys.*, **71**, 125
- Landini, M., and Monsignori Fossi, B.C., :1975, *Astron Astrophys.*, **42**, 213
- Landini, M., and Monsignori Fossi, B.C., :1981, *Astron. Astrophys.*, **102**, 391
- Leroy, J.L. :1988, p33 of Ballester and Priest (1988)
- Leroy, J.L., Bommier, V., and Sahal-Brechot, S.: 1984, *Astron. Astrophys.*, **131**, 33

- Levine, R.H., and Withbroe, G.L. :1977, *Solar Phys.*, **51**, 83
- Low, B. C. :1981, *Astrophys. J.*, **251**, 352
- Low, B.C. :1986, in J.P. Swings (ed.) *Highlights of Astron.*, IAU Symp. **7**, 243
- McWhirter, R.W.P., Thoneman, P.C., and Wilson, R. :1975, *Astron. Astrophys.*, **40**, 63
- MacQueen, R.M. :1980, *Phil. Trans. R. Soc. London.*, **297**, 605
- MacQueen, R.M., and Cole, D.M. :1985, *Astrophys. J.*, **299**, 526
- Malherbe, J.M., Schmieder, B., Ribes, E. and Mein, P. :1983, *Astron. Astrophys.*, **119**, 197
- Martres, M.J., Mein, P., Schmieder, B., and Soru-Escout, I. :1981, *Solar Phys.*, **69**, 301
- Menzel, D.H. :1951, *Proceedings of Conference on Dynamics of Ionised Media*, London
- Mouschovias, T.C. and Poland, A.I. :1978, *Astrophys. J.* **220**, 675
- Munro, R.H., Gosling, J.T., Hildner, E., MacQueen, R.M., Poland, A.I., and Ross, C.L. :1979, *Solar Phys.*, **61**, 201
- Pneuman, G.W. :1980, *Solar Phys.*, **65**, 369
- Poland, A.I. and Anzer, U. :1971, *Solar Phys.*, **19**, 401
- Priest, E.R. :1978, *Solar Physics*, **58**, 57
- Priest, E.R. :1981, *Solar Active Regions*, (Ed. F. Orral), Cole Ass. Univ. Press, p213
- Priest, E.R. :1982 *Solar Magnetohydrodynamics*, D. Reidel Publ. Co., Dordrecht, Holland
- Priest, E.R. :1988a, *Astrophys. J.* **328**, 848
- Priest, E.R. :1988b, *The Dynamics and Structure of Quiescent Solar Prominences*, D. Reidel
- Priest, E.R., and Forbes, T.G. :1989, *Solar Phys.*, submitted
- Priest, E.R., Hood, A.W., and Anzer, U. :1989, *Astrophys. J.* (In Press)
- Priest, E.R. and Smith, E.A. :1979, *Solar Phys.*, **64**, 267

- Raadu, M. :1972, *Solar Phys.*, **22**, 425
- Rabin, D., and Moore R.L., :1984, *Astrophys. J.* **285**, 359
- Raymond, J.C., and Smith, B.W. :1977, *Astrophys J. Suppl.*, **35**,
419
- Rosner, R., Tucker, W.H., and Vaiana, G.S. :1978. *Astrophys J.*, **220**,
643
- Sakurai, T., and Levine, R.H. :1981. *Astrophys. J.*, **248**, 817
- Serio, S., Vaiana, G.S., Godoli, G., Matta, S., Pirronello, V.,
and Zappala, R. :1978, *Solar Phys.* **59**, 65
- She, Z.S., Malherbe, J.M. and Raadu, M.A. :1986, *Astron. Astrophys*
164, 364
- Sheeley, N.R., Bohlin, J.D., Breuckner, G.E., Purcell, J.D.,
Sherrer, V., and Tousey, R. :1975, *Solar Phys*, **40**, 103
- Sheeley, N.R.Jr., Howard, R.A., Michels, D.J. and Koomen, D.J.
:1980 in IAU Symp. 91, *Solar and Interplanetary
Dynamics*, Dryer and Tandberg-Hanssen (eds.), D. Reidel.
- Sime, D.G. :1989, *J. Geophys. Res.*, **94**, 158
- Spitzer, L. :1962, *Physics of Fully Ionised Gases*, 2nd edition,
Wiley, Inter-Science, New York.
- Steele, C.D.C., Hood, A.W., Priest, E.R., and Amari, T. :1989,
Solar Phys., **123**, 127
- Steele, C.D.C., and Priest, E.R. :1988, *Dynamics and Structure
of Solar Prominences*, Universitat de les Iles Balears.
eds. J.L. Ballester and E.R. Priest, p. 157
- Steele, C.D.C., and Priest, E.R. :1989a, *Solar Phys.*, **119**, 157
- Steele, C.D.C., and Priest, E.R. :1989b, *Solar Phys.*, in Press
- Steele, C.D.C., and Priest, E.R. :1989c, *Solar Phys.*, submitted
- Tandberg Hanssen, E. :1974, *Solar Prominences*, Geophysics
and Astrophysics Monographs **12**, D. Reidel, Dordrecht.
- Tandberg Hanssen, E., and Anzer, U. :1970, *Solar Phys*, **15**,
158

- Tucker, W.H., and Koren, M. :1971, *Astrophys. J.*, **168**, 283
- Vaiana, G. S., Krieger, A.S., and Timothy, A.F., :1973, *Solar Phys.*, **32**, 81
- Van Tend, W., and Kuperus, M. :1978, *Solar Phys.*, **59**, 115
- Vernazza, J.E., Avrett, E.H., and Loeser, R. :1981, *Astrophys. J. Supplement*, **45**, 635
- Wagner, W.J. :1984, *Ann. Rev. Astron. Astrophys.*, **22**, 267
- Webb, D.F., and Hundhausen, A.J. :1987, *Solar Phys.* **108**, 383
- Wolfson, R.L.T. :1982, *Astrophys. J.* **255**, 774
- Wragg, M.A., and Priest. E.R., :1981. *Solar Phys.* **70**, 293
- Yeh, T and Dryer, M :1981, *Solar Phys.* **71**, 149
- Zwingmann, W. :1985, PhD thesis, Bochum University